THE THERMAL-MECHANICAL ANALYSIS OF TARGETS FOR THE HIGH VOLUME PRODUCTION OF MOLYBDENUM-99 USING A LOW-ENRICHED URANIUM METAL FOIL

A Dissertation

presented to

the Faculty of the Graduate School

at the University of Missouri

In Partial Fulfillment

of the Requirement for the Degree

Doctor of Philosophy

By

KYLER KRIENS TURNER

Dr. Gary Solbrekken, Dissertation Supervisor

JULY 2012

The undersigned, appointed by the dean of the Graduate School, have examined the dissertation entitled

THE THERMAL-MECHANICAL ANALYSIS OF TARGETS FOR THE HIGH VOLUME PRODUCTION OF MOLYBDENUM-99 USING A LOW-ENRICHED URANIUM METAL FOIL

presented by Kyler Kriens Turner,

a candidate for the degree of Doctor of Philosophy

and hereby certify that in their opinion it is worthy of acceptance.

_____

Dr. Gary Solbrekken

_____

Dr. Robert Winholtz

_____

Dr. Hongbin Ma

_____

Dr. William Miller

_____

Dr. Stephen Montgomery-Smith

DEDICATION

For my Mom, Dad, Brother, Aunts, Uncles and Grandparents.

ACKNOWLEDGMENTS

TABLE OF CONTENTS

LIST OF FIGURES

xiii

LIST OF TABLES

NONMENCLATURE

General

A	area
C	Celsius
Ci	Curie
E	Young's Modulus
f	fission
g	gram
h	heat transfer coefficient
J	Joule
K	Kelvin
k	thermal conductivity
L	length
L_c	characteristic length
M_T	thermal moment
m	meters
n	neutron
Pa	Pascal
P	pressure
q	power
q"	heat flux
R	thermal resistance
R_g	gas constant
r	radius
s	seconds
T	temperature
TC	thermocouple
t	thickness
v	volume
V	volts
W	watts

Greek

α	coefficient of thermal expansion
β	beta particle
γ	gamma-ray
Δ	difference
υ	Poisson's ratio
ω	z-axis deflection

Abbreviations

AHR	aqueous homogenous reactor
ANL	Argonne National Lab
BR2	Belgium Reactor 2
DOE	Department of Energy
FGR	fission gas release
GTRI	Global Threat Reduction Initiative
HEU	highly enriched uranium
HFR	High Flux Reactor
IAEA	International Atomic Energy Agency
IRE	Institute for Radioelements
LEU	low enriched uranium
MAPLE	Multipurpose Applied Physic Lattice Experiment
MIR	Morgridge Institute for Research
MURR	University of Missouri Research Reactor
NNSA	National Nuclear Security Administration
NRC	Nuclear Regulatory Commission
NRU	National Research Universal
OECD	Organisation for Economic Co-operation and Development
RERTR	Reduced Enrichment for Research and Test Reactors Program

ABSTRACT

Molybdenum-99 diagnostic imaging is the most commonly practiced procedure in nuclear medicine today with the majority molybdenum-99 produced with proliferation sensitive HEU. International and domestic efforts to develop non-HEU production techniques have taking the first steps toward establishing a new non-HEU molybdenum-99 based supply chain. The focus of the research presented in this work is on the analysis of a new high U-235 density LEU based molybdenum-99 production target. Converting directly to LEU using current manufacturing techniques greatly reduces the molybdenum-99 yield per target making high volume production uneconomical. The LEU based foil target analyzed in this research increases the yield per target making economic high volume production with LEU possible.

The research analyzed the thermal-mechanical response of an LEU foil target during irradiation. Thermal-mechanical studies focused on deflections and stresses to assess the probability of target failure. Simpler analytical models were used to determine the proper shape of the target and to benchmark the numerical modeling software. Numerical studies using Abaqus focused on analyzing various heating and cooling conditions and assessing the effects of curvature on the target. Finally, experiments were performed to simulate low power heating and further benchmark the models. The results from all of these analyses indicate a LEU foil target could survive irradiation depending on the conditions seen during irradiation.

CHAPTER 1: INTRODUCTION

Forward: A Brief History of Nuclear Medicine

The use of radiation in medicine to both diagnose and treat various ailments has been in practice since its discovery. In 1895 the German physicist Wilhelm Konrad Roentgen observed crystals of barium platinocyanide luminescing when placed near a highly evacuated electrical discharge tube. Experimentation indicated the density of the object greatly affected the attenuation of this luminescent energy and would ultimately lead to the development of X-ray imaging technology; the first use of radiation in the medical field [1].

In 1932 Cockcraft and Walton produced the first man-made neutron deficient isotopes using a particle accelerator. Shortly after, in 1938, Dr. Robley D. Evans of the Massachusetts General Hospital and members of the Massachusetts Institute of Technology used iodine-138 to observe isotope uptake in the thyroid gland of rabbit. In 1950 the first localized radiation scanner was developed and designed specifically for the study of iodine-138 uptake in the thyroid gland. Soon after the first whole body scanner was developed by Donner Laboratory. In the 1960's technology continued to advance developing to the point where nuclear medicine was considered a medical specialty in its own right [1].

Radiopharmaceuticals

Approximately 95% of all radiopharmaceuticals are used for diagnostic purposes. Diagnostic radiopharmaceuticals are designed to develop internal images of the patient with damaging tissue while therapeutic radiopharmaceuticals are designed to damage the

target tissue. Radiopharmaceuticals consist of two components, the radionuclide, which is the radioactive isotope and the pharmaceutical, which is delivery agent. The characteristics of both will determine how the radiopharmaceutical is administered and used. Designing a radiopharmaceutical starts by finding a non-toxic pharmaceutical that will concentrate in the target organ such as the heart. Next the radionuclide is paired (tagged) with this pharmaceutical and injected into the patient. The uptake of the radiopharmaceutical and the emission of radiation that follows allows imaging of the organ [2].

The ideal diagnostic radiopharmaceutical will have several characteristics making it both safe and effective. First, a reliable and readily available supply should exist. Second, the effective half-life, a combination of the physical half-life and the biological half-life, should be short minimizing patient dose. Finally, a diagnostic radiopharmaceutical must emit a gamma-ray allowing for the radiation to escape the patient's body for imaging. [2].

Technetium-99m

Technetium-99m is only one example of the many medical man-made isotopes utilized today. Technetium-99m is the product of molybdenum-99 decay, has an atomic number of 43, has an approximate half-life of six hours, and is in a metastable state [3]. The nuclear decay equations below show the complete decay chain of molybdenum-99 into stable ruthenium-99,

$$^{99}Mo \rightarrow ^{99m}Tc + \beta^-$$

$$^{99m}Tc \rightarrow ^{99}Tc + \gamma$$

$$^{99}Tc \rightarrow ^{99}Ru_{Stable} + \beta^-$$
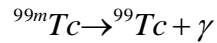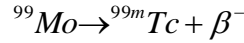
where Mo is molybdenum, Tc is technetium, Ru is ruthenium, γ is a gamma ray, and β^- is a beta particle. A visual representation of these equations can be seen in the decay scheme of molybdenum-99 in Figure 1.
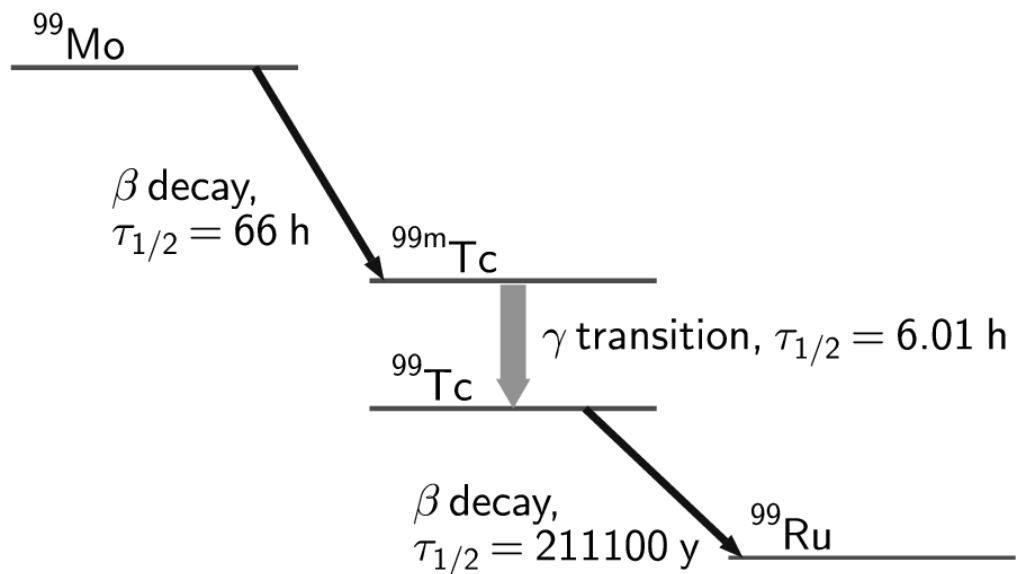
Figure 1. Molybdenum-99 decay scheme [4]

In 1965 Brookhaven National Lab produced the first technetium-99m generator allowing for the collection or "milking" of the technetium-99m from molybdenum-99 decay [5, 6]. Technetium-99m's short half-life makes stockpiling and long distance transportation difficult, thus molybdenum-99's longer half-life is used to increase stockpiling and transportation distance. The parent daughter relationship between molybdenum-99 and technetium-99m is a non-equilibrium relationship meaning, the

daughter's half-life is shorter than the parent's half-life. The half-lives of molybdenum-99 and technetium-99m allow for the milking, or removal of technetium-99 from the generator, once a day. Column chromatography is used to separate the two isotopes during the milking process. This process separates the isotopes into negatively charged particles of TcO_4^- and MoO_4^{2-}. The single negative charge on the TcO_4^- adheres to the alumina sorbent in the generator far less than the double negative charge on the MoO_4^{2-}. A saline solution is used to flush the free floating TcO_4^- from the generator producing a saline solution full of technetium-99m [5, 6]. An image of a technetium-99m generator and a diagram illustrating the internal layout of a generator can be seen in Figure 2.
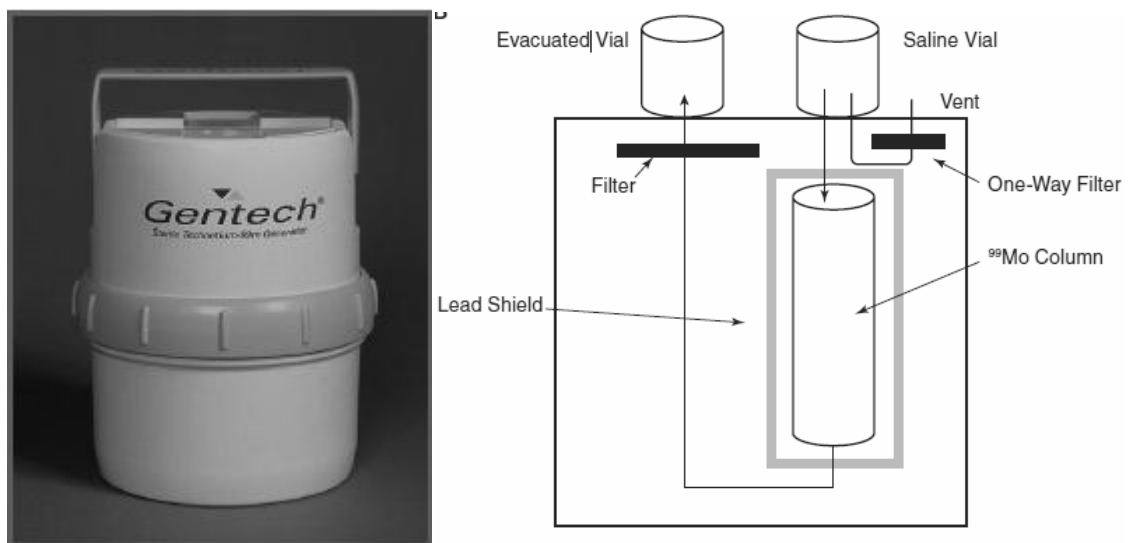
Figure 2. Technetium-99m generator and diagram showing its function [7]

Technetium-99m, from a medical stand point, is the ideal radiopharmaceutical for several reasons. First, the technetium-99m generator is easy to transport and store with limited exposure. Shielding required for the average activity transported is approximately 2 cm of lead. Second, a six hour half-life is short; minimizing the patient's radiation dose. On average a person injected with technetium-99m will return to background radiation

4

levels within 2.5 days. Finally, technetium-99m only emits gamma rays at 140 keV, allowing the gamma-rays to leave the patient's body while limiting the radiation dose administrated [6].

Examples of Technetium-99m Usage

Technetium-99m is used globally to diagnose various diseases and image various organs. Technetium-99m is used in a wide variety of imaging test such as bone scans, functional brain imaging, cardiac stress test, and Single Photon Emission Computed Tomography (SPECT). Bone scans are used to investigate areas of unusual bone building activity. The osteoblast of the bone is the target for technetium-99m uptake and can be used to identify possible fractures and bone tumors [2]. An image of technetium-99m uptake during a bone scan can be seen in Figure 3 where the dark areas indicate the greatest amount of technetium-99m uptake.
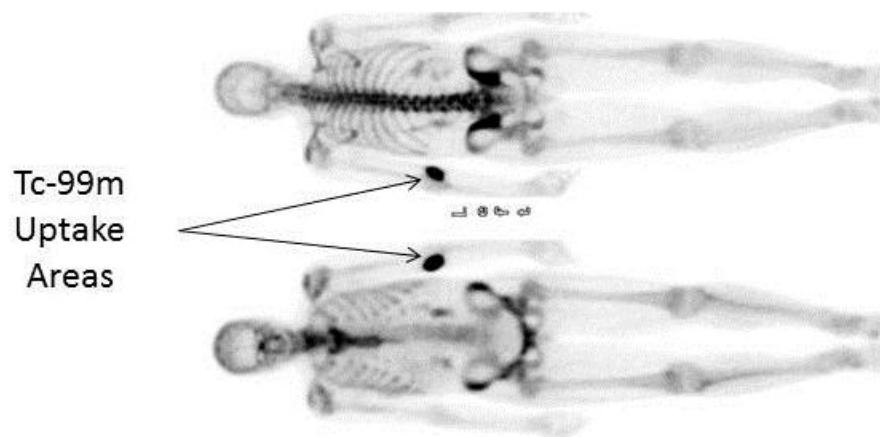
Figure 3. Bone scan using technetium-99m [8]

Functional brain imaging is used to investigate the blood flow and metabolism in the brain. An example of a functional brain image can be seen in Figure 4.
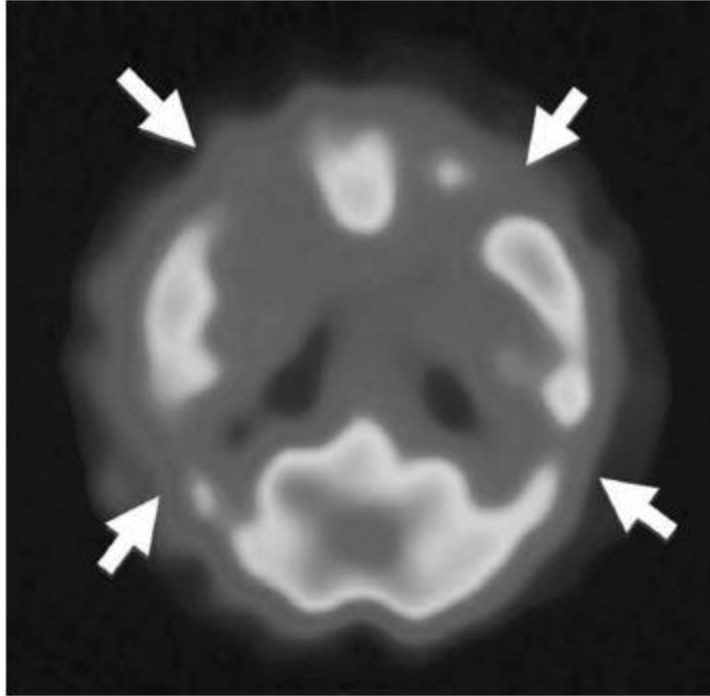
Figure 4. Functional brain image example [7]

The patient in this image is suffering from Alzheimer's and the arrows indicate areas of low blood flow caused by the disease [7].

Cardiac stress tests measure the heart's response to external stress such as exercising. Myocardial perfusion imaging (MPI) is commonly used to perform this investigation. An image of a MPI can be seen in Figure 5 where arrows indicate areas of concern identified during the stress test.
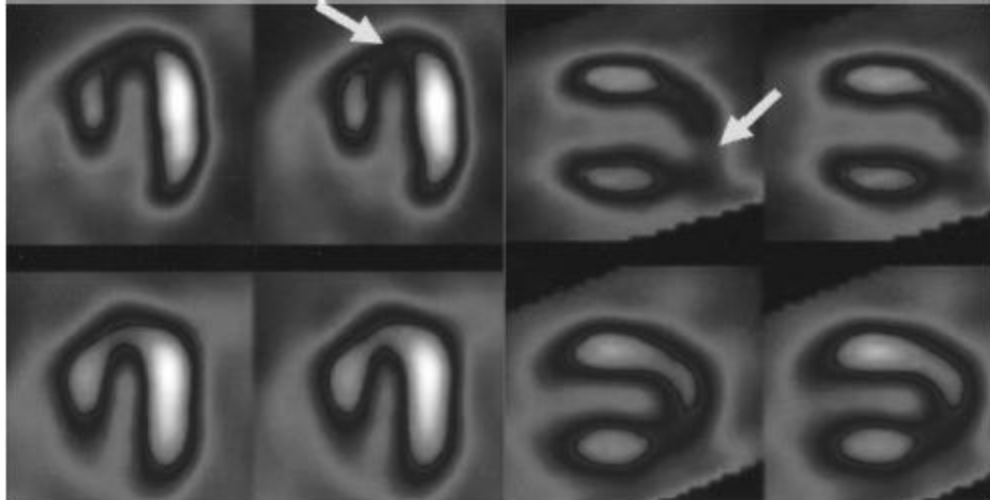
Figure 5. MPI image during stress test [7]

SPECT is similar to MPI but it can obtain real-time three dimensional images of various organs. A heart image obtained through SPECT can be seen in Figure 6 where the arrows indicate areas of concern found during the test.
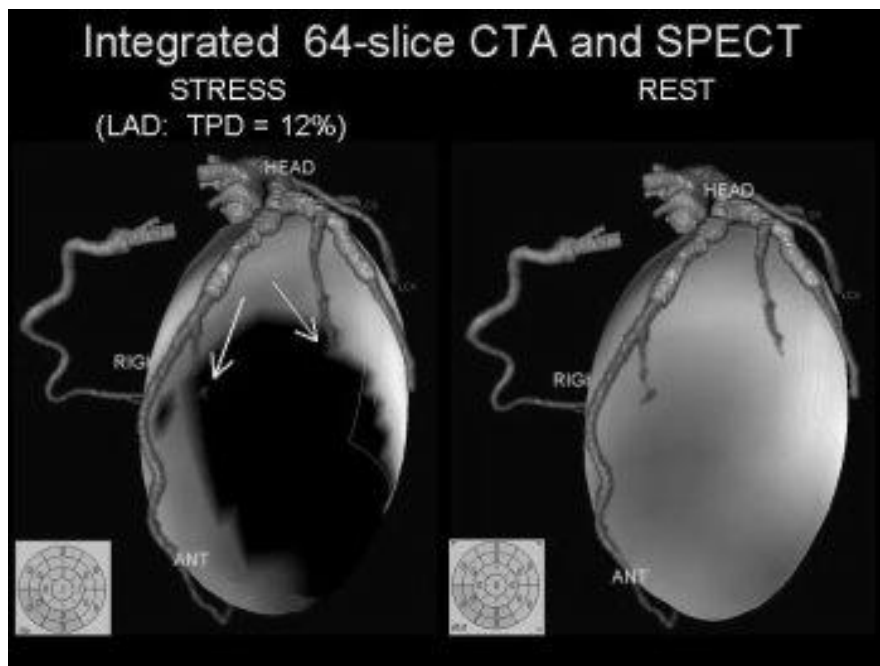
Figure 6. SPECT image during a heart stress test [9]

The MAPLE Reactors and Recent Molybdenum-99 Shortages

Recently maintaining a consistent reliable supply of molybdenum-99 has been an issue for the molybdenum-99 production community. In the mid 1990's Canada began developing the Multipurpose Applied Physics Lattice Experiment (MAPLE) reactors. The MAPLE reactors were built to replace the aging National Research Universal (NRU) reactor in Chalk River, Ontario, which has been operating since 1957. The NRU reactor is the largest global supplier of molybdenum-99, providing 40% of the global supply and 60% of the United States' supply [10]. When completed the MAPLE reactors would supply up to 200% of the global molybdenum-99 demand reliving the aging infrastructure of this duty. An image of the MAPLE reactors facility can be seen in Figure 7.

Figure 7. MAPLE reactor facilities in Canada [11]

During commissioning in 2000, the MAPLE reactors experienced an unexpected and alarming behavior. In June 2003 it was announced the reactors had a positive

coefficient of reactivity, meaning the reactors could become unstable and uncontrollable. After five years and millions of dollars' worth of investigation and modification, the exact cause of the positive coefficient could not be identified and in May 2008 the MAPLE reactor project was terminated [10].

The MAPLE reactors were expected to supply an abundance of molybdenum-99 throughout the world, thus governments and industry did not invest in new molybdenum-99 production facilities or alternative forms of production. Recently the unexpected shutdown of the NRU reactor and the Petten reactor in 2008 and 2010 created a global molybdenum-99 shortage. This revealed the many weaknesses in the current molybdenum-99 production system and illustrated the need to develop new molybdenum-99 production methodologies [12].

International Molybdenum-99 Production Conversion Issues

Currently the majority of international of molybdenum-99 production is based on highly enriched uranium (HEU) or uranium that contains at least 20% fissionable U-235. The international nuclear nonproliferation community focuses on the minimization of HEU, as HEU is the main component in a uranium based nuclear weapon. Low enriched uranium (LEU) which contains less than 20% fissionable U-235, is the preferred alternative to HEU, as it is impractical in a uranium based nuclear weapon [7].

During irradiation, U-235 in either the HEU or LEU is bombarded with neutrons causing nuclear fission. During this reaction energy is released along with fragments, commonly called fission products, from the U-235 nucleus. Many different isotopes can be produced as fission produces but certain isotopes will be produced in greater amounts.

Molybdenum-99 is one of the most abundant isotopes produced during fission at a 6% fission yield. The yield of various other fission products including molybdenum-99 can be seen in Figure 8.
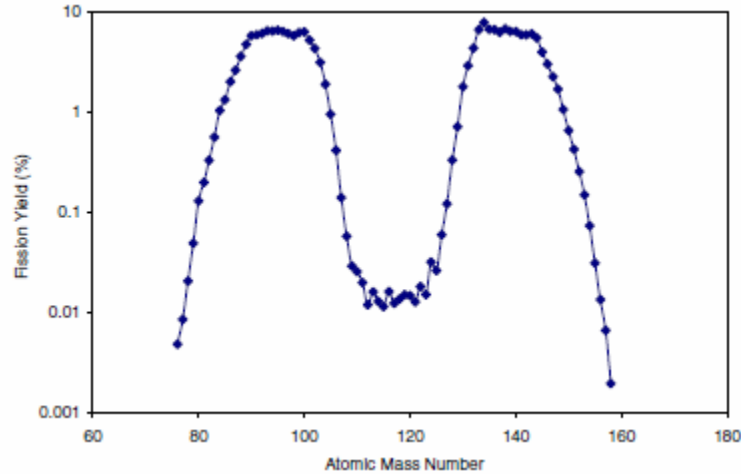
Figure 8. Fission yield from U-235 [7]

The majority of reactors currently irradiate targets manufactured using HEU dispersion technology, enriched to approximately 90% U-235. Producing an HEU dispersion target begins by mixing HEU powder with aluminum powder. The powders are then heated and compressed into various geometries, forming a solid target. When using HEU dispersion methods the total uranium density is ~2.0 g/cm^3 with a U-235 density at 90% enrichment, of ~1.8 g/cm^3. When using dispersion technology with LEU, the total uranium density is still ~2.0 g/cm^3, but the U-235 density will decrease to ~0.4 g/cm^3, 20% of the total uranium density. The decrease in U-235 will reduce the amount of molybdenum-99 yield per target. Molybdenum-99 production using LEU will require the irradiation of five times the amount of targets to obtain HEU comparable yields. Increasing the number of targets will increase the cost of molybdenum-99 production making it uneconomical and unattractive to the high volume molybdenum-99 production

community. Figure 9 gives the molybdenum-99 activities produced with the HEU powder

dispersion method and the LEU dispersion method under irradiation conditions at the

University of Missouri Research Reactor (MURR), which are a 7 day irradiation time, a

6% fission yield for molybdenum-99, and a thermal neutron flux of 2.0 x 10^{14} n/cm^{2}s. It

is clear there is a drastic decrease in molybdenum-99 yield when LEU is used in the

dispersion target.
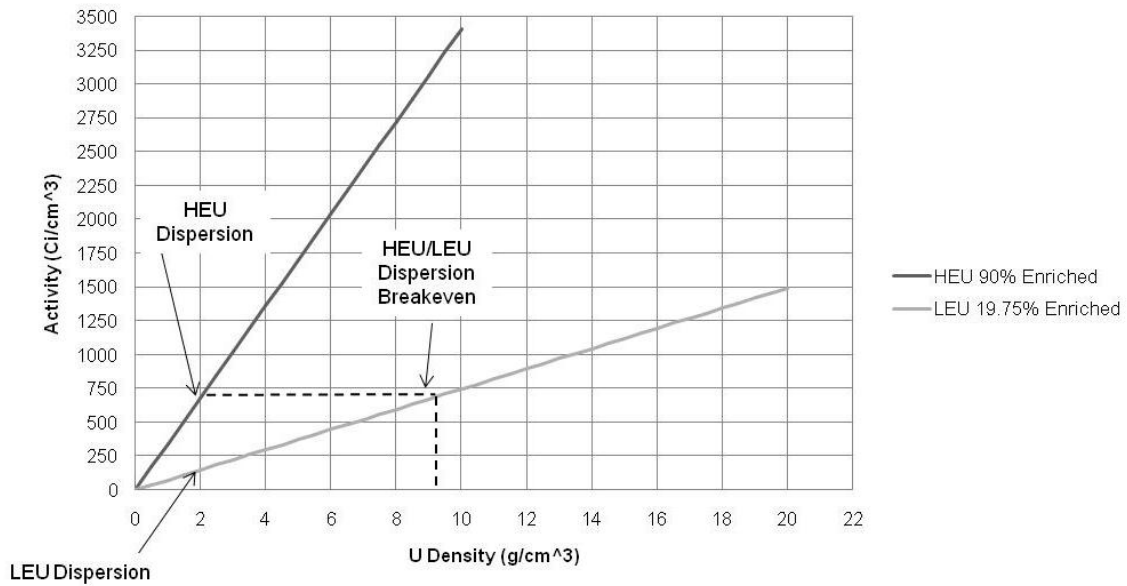
Figure 9. Comparison of activities with HEU and LEU dispersion

Future Techniques for International Moolybdenum-99 Production without HEU

It is obvious a direct conversion to LEU will produce a drastic decrease in

molybdenum-99 yield. A uranium density of ~9.0 g/cm^3, which is not technically feasible

with dispersion target technology, is needed to reach the HEU/LEU dispersion breakeven

point. As part of the first step toward conversion, all the current international

molybdenum-99 producers have committed to convert to LEU dispersion targets by the

end of 2015 [13-16], greatly affecting their molybdenum-99 yields. In the current high volume molybdenum-99 production environment this will be uneconomical and impractical for long term production [7]. A new target technology is needed to reach practical and economical production.

Several technologies have been developed to each economical production. The U_3Si_2 dispersion target is manufactured in a similar fashion as the traditional dispersion target. The uranium density using this technique is ~6 g/cm^3, three times the uranium density as a traditional LEU dispersion target. However, this is still below the 9 g/cm^3 LEU/HEU breakeven point and will only produce a ~450 Ci/cm^3 worth of activity [17]. An LEU atomized powder method is currently under development by the Korea Atomic Energy Research Institute (KAERI) [18, 19]. The atomized process uses a novel approach to pack the uranium in the target and has a theoretical uranium density of 8.5 g/cm^3. However it will be many years before this technique can be implemented in a high volume production environment. LEU foil technology uses a metal foil composed of LEU, with thicknesses between 125 μm-140 μm[20] incased in aluminum cladding. Total uranium densities using this technique will be ~18 g/cm^3; yielding a U-235 density of 3.8 g/cm^3 and activities around 1400 Ci/cm^3. The high uranium density and corresponding activity make this approach an attractive option for future high volume molybdenum-99 production.

Argonne National Laboratory (ANL) developed an LEU foil design using two annular cylinders to encase the LEU foil [20]. This design is somewhat complex and is difficult to produce from a manufacturing standpoint, making this approach unattractive in a high volume production environment. A safety case, characterizing the target

behavior during irradiation, which is needed for target qualification has also not been developed. For these reasons, high volume production reactors have been reluctant to convert using the ANL LEU foil design.

MURR has developed a design it believes will overcome the ANL design issues. MURR's design uses two nominally flat or curved aluminum plates to encase the LEU foil. The intent of this design is to create a target that is economical in a high volume production environment while maintaining HEU comparable molybdenum-99 yields. Simplifying the design, which in turn simplifies the pre- and post-irradiation processes, reduces the cost leading to better economics [21]. Questions have been raised though regarding the target's survivability during irradiation. Investigation and characterization of the target's behavior during irradiation must be performed before reactors will consider this target type.

Future Techniques for Domestic Molybdenum-99 Production without HEU

Currently there are no molybdenum-99 producers or irradiators in the United States. Major shortages in 2008 and 2010 significantly reduced the amount of molybdenum-99 entering the United States, greatly affecting the molybdenum-99 procedures performed in the medical community. The shortages gained a great amount of attention from the public, medical community, and United States government. Several major lessons learned during the 2008 and 2010 shortages were the U.S. needs a reliable supply of molybdenum-99, diversity in the supply chain needs to be implemented insuring no single point technology failure exist, and the current subsidized molybdenum-99 market must switch to full cost recovery. The U.S. government signed cooperative

agreements with four commercial entities to accelerate the establishment of a reliable

domestic molybdenum-99 supply. These four technologies are a fission based aqueous

homogenous reactor (AHR), neutron capture with molybdenum-98, a (γ,n) reaction on

molybdenum-100, and a fission based accelerator driven subcritical assembly [13].

Purpose

High volume molybdenum-99 production reactors have not converted to LEU

dispersion or LEU foil targets, because of the unsustainable economics. Many different

non-HEU based methodologies are being explored to replace HEU production, but fission

based production will remain the preferred methodology in the international community.

LEU dispersion targets can be used in molybdenum-99 production but the decreased

yield makes long term high volume production impractical. The LEU foil method was

developed to increase the U-235 density leading to HEU comparable yields. The ANL

LEU foil target is a possible target choice but the difficulties with manufacturing and no

safety case have prevented its adoption by high volume reactors. The flat plate or curved

plate LEU foil based design increases molybdenum-99 yields and remains economical

through its simple design. Questions remain though about the survivability of the target

during irradiation.

The purpose of this research is to support the conversion of internationally

produced molybdenum-99 by evaluating the thermal-mechanical behavior of the flat,

curved, and ANL annular LEU foil design with emphasis placed on the flat and curved

plate target designs. Analytical, numerical, and experimental studies have been

performed to characterize the target separations, von Mises stresses, and thermal contact resistance during irradiation.

Plate target analytical studies used a non-dimensionalzed simply supported plate to uniquely assess how plate aspect ratio and thickness will affect deflection. The analytical models were also used to benchmark the Abaqus numerical models. The effect of various edge holding conditions with uniform heating on the thermal deflections and stress was the first study performed. A more prototypical non-uniform heating was applied to the model to further determine its effect on thermal stresses and deflections. Next, the models were used to compare uniform and non-uniform heating giving insight into the effect of foil size on thermal-mechanical behavior. Finally, a simulated LEU foil and curvature were added to investigate the separation at the foil cladding interface and thermal stresses.

The effects of fission gas pressure and uranium swelling were also examined in the study. An experiment planned at the Pitesti research reactor in Romania, will provide data on the effects if fission gas pressure and uranium swelling by the end of 2012. The data will then be used to calibrate the numerical models and give direction to the proper application of these loads. Fission gas pressure was simulated through application of a uniform pressure at the foil cladding interface. Uranium swelling was simulated using a thermally independent swelling material property in the form of a volumetric strain rate.

Experimental studies focused on developing surrogate targets which replicate target thermal-mechanical behavior during irradiation. Results from these studies were used to calibrate and benchmark the numerical studies. Reproducing irradiation power levels on the order of 30 kW is impossible with current laboratory electrical capacities

thus a practical goal of 5 kW was set. A custom flow loop was designed and built to cool and collect data from the surrogate target. A resistive heater, unique to this plate target design, was also designed and manufactured.

CHAPTER 2: MOLYBDENUM-99 PRODUCTION BACKGROUND

Current Fission Based Molybdenum-99 Production Techniques with HEU

The HEU powder dispersion method is the traditional process used for

molybdenum-99 production throughout the world. In this process HEU is mixed in

powder form with aluminum powder. The two powders are then heated and compressed

between two aluminum plates creating a solid plate target. The completed target has a

uranium-aluminum fuel core and an aluminum picture frame and cladding [22, 23]. A

diagram showing the aluminum frame and uranium-aluminum core can be seen in Figure

10.
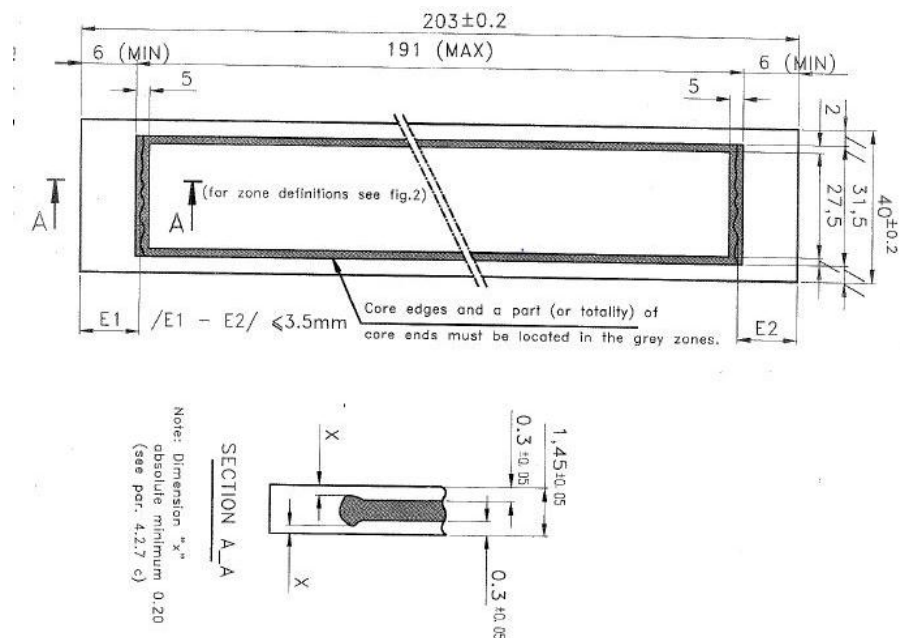
Figure 10. HEU dispersion plate target [22]

The solid nature of the HEU dispersion target ensures there is no gas gap between

the uranium and the aluminum leading to a low thermal contact resistance through the

target. The molybdenum-99 is collected by dissolving the entire plate through chemical

processing [23]. A simplified diagram showing this process can be seen in Figure 11
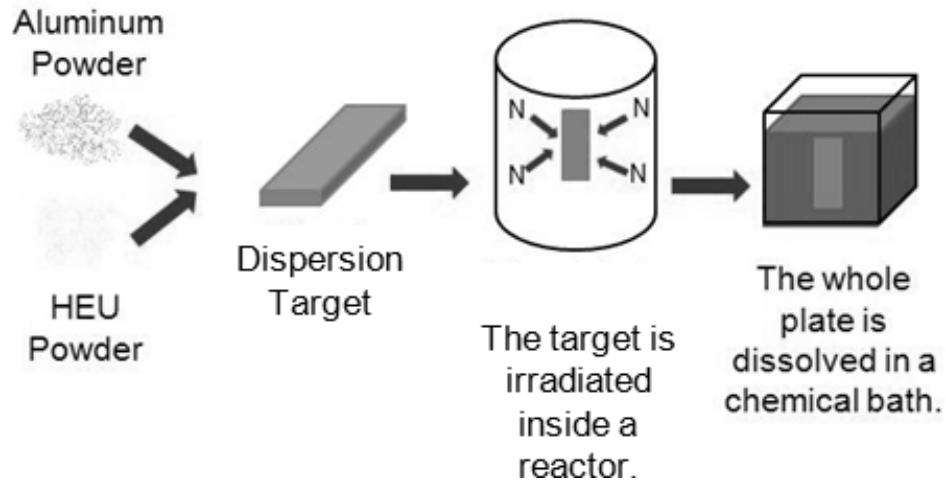
Figure 11. Simplified HEU powder dispersion method process [21]

An annular dispersion target is another currently used HEU target type. In essence

an annular dispersion target is a dispersion plate target that has been curved to form an

annular cylinder. The annular geometry provides high production and creates effective

cooling using a solid target structure. After irradiation the target is dissolved in a process

similar to the dispersion plate target [24]. A diagram of the annular target can be seen in
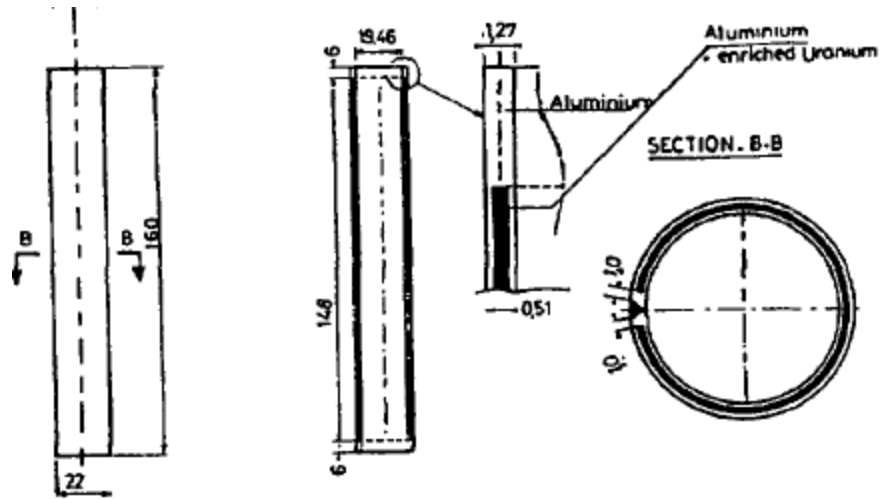
Figure 12.

Figure 12. Diagram of HEU annular dispersion target [24]

The final HEU target type used in molybdenum-99 production is a pin target. In this design the uranium-aluminum core is arranged in pins similar to Pressurized Water Reactor (PWR) and Boiling Water Reactor (BWR) fuel elements. The target core is surrounded by a fined outer aluminum shell to improve target cooling. After irradiation the target is dissolved in a process similar to the dispersion plate and annular dispersion targets [25]. An image of the pin target can be seen in Figure 13.
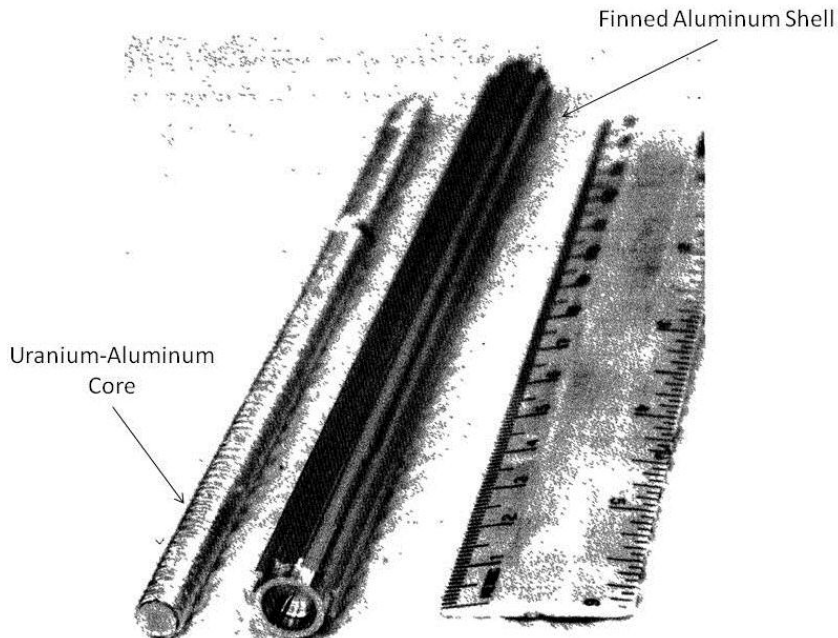
Figure 13. HEU pin type target design [25]

Current Molybdenum-99 Reactors and Producers

There are currently six reactors used by high volume molybdenum-99 producers, most of which use HEU [7, 12]. Table 1 gives information, such as location and target type, used at each reactor.

Table 1. Reactors used by high volume producers [7, 12]

Reactor Name	Location	Owner	Target Type
NRU	Chalk River, Canada	AECL	HEU Pin
HFR	Petten, Netherlands	European Commission	HEU Dispersion Plate
BR2	Mol, Belgium	SKC-CEN	HEU Dispersion Annular
Osiris	Saclay, France	CEA	HEU Dispersion Plate
SAFARI-1	Pelindaba, South Africa	NECSA	HEU and LEU Dispersion Plate
OPAL	Lucas Heights, Australia	ANSTO	LEU Dispersion Plate

A pie chart showing the percentage each reactor supplies to the global molybdenum-99 market can be seen in Figure 14 minus OPAL.
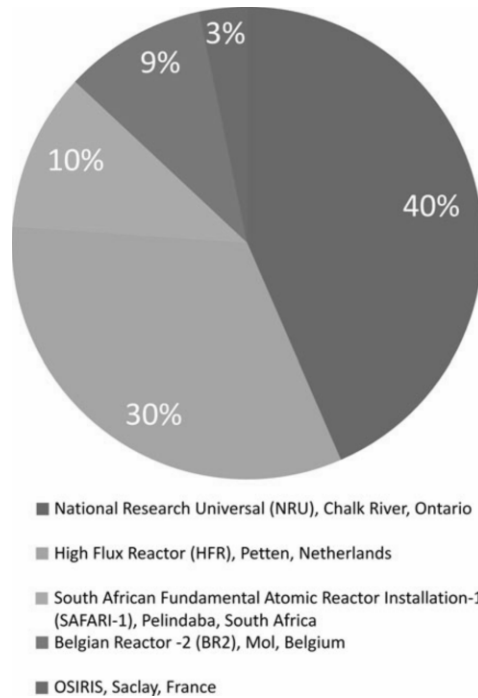
Figure 14. Percentage of molybdenum-99 that each reactor supplies [10]

A few reactors also create small amounts of molybdenum-99 for domestic and limited regional use with both RA-3 and GA SIWABESS Y MPR using LEU targets. Table 2 gives information such as location and the target type used by these regional reactors.

Table 2. Reactors used by regional producers [7, 12]

Reactor Name	Location	Owner	Target Type
RA-3	Buenos Aires, Argentina	CNEA	LEU Dispersion Plate
GA SIWABESS Y MPR	Batan, Indonesia		LEU Dispersion Plate

After irradiation, targets are shipped to the molybdenum-99 processers where they are dissolved, extracting the molybdenum-99. The bulk molybdenum-99 is then shipped

to generator manufactures where it is packaged into technetium-99m generators before finally being shipped to a radiopharmacy or hospital. Figure 15 illustrates, in brief, the global molybdenum-99 supply chain.
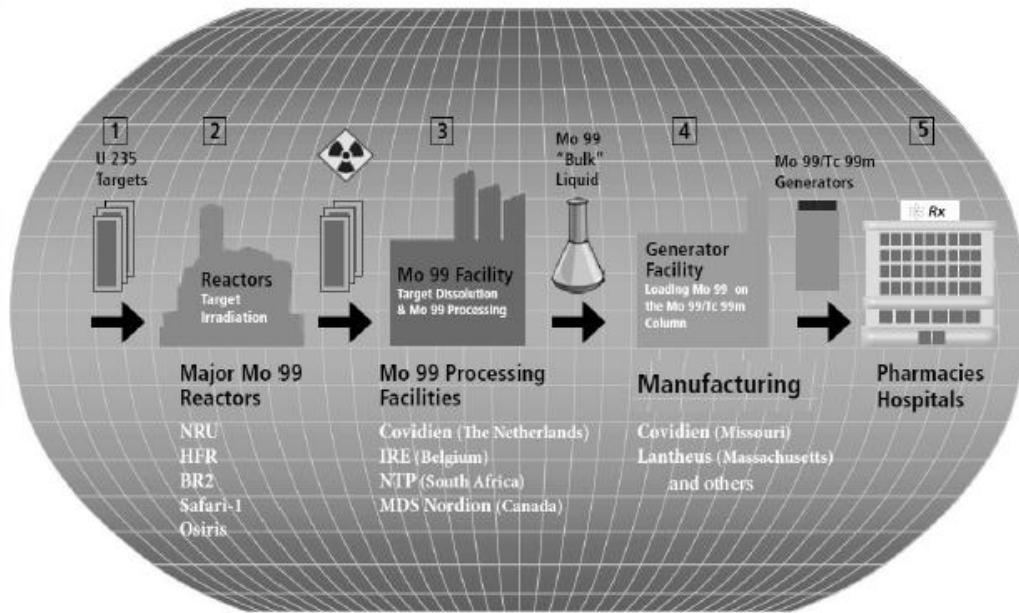
Figure 15. Global supply chain of molybdenum-99 [12]

There are three high volume producers dissolving irradiated targets. Convidien is located in the Netherlands and produces approximately 40% of the United States supply and about 25% of the global supply from targets supplied by HFR and BR2. IRE which is located in Belgium produces about 20% of the global supply from targets supplied by the HFR, BR2, and Osiris reactors. MDS Nordion located in Canada provides 60% of the United States supply and 40% of the global supply from targets irradiated at the NRU reactor. NTP Radioisotopes located in South Africa produces 10% of the global supply and can assist with the United States supply during shortages with targets coming from the SAFARI-1 reactor [7]. A diagram showing the reactor and producer relationships can be seen in Figure 16. South Africa is currently converting to full LEU dispersion target

production and is temporarily using both HEU and LEU dispersion targets. Recent

developments and statements by Russia have indicated they are developing HEU based

molybdenum-99 production but this is yet to be confirmed [26].
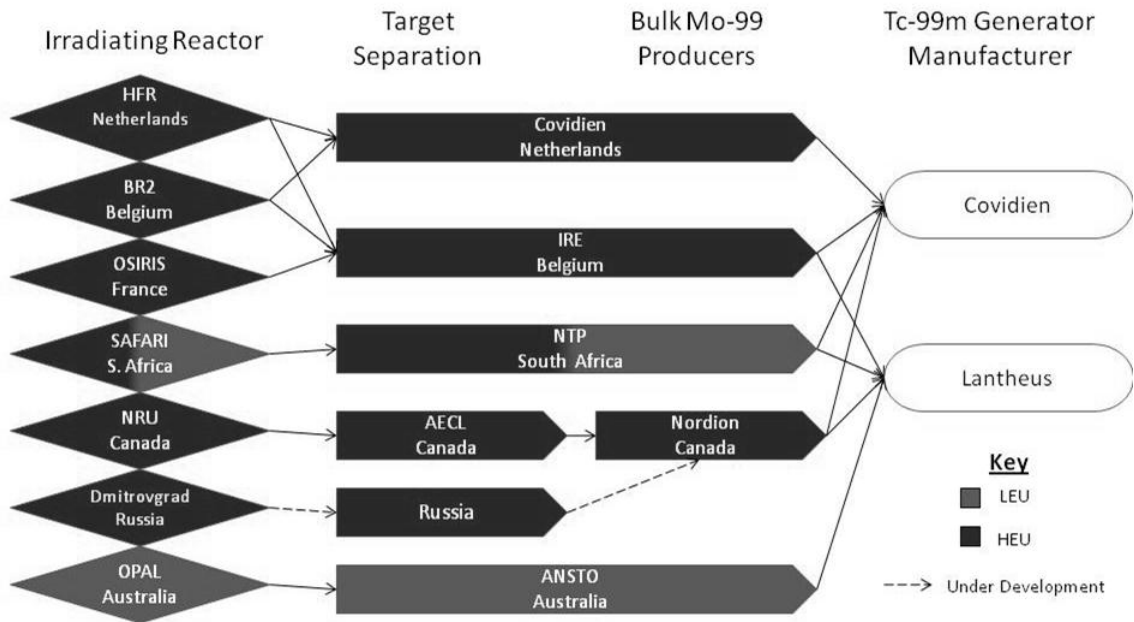
Figure 16. Diagram showing reactor producer relationships [26]

U.S. Government Molybdenum-99 Efforts: The Office of Global Threat Reduction

In 2004 the Bush administration announced the formation of the Global Threat

Reduction Initiative (GTRI). "The mission of GTRI is to reduce and protect vulnerable

nuclear and radiological material located at civilian sites worldwide [27]." Under this

initiative the National Nuclear Security Administration would consolidate the

Department of Energy nuclear material removal efforts, complete an inventory of

vulnerable nuclear material, and convert research reactors worldwide. Further, the NNSA

consolidated DOE's programs concerning nuclear materials, which included the Russian

Research Reactor Fuel Return Program (RRRFR), the Foreign Research Reactor Spent

Nuclear Fuel (FRRSNF), the Radiological Threat Reduction Program (RTR), and the Reduced Enrichment for Research and Test Reactors Program (RERTR) [27].

GTRI includes three program-offices that have regional responsibilities along with managing one of the key mission goals. The three program-offices are the Office of North and South American Threat Reduction that manages the protect subprogram, the Office of European and African Threat Reduction that manages the convert program, and the Office of Former Soviet Union and Asian Threat Reduction that manages the remove subprogram.

The Office of European and African Threat Reduction's convert program supports the conversion of both domestic/international research reactors and establishment of non-HEU based medical isotope production. The ultimate goal is to eliminate all HEU in research reactors and medical isotope production thus permanently reducing the amount of HEU in the civilian sector [28].

The Office of European and African Threat Reduction also supports the establishment of a reliable domestic supply of molybdenum-99. The office has many ties to the molybdenum-99 industry developed through international reactor conversion efforts making the office an ideal choice to lead this effort. Four commercial technologies were chosen based on merit to receive government funding for the acceleration of their domestic molybdenum-99 production projects. The office entered into cooperative agreements with four companies in the form of a 50%-50% government cost share currently limited to $25 million. Additional funding is provided outside the cooperative agreement to the DOE's National Laboratories for the development of open-source technology. All of this support is intended to accelerate these technologies to the point

where they can produce 3,000 6-day Ci of molybdenum-99, which is the current United

States demand, by the end of 2014 and before the shutdown of the Canadian NRU reactor

in 2016 [29].

Economic Issues with the Current Molybdenum-99 Production Market

The current molybdenum-99 production industry is a complex and fragile system

that is susceptible to any change in market conditions. Following the large supply

shortage in 2008 and 2010 the Organisation for Economic Co-Operation and

Development's Nuclear Energy Agency (OECD-NEA) analyzed the current

molybdenum-99 market and provided recommendations for its improvement [30].

The OECD-NEA established the High-Level Group on the Security of Supply of

Medical Radioisotopes (HLG-MR) in 2009 to specifically address this issue. The HLG-

MR includes representatives from the molybdenum-99 production industry and

governments where molybdenum-99 is produced. The OECD-NEA began by first

examining the current molybdenum-99 production market and examining the ability of

the current market structure to provide molybdenum-99 in the future. Their findings can

be seen in Figure 17.
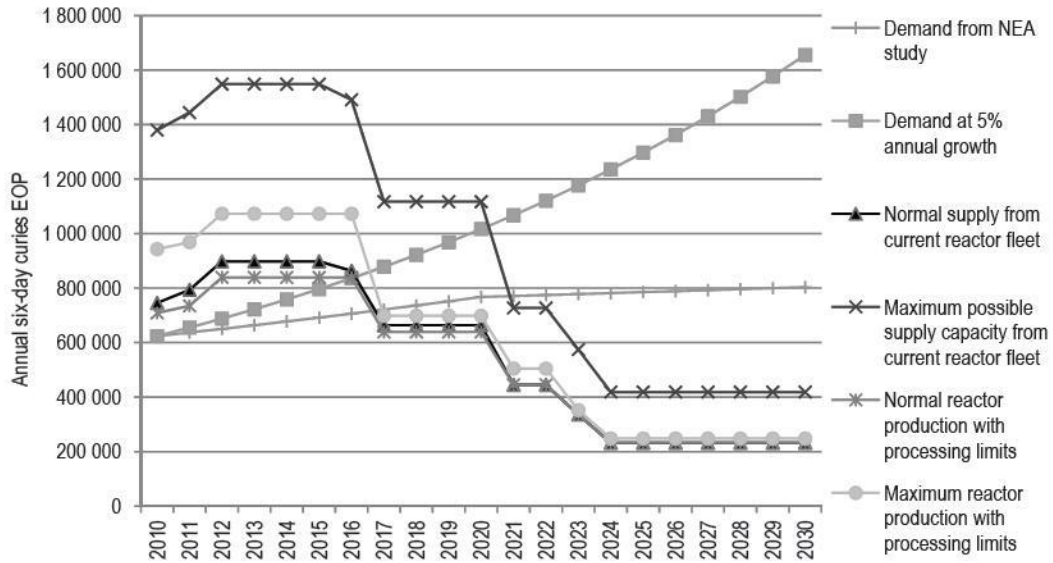
Figure 17. Projections for the current molybdenum-99 market in the future [30]
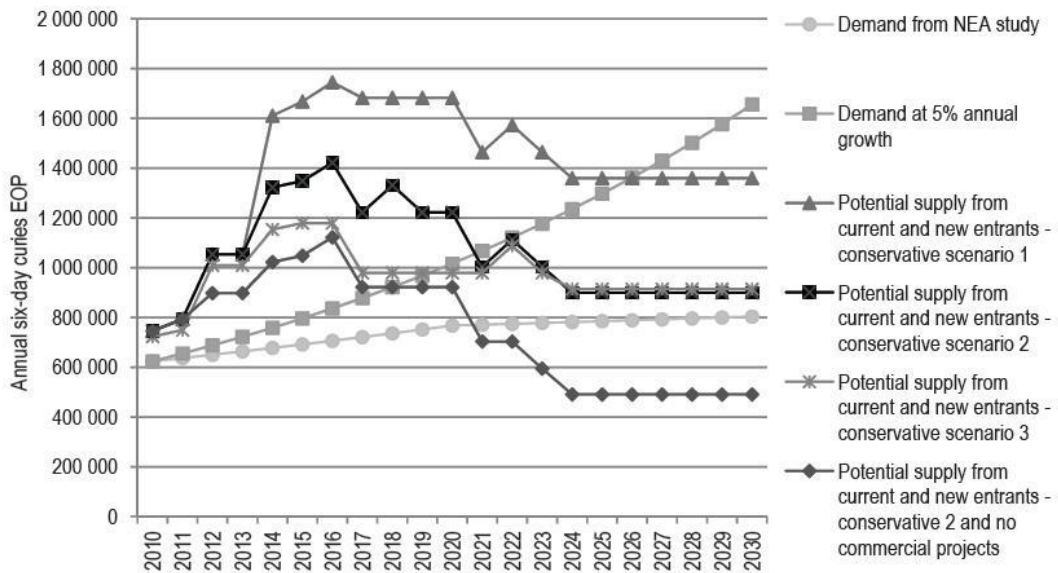
Figure 18. Project with the current market and new entrants [30]

OECD-NEA projections indicate the molybdenum-99 production community will

be unable to support demand beginning in 2021 timeframe. When including the current

market with new entrants, the projections on supply appear much more sustainable.

Creating the market in Figure 18 has many obstacles to overcome. In 2011 the first HLG-

MR concluded and developed a set of six principles needed to establish this market condition.

First, all of the participants involved in the molybdenum-99 production chain should implement full-cost recovery including cost related to capital replacement. The OECD-NEA concluded a removal of subsidies and a move to a full-recovery market is the only way to create an economical sustainable production market. Second, is management of the production reserve capacity, which is the ability of the production community to supply molybdenum-99 during reactor outages. OECD-NEA recommends irradiating reactors coordinate their schedules more closely, insuring waste in the supply chain can be minimized through effective administration. Third, is government should not directly supply molybdenum-99 to the market and that its role should be in the establishment of proper infrastructure for full-cost recovery. The role of government has been extremely detrimental to the molybdenum-99 market and has been one of greatest deterrents for new entrants in the market through government subsidization. Forth, is government through their international commitments to nuclear nonproliferation and security should provide appropriate support to the reactors and processers in the conversion to LEU. Governments can implement this by supporting R&D on new LEU based targets providing an economical way of producing molybdenum-99 with LEU. It is also recommended is that the International Atomic Energy Agency (IAEA) be used as the conduit to share technologies developed with the global community. Fifth, is international collaboration should continue as molybdenum-99 is an international issue and implementation of this policy will insure a level playing field for all producers. Sixth, the OECD-NEA's final recommendation is a periodic review of the market and supply

chain insuring producers are implementing full-cost recovery, thus insuring an economically sustainable market exist [30].

The implementation of the HLG-MR's principles are extremely important in insuring the establishment of a fair and full-cost recovery market favorable to new entrants and non-HEU based production. It is imperative the current supply chain and production community transition warding off the possibility of another extended shortage comparable to the 2008 and 2010 shortages.

Current Molybdenum-99 Production with LEU

There are four reactors currently irradiating LEU dispersion targets for molybdenum-99 production. An image of CNEA's LEU dispersion target, which has been used since 2002, can be seen Figure 19.
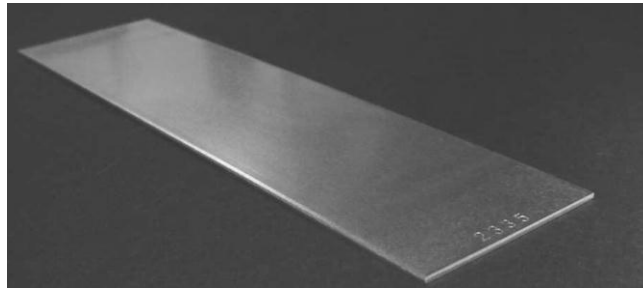
Figure 19. CNEA LEU dispersion target [7]

Manufacturing the LEU dispersion target is similar to the HEU dispersion target. In this process LEU is mixed in powder form with aluminum powder. The two powders are then heated and compressed between two aluminum plates creating a solid LEU plate. The completed target has a uranium-aluminum fuel core and an aluminum picture frame and cladding. Current HEU targets use uranium enriched to ~ 90% U-235 meaning

approximately five times the amount LEU is needed to match the HEU target yields [12].

The LEU foil increases the density of U-235 in each target thus producing more

molybdenum-99 [23].

The ANL LEU foil target design consists of two concentric aluminum cylinders.

The LEU foil is placed between the two cylinders, a drawing process compresses the two

cylinders sandwiching the foil between them. The ends of the cylinder are then welded

producing an enclosed environment for the LEU, preventing the escape of fission

products during irradiation [31]. A diagram showing the placement of the foil can be seen

Figure 20.
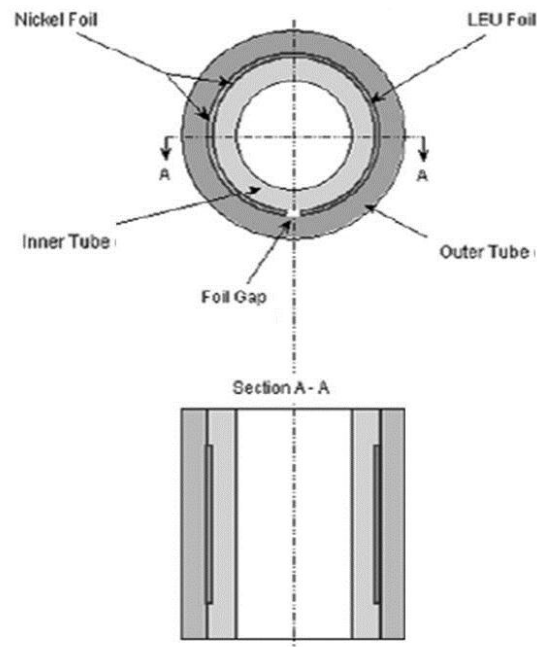
Figure 20. ANL LEU based target design [31]

The ANL design has been successfully tested at GA SIWABESS Y MPR

producing small amounts of molybdenum-99 [20]. This design is difficult to produce in a

high volume production environment thus adoption by the high volume reactors has been slow.

Future Domestic Molybdenum-99 Production Techniques

A variety of technologies are currently being developed as possible paths to establish domestic molybdenum-99 production. For the purposes of this research NNSA's four cooperative agreement partners will be the focus of future domestic molybdenum-99 production discussions.

As a consequence of the 2008 and 2010 supply shortages, a program within GTRI was developed to support and accelerate the establishment of a reliable domestic supply of molybdenum-99 produced without HEU. Four companies were selected to develop molybdenum-99 production utilizing four different non-HEU technologies avoiding a possible single technology point of failure.

Babcock and Wilcox (B&W) in Lynchburg, VA has been developing an AHR for many years and was selected by NNSA to further develop their solution reactor technology. In an AHR the uranium fuel, which is both a neutron source and molybdenum-99 production target, is in an aqueous salt solution of either uranyl nitrate or uranyl sulfate [32, 33]. The AHR developed by B&W will operate at 200 kW and will produce enough high specific activity molybdenum-99 for half of the United States molybdenum-99 demand [34]. The reactor, called the Medical Isotope Production System (MIPS), is a compact modular cylindrical reactor. Molybdenum-99 is produced by the irradiation of the uranyl solution and the fissioning of U-235. The basic nuclear reaction producing molybdenum-99 can be seen in Figure 21.

LEU Fission Based: $U^{235}(n,f)$

n^1

U^{235}

n^1

Neutron

The neutron is
captured by a
Uranium-235 nucleus.

Mo^{99}

Other Fission
Products

Neutrons and fission products are ejected, Mo-99
is six percent of the fission products produced.
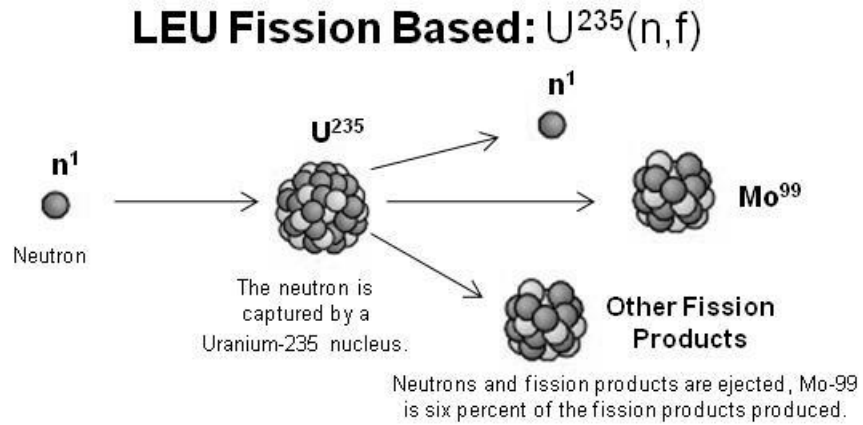
Figure 21. Basic physics process in the AHR [26]

The reactor will operate in batch or continuous mode and the molybdenum-99 will be separated from the solution once the optimal amount had been produced [7, 35]. The design is attractive because it does not require a physical target and can operate at power levels much lower than traditional research reactors [35]. An image of the conceptual design can be seen in Figure 22.
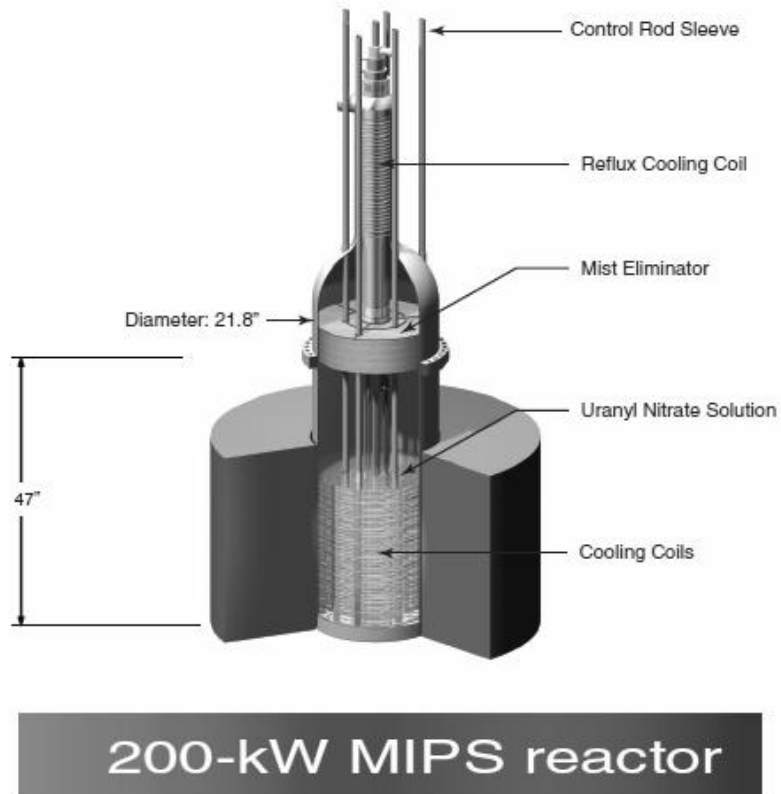
Figure 22. B&W MIPS aqueous homogenous solution reactor [7]

General Electric Hitachi Nuclear Energy (GE-H) in Wilmington, NC was also selected by NNSA to develop their neutron capture technology. Their project utilizes neutron capture on molybdenum-98 producing molybdenum-99 in a nuclear process known as transmutation. The basic nuclear reaction can be seen in Figure 23.
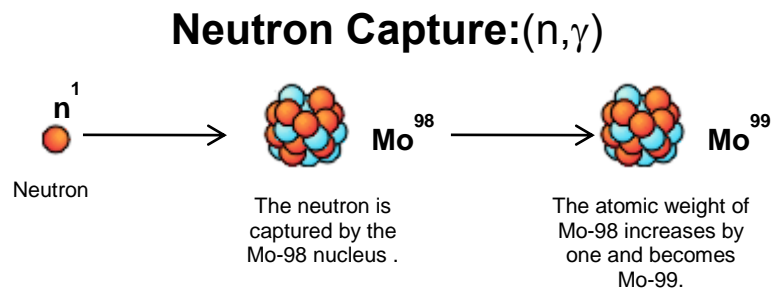
Figure 23. Basic physics process of the GE-H neutron capture [26]

GE-H will irradiate the molybdenum-98 in a commercial BWR producing up to 3,000 6-day curies of low specific activity molybdenum-99 per week [36].The molybdenum target will enter the BWR through small openings in the containment vessel where it will be irradiated in the high neutron flux within the reactor fuel. The target would be irradiated for approximately one week then extracted through the same opening allowing the reactor to continue normal operation without disruption from molybdenum-99 production [37].

NorthStar Medical Technologies was also selected by NNSA to develop their accelerator technology. NorthStar is located in Madison, WI and is a recent addition to the medical isotope production community only being founded in 2004 [38]. Their technology produces molybdenum-99 through a (γ,n) reaction on molybdenum-100. The basic nuclear reaction can be seen in Figure 24.
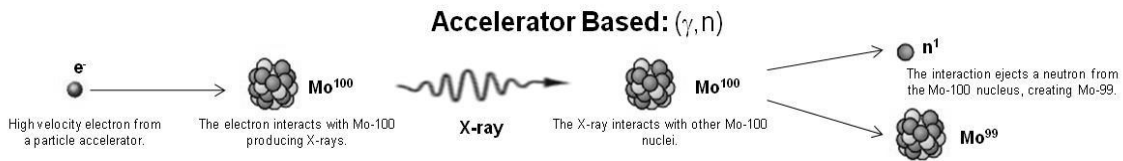
Figure 24. Basic physics of the NorthStar molybdenum-99 production process [26]

In this process molybdenum is bombarded by high energy electrons from a particle accelerator. These electrons interact with the molybdenum target and, through a process known as Bremsstrahlung radiation, produce X-rays [15]. These high energy X-rays then interact with the molybdenum-100 ejecting a neutron from its nucleus producing molybdenum-99. NorthStar's goal is to produce 3,000 6-day Ci of low specific activity molybdenum-99. NorthStar has developed the TechneGen system to make low specific activity molybdenum-99 activities comparable to high specific activity fission based

production. [38-40]. A picture of the TechneGen can be seen in Figure 25. The TechneGen can accept both low specific activity and high specific activity molybdenum-99 and still produce the necessary specific activity technetium-99m.

Figure 25. NorthStar TechneGen[39]

Morgridge Institute for Research (MIR) in close collaboration with SHINE Medical Technologies was selected by NNSA to develop another accelerator based technology. MIR is also located in Madison, WI and a recent addition the medical isotope production community. While the MIR technology is similar to an AHR in that it utilizes an LEU solution, it is different because the solution remains at a subcritical state and uses an accelerator, in the form of a deuterium-tritium generator (D-T generator), to drive the fission reaction [41, 42]. The basic nuclear reactions taking place can be seen in Figure 26.

Accelerator Based
D(t,n) and U235(n,f)

Tritium=H^3

Fusion Reaction

He^4

Deuterium=H^2

A 300KeV deuterium beam is directed toward a tritium target causing a fusion reaction.

Neutron from the fusion reaction.

n^1

U^{235}

The neutron enters a LEU solution and is captured by a uranium-235 atom.

Neutrons and fission products are ejected. Six percent of the fission products produced are Mo-99 atoms.

n^1

Mo^{99}

Other Fission Products

Figure 26. MIR nuclear reactions [26]

The neutrons driving the fission reaction are produced by a D-T generator and not from a critical fission reaction. The neutrons created by the D-T generator interact with the U-235 atoms in an aqueous salt solution of either uranyl nitrate of uranyl sulfate causing the U-235 atoms to fission and produce molybdenum-99 at a 6% yield. The molybdenum-99 is then extracted from the solution and sent to a generator manufacturer [42].

Future International Molybdenum-99 Production Techniques

All indications signal international molybdenum-99 production will continue to be dominated by fission for the foreseeable future. Fission may remain the dominate production method but there are international groups focusing on the development of non-fission based modalities as well.

TRIUMF, a Canadian based company, is investigating cyclotrons as a possible production path. Unlike many of the other methodologies TRINMF's approach will directly produce technetium-99m from molybdenum-100 [43]. Direct technetium-99m

production, limits the distance the isotope can travel before it decays to an unusable

activity. TRIMF's success will heavily rely on strategically placing cyclotrons in highly

populated areas, providing coverage to the majority of the Canadian population. Efforts

to develop and commercialize non-fission based international production are extremely

small, in both financing and participation.

International conversion will be done in two phases. The first conversion phase

will directly substitute LEU for HEU in the dispersion target. Currently South Africa is

partially through phase 1 and by 2015 all of the majority producers will convert to LEU

in phase 1 [15, 16, 44]. LEU dispersion targets are a proven technology with many

successfully irradiations occurring. The LEU dispersion target's weakness is the low U-

235 density within the target. The U_3Si_2 dispersion target was developed to increase the

dispersion target's U-235 density but, as can be seen Figure 27, it is still lower than the

HEU dispersion target. Figure 27 gives the uranium loading of various target designs

with their enrichments and the corresponding molybdenum-99 activity once irradiated.

Figure 27 which is an estimate of the activity after irradiation, in Ci_{Mo-99} /grams$_{U-235}$, and

was calculated using equation (2.7.1) [45].

$$A_{Mo99} = \frac{1}{k}\left(\frac{N_A}{M_{U235}}\right)\left(\gamma_{Mo99}\right)\left(\sigma_{f,U^{235}}\right)\left(\phi_{th}\right)\left(1-e^{-\frac{Ln(2)}{t_{1/2Mo99}}t_{irr}}\right) \qquad (2.7.1)$$

Activities produced are based in MURR's specifications and assumes a 7 day irradiation

time, a 6% fission yield for molybdenum-99, and a thermal neutron flux of 2.0 x 10^{14}

n/s•cm^2.
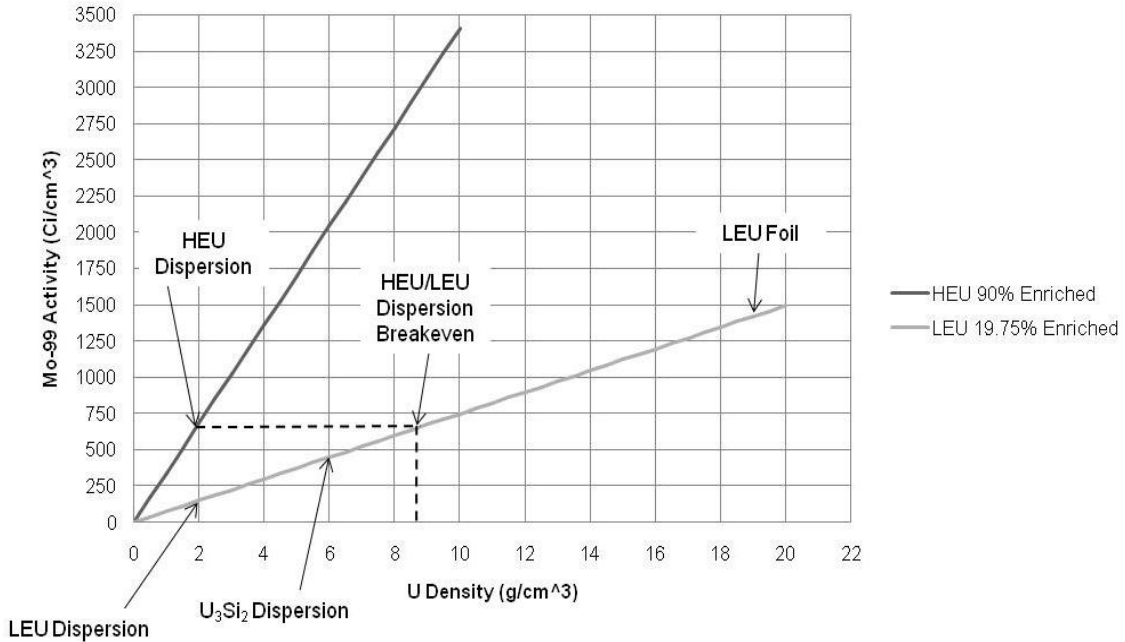
Figure 27. HEU vs. LEU based production methods [45]

A uranium density of $9g/cm^3$ is the breakeven point where the activity produced from LEU is equal to HEU. It is clear LEU foil is the only target type capable of reaching or exceeding the breakeven point. The high uranium density and high molybdenum-99 activity are attractive to the reactors/producers. Three designs have been developed and are the ANL annular, flat plate, and curved plate designs.

Pakistan Research Reactor-1 (PARR-1) has performed several safety test irradiations on the ANL design. The results from various computer codes indicate safe operation in PARR-1 [46]. Further, GA SIWABESS Y MPR has also performed successful preliminary test on the ANL design [14, 47]. Questions remain though regarding the economic viability of this design in a high production environment [23].

A nominal flat plate target design has been developed by the MURR and is designed for economical high volume molybdenum-99 production. The nominally flat plate LEU foil based approach, is illustrated in Figure 28.

37
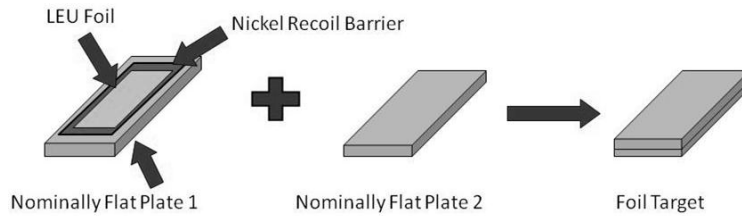
Figure 28. LEU foil based nominally flat plate design [21]

The MURR concept places LEU foil between two pieces of aluminum cladding then sealing the edges. Sealing, in the form of a weld, prevents the escape of fission products into the reactor cooling system. After irradiation, the welds are removed allowing for easy retrieval of the LEU foil, which is then chemically processed using the Modified Cintichem Process, obtaining molybdenum-99 [48]. The advantage of this design is in its simplicity, reducing the time and cost compared to the ANL annular target [21]. The ANL annular target is difficult to manufacture and has many different manufacturing steps. Disassembly after irradiation involves cutting the cladding along the small 11.4 mm gap in the foil and recovering the LEU foil without tearing. The MURR plate target is much simpler to process, with only four welded edges needing removal. The simplicity of the design also decreases that amount of time spent on each target lowering the cost of each target. Questions have been raised about the survivability of the target during irradiation. Unlike the powder dispersion plate designs, a solid target structure is not created. The laminated structure implies there will be a significant thermal contact resistance between the layers of uranium, nickel, and aluminum limiting heat transfer.

A curved geometry was also developed to strike a balance between the ANL and MURR designs. The curved design takes advantage of the positive attributes for both the

nominally flat plate target and the ANL annular target. The curved plate design would be

manufactured in the same way as the nominally flat plate target with curvature added in

toward the end of the manufacturing process. Adding curvature to the target should

decrease the chance of target failure during irradiation.

CHAPTER 3: FISSION BASED TARGET APPROACHES USING LEU FOIL

Fission based molybdenum-99 production has been a staple of the isotope

production community for many years and will continue into the foreseeable future.

Three primary design concepts are considered and thermal-mechanical analyzed

assessing their behavior during irradiation.

ANL Annular Target Design

The ANL annular target design consists of two concentric aluminum cylinders

welded at their ends containing the LEU foil and a nickel recoil barrier. The nickel recoil

barrier prevents the LEU foil and the aluminum cladding from fusing together during

irradiation. A sketch of the approach can be seen in Figure 29 with an image of a mock

target in Figure 30.
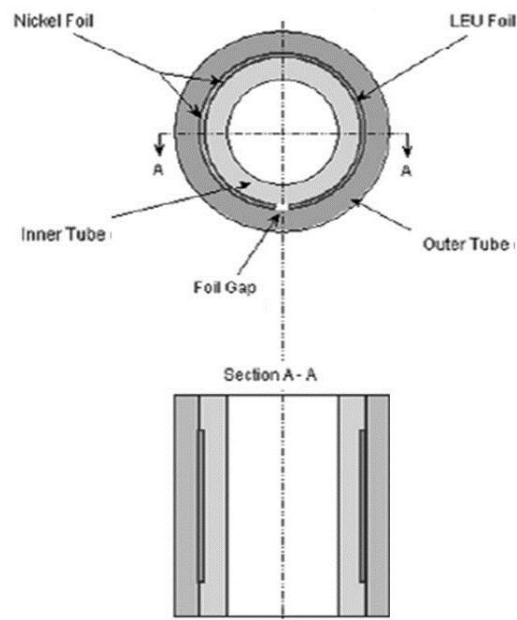
Figure 29. Dimensions and Cross Sectional view of the LEU annular target [31]
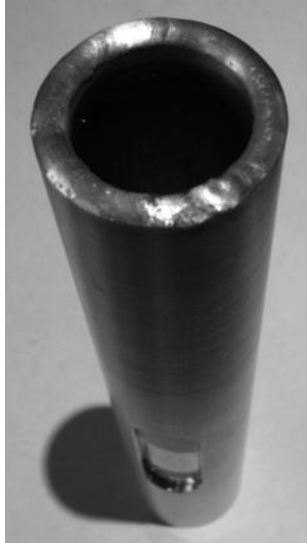
Figure 30. Image of a mock ANL annular target [49]

The LEU foil and nickel recoil barrier are placed between two aluminum cylinders which are drawn together using a plug die. The ends of the cylinders are welded completely sealing the LEU foil in the target.

The ANL annular target was not designed with high volume production or the existing reactor infrastructure in mind. There is no reason to believe it is the most cost effective design. In fact, one can consider the annular target to be a special case of a more general plate design concept. The plate design can be curved to the point that its ends meet reproducing the annular target. Further, the majority of the large reactors use HEU dispersion plate targets and the infrastructure for irradiating, processing, and disposing of a plate target geometry is already in place. New infrastructure would need to be added at high cost to implement the annular design.

Nominally Flat Plate Target Design

The plate target structure is an LEU foil sandwiched between two nickel recoil barriers and two aluminum plates approximately 1 mm think. The aluminum plates are pressed and welded together on their edges. Figure 31 shows an illustration of the plate target structure and Figure 32 shows a mockup of the plate target.
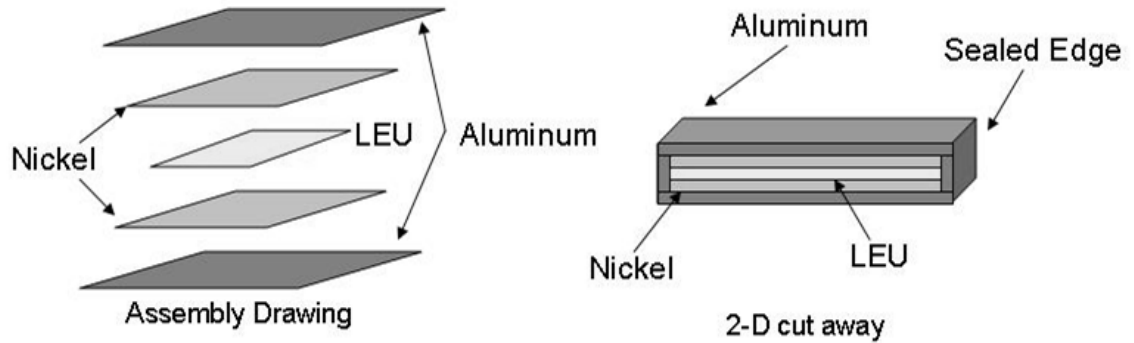
Figure 31. Plate target configuration
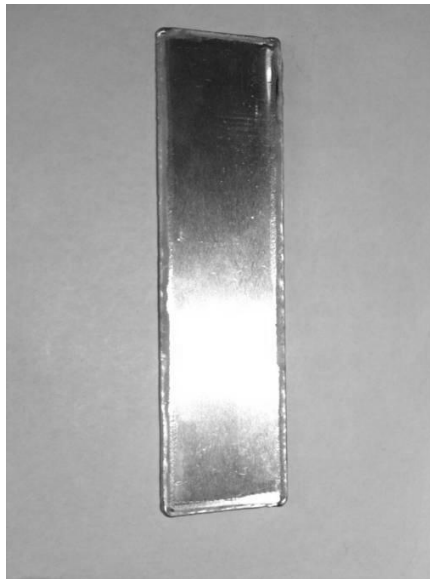
Figure 32. Image of a mock plate target [49]

42

During irradiation a large amount of heat is generated within the LEU on the order of 750 W/g U-235. Sufficient cooling must be provided to remove heat produced by the fission reaction.

One of the greatest areas of concern is thermal expansion. Non-uniform heating within the target will create a three dimensional temperature profile. Thermal expansion due to the temperature distribution could cause pillowing. This behavior will open a gap between the LEU and the cladding possibly causing the LEU to overheat and target failure. An example of pillowing can be seen in Figure 33.
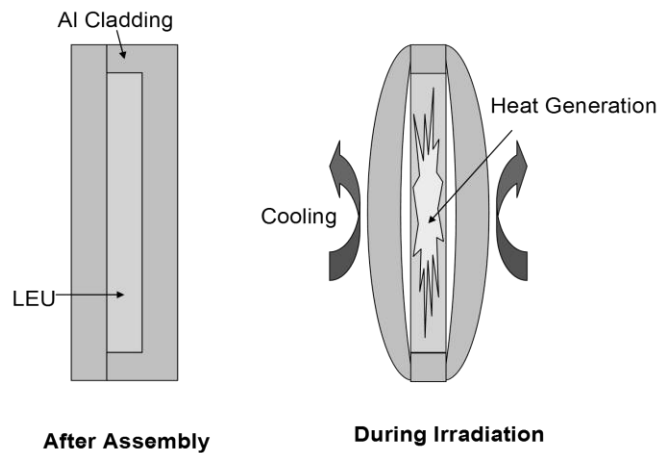
Figure 33. Example of plate target pillowing [23]

Numeric and analytic models were used to investigate plate target behavior. In conjunction with the numeric and analytic models experimental data was collected for the flat plate target geometry using a water flow loop. Unlike the annular target which has been successfully irradiated producing molybdenum-99, the plate target is a completely new design. The new nature of the design means there are many unknowns regarding its thermal-mechanical behavior.

Curved Plate Design

The curved plate target is LEU foil sandwiched between two nickel recoil barriers and two aluminum plates approximately 1 mm thick. The aluminum plates are pressed and welded together on their edges in a process similar to the nominally flat plate target.
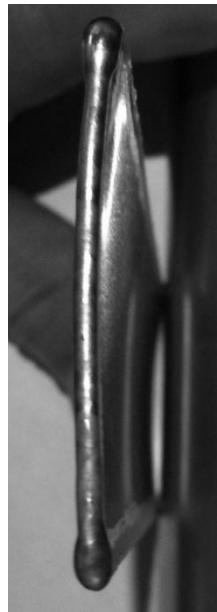
Figure 34. Curved plate target mock up [49]

One of the greatest areas of concern is the behavior of the curved plate target under irradiation. During irradiation a great amount of heat is produced causing the aluminum to expand. The non-uniform heating within the target will create a three dimensional temperature profile. Thermal expansion could cause pillowing similar to the nominally flat plate target. It is believed, however, the added curvature will decrease the likelihood of target failure.

Numeric and analytic models were used to perform the analysis on the curved plate target. The curved plate target along with the nominally flat plate target is a completely new design. The new nature of the design means many unknowns regarding the thermal-mechanical behavior of both targets.

CHAPTER 4: ANL ANNULAR TARGET BACKGROUND

Annular Target Modeling for Plate Comparison

Previous analysis work was completed on the ANL annular target. A potential failure mode for the LEU foil based target is temperature excursion during irradiation due to poor thermal contact between the foil and the target cladding. The purpose of this of this previous work was to establish the theoretical basis for experimentally measuring the thermal contact resistance in the target. Thermal contact resistance through the target will greatly affect the heat transfer characteristics of the target and must be profiled.

The results gathered from the study indicated the proper experimental method and can be used in LEU foil plate target comparison [50]. For these reasons the ANL annular target modeling efforts have been included in this research work.

Previous Thermal/Mechanical Analytic Modeling for Plate Comparison

A thermal/mechanical modeling approach was used to determine an appropriate experimental strategy. The general idea is to evaluate the thermally induced stress in a cylinder due to the different heating conditions shown in Figure 35.

Interfacial Heating Inner Surface Heating Outer Surface Heating
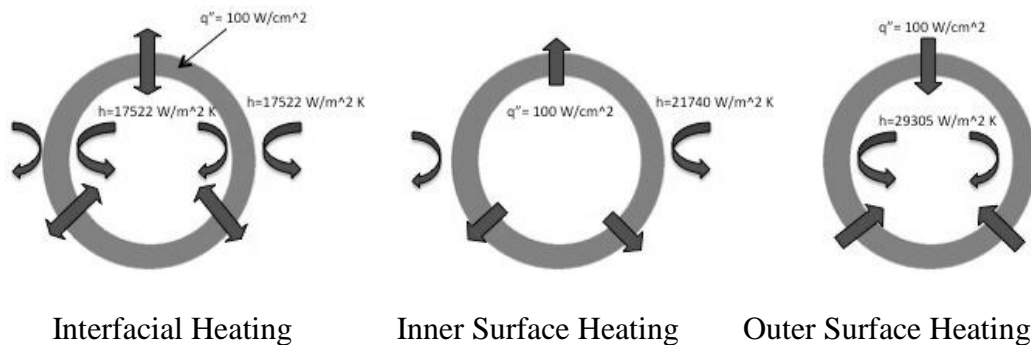
Figure 35. Cut away diagram of the three different heating situations

By examining the resulting stress distribution, it can be inferred whether the heating condition will increase or decrease the interfacial pressure, and hence the contact resistance. A plane-stress analytic model for the stress in a long circular cylinder as a function of radius and can be seen in equation(4.1.1) [51].

$$\sigma_r(r) = \frac{E}{1+v} \left[\frac{-(1+v)\alpha}{(1-v)r^2} \int_a^r Trdr + \frac{c_1}{1-2v} - \frac{c_2}{r^2} \right]$$

(4.1.1)

where r is the location along the radius and c_1/c_2 are the constants of integration. Assuming that the cylinder has a central circular hole the boundary conditions $(\sigma_r)_{r=a} = (\sigma_r)_{r=b} = 0$ are applied and the constants of integration are

$$c_1 = \frac{(1+v)(1-2v)\alpha}{(1-v)(b^2-a^2)} \int_a^b Trdr - v\varepsilon_z$$

(4.1.2)

$$c_2 = \frac{(1+v)a^2\alpha}{(1-v)(b^2-a^2)} \int_a^b Trdr$$

(4.1.3)

where (a) is the cylinder's inner radius and (b) is the cylinder's outer radius. The integration of $\int_y^x rTrdr$ requires knowledge of the radial temperature distribution. The T(r) will differ depending on the heating condition as illustrated in Figure 35. An expression for T(r) was found for the inside heating condition and the outside heating conditions based on the resistance network in Figure 36. The inside heating condition equation and outside heating condition are given by

q"

T Cylinder

R Conduction

R Convection

T Infinite

Cylinder

Cylinder Surface
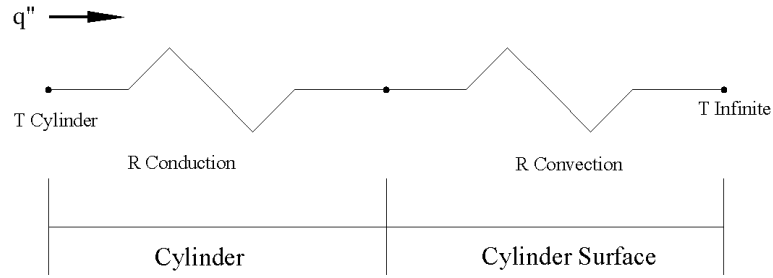
Figure 36. Heat transfer resistance network for the annular target

$$T(r) = T_\infty + \frac{q''a}{k}\left[\ln\left(\frac{b}{r}\right) + \frac{k}{hb}\right]$$

(4.1.4)

$$T(r) = T_\infty + \frac{q''b}{k}\left[\ln\left(\frac{a}{r}\right) + \frac{k}{ha}\right]$$

(4.1.5)

Equations (4.1.4) and (4.1.5) are then used in $\int_y^x rTrdr$ and integrated using the

appropriate limits of integration. The integration of the two equations for both the inside

heating condition and the outside heating condition are

$$(Inside)\int_a^r rTrdr = \int_a^r r\left(T_\infty + Q\left[\ln\left(\frac{b}{r}\right) + \frac{k}{hb}\right]\right)dr$$

(4.1.6)

where $Q = \dfrac{q''a}{k}$ and

$$(Outside)\int_r^b rTrdr = \int_r^b r\left(T_\infty + Q\left[\ln\left(\frac{a}{r}\right) + \frac{k}{ha}\right]\right)dr$$

(4.1.7)

where $Q = \dfrac{q''b}{k}$.

After integration the following are produced

$$\int_{a}^{r} rTr dr = (Inside)\left(T_{\infty} + Q\ln a + \frac{Qk}{hb}\right)\frac{\left(r^2 - a^2\right)}{2} - \frac{Q}{2}\ln\left(\frac{r^{r^2}}{a^{a^2}}\right)$$

(4.1.8)

$$\int_{r}^{b} rTr dr = (Outide)\left(T_{\infty} + Q\ln b + \frac{Qk}{ha}\right)\frac{\left(b^2 - r^2\right)}{2} - \frac{Q}{2}\ln\left(\frac{b^{b^2}}{r^{r^2}}\right)$$

(4.1.9)

Substituting equation (4.1.8) and (4.1.9) into equation (4.1.2) yields,

$$\sigma_r(r)(Inside) = \frac{E}{1-v}\left[\begin{array}{c}-\frac{\alpha}{r^2}\left[\left(T_{\infty} + \frac{q''a}{k}\ln b + \frac{\left(\frac{q''a}{k}\right)k}{hb}\right)\frac{(r^2-a^2)}{2} - \frac{\left(\frac{q''a}{k}\right)}{2}\ln\left(\frac{r^{r^2}}{a^{a^2}}\right)\right]+\\ \frac{\left(r^2-a^2\right)\alpha}{r^2\left(b^2-a^2\right)}\left[\left(T_{\infty} + \frac{q''a}{k}\ln b + \frac{\left(\frac{q''a}{k}\right)k}{hb}\right)\frac{(b^2-a^2)}{2} - \frac{\left(\frac{q''a}{k}\right)}{2}\ln\left(\frac{a^{a^2}}{b^{b^2}}\right)\right]\end{array}\right]$$

(4.1.10)

$$\sigma_r(r)(Outside) = \frac{E}{1-v}\left[\begin{array}{c}-\frac{\alpha}{r^2}\left[\left(T_{\infty} + \frac{q''a}{k}\ln b + \frac{\left(\frac{q''b}{k}\right)k}{ha}\right)\frac{(b^2-r^2)}{2} + \frac{\left(\frac{q''b}{k}\right)}{2}\ln\left(\frac{r^{r^2}}{b^{b^2}}\right)\right]+\\ \frac{\left(r^2-a^2\right)\alpha}{r^2\left(b^2-a^2\right)}\left[\left(T_{\infty} + \frac{q''a}{k}\ln b + \frac{\left(\frac{q''a}{k}\right)k}{hb}\right)\frac{(b^2-a^2)}{2} + \frac{\left(\frac{q''a}{k}\right)}{2}\ln\left(\frac{a^{a^2}}{b^{b^2}}\right)\right]\end{array}\right]$$

(4.1.11)

which give the radial stress in the cylinder as function of temperature and radius.

The boundary conditions used to complete the thermal stress analysis can be seen in Table 3.

48

Table 3. Model surface boundary conditions

	Inner Surface	Interfacial Surface	Outer Surface	Cylinder Ends
Inner Heating Condition	q"= 1,000,000 W/m^2	N/A	h= 21740 W/m^2 K	h= 0 W/m^2 K
Interfacial Heating Condition	h= 17522 W/m^2 K	q"= 1,000,000 W/m^2	h= 17522 W/m^2 K	h= 0 W/m^2 K
Outer Heating Condition	h= 29305 W/m^2 K	N/A	q"= 1,000,000 W/m^2	h= 0 W/m^2 K

The radial temperature distribution as a function of radius for the interior, exterior and interfacial heating cases can be seen in Figure 37. The resulting radial thermal stress is shown in Figure 38.
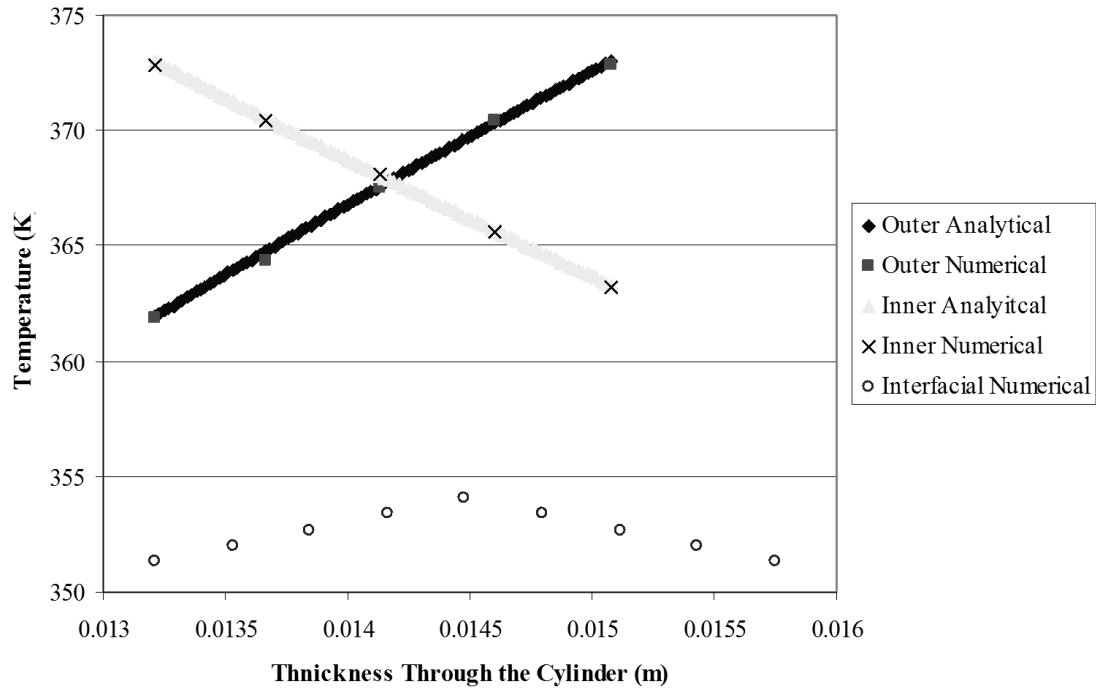
Figure 37. Temperature distribution as a function of radius for the inner, interfacial and outer heating conditions
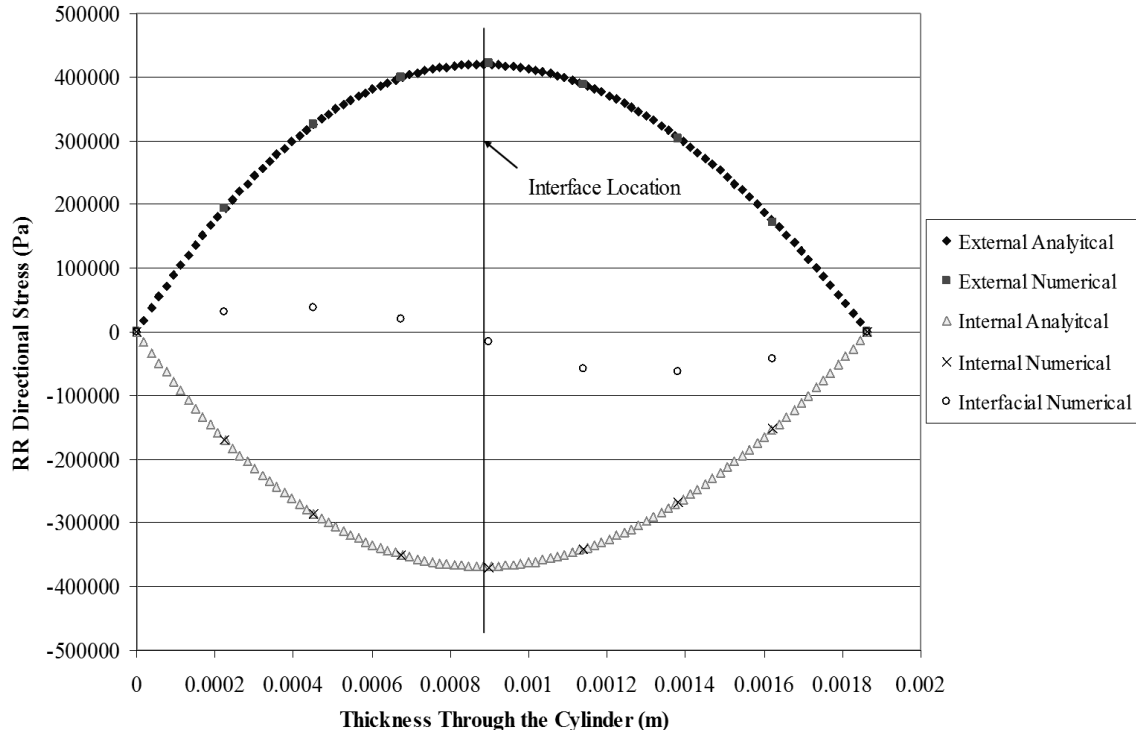
Figure 38. Radial stress as a function of target thickness for the inner, interfacial and outer heating conditions

The results show that the radial stress at the surfaces for the internal and external conditions is zero and that the interior of the cylinder experiences either a compressive or tensile stress depending on the heating direction. A negative radial stress represents a compression force while a positive radial stress implies a tensile force. A compressive force at the interface implies that there will be an increase in the interfacial pressure and a decrease in thermal contact resistance. A tensile force at the interface implies that there will be a decrease in the interfacial pressure and an increase in thermal contact resistance. This latter condition could eventually result in a condition where the cylinders pull apart from one another and create a gap. It should be noted that if a gap were to open at the interface the radial stress at the interface would become zero. Finally, all of the stresses

both tensile and compressive are less than the yield strengths for Al 1100, Al 3003, and Al 6061, which are 105 MPa, 125 MPa, and 275 MPa respectively.

Figure 38 indicates that the inner heating condition causes a compressive thermal stress to develop in the cylinder. This suggests that if a test bed were created that heated a target from the inside, the interface would experience an increase in contact pressure, and hence a reduction in thermal contact resistance. Conversely, when the target is heated form the outside, a tensile stress is developed at the interfacial region. The stress magnitude for the two heating conditions is not symmetric. The results for the external surface heating have an absolute value greater than the absolute value of the internal surface heating condition. The different surface areas of the inner and outer cylinder surfaces are the reason for the asymmetric distribution. The Matlab code used to develop these models can be seen in Appendix 1.

Annular Target Numerical Model

The goal of the numerical model was to validate the analytical model and explore interfacial heating as experienced in the real target. The numerical model was created using Pro-Engineer/Pro-Mechanica. A CAD model was first created in Pro-engineer and then transferred into Pro-Mechanica where it was meshed and analyzed.

Contour plots of the radial stress for the internal and external surface heating conditions can be seen in Figure 39 and Figure 40 respectively. As was noted from the analytic model results, the internal surface heating condition put the interface of the cylinders in compression while the external surface heating condition put the interface of the cylinders in tension.
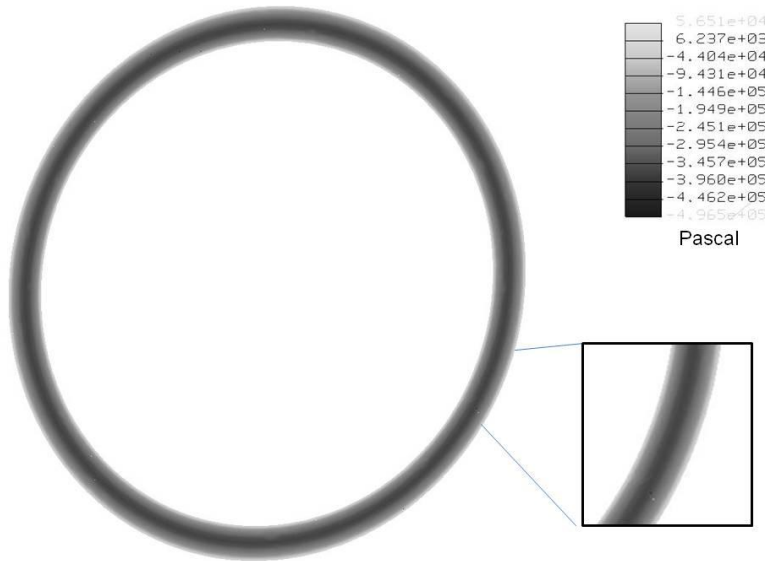
Figure 39. Radial stress distribution for inner surface heating
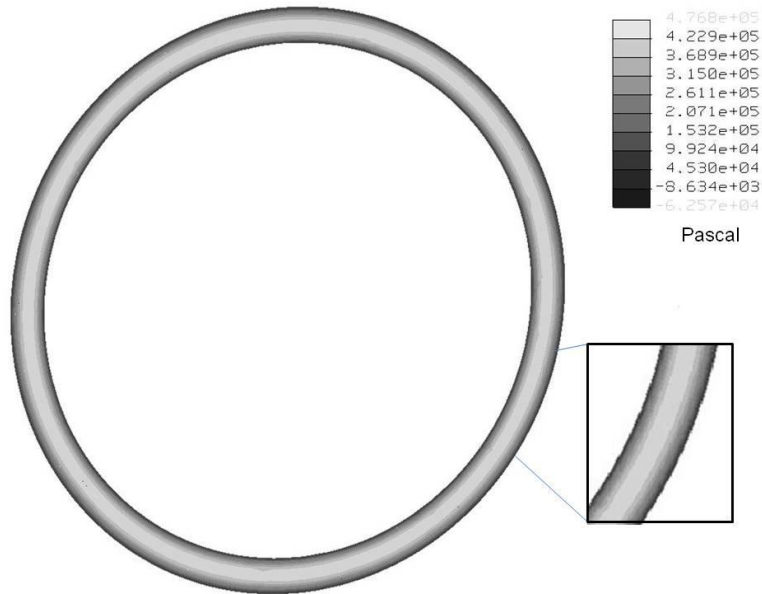
Figure 40. Radial stress distribution for outer surface heating

A comparison of the radial stress values from the analytic and numeric models is shown

in Table 4, Table 5, and Figure 38.

The percent difference between all of the compared values is below ten percent

and even smaller at the location of the interface. The similar results between the models

provide the confidence to use the numerical model to evaluate the stress that is developed

when heating at the interface.

Table 4. Internal surface heating condition comparison with percent difference

Thickness Distance (mm)	Analytical Radial Results (Pa)	Numerical Radial Results (Pa)	Percent Difference (%)
0	0	0	0
0.225	-1.69E+05	-1.82E+05	7.5
0.45	-2.85E+05	-2.86E+05	0.4
0.675	-3.49E+05	-3.50E+05	0.3
0.9	-3.70E+05	-3.68E+05	0.5
1.14	-3.42E+05	-3.39E+05	1.1
1.38	-3.68E+05	-2.70E+05	1.0
1.62	-1.51E+05	-1.55E+05	2.4
1.87	0	0	0

Table 5. External surface heating condition comparison with percent difference

Thickness Distance (mm)	Analytical Radial Results (Pa)	Numerical Radial Results (Pa)	Percent Difference (%)
0	0	0	0
0.225	2.08E+05	1.94E+05	7.3
0.45	3.26E+05	3.25E+05	0.3
0.675	4.00E+05	3.99E+05	0.2
0.9	4.20E+05	4.22E+05	0.5
1.14	3.86E+05	3.89E+05	0.6
1.38	3.08E+05	3.04E+05	1.6
1.62	1.77E+05	1.72E+05	2.5
1.87	0	0	0

Interfacial Heating Condition

The primary goal of the numerical study is to provide direction in establishing a

measurement methodology for the next phase of the target development. The interfacial

heating which is impossible to replicate in the lab, must be compared to the internal and

external surface heating experimental configurations. Figure 37 compares the temperature

distributions of the inner, interfacial, and outer heating conditions. The plot indicates the same heating load will produce the same overall temperature drop. More importantly from a thermal stress standpoint, the qualitative temperature distribution within the cylinder is parabolic as opposed to linear. A plot of the radial stresses as a function of the target thickness compared to the inner and outer surface heating can be seen in Figure 38.

Figure 38 indicates interfacial radial stress is zero at the inner and outer surfaces. However, unlike the inner and outer heating cases, there is an interior point where the stress is zero. The stress located between the inner surface and the zero point is a positive tensile stress and the stress from this point to the outer surface is a negative compressive stress. Overall the stress level is also much smaller than interior or exterior heating at the same thermal load.

From a metrology perspective, it is clear heating from the external surface will tend to increase the thermal contact resistance while internal surface heating will decrease the thermal contact resistance. To ensure that the measurements provide conservative results with respect to evaluating the interface contact resistance, external heating is preferred. In other words, if the thermal contact resistance measured when the interface is put in tension still meets performance requirements, there will be a low risk of target failure due to thermal contact resistance. Further, it is clear the total thermal load for testing can be significantly reduced to achieve a stress field closer in magnitude to the internal heating case.

CHAPTER 5: NON-DIMENSIONAL SIMPLY SUPPORTED PLATE

Understanding the fundamental thermal-mechanical behavior of plates will give guidance for more complex models. An analytical model produced first order analysis results for a plate with a uniform thermal gradient through the thickness. The edges of the plate were simply supported meaning they were not allowed to translate in the X, Y, or Z directions. Simply supported also means there is no moment applied to the edge and a point on that edge is free to rotate as if on a hinge. An image illustrating the simply supported boundary condition can be seen in Figure 41.

Wall

Plate

No XYZ movement is
allowed but rotation is
allowed i.e. no moment is
produced.
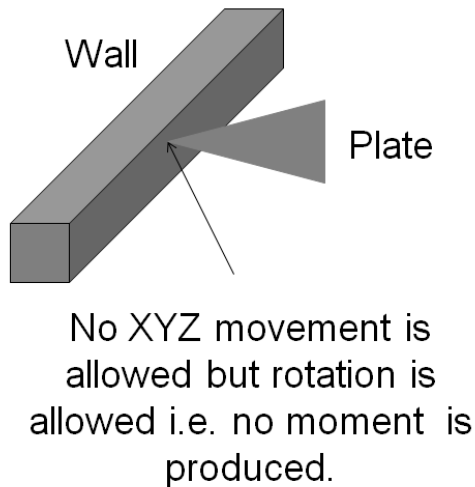
Figure 41. Simply supported boundary condition

The focus of this chapter is on the development of non-dimensional analytic model describing the thermal-mechanical behavior of a simply supported plate providing direction to the length, width, and thickness for a molybdenum-99 production target.

Setup

Non-dimensional analytical modeling started with a simply supported model based on work done by Noda, Hetnarski, and Tanigawa [52]. A sketch with a labeled plate can be seen in Figure 42.
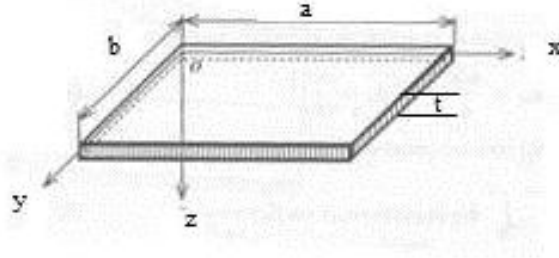
Figure 42. Sketch of plate with labels

The governing equation for a simply supported plate is

$$\nabla^2 \omega = -\frac{1}{(1-\upsilon)D} M_T$$

(5.1.1)

where $D = \frac{Et^3}{12(1-\upsilon^2)}$ represents the flexural rigidity of the plate, and $M_T = \alpha E \int_{-t/2}^{t/2} \tau z dz$ represents the thermally induced pressure exerted on the plate, and ω is the out of plane deflection[52]. Four non-dimensional variables were introduced to the model and are

$$x^* = \frac{a}{L_c}$$

(5.1.2)

$$y^* = \frac{b}{L_c}$$

(5.1.3)

$$t^* = \frac{t}{L_c}$$

(5.1.4)

56

$$\omega^* = \frac{\omega - \omega_o}{L_c}$$

(5.1.5)

where all of the star values represent the non-dimensional variables, L_c represents the

characteristic length equal to the length of the plate in the X direction, and ω_o is the initial

deformation. The non-dimensional boundary conditions for the model are

$$\omega^* = \frac{0 - \omega_o}{L_c} = 0 \quad x^* = 0 \quad x^* = 1$$
$$\text{at} \quad \text{and}$$

(5.1.6)

$$\omega^* = \frac{0 - \omega_o}{L_c} = 0 \quad y^* = 0 \quad y^* = b/a$$
$$\text{at} \quad \text{and}$$

(5.1.7)

solving the governing equation using Helmholtz's method gives a solution as a function

of two infinite summations [53],

$$\omega^*(x, y) = -\sum_{m=1}^{\infty}\sum_{n=1}^{\infty} F_{mn} \frac{\sin\left(\frac{m\pi x^*}{1}\right)\sin\left(\frac{n\pi y^*}{b/a}\right)}{\left(\frac{m\pi}{1}\right)^2 + \left(\frac{n\pi}{b/a}\right)^2}$$

(5.1.8)

where F_{mn} is given by

$$F_{mn} = -\left(\frac{0.014177}{(b/a)t^*}\right)\left(-\frac{1}{m\pi}\cos(m\pi) + \frac{1}{m\pi}\right)\left(-\frac{b/a}{n\pi}\cos(n\pi) + \frac{b/a}{n\pi}\right)$$

(5.1.9)

57

A parametric study of the non-dimensional deflection, using 100 terms for convergence, was done at various aspect ratios of X length versus Y length and at various plate thicknesses. The Matlab code used to produce the results for this chapter can be seen in Appendix 2.

Results

A temperature difference of 230 K was considered the worst case scenario and was applied across the thickness of the plate.   A plot of the non-dimensional maximum deflection, located in the center of the plate, versus the non-dimensional thickness and length and width aspect ratio can be seen in Figure 43. A changing thickness with a constant temperature difference will change the deflection values. This occurs because the thermal moment M_T will remain the same while the stiffness value D will increase. The relationship between M_T and D will continue to be important in Chapter 6. A profile plot of the simply supported plate with a one to one aspect ratio and a non-dimensional thickness of 0.001 can be seen in Figure 44.
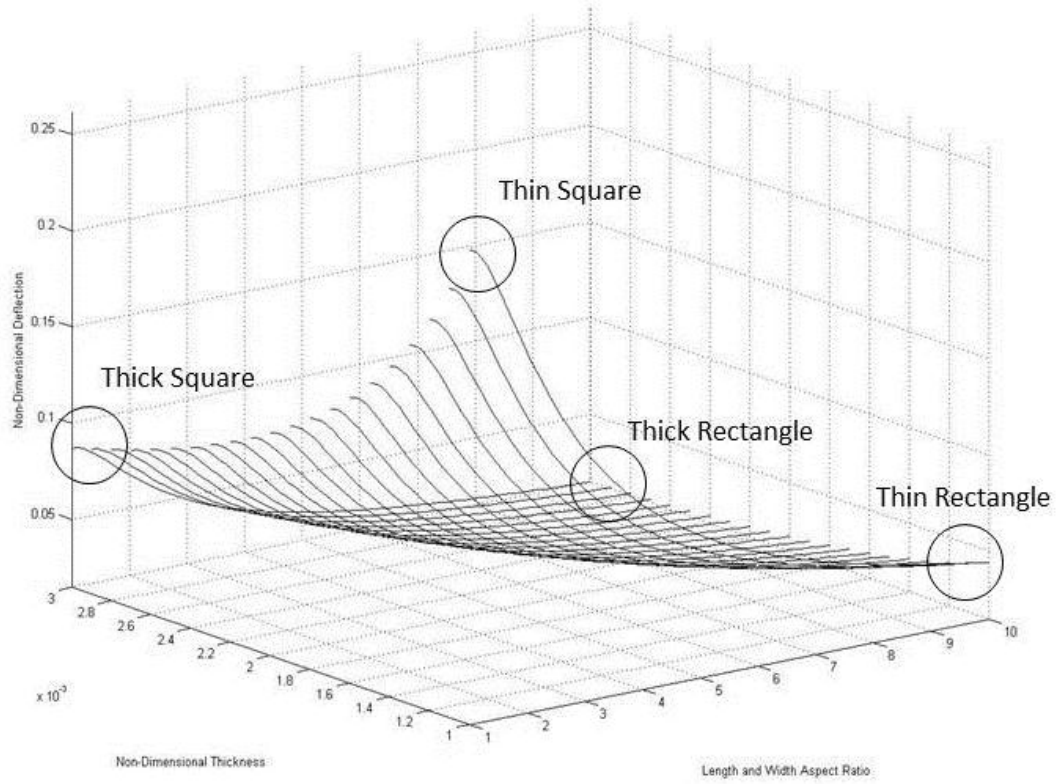
Figure 43. Non-dimensional deflection
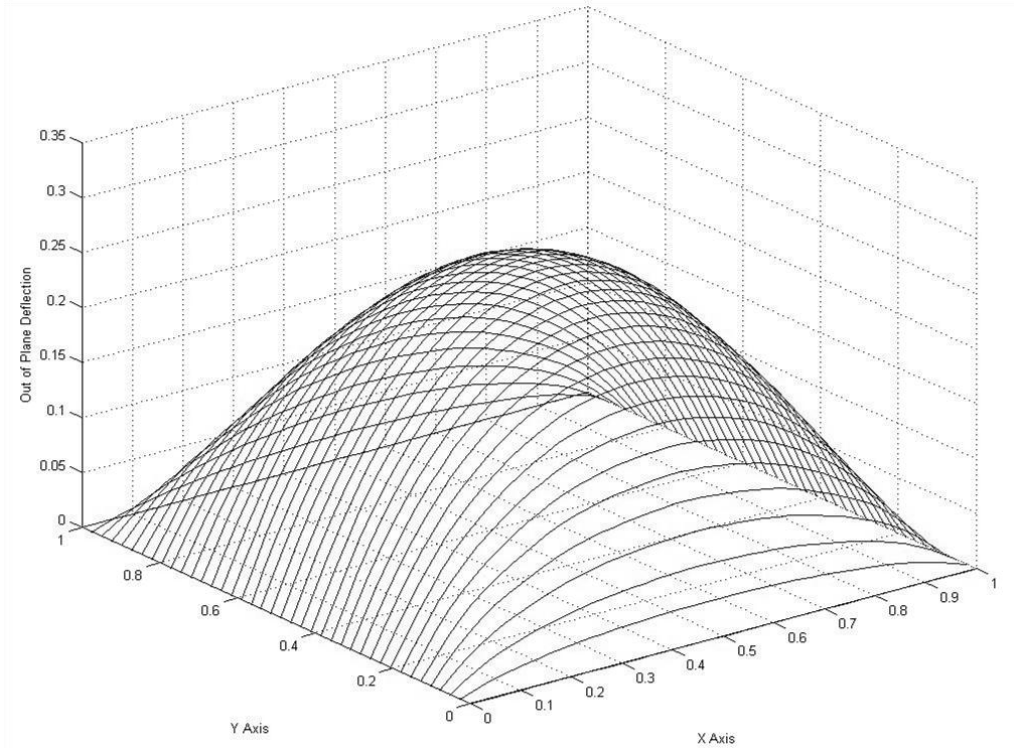
Figure 44. Non-dimensional simply supported plate profile at a one to one aspect ratio and a non-dimensional thickness of 0.001

Figure 43 clear shows the greatest deflection will occur when the thickness of the plate is small and when the aspect ratio of the plate is equal to 1. The plot in Figure 43 also indicates the thermal-mechanical behavior is non-linear as both the thickness and aspect ratios are adjusted. The behavior indicates there is a point when a change in the aspect ratio will not greatly affect the thermal-mechanical deflection. Further they indicate there is an optimal combination of the two aspect ratios that will produce a target that minimizes thermal-mechanical deflection.

CHAPTER 6: THICKNESS AND DEFLECTION RELATIONSHIP

Thickness and Deflection Investigation on Uniform Heating

Investigating the relationship between the thickness and the thermal-mechanical

deflection began using a one dimensional heat transfer resistance network to describe the

thermal profile of the plate. The resistance network used can be seen in Figure 45 and a

diagram showing the conditions on the plate can be seen in Figure 46.
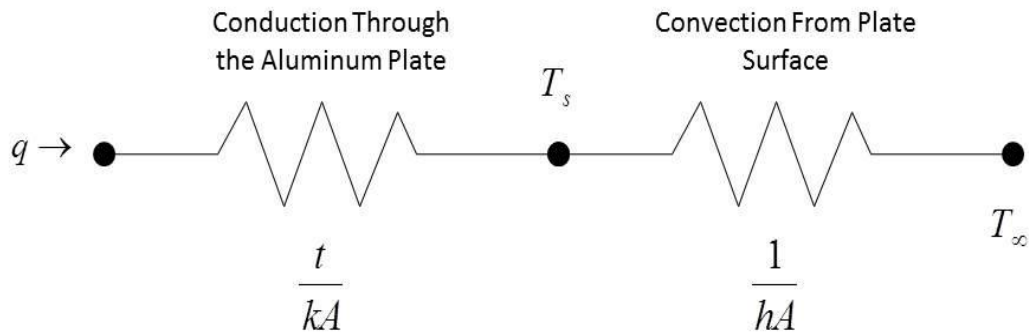
Figure 45. Heat transfer resistance network [54]
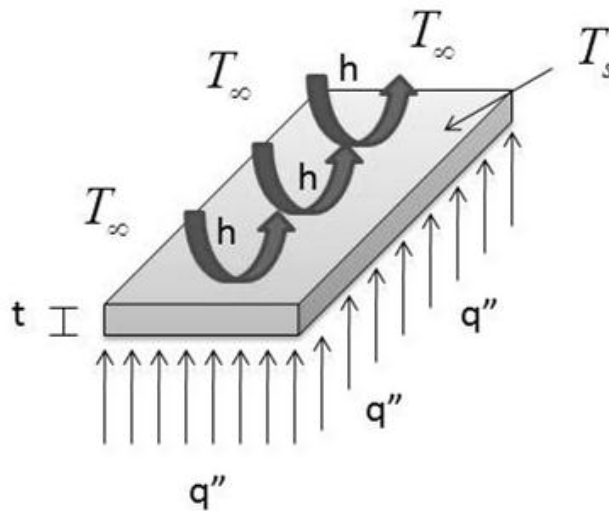
Figure 46. Plate conditions

A heat flux is applied to one side of the plate which is then transferred through conduction then convection to a cooling medium. The thermal moment created in the plate can found using

$$M_T = \alpha E \int_{-t/2}^{t/2} \Delta T z \, dz$$

(6.1.1)

where M_T is the thermal induced moment, α is the coefficient of thermal expansion, E is the Young's modulus, z is the location through the thickness, and $\Delta T = T - T_\infty$ is determined using

$$q = \frac{\Delta T}{R}$$

(6.1.2)

where q is the total energy and R is the thermal resistance. The thermal resistance is a combination of the various heat transfer modes in Figure 46 and is given by

$$R = \frac{t}{kA} + \frac{1}{hA}$$

(6.1.3)

where t is the total thickness of the plate, k is thermal conductivity, A is the cross-sectional area, and h is the heat transfer coefficient. Combining equations (6.1.2) and (6.1.3) then solving for T gives the temperature as a function of thickness $\tau(z)$.

$$\Delta T = T - T_\infty = q^{''}\left(\frac{t/2 - z}{k} + \frac{1}{h}\right)$$

(6.1.4)

Combining equations (6.1.1) and (6.1.4), then integrating gives the thermal induced moment.

$$M_T = -\alpha E q^{''}\frac{t^3}{12k}$$

(6.1.5)

The governing equation for a simply supported plate is

$$\nabla^2\omega = -\frac{1}{(1-v)D}M_T$$

(6.1.6)

where ω is the out of plane deflection and $D = \frac{Et^3}{12(1-v^2)}$ is the stiffness of the plate [52].

The combined equation is then

$$\nabla^2\omega = -\frac{-\alpha E q^{''}\frac{t^3}{12k}}{(1-v)\left(\frac{Et^3}{12(1-v^2)}\right)}$$

(6.1.7)

simplifying gives.

$$\nabla^2\omega = -\frac{-\alpha q^{''}(1-v^2)}{(1-v)k}$$

(6.1.8)

Equation (6.1.8) indicates the deflection will be a function of only the heat flux, coefficient of thermal expansion, Possion's ratio, and thermal conductivity. This seems counterintuitive and opposite of what the results indicated in Chapter 5. The thickness does not affect the deflection because the thickness is directly proportional in the M_T and D values. This was not the case in Chapter 5 since a constant temperature difference was used thus producing a constant M_T. M_T is the force causing deflection and the D is the force restricting deflection. Since a change in thickness will affect both the same amount, the ratio between M_T and D will always be the same no matter the thickness value.

CHAPTER 7: PLATE UNIFORM HEATING BOUNDARY CONDITION STUDY

The purpose of the boundary condition study was to determine the effect of edge holding conditions on the thermal-mechanical behavior of the simulated target using two edge bonded plates. This is a departure from previous analytic work where only one plate was analyzed. Abaqus, a commercial finite element analysis (FEA) software package, can model more complex simulations of the target. The simply supported plate model discussed in previous chapters was used for benchmarking the numerical models which was followed by the establishment of mesh independence. Finally, a uniform heating model was used to analyze the effect of various boundary conditions i.e. edge holding conditions on the target thermal-mechanical behavior.

Benchmarking

The numerical modeling software was benchmarked against another analysis technique to validate the Abaus solution. The previous simply supported plate model was chosen as the benchmark [5]. Unlike previous uses, the model was not non-dimensionalized and the equations for the out of plane deflection are

$$\omega(x, y) = -\sum_{m=1}^{\infty}\sum_{n=1}^{\infty} \frac{F_{mn}}{\left(\dfrac{m\pi}{a}\right)^2 + \left(\dfrac{n\pi}{b}\right)^2} \sin\left(\frac{m\pi x}{a}\right) \sin\left(\frac{n\pi y}{b}\right)$$

(7.1.1)

where F_{mn} can be seen in equation (7.1.2).

$$F_{mn} = -\frac{4}{ab}\left(\frac{\alpha(\Delta T)(1-\upsilon)}{t}\right)\left(-\frac{a}{m\pi}\cos(m\pi)+\frac{a}{m\pi}\right)\left(-\frac{b}{n\pi}\cos(n\pi)+\frac{b}{n\pi}\right)$$

(7.1.2)

A single plate solid model was drawn using the Abaqus pre-processor. The geometric dimensions matched those of the analytic model and are shown in Table 1. The edge boundaries were simply supported matching with the analytic model. An 8-node thermally coupled brick with tri-linear displacement and temperature, reduced integration, and hourglass control was the chosen element. Reading the Abaqus documentation indicated this element type was well suited for this problem. A roller condition was applied to the edge simulating the simply supported boundary condition. It was determined through reading outside sources this boundary condition would reproduce the simply supported boundary condition with three dimensional elements. The meshed model is shown in Figure 47 with dimensions of 0.205 m x 0.06 m x 0.001 m.

.
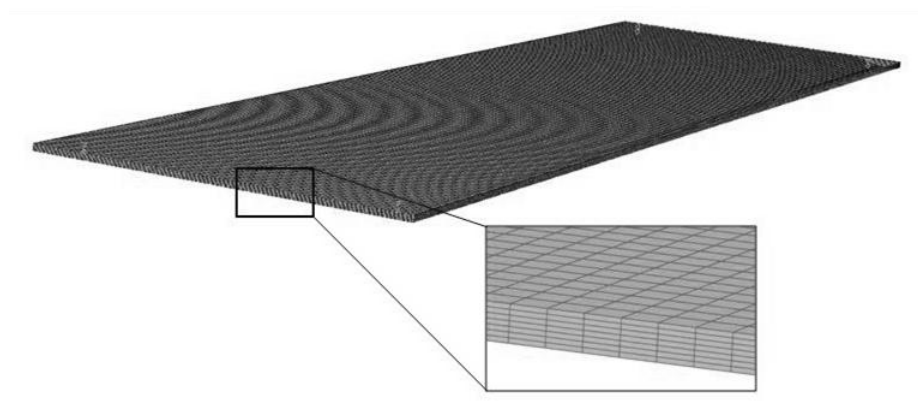
Figure 47. Image of meshed model used for benchmark

A linear temperature profile was applied across the thickness of the plate inducing a thermal deflection. The temperature differences applied across the plate thickness for simulation are in Table 6.

Table 6. Benchmark model geometry and boundary conditions

Temperature Difference through the Plate used for Benchmarking (K)
5
10
50
100
500
1000

Various global seeds and elements through the thickness were used to find the benchmarked optimized mesh. The benchmarked mesh independent model had a global spacing of 0.001 with 7 elements through the thickness of the plate. The results from the benchmarking study can be seen in Table 7.

Table 7. Maximum deflection benchmarking study

ΔT (K)	Analytic (mm)	Numeric (mm)	Percent Difference
5	0.06829	0.06864	0.51121
10	0.1366	0.1373	0.51114
50	0.6829	0.6864	0.51121
100	1.366	1.373	0.51114

The results in Table 7 show that the percent difference at all of the various ΔT values was approximately 0.5% which is an acceptable value. Contrary to accepted practice a denser

mesh did not lower the percent difference between the models and actually increased the percent difference when increased beyond the optimized settings.

Setup

The effect of boundary conditions on plate deflection and plate stress was evaluated numerically with the optimized mesh. Two flat plates were drawn to the dimensions in Table 6 and meshed using three-dimensional elements as shown in Figure 48. The edges were subjected to different mechanical constraints consistent with real target irradiation holding conditions. LEU fission heat generation was simulated by applying a uniform temperature difference across the thickness of the plates. The material properties for Al 6061 T-6 aluminum used in the simulations can be seen in Table 8.
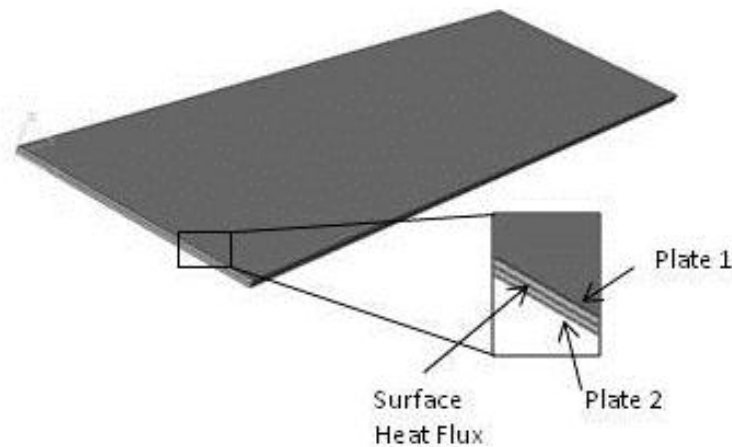
Figure 48. Plate Geometry used for boundary condition study

Table 8. Material properties of aluminum 6061 T-6

Young's Modulus (Pa)	Poisson's Ratio	Coefficient of Thermal Expansion (1/K)	Thermal Conductivity (W/mK)
6.89e10	0.33	2.358e-5	167

For all simulations it was assumed the edges of the two plates were welded together. For simulations where a given edge was rigidly constrained a no translation/rotation boundary condition was applied. When an edge was welded it was allowed to expand laterally, the Zsymm boundary condition in the Abaqus software was used. Zsymm allows no translation in the Z direction (bonded condition) and no rotation about the X and Y axis. The plates are free to expand in the X and Y direction however.

The three holding conditions evaluated in this study are fully constrained, partially constrained, and free edges. A description of the boundary conditions applied for each of the holding conditions can be seen in Figure 49. It should be noted the free edge boundary condition analysis has one end of the target was fully constrained allowing for numerical convergence. Symmetry in the model was assumed and reported values taken from the edge opposite the fully constrained edge.
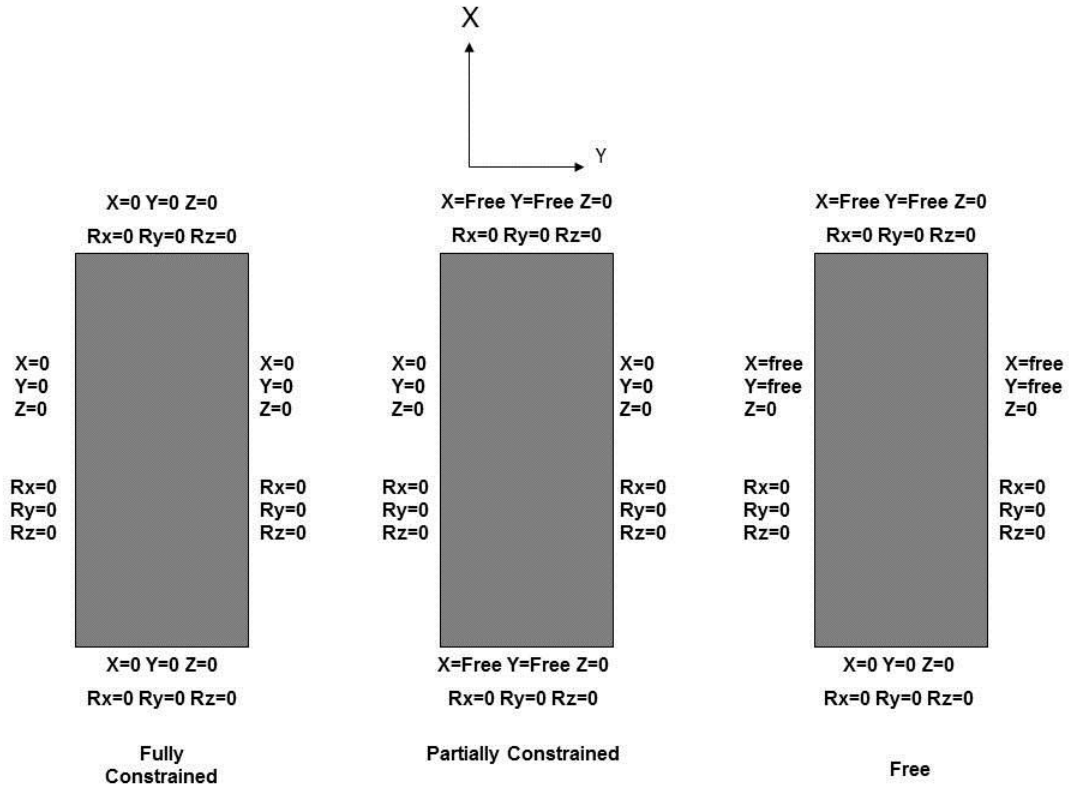
Figure 49. Applied boundary conditions for the uniform numeric simulations

The temperature applied to the outer and inner surfaces of the plate produced a ΔT corresponding to a different thermal load. A list of the various thermal loads used along with the corresponding temperatures determined by splitting the thermal load between the two plates can be seen in Table 9.

Table 9. Thermal loads with their corresponding heat fluxes and ΔT used on simulation target

Power (W)	Heat Flux (W/m²)	ΔT through the thickness of the plate (K)
1,000 =	8.13e4 =	0.49
5,000 =	4.06e5 =	2.43
10,000 =	8.13e5 =	4.87
20,000 =	1.62e6 =	9.74
30,000 =	2.43e6 =	14.60
40,000 =	3,25e6 =	19.47
50,000 =	4.06e6 =	24.34
60,000 =	4.87e6 =	29.21

Temperature differences corresponding to the thermal load were determined using a simple conduction heat transfer resistance network through a single plate. The heat transfer resistance network can be seen in Figure 50 with the corresponding equation [54]
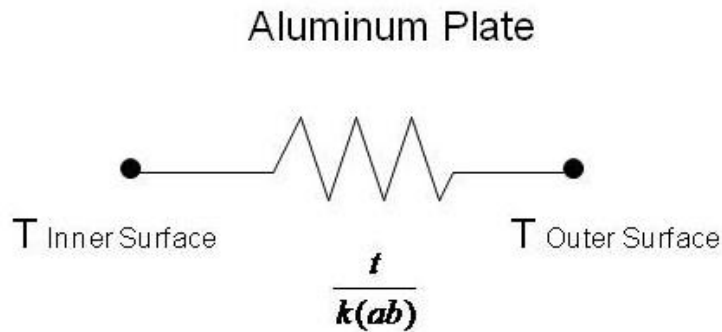
Figure 50. Heat transfer resistance network through a plate [54]

$$T_{Inner} = \frac{t}{k(a(b))} q + T_{Outer} \qquad (7.2.1)$$

where T_{Inner} is the temperature of the surface in contact with the other plate, t is the thickness of the plate, k is the thermal conductivity of aluminum 6061, q is the thermal load, and T_{Outer} is the surface temperature of the plate not in contact with the other plate.

Results

Figure 51 shows a comparison of the maximum plate deflection for the three boundary conditions identified in Figure 49 along with Table 10. The plot shows as thermal load increases, the amount of deflection increases. This trend is consistent with the understanding that a higher thermal load induces a larger temperature difference across the aluminum plate, and hence increases the difference in surface thermal expansion.

The figure also shows the greatest amount of deflection occurs in the fully constrained boundary condition, followed closely by the partially constrained boundary condition. The fully constrained boundary condition produces the greatest amount of deflection because the edges are not allowed to translate forcing the free central part of the plate to bow outward. In contrast the partially constrained and free edge cases both allow either partial or total expansion of their edges. This in turn allows some of the expansion energy to be relieved through edge expansion. The greater the amount of freedom the edges are given, the lower the deflection. The relevance with respect to target design is a large deformation will cause an internal gas gap as suggested by the exaggerated deflection plot shown in Figure 52. The internal gap will increase the thermal resistance between the LEU foil and the aluminum cladding, increasing the risk the target will violate specified temperature limits.
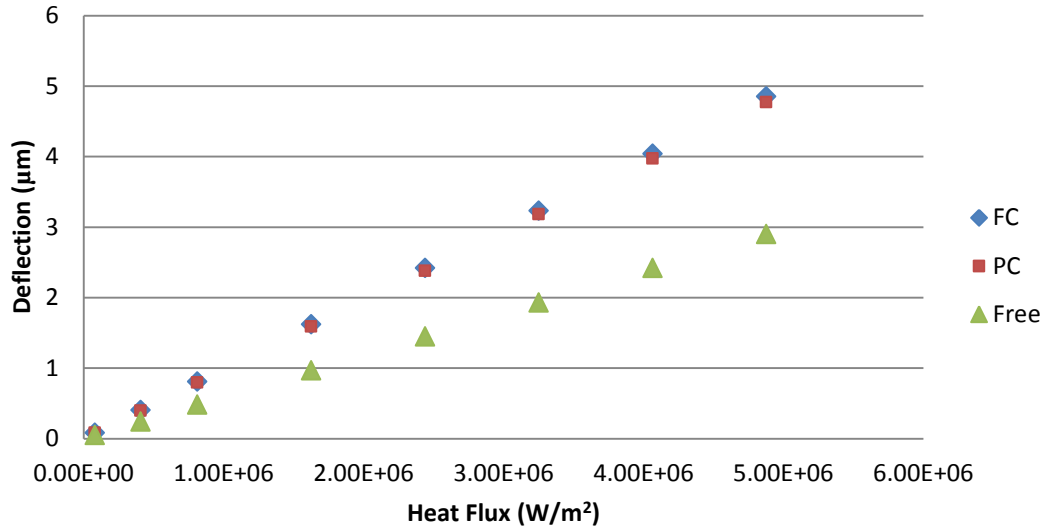
Figure 51. Comparison of the maximum plate deflection

Table 10. Deflection for uniform heating

Power (W)	Heat Flux (W/m²)	Fully Constrained Deflection (μm)	Partially Constrained Deflection (μm)	Free Deflection (μm)
1,000 =	8.13e4	0.081	0.080	0.048
5,000 =	4.06e5	0.404	0.397	0.241
10,000 =	8.13e5	0.808	0.795	0.483
20,000 =	1.62e6	1.620	1.590	0.966
30,000 =	2.43e6	2.420	2.380	1.450
40,000 =	3,25e6	3.230	3.180	1.930
50,000 =	4.06e6	4.040	3.970	2.420
60,000 =	4.87e6	4.850	4.770	2.900

Figure 52. Exaggerated deflection of fully constrained boundary condition simulation
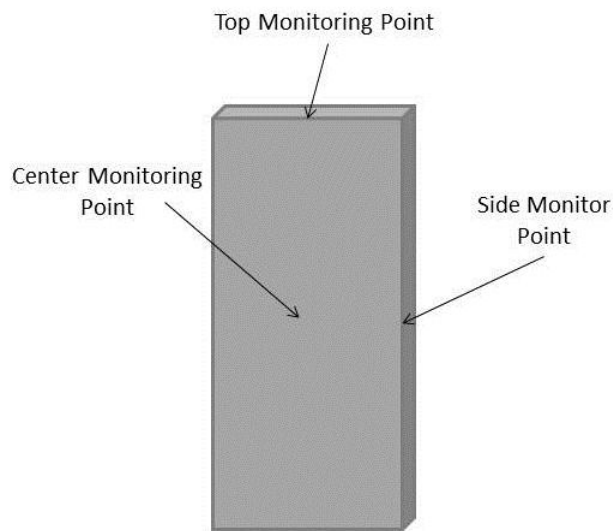
Figure 53. Monitoring points

A comparison of the von Mises stress at the monitoring points indicated in Figure 53 is shown in Figure 54, Figure 55, and Figure 56. The plots illustrate an increase in thermal load increases stress at all monitoring locations. For the center monitoring point, the largest stress occurs for the free edges condition which can be explained by recognizing allowing the edges to freely expand strains the central part of the plate. It is interesting to note that the stress level at the plate center is about the same for the fully constrained and partially constrained boundary conditions.

74
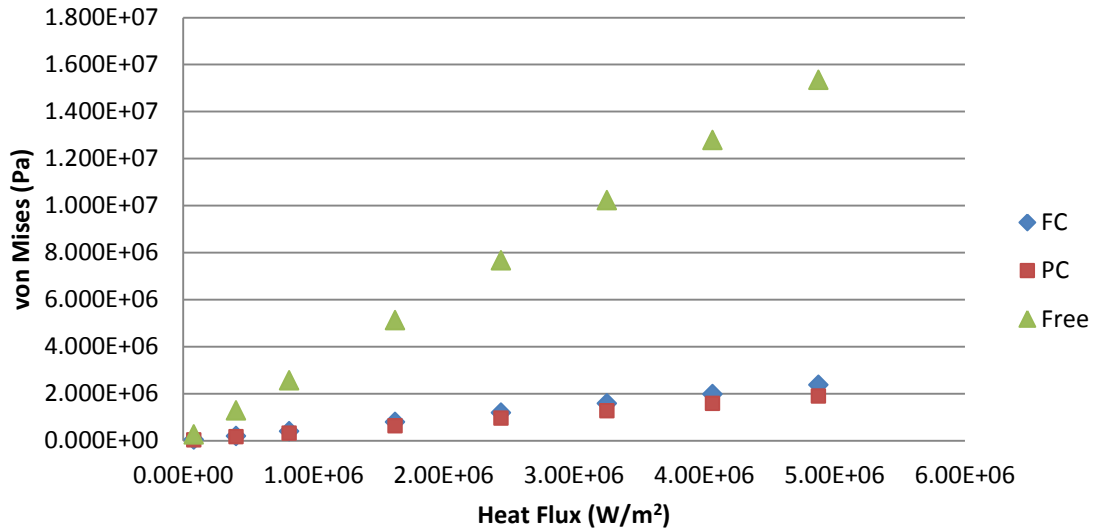
Figure 54. Comparison of center von Mises Stress

Table 11. Comparison of center von Mises stress values

Power (W)	Heat Flux (W/m²)	Fully Constrained von Mises Stress (Pa)	Partially Constrained von Mises Stress (Pa)	Free von Mises (Pa)
1,000 =	8.13e4	3.95e4	3.15e4	2.55e5
5,000 =	4.06e5	1.97e5	1.57e5	1.27e6
10,000 =	8.13e5	3.95e5	3.15e5	2.55e6
20,000 =	1.62e6	7.90e5	6.31e5	5.11e6
30,000 =	2.43e6	1.18e6	9.47e5	7.67e6
40,000 =	3,25e6	1.58e6	1.26e6	1.02e7
50,000 =	4.06e6	1.97e6	1.57e6	1.27e7
60,000 =	4.87e6	2.37e6	1.89e6	1.53e7

The relative stress magnitudes reverse when comparing the stress at the side monitoring point as seen in Figure 55. The partially and fully constrained boundary conditions have stress levels higher than the free edges case. A significant amount of deformation takes place on these edges producing this behavior. This can be qualitatively seen in Figure 52 where a significant amount of bending takes place.
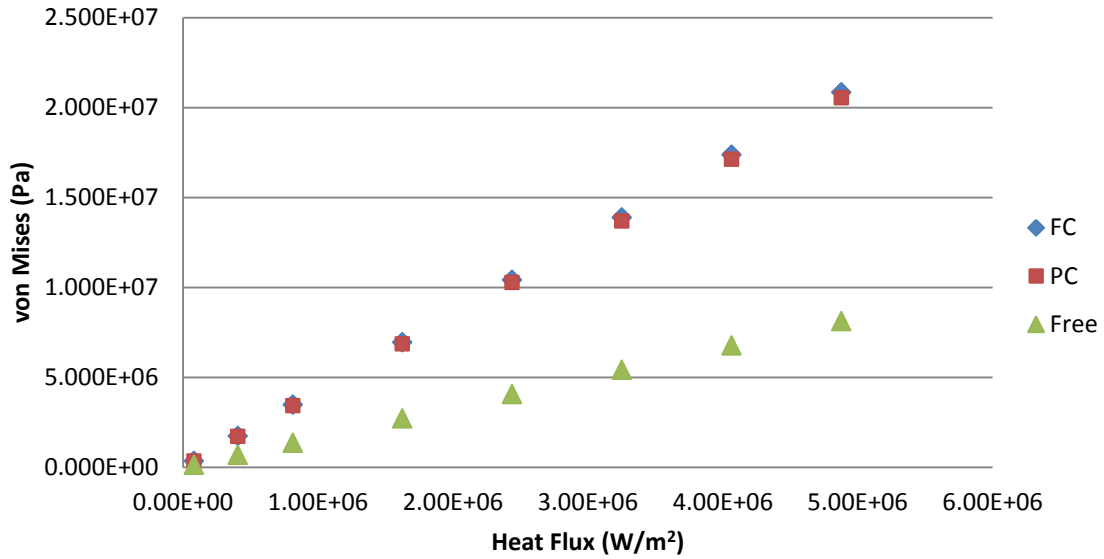
Figure 55. Comparison of side weld von Mises stress

Table 12. Comparison of side weld von Mises stress values

Power (W)	Heat Flux (W/m²)	Fully Constrained von Mises Stress (Pa)	Partially Constrained von Mises Stress (Pa)	Free von Mises (Pa)
1,000 =	8.13e4	3.47e5	3.42e5	1.35e5
5,000 =	4.06e5	1.73e6	1.71e6	6.76e5
10,000 =	8.13e5	3.47e6	3.42e6	1.35e6
20,000 =	1.62e6	6.94e6	6.84e6	2.70e6
30,000 =	2.43e6	1.04e7	1.02e7	4.06e6
40,000 =	3,25e6	1.38e7	1.36e7	5.41e6
50,000 =	4.06e6	1.73e7	1.71e7	6.76e6
60,000 =	4.87e6	2.08e7	2.05e7	8.12e6

The relative stress magnitudes at the top monitoring location are shown in Figure 56. Interestingly, the free edge and partially constrained boundary conditions have stress levels lower than the fully constrained boundary condition. For the partially constrained case, this is in contrast to the side monitoring location where the stress level was similar to the fully constrained boundary condition.

76
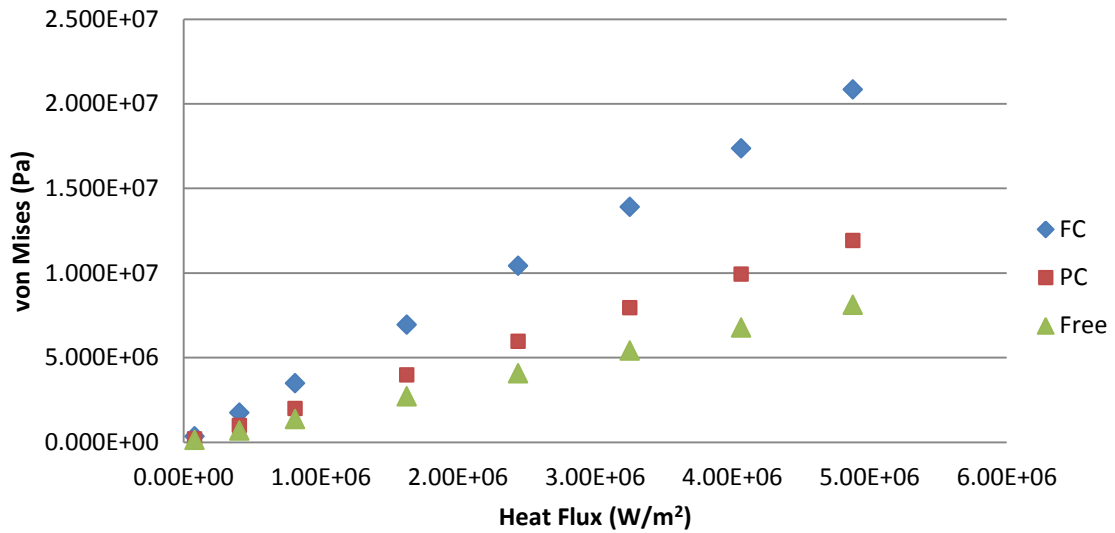
Figure 56. Comparison of top weld von Mises stress

Table 13. Comparison of top weld von Mises stress values

Power (W)	Heat Flux (W/m²)	Fully Constrained von Mises Stress (Pa)	Partially Constrained von Mises Stress (Pa)	Free von Mises (Pa)
1,000 =	8.13e4	3.47e5	1.98e5	1.35e5
5,000 =	4.06e5	1.73e6	9.92e5	6.76e5
10,000 =	8.13e5	3.47e6	1.98e6	1.35e6
20,000 =	1.62e6	6.94e6	3.96e6	2.70e6
30,000 =	2.43e6	1.04e7	5.95e6	4.05e6
40,000 =	3,25e6	1.39e7	7.93e6	5.41e6
50,000 =	4.06e6	1.73e7	9.92e6	6.76e6
60,000 =	4.87e6	2.08e7	1.19e7	8.11e6

When comparing the stress levels between the three different locations, it is clear for a given thermal load, the stress is highest at the welded edges for the fully constrained and partially constrained boundary conditions. For the free edges boundary condition, the maximum stress occurs in the center of the plate. This is confirmed by examining

77

contour plots of the von Mises stress for each holding condition in Figure 57, Figure 58, and Figure 59 where the dark areas represent lower stress and the lighter areas represent higher stress.
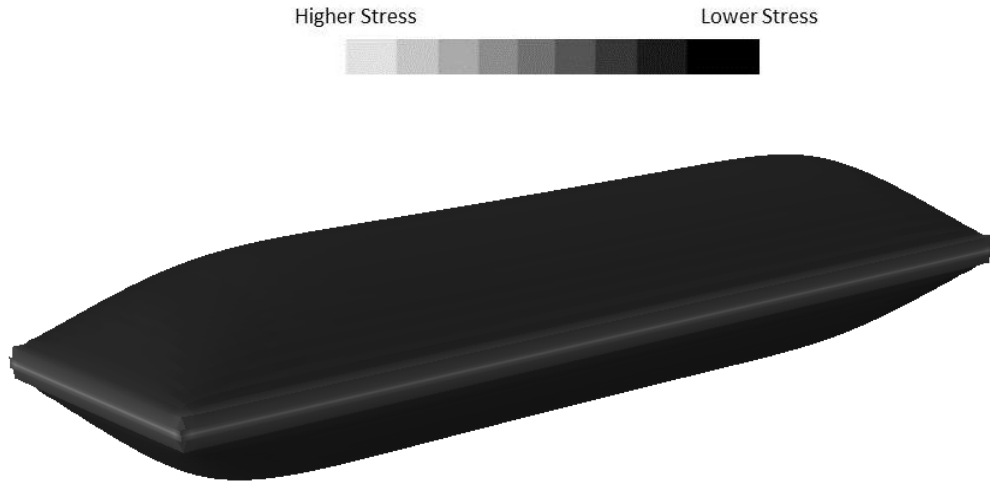
Figure 57. Fully constrained uniform heating von Mises stress contour plot
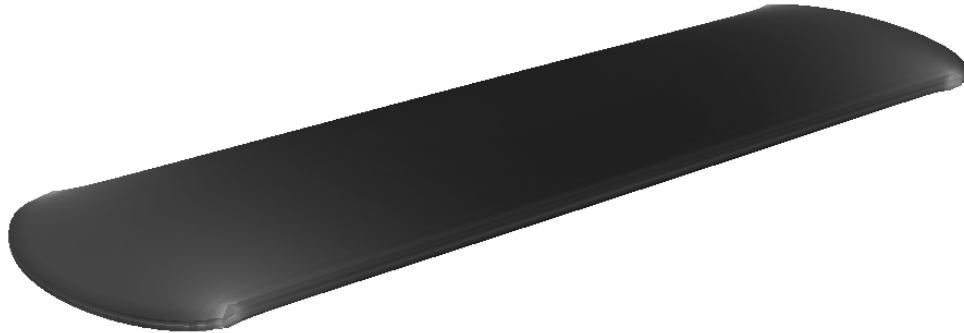
Figure 58. Partially constrained uniform heating von Mises stress contour plot
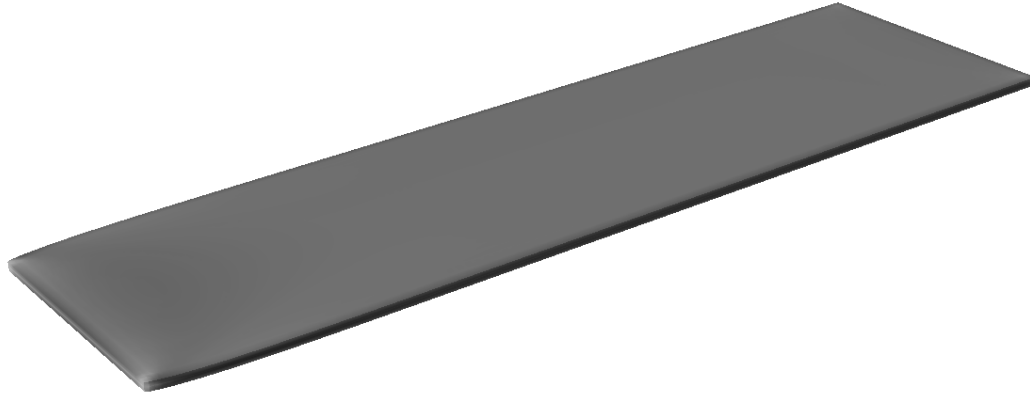
Figure 59. Free uniform heating von Mises stress contour plot

In terms of overall magnitude, the partially and fully constrained have higher stress than the free edge case at a given thermal load. Therefore, it appears free expansion of a plate target while being irradiated will minimize both the amount of plate deformation and the stress.

Plate Von Mises Stress and Aluminum Yield Strengths

The maximum von Mises stresses at each of the stress monitoring points were compared to the yield strengths of various aluminum alloys. The maximum stress values can be seen in and the aluminum alloy yield strengths can be seen in Table 14 and Table 15.

Table 14. Maximum von Mises Stresses at each monitoring point

Center Monitoring Point (Pa)	Side Monitoring Point (Pa)	Top Monitoring Point (Pa)
1.53e7	2.08e7	2.08e7

Table 15. Aluminum alloy yield strengths

Al 1100 Yield Strength (Pa)	Al 3003 Yield Strength (Pa)	Al 6061 Yield Strength (Pa)
2.75e8	1.25e8	1.05e8

The tables clearly show the maximum von Mises stresses do not exceed the yield strength of any alloy, indicating the target will not fail do to stress under the applied conditions.

CHAPTER 8: PLATE NON-UNIFORM HEATING

The purpose of the non-uniform heating study was to build upon what was learned in the uniform heating study and apply it to a more prototypical model. In the actual plate target the LEU foil has a smaller surface area than the aluminum cladding. During irradiation the LEU foil will produce a great amount of heat that will conduct through the cladding and convect off the cladding surface to the cooling water. In the uniform heating study the thermal profile through the thickness of each plate was the same at every XY point in the model. In the non-uniform heating situation the thermal profile will be a function of XY position and will be three dimensional in nature. An example of the uniform and non-uniform thermal profiles can be seen in Figure 60 where the lighter areas are the hotter sections and the darker areas are colder areas.

Uniform Thermal Profile
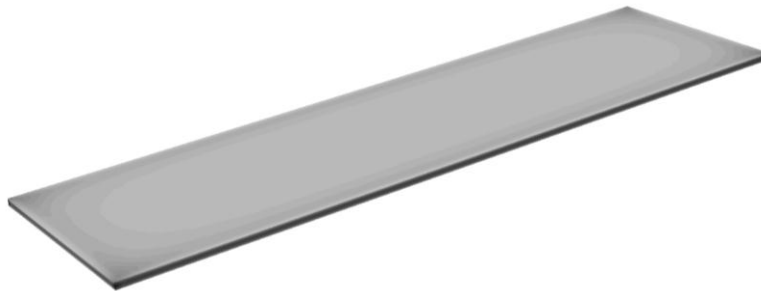
Non-Uniform Thermal Profile

Figure 60. Comparison of uniform and non-uniform thermal profile

Setup

The mesh developed for the uniform benchmark study was used in the non-uniform study. It was assumed a non-uniform thermal profile would not affect the effectiveness of the mesh. Two flat plates drawn to the dimensions from the uniform study were used. The edges were again subjected to different mechanical constraints consistent with actual reactor irradiation positions. LEU fission heat generation was simulated by applying uniform surface heat fluxes on the foil footprint on the aluminum cladding. The heat flux was again applied to the interface surfaces of the two plates. An image showing one of the plates with the surface heat area heighted can be seen in Figure 61 and the plate geometry can be seen in Figure 62. The edges of the heated area were 5 mm from the edges of the plates giving a heated area that was 195 mm x 50 mm.
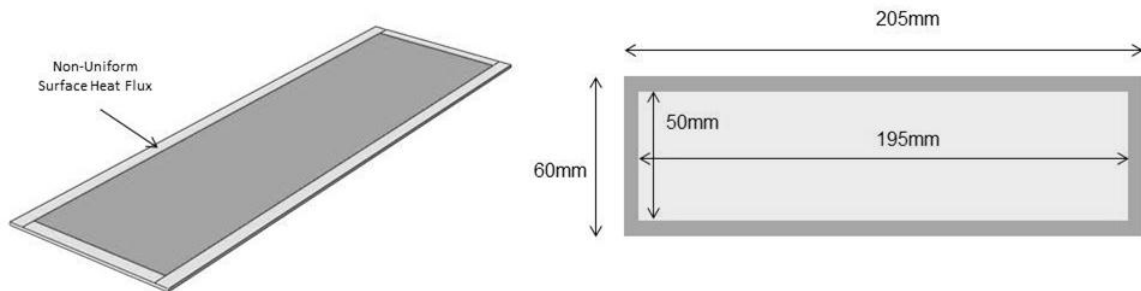
Figure 61. Non-uniform LEU foil footprint
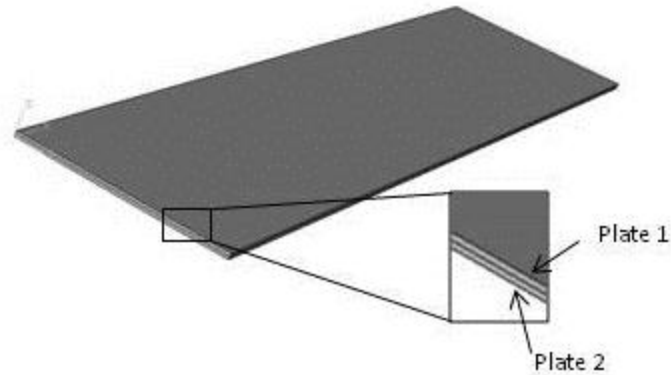
Figure 62. Plate geometry used for boundary condition study

      The three holding conditions were again evaluated in this study and are fully

constrained, partially constrained, and free edges. A description of the boundary

conditions applied for each of the holding conditions can be seen in Figure 63. It should

be noted the free edge boundary condition uses tie constraints on the free edges to

simulate the weld instead of the Zsymm boundary condition. The tie constraint simulates

a weld by connecting the nodes in contact between the two plate edges together.

Symmetry was assumed in the free model and reported values taken from the edge

opposite of the fully constrained edge.
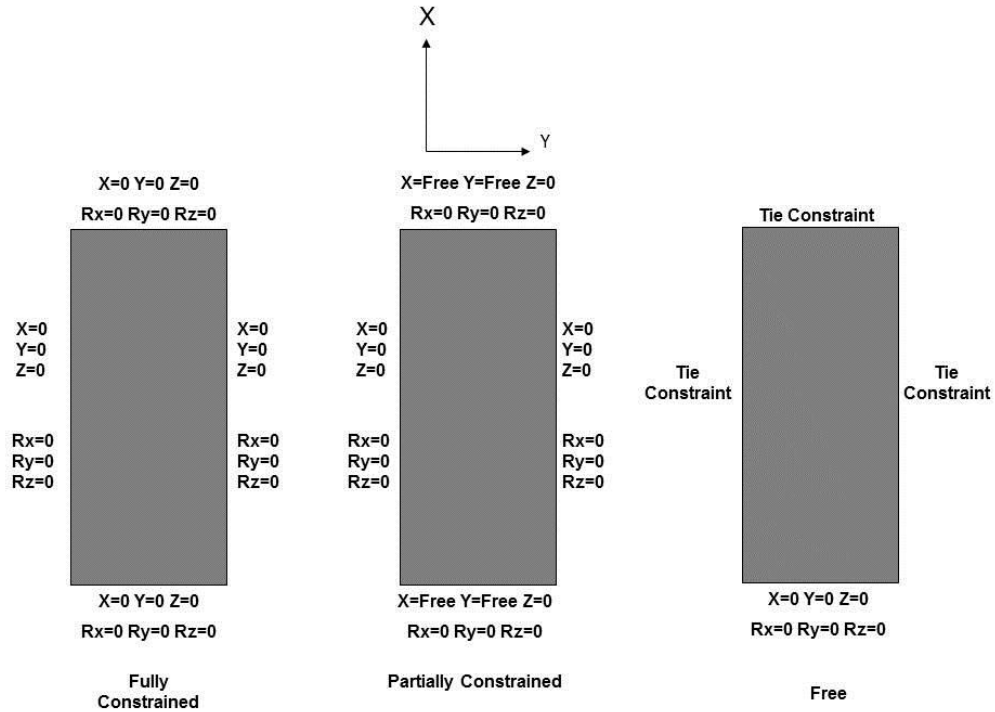
Figure 63. Applied boundary conditions for the non-uniform numeric simulations

Various thermal loads and heat transfer coefficients were examined in a

parametric study to determine their effect on the thermal-mechanical behavior of the

target. A list of the various thermal loads and heat transfer coefficients can be seen in

Table 16.

Table 16. Thermal Loads and heat transfer coefficients used on simulation target

Power (W)	Surface Heat Flux Applied to Each Side (W/m^2)	Heat Transfer Coefficients (W/m^{2}K)
1,000 =	5.13e4	
5,000 =	2.56e5	
10,000 =	5.13e5	
20,000 =	1.03e6	500; 1,000; 5,000; 10,000; 20,000
30,000 =	1.54e6	
40,000 =	2.05e6	
50,000 =	2.56e6	
60,000 =	3.08e6	

Operational limits established by MURR were used to develop a thermal resistance network used to estimate the allowable air gap during irradiation. The thermal resistance network used can be seen in Figure 64 and the values used in the network can be seen in Table 17. The calculated allowable air gap can be seen in Table 18.
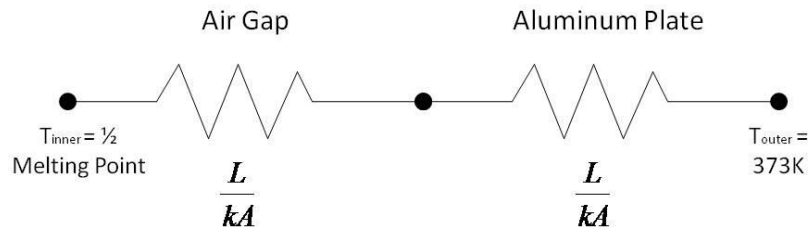
Figure 64. Thermal resistance network used to determine allowable air gap

Table 17. Values used in the thermal resistance network

Aluminum Alloy	Half Al 6061 Melting Point (K)	Thermal Conductivity Al 6061 (W/mK)	Yield Strength Al 6061 (MPa)	Thermal Conductivity Air (W/mK)
Al 6061	430	180	275	0.0314

Table 18. Allowable air gap with Al 6061

Power (W)	Surface Heat Flux Applied to Each Side (W/m^2)	Allowable Gap Al 6061 (m)
1,000 =	5.13e4	0.0526
5,000 =	2.56e5	0.0103
10,000 =	5.13e5	0.00510
20,000 =	1.03e6	0.00246
30,000 =	1.54e6	0.00158
40,000 =	2.05e6	0.00114
50,000 =	2.56e6	0.00087
60,000 =	3.08e6	0.00071

Deflection Results

        Figure 65, Figure 66, and Figure 67 show the maximum out of plane deflection for the fully constrained, partially constrained, and free conditions respectively. An estimate of the allowable air gap in the target during irradiation using Al 6061 was also included. Some data points are missing in certain plots because of convergence difficulties but the trends are assumed linear in these missing sections.
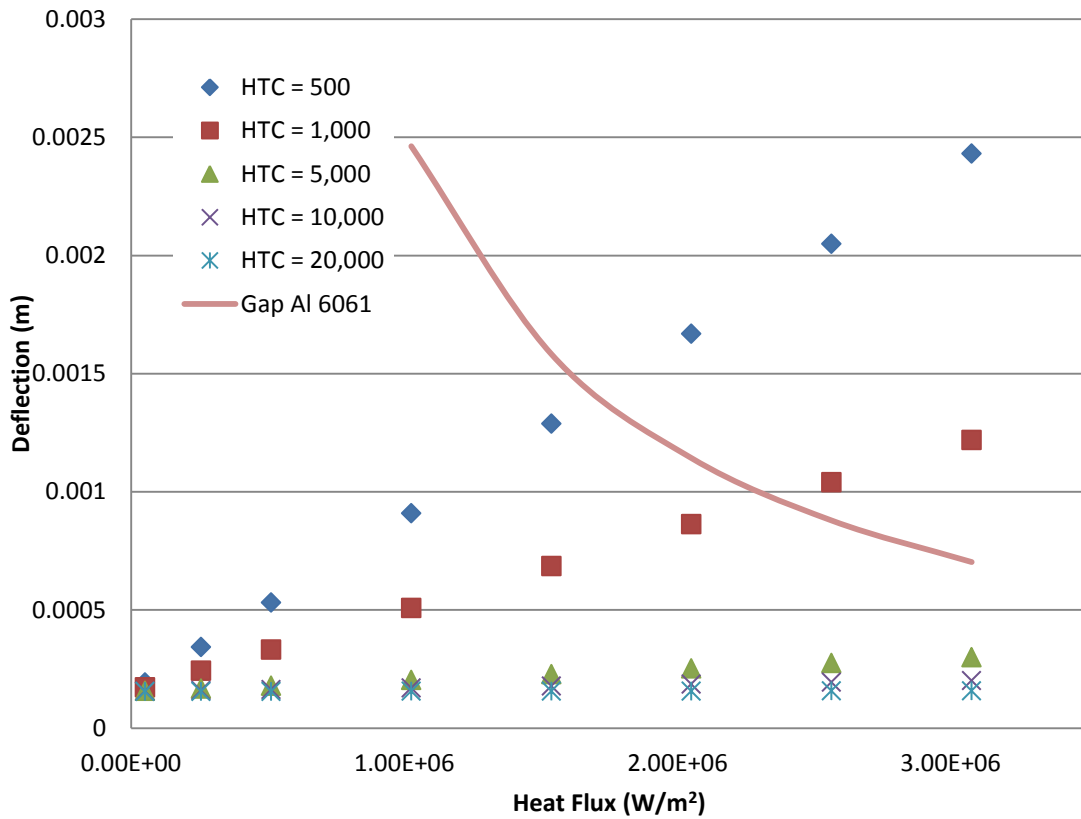
Figure 65. Fully constrained deflection at various heat transfer coefficients
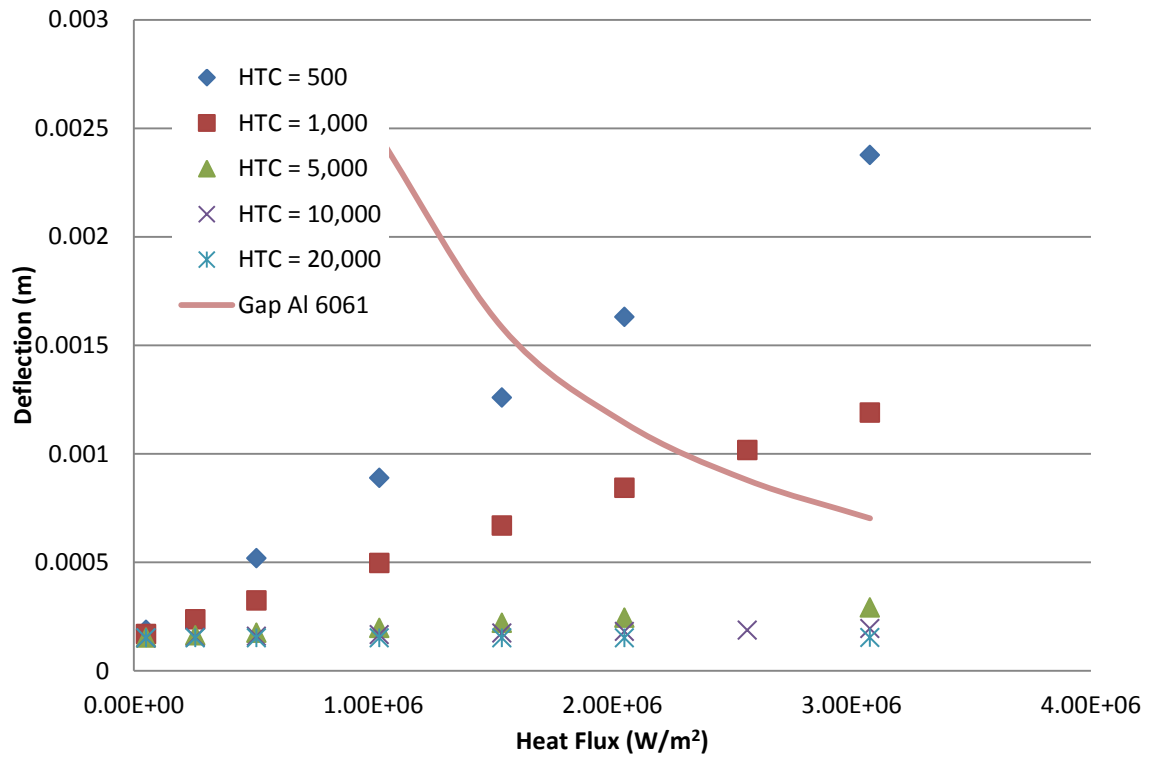
Figure 66. Partially constrained deflection at various heat transfer coefficients
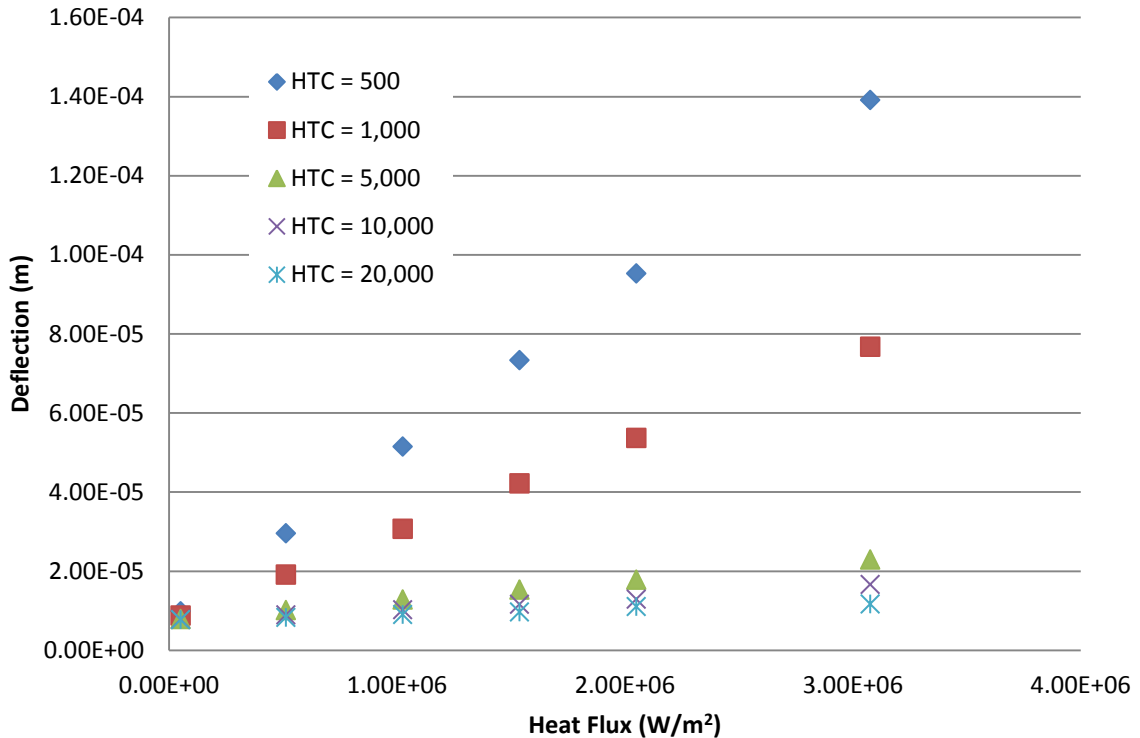
Figure 67. Free deflection at various heat transfer coefficients

The plots show that as the thermal load increases, the amount of deflection increases. This trend is consistent with the understanding that a higher thermal load induces a larger temperature difference across the aluminum plate, and hence increases the thermal expansion. The plots also show that an increase in the heat transfer coefficient will decrease the overall deflection. When the heat transfer coefficient is low, temperatures seen on the inside and outside plate surfaces will be higher than when the heat transfer coefficient is high. The higher temperatures in turn cause more thermal expansion in the plate thus more deflection.

A comparison of the deflection and allowable air gap indicate situations exist where target deflection could exceed the design specifications. The partially constrained and the fully constrained could fail at high heat fluxes and low cooling. The free

condition does not exceed the design specifications at any combination of heating and cooling, furthering the free condition will produce overall lower deflection values.

A comparison of the out of plane deflection at various heat transfer coefficients and a 60,000W thermal load for the three holding conditions can be seen in Figure 68.
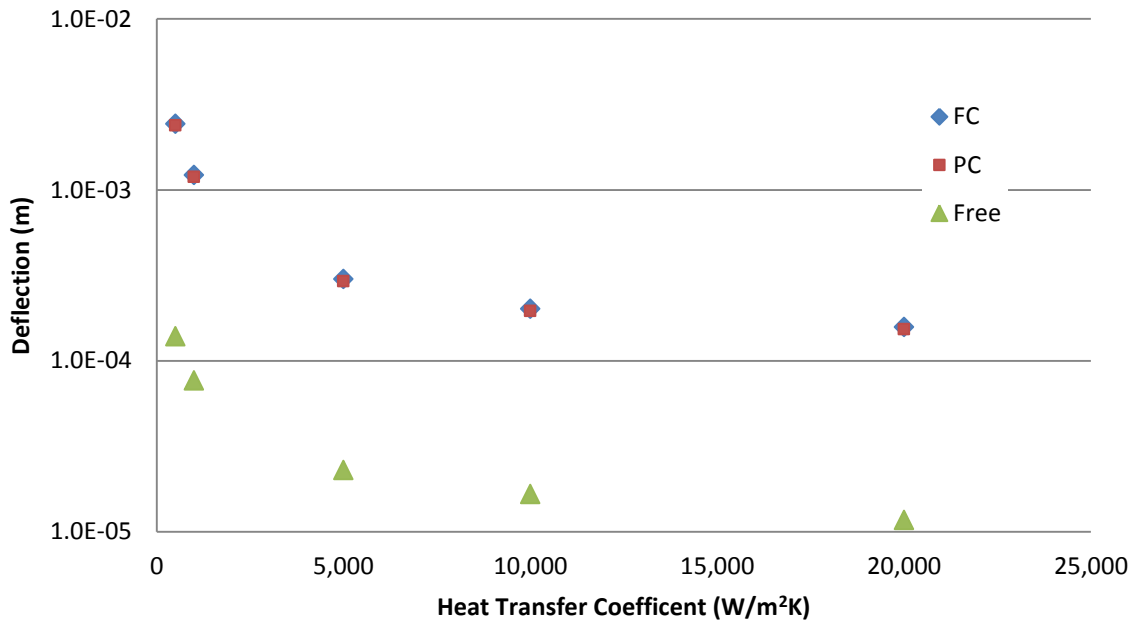
Figure 68. Comparison of deflection at q=60,000W

The results above indicate several trends. First, the applied holding condition will greatly affect the deflection results. The free deflection is less than the other conditions because the edges are allowed to freely expand. Constraining the edges in the other conditions causes the center area of the target to expand in the out of plane direction. Applying tie constraints to the edges of the plate allows the energy to be transferred into in plane deflection thus lowering the out of plane deflection. Images of the X-axis deflection in Figure 69, Figure 70, and Figure 71 show the free expands greatest in the XY plane, similar images for the Y-axis deflection show the same trends.
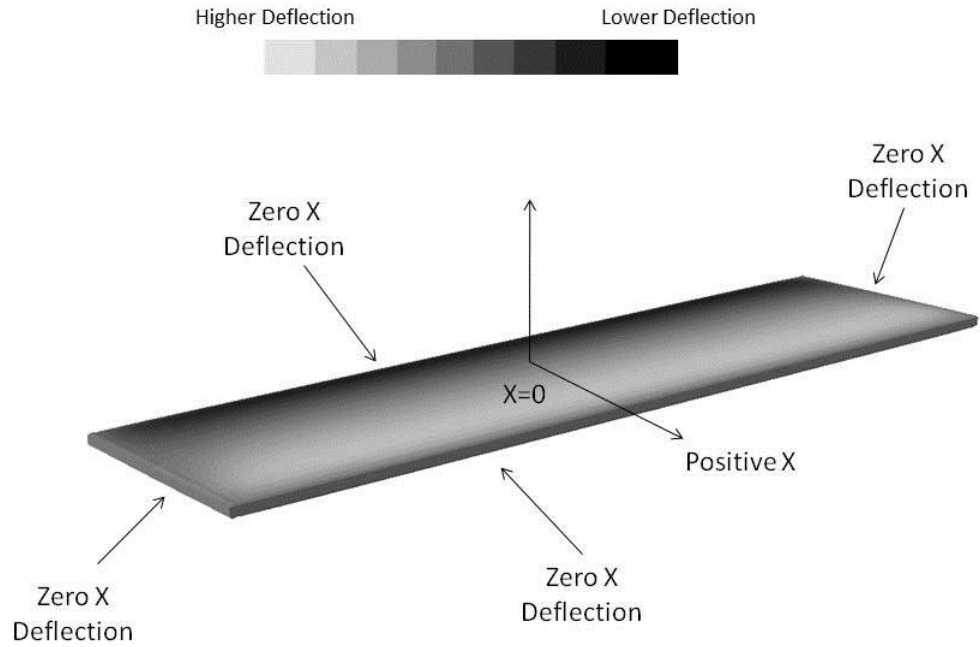
Figure 69. Fully constrained X-Axis deflection
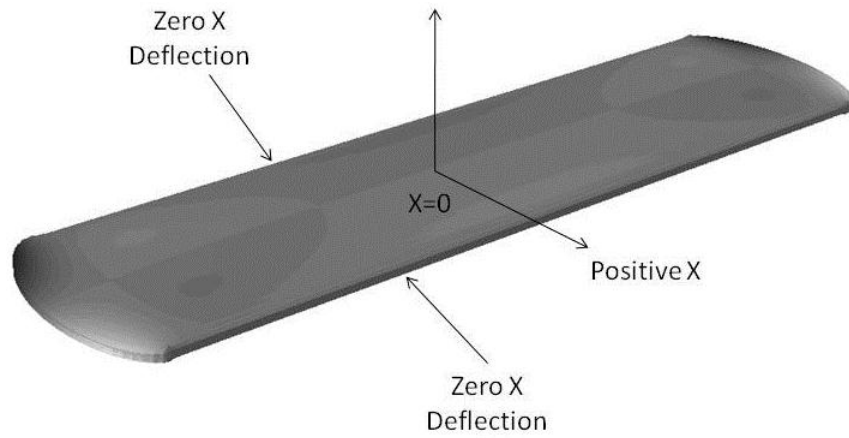
Figure 70. Partially constrained X-Axis deflection
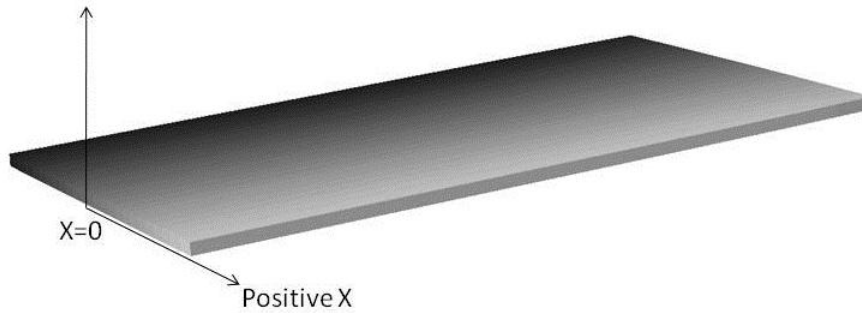
Figure 71. Free X-Axis deflection

When the heat transfer coefficient is changed in the lower regime there is a substantial change in the deflection values at both the 60,000 W and 30,000 W thermal loads. When high heat transfer coefficients are reached they appear to have little effect on the deflection. When they are lower a change in the heat transfer coefficient will greatly affect the thermal expansion and deflection. At a point between 5,000 W/m^{2}K and 10,000 W/m^{2}K in both thermal loads a change in the heat transfer coefficient will not greatly affect thermal expansion and deflection and at 10,000 W/m^{2}K and 20,000 W/m^{2}K there is little change.

Von Mises Stress Results

The von Mises stresses in the non-uniform heating condition were also examined. The von Mises stress for each holding condition exhibited a similar linear behavior as was seen in the deflections for each holding condition. Further the stresses all increased as the thermal load in the target was increased. The von Mises stress for the various holding conditions, with the yield strength of Al 6061, can be seen in Figure 72, Figure 73, and Figure 74. Plastic deflection when surpassing the elastic strength is considered

target failure because plastic deflection could produce undesired and unpredictable results during irradiation.
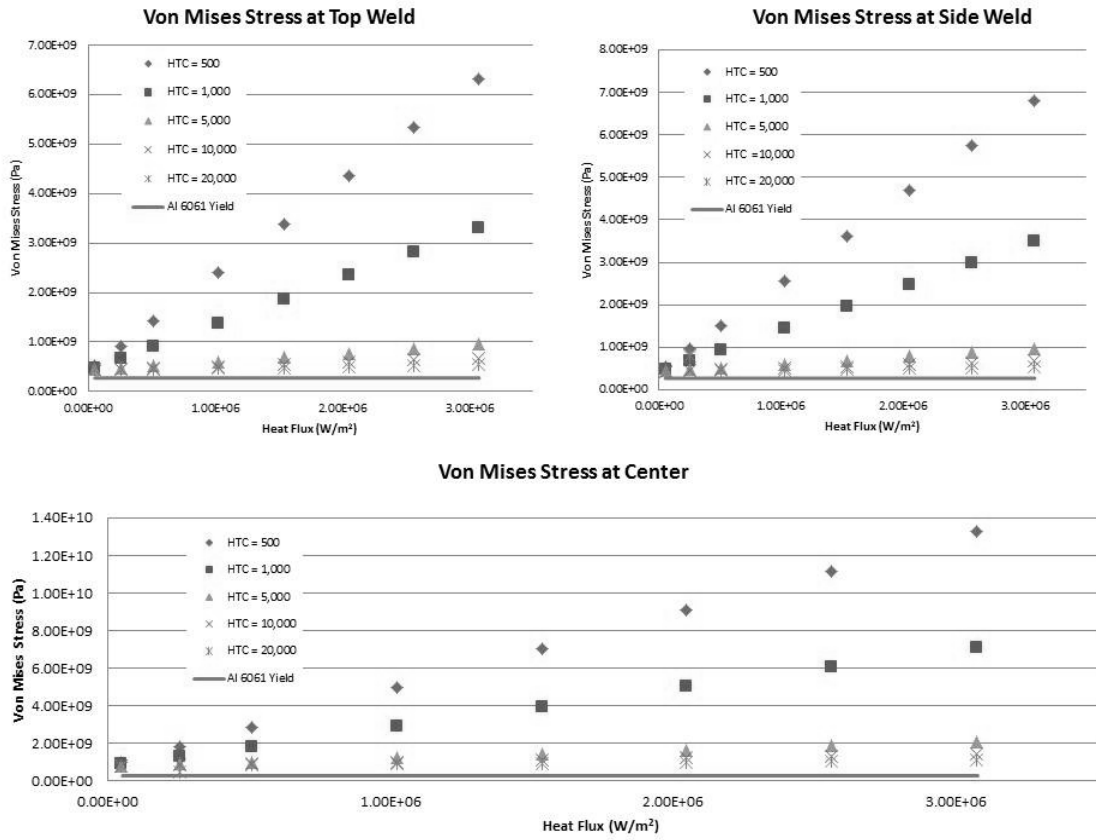
Figure 72. Fully constrained non-uniform heating von Mises stresses
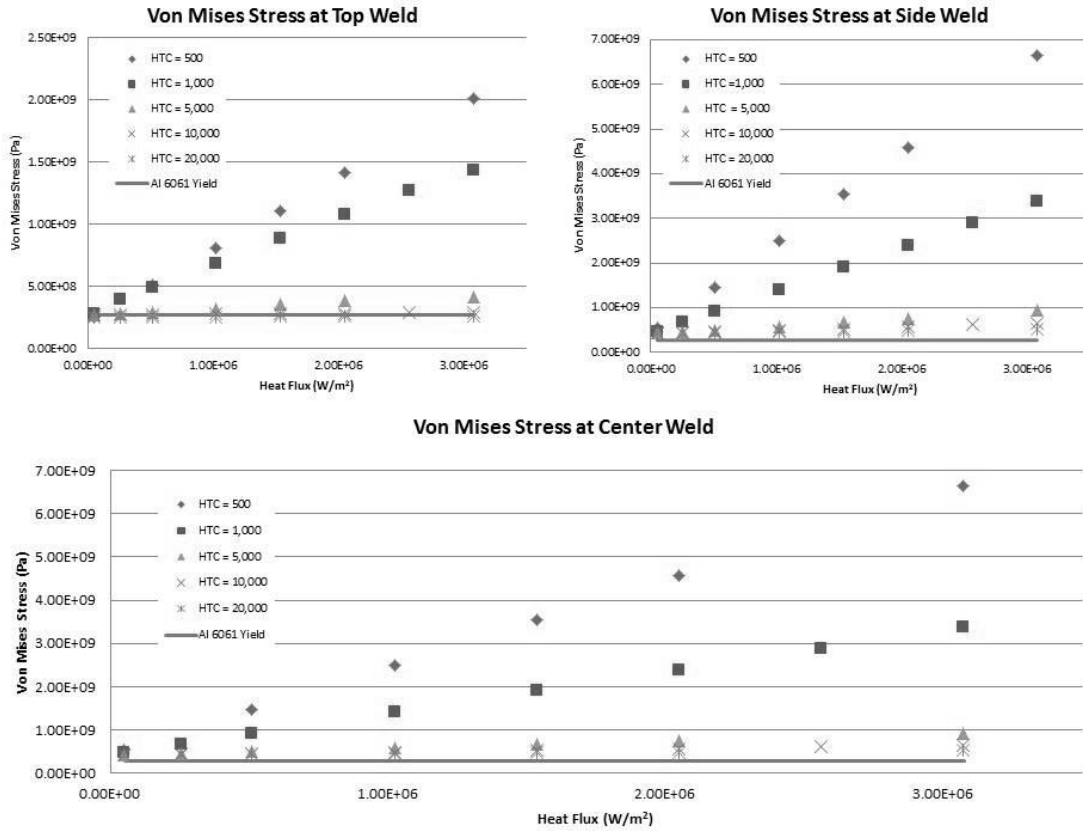
Figure 73. Partially constrained non-uniform heating von Mises stresses
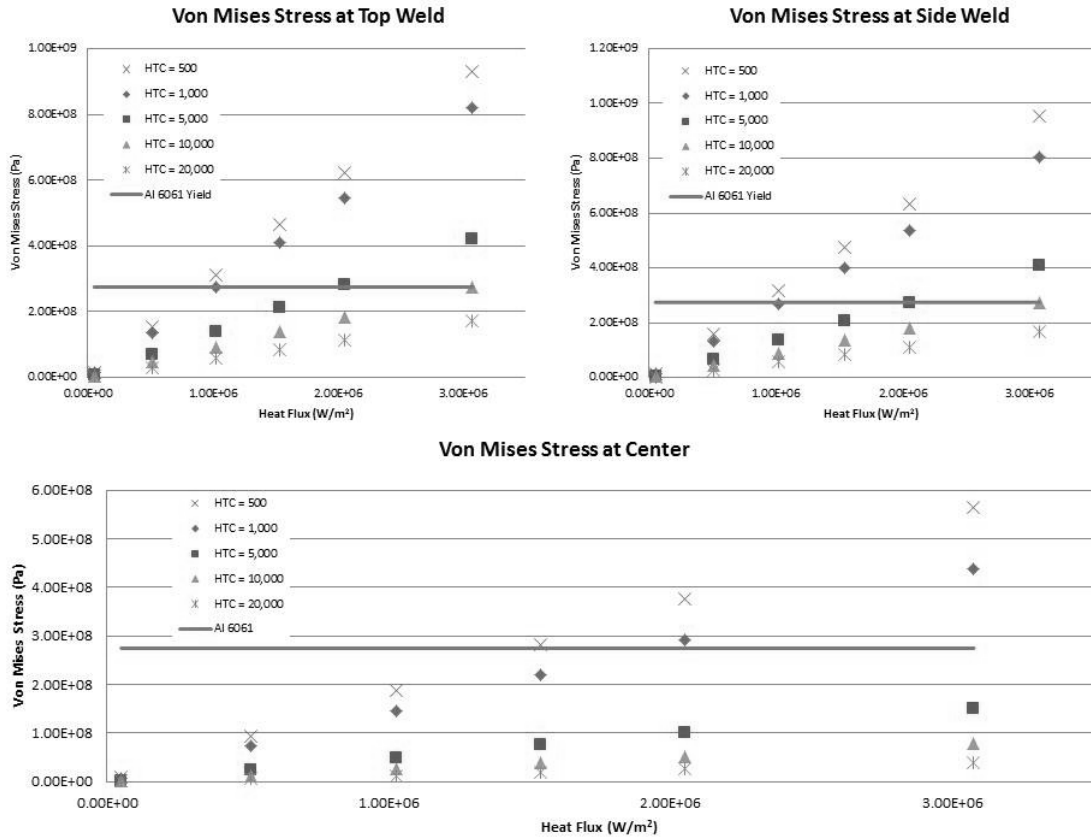
Figure 74. Free non-uniform heating von Mises stresses

The plots indicate the greatest von Mises stresses will occur in the fully constrained followed by the partially constrained and free. This trend is to be expected and makes sense given what was learned in the deflection investigation. The plots also indicate that under certain conditions the target could experience plastic deflection and failure due to stress when the stress values surpass the Al 6061 yield strength.

Von Mises stress in each of the holding conditions was also compared to see their effect on the von Mises stress profile. The highest thermal load was used for the comparison since it would have the greatest stress and show the trending best.
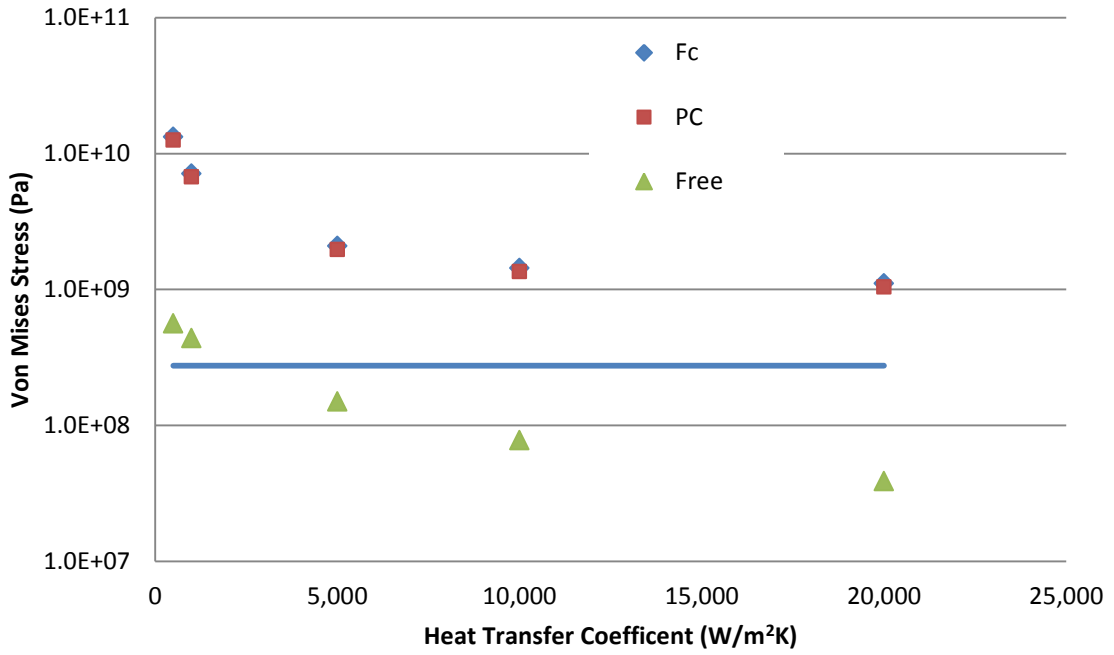
Figure 75. Non-uniform heating center von Mises comparison
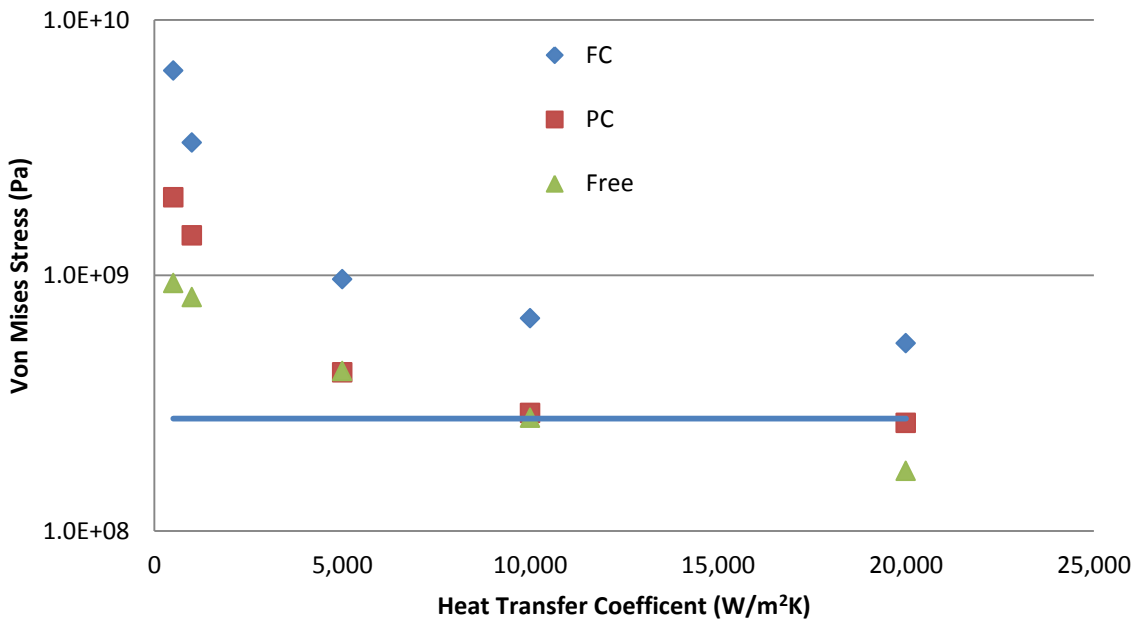
Figure 76. Non-uniform heating top weld von Mises comparison
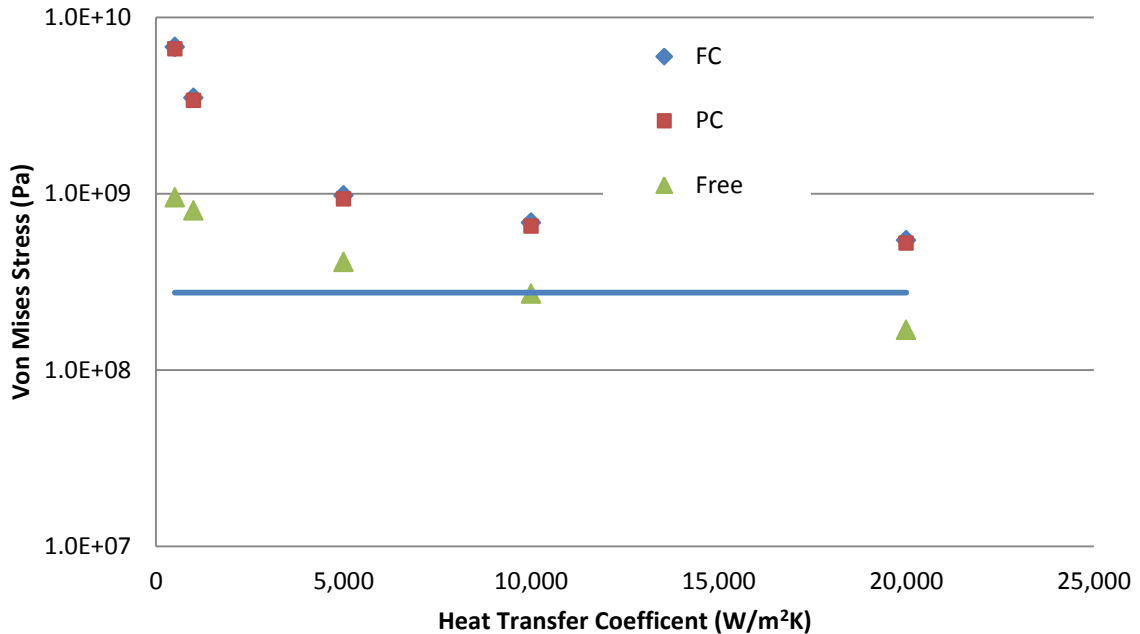
Figure 77. Non-uniform heating side weld von Mises comparison

The plots indicate the applied holding condition will have a significant effect on the stress profile. The fully constrained holding condition has the greatest von Mises stress in all conditions followed by the partially constrained and free condition. This is to be expected since the fully constrained has the greatest number of applied constraints. Von Mises stresses in the center were greatly lower for the free holding condition compared to the two other holding conditions. The free expansion of the tie constraint edges produces the lower stress. Stresses on the top weld were greatest in the fully constrained condition due to the zero translation/rotation boundary condition applied to that edge. The partially constrained and the free conditions are much closer to each other because the boundary conditions applied to the edge in both are similar. The partially constrained condition is still higher because of the zero translation/rotation boundary condition applied to the long edges. Stresses in the side weld were similar in the fully and partially constrained conditions because of the similar boundary conditions applied to the

96

edges. The free condition is once again lower because the tie constraint applied to this edge. Contour plots of the fully, partially, and free constrained conditions can be seen in Figure 78, Figure 79 and Figure 80. Dark areas indicate areas of low stress and light areas indicate high stress areas.
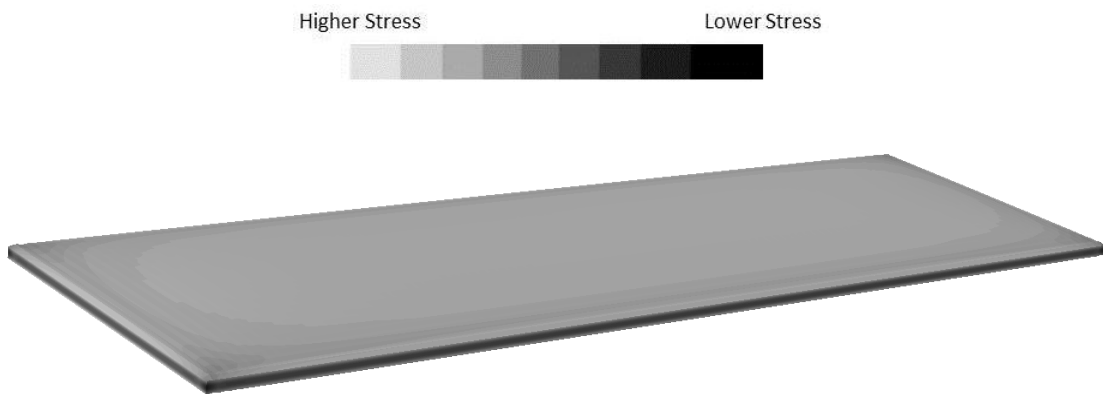
Figure 78. Fully constrained von Mises contour plot for non-uniform heating

Figure 79. Partially constrained von Mises contour plot for non-uniform heating
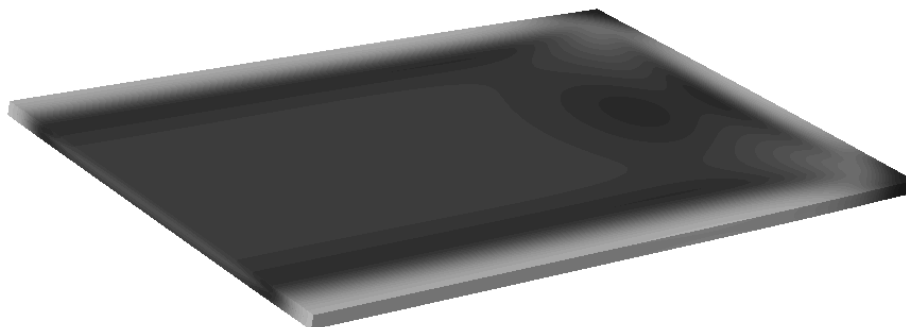
Figure 80. Free von Mises contour plot for non-uniform heating

The images confirm what the plots indicated. The fully constrained condition will have the highest von Mises stresses in the center and lower stress on the edges. The partially constrained has the highest stress at the four corners where the boundary conditions switch from zero translation/rotation to the tie constraint. The other high areas of stress are located in the center of the plates. The two short edges show the lowest stress values because of the applied tie constraint. The free edge condition indicates the highest stress areas will be on the edges of the plates on the tie constraint and the lower stress areas will be located in the center.

Knowing the thermal-mechanical behavior is valuable to determine what conditions should be used in the real target. Adjusting the holding conditions, thermal loads, and heat transfer coefficients will greatly affect the deflections and stresses. Knowing a range of behavior will allow the conditions in and around the target to be designed to certain specifications.

CHAPTER 9: UNIFORM AND NON-UNIFORM HEATING COMPARISON

A comparison of the uniform and non-uniform heating conditions evaluated the effects of both heating conditions on thermal-mechanical behavior subject to the same conditions. Surface heat fluxes and heat transfer coefficients were used to produce similar thermal profiles.

Setup

The goal of this study was to obtain a direct comparison between the two heating types. The same thermal loads and heat transfer coefficients were applied to both and can be seen in Table 19 along with the dimensions used to determine heat flux in Figure 81.
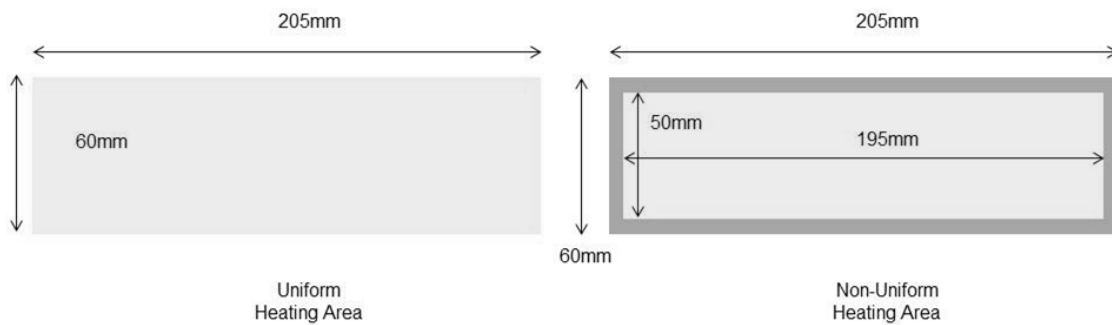
Figure 81. Uniform and Non-Uniform dimensions for determining heat flux

Table 19. Total power and heat transfer coefficients used in comparison

Total Power (W)	Uniform Heat Flux per Side (W/m^2)	Non-uniform Heat Flux per Side (W/m^2)	Heat Transfer Coefficient (W/m^{2}K)
60,000	2.439e6	3.076e6	20,000/ 5,000/ 500
30,000	1.219e6	1.538e6	20,000/ 5,000/ 500
1,000	4.065e4	5.128e4	20,000/ 5,000/ 500

The same procedure used in the previous sections to apply thermal loads, heat transfer coefficients, and non-uniform heating dimensions were used in these models.

Results

The uniform and non-uniform defections and von Mises stress were directly compared determining the effect of heating area on thermal-mechanical behavior. A comparison of the deflection for the fully constrained, partially constrained, and free conditions can be seen in Figure 82, Figure 83, and Figure 84.
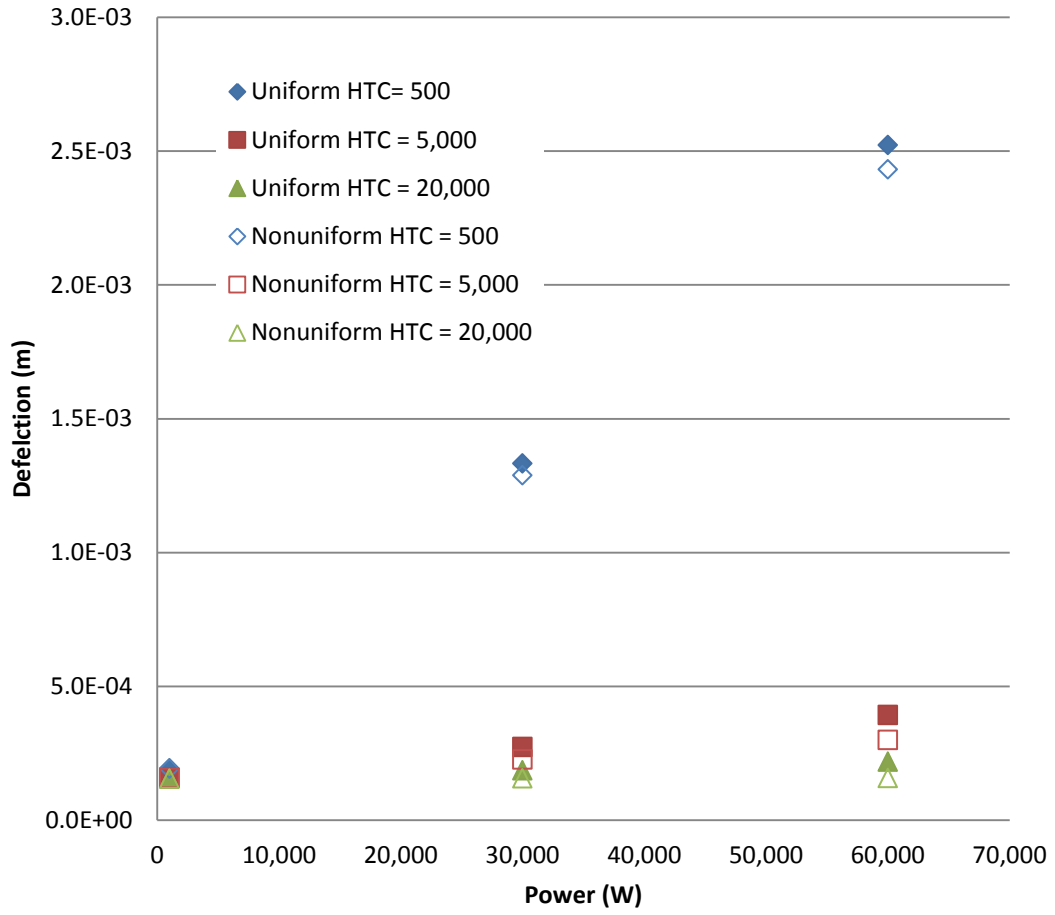
Figure 82. Fully constrained uniform and non-uniform heating deflection
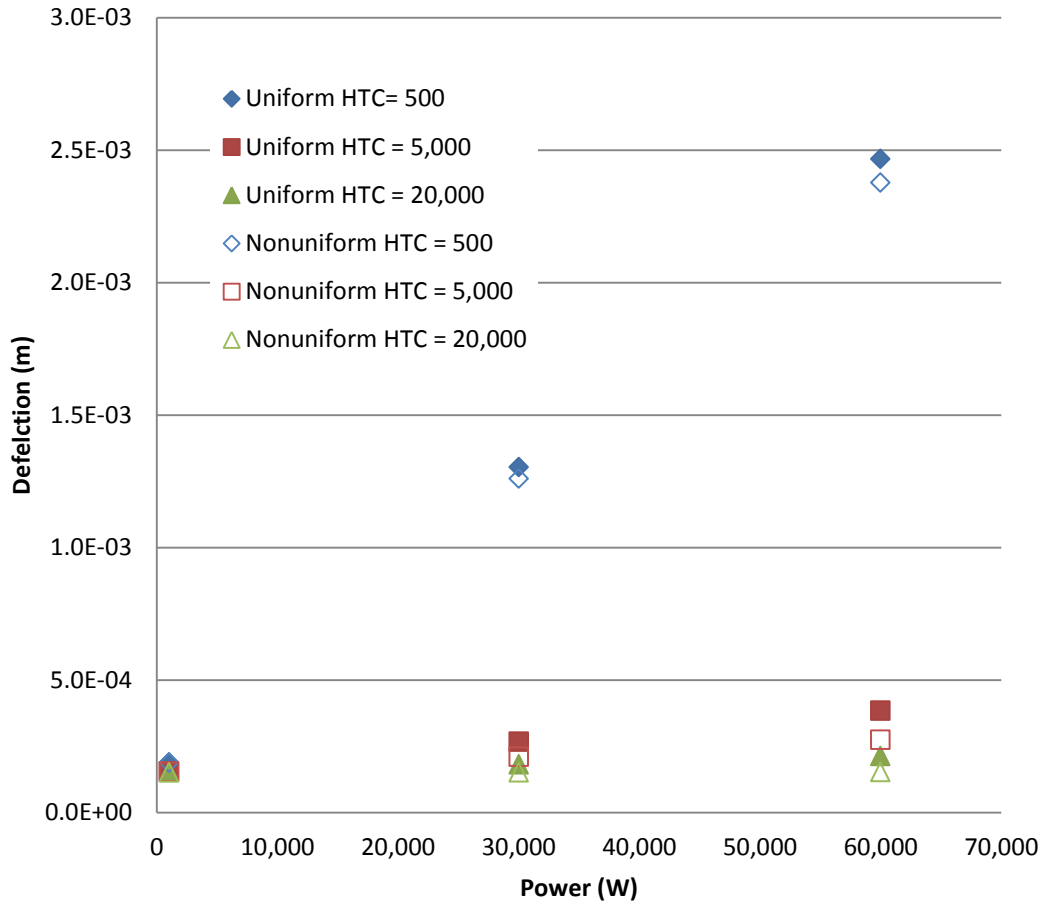
Figure 83. Partially constrained uniform and non-uniform heating deflection
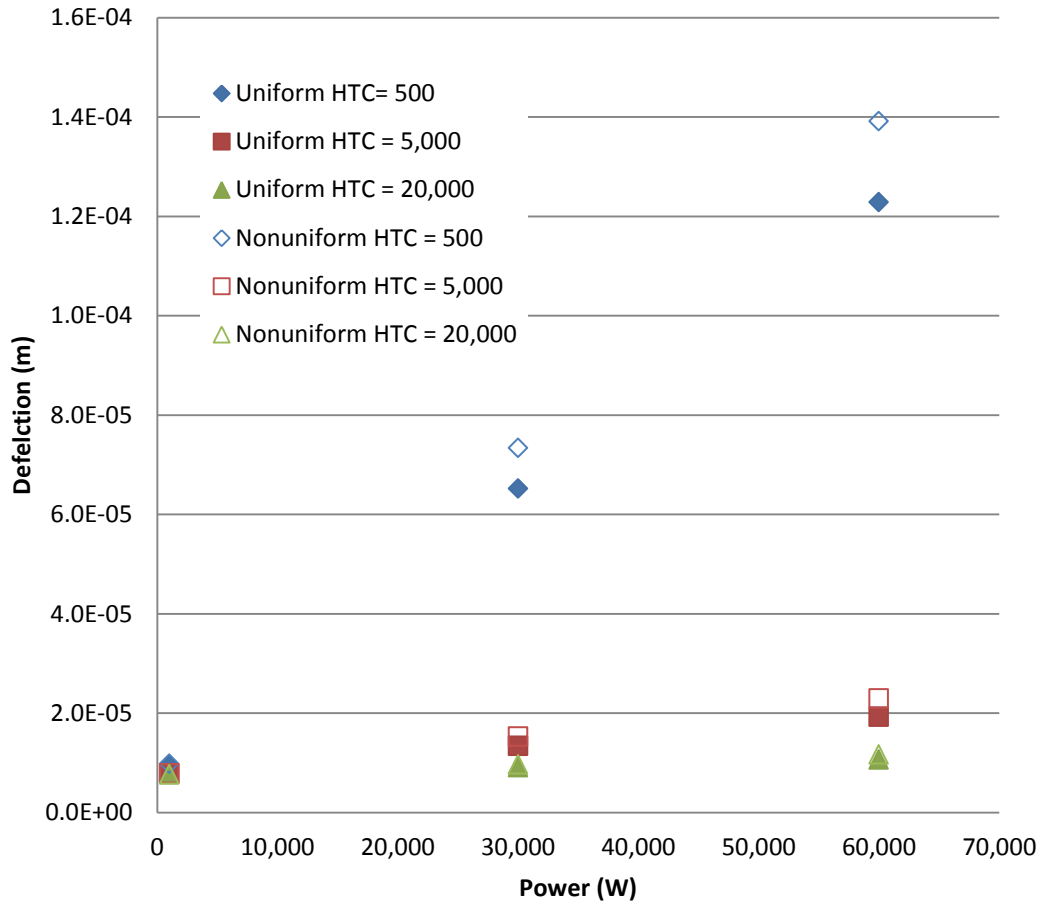
Figure 84. Free uniform and non-uniform heating deflection

All relationships are linear as the power is increased. Second, the fully constrained and partially constrained uniform deflection will be slightly lower than the non-uniform heating condition. The trend doesn't hold in the free condition and the non-uniform heating will be greater than uniform heating. Further the magnitude of the difference will be great then the fully constrained and the partially constrained. The von Mises stresses in the plates can be seen in Figure 85.
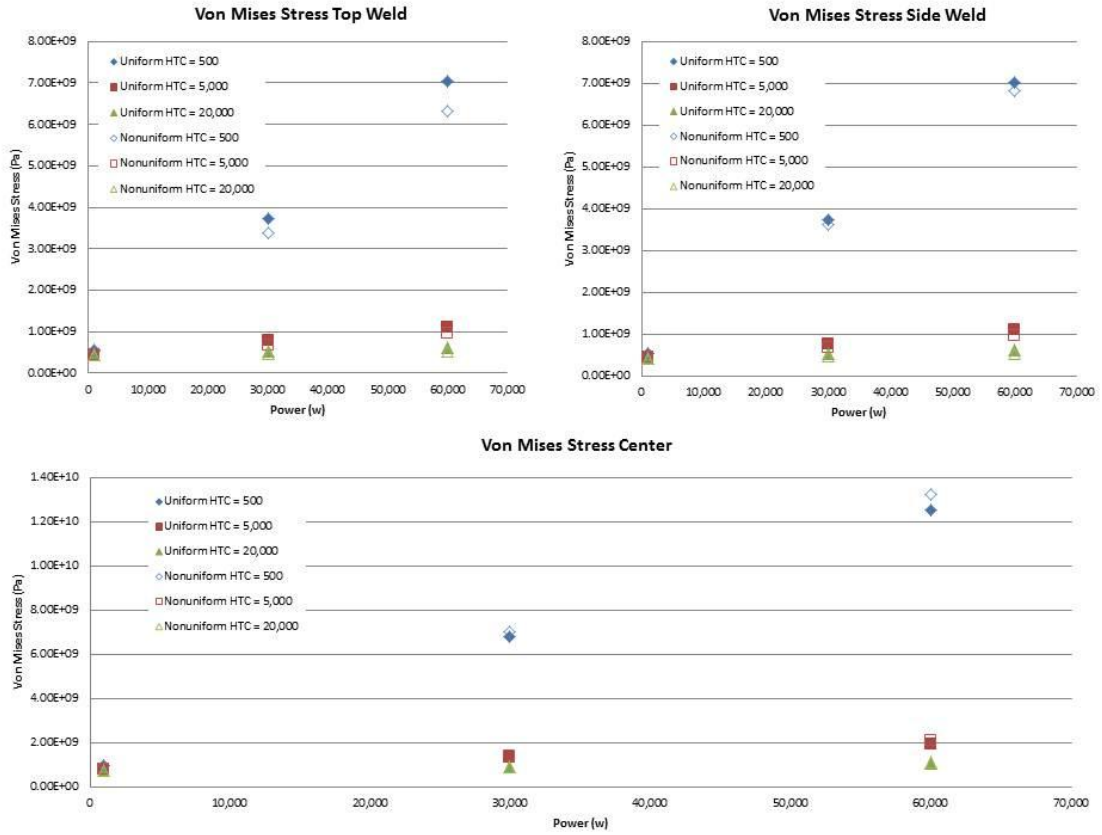
Figure 85. Fully Constrained uniform and non-uniform heating von Mises stress
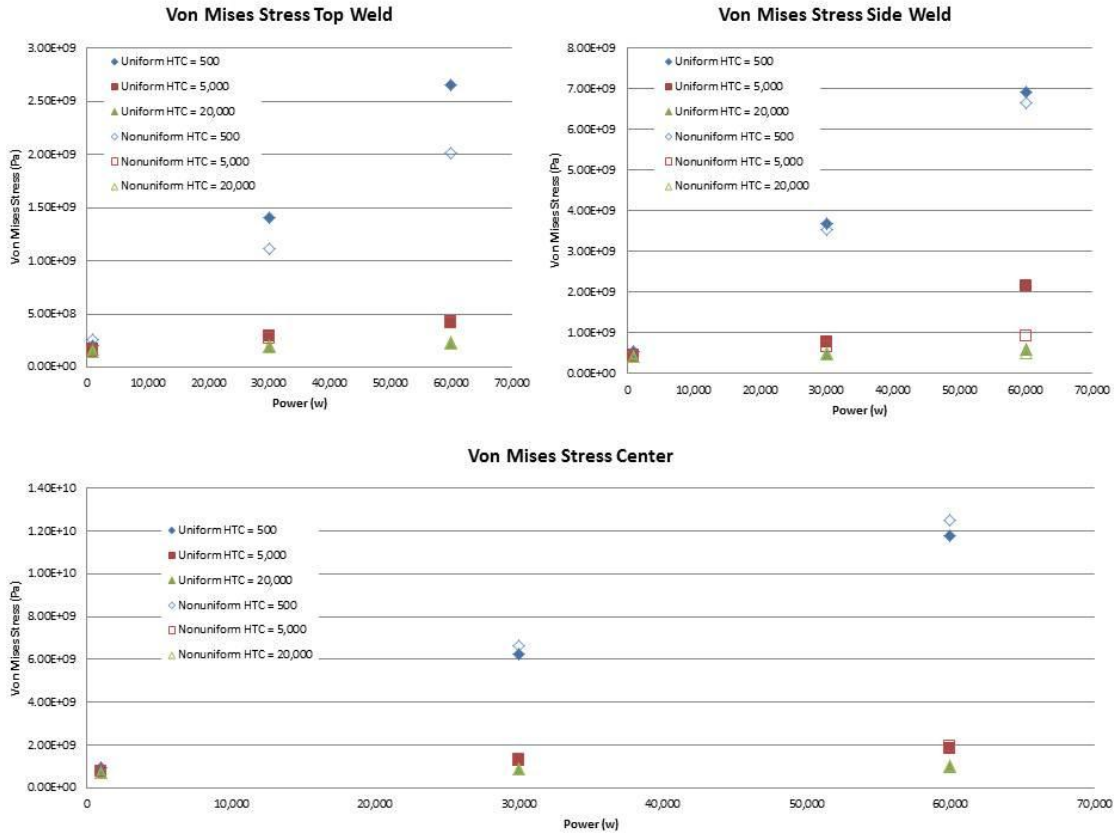
Figure 86. Partially Constrained uniform and non-uniform heating von Mises stress
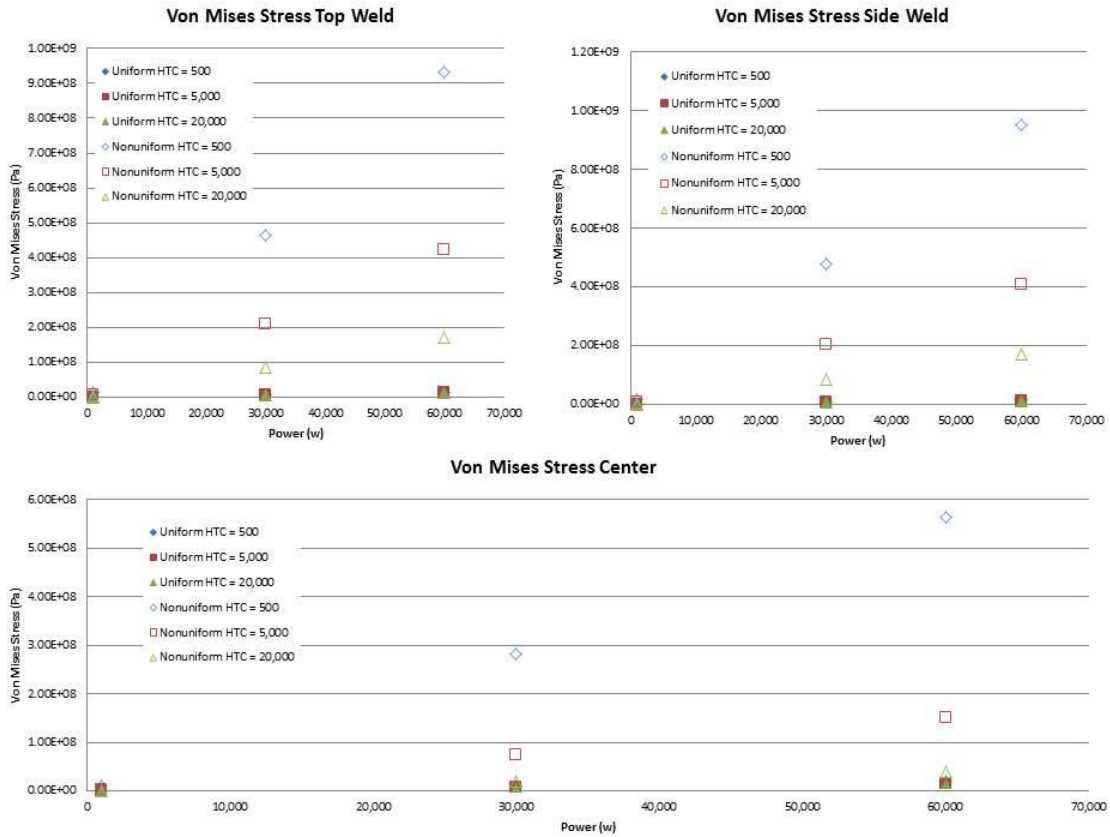
Figure 87. Free uniform and non-uniform heating von Mises stress

In the fully constrained stress plots the non-uniform stress on the top and side weld is lower than the uniform heating condition. The central stress exhibits the opposite behavior with the uniform stress being lower than the non-uniform. The partially constrained stress is similar to the fully constrained with the top and side weld stresses being lower in the non-uniform and the central stress being higher in the non-uniform. The stresses in the free condition behave differently than the stresses in the other holding conditions. In the free condition stresses in the uniform models are significantly lower than the non-uniform stresses at all locations. The results in the free condition are interesting since they seem to indicate a larger foil footprint will cause a significant drop in the amount of stress throughout the entire target, further there is only slight increase in deflection. This relationship is useful when determining the size of foil since it appears

106

the surface area will play a significant role in the magnitude of the von Mises stresses that form.

The results in this chapter indicate uniform and non-uniform heating will have different effects on both the deflection and von Mises stress. The greatest difference between the uniform and non-uniform heating will be in the free edge holding condition with non-uniform heating displaying the greatest deflection and von Mises stress.

CHAPTER 10: FOIL TARGET ANALYSIS WITH CURVATURE

The previous boundary condition studies indicate holding conditions will greatly affect the locations and magnitudes of deflections and stress during irradiation. The results from these studies show the free edge holding condition will produce the lowest amount of stress and deflection. The purpose of the foil target analysis is to build upon the conclusions from the simpler cladding only two aluminum plate models, and produce results of more prototypical target behavior. One advantage a foil target model has over the cladding only model is analyzing the interaction between the foil and the plates. Abaqus was again used to perform the study and the same benchmarking results were used to define the proper meshing requirements.

The goal of this study was to analyze the thermal-mechanical separation and stress in a target with a uranium foil and examine the effects of curvature. Examples of the various curvature models used during the analysis can be seen in Figure 88.
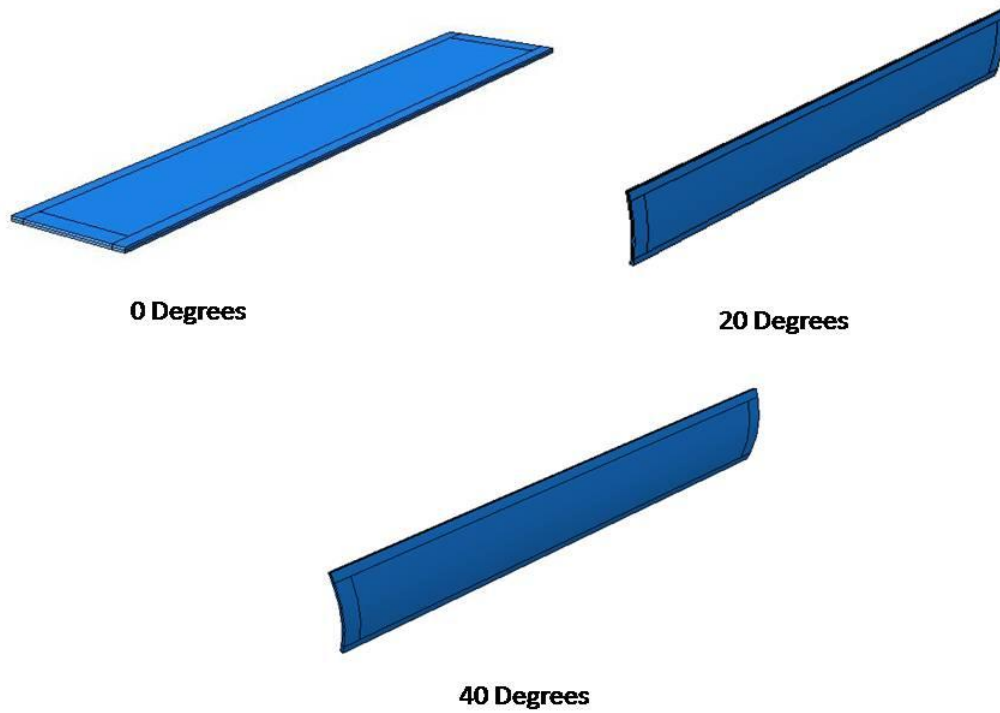
Figure 88. Examples of models used in curvature study

Foil Target Setup

The purpose of this study was to analyze more prototypical target irradiation conditions. Several reactor plate target designs were examined as possible models for the foil target analysis. The HFR design was chosen as the dimensional basis for the study because of the high volume of molybdenum produced at the reactor. The dimensions of this target differ from the dimensions used in previous modeling and can be seen in Figure 89 where yellow represents the uranium and grey the aluminum cladding.
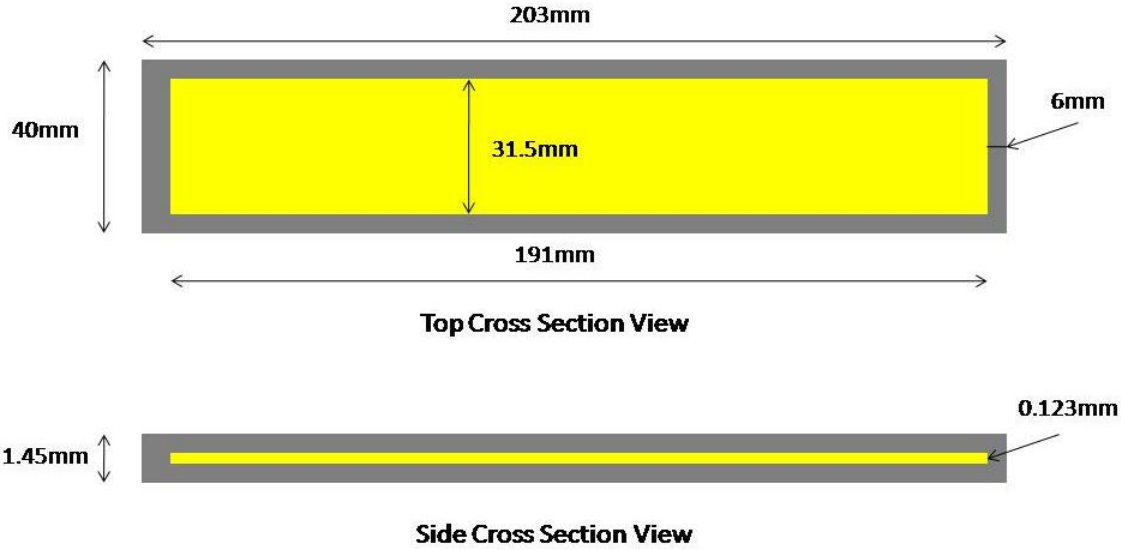
Figure 89. Petten target dimensions

The material properties for Al 6061 T-6, used in the previous studies and uranium, can be seen in Table 20.

Table 20. Material properties of aluminum 6061 T-6 and uranium

Material	Young's Modulus (Pa)	Poisson's Ratio	Coefficient of Thermal Expansion (1/K)	Thermal Conductivity (W/mK)
Aluminum 6061 T-6	6.89e10	0.33	2.358e-5	167
Uranium	2.08e10	0.23	1.39e-5	27.5

Several different levels of curvature were examined during this study and can be seen in Table 21. The arc length was determined using the degree of curvature and the process used can be seen in Figure 90.

110

Table 21. Angles of curvature used in various models

Angle of curvatures used in models	Radius
θ = 0° (Flat)	r = ∞
θ = 20°	r ~ 0.115
θ = 40°	r ~ 0.057
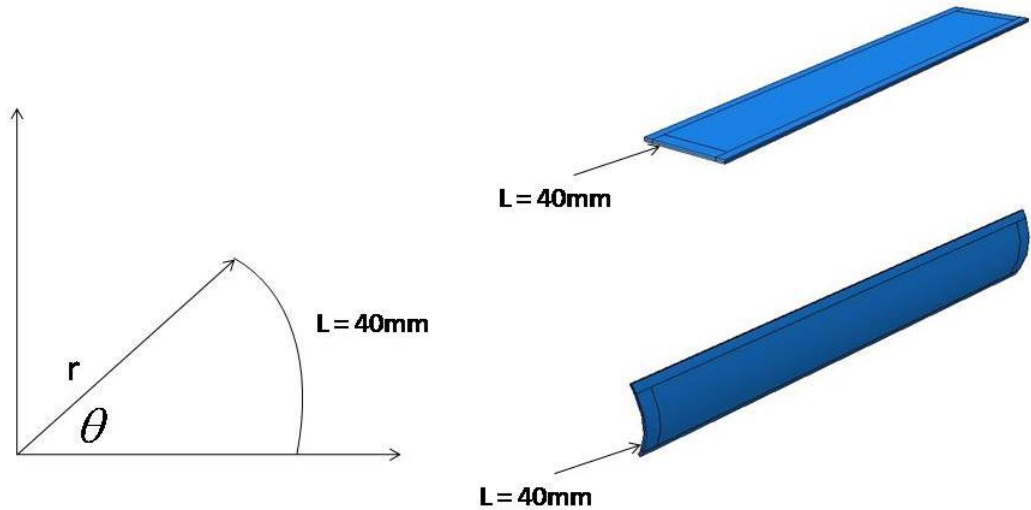
Figure 90. Defined curvature in the curved target

Results from the previous studies indicate a free edge holding condition produces the lease amount of stress and deflection. Foil target modeling will only focus on the free edge condition as this is a more prototypic holding condition. Tie constraints, which bind and do not allow corresponding nodes to separate, were used to simulate the welded edges between the two plate edges. For model convergence reasons one end of the model was not allowed to translate or rotate, using a zero translation/rotation boundary condition. Symmetry was assumed in these models and reported values taken from the edge opposite of the fully constrained edge. The boundary conditions used during modeling can be seen in Figure 91.
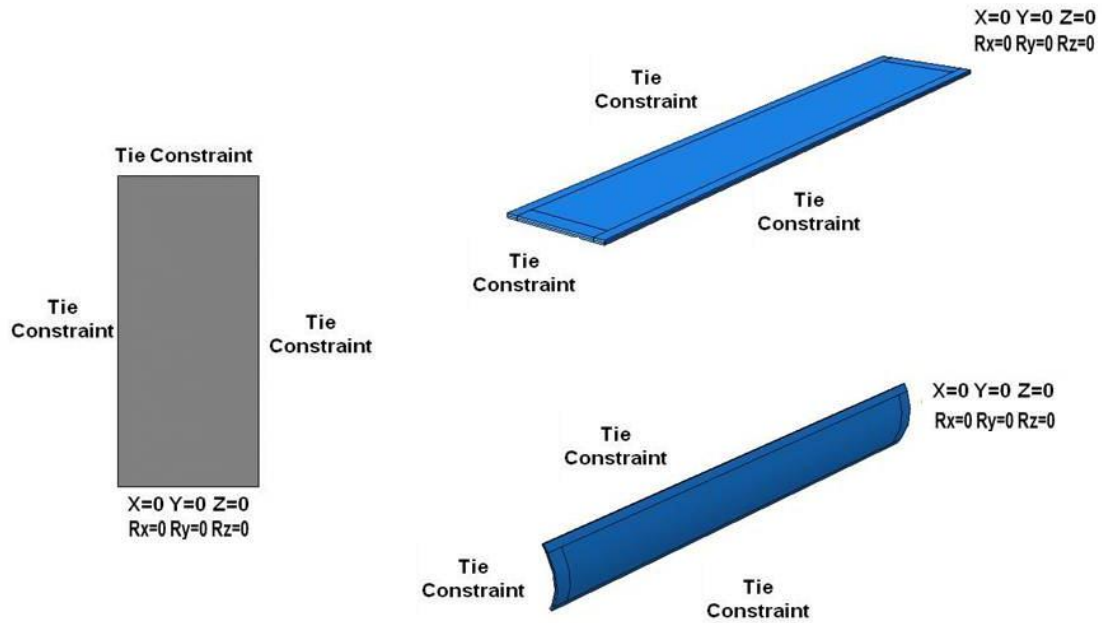
Figure 91. Applied boundary conditions for the non-uniform numeric simulations

Various thermal loads and cooling conditions were applied simulating heating and cooling conditions seen during irradiation. These values were based on two documents from the HFR Reactor and the IRE Reactor, two of the current highest volume molybdenum-99 production reactors. A safety document from HFR gave a thermal target power of 27.3 kW and a maximum heat transfer coefficient of 38830 W/m^{2}K [22]. As part of an IAEA survey on molybdenum-99 production, IRE provided a target thermal power of 28.8 kW [55]. It is assumed the new target would be designed to produce similar thermal powers and experience similar cooling conditions thus the values in Table 22 were based on these reported values.

The thermal load was applied to the foil as a volumetric heat generation load. Cooling conditions where simulated by applying a uniform heat transfer coefficient to the outer surface of the target. Values used for the parametric study can be seen in Table 22.

Table 22. Thermal loads, heat generation values, and heat transfer coefficients

Thermal Load (W)	Heat Generation Applied to the Foil (W/m^3)	Heat Transfer Coefficients (W/m^{2}K)
22,500 =	3.040e10	
25,000 =	3.378e10	30,000; 35,000; 40,000;
27,500 =	3.716e10	45,000; 50,000
30,000 =	4.054e10	
32,500 =	4.392e10	

The values in Table 22 were chosen based on the reported values and the ranges chosen are meant to capture the possible heating and cooling conditions seen during irradiation.

On goal of the study was to examine the amount of separation forming between the uranium foil and the aluminum cladding. Separation will lead to an increase in thermal contact resistance and thus an increase in foil temperature. Various locations were chosen to monitor separation between the foil and cladding and are known as the center 1, center 2, top, and side monitoring points. The location of the monitoring points and a diagram of the separations in a target cross-section can be seen in Figure 92.
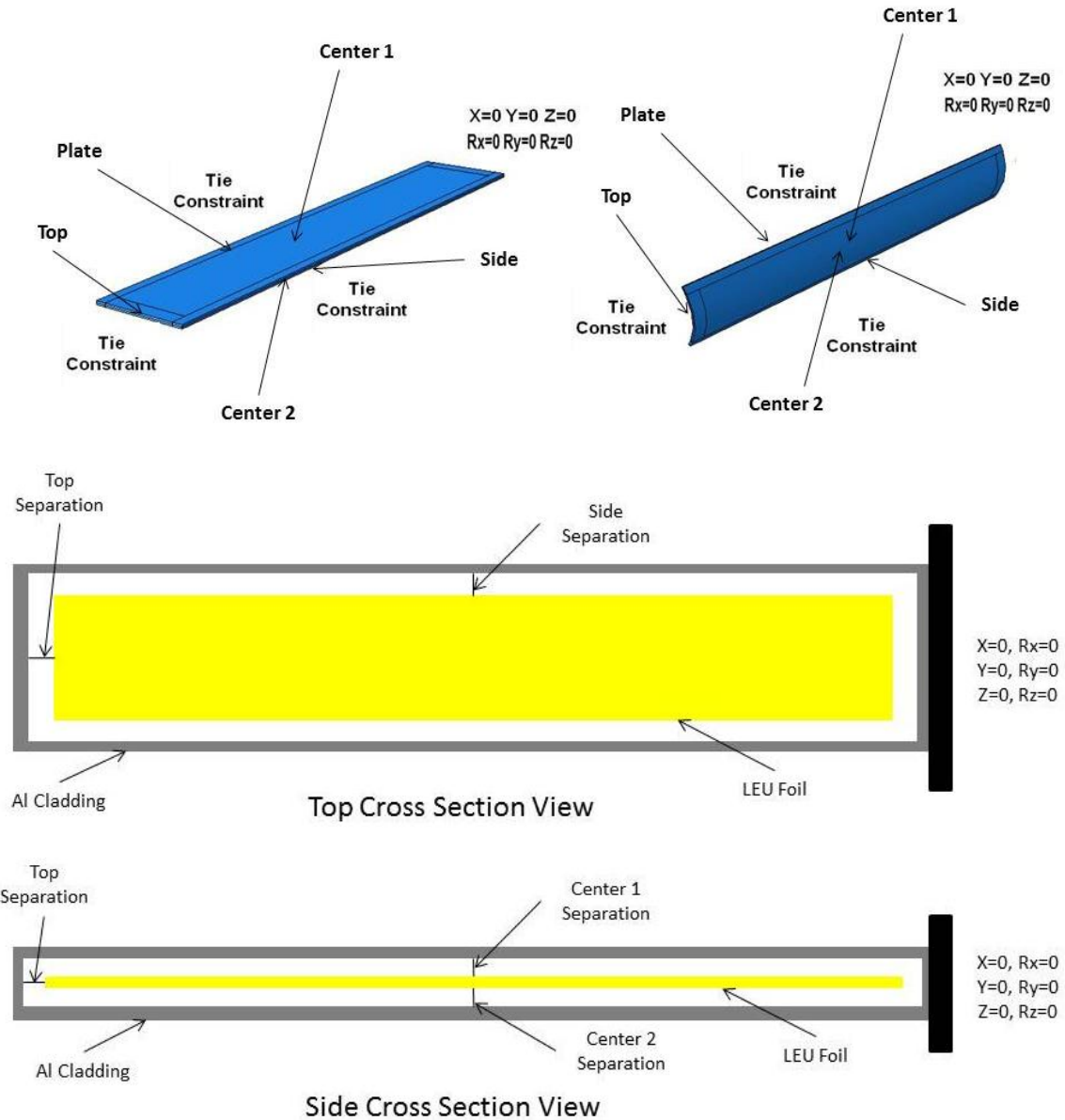
Figure 92. Monitoring points for separation in the foil targets

Target failure could also occur from thermal stress development. Von Mises stress was again used to determine the stress magnitude. Monitoring points were located along the weld and at the center of the target cladding, similar to previous modeling. The top monitoring point from the cladding only models was moved from the top edge center to a

corner location because of the high stress values observed at this location. The locations of the von Mises monitoring points can be seen in Figure 93.
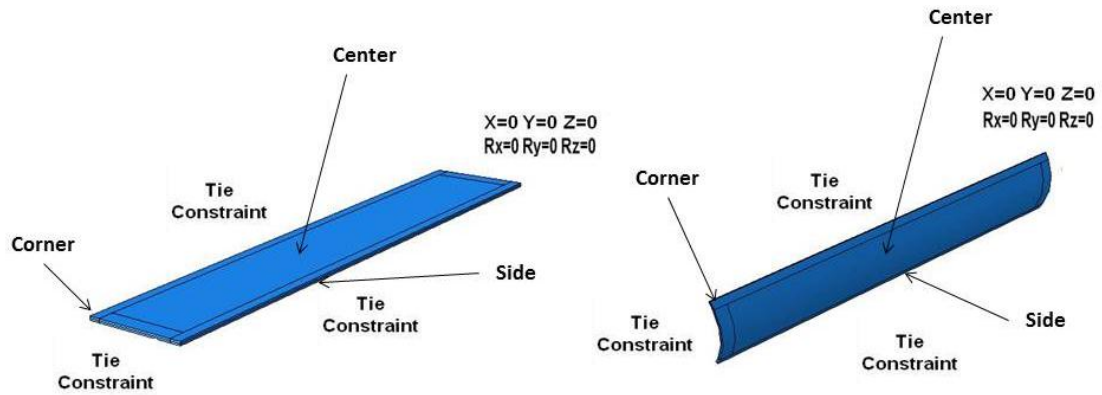
Figure 93. Monitoring points for von Mises stress

Separation Results

The main focus of the deflection study was to examine separation between the uranium foil and the aluminum cladding during irradiation. Separation will lead to an increase in thermal contact resistance and thus an increase in foil temperature, leading to a possible target failure and a release of fission products into the reactor cooling loop. In an effort to assess the allowable separation with regards to heat transfer and target failure, a simple one dimensional heat transfer resistance network was used to determine the allowable gap between the foil and the aluminum cladding. Operational limits established by MURR were used to develop the thermal resistance network. The thermal resistance network used can be seen in Figure 94 and the values used in the network can be seen in Table 23.
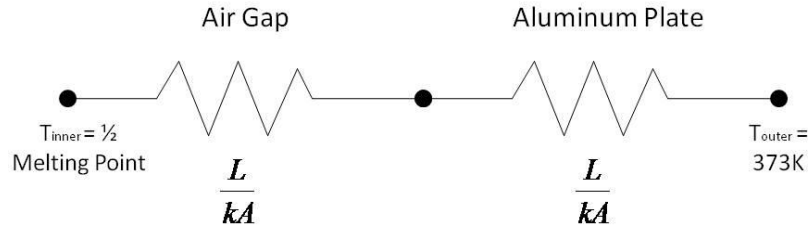
Figure 94. Thermal resistance network used to determine allowable air gap

Table 23. Values used in the thermal resistance network

Aluminum Alloy	Half Al 6061 Melting Point (K)	Thermal Conductivity Al 6061 (W/mK)	Yield Strength Al 6061 (MPa)	Thermal Conductivity Air (W/mK)
Al 6061	430	180	275	0.0314

The resistor network was expanded to include Al 3003 and Al 1100 along with Al 6061. The allowable air gaps with these various alloys can be seen in Table 24.

Table 24. Allowable air gap with various alloys

Power (W)	Surface Heat Flux Applied to Each Side (W/m^2)	Allowable Gap Al 6061 (m)	Allowable Gap Al 3003 (m)	Allowable Gap Al 1100 (m)
22,500 =	3.040e10	1.32E-03	1.32E-03	1.32E-03
25,000 =	3.378e10	1.18E-03	1.18E-03	1.18E-03
27,500 =	3.716e10	1.06E-03	1.06E-03	1.06E-03
30,000 =	4.054e10	9.55E-04	9.55E-04	9.55E-04
32,500 =	4.392e10	8.70E-04	8.70E-04	8.70E-04

The flat plate was the first design analyzed and the results were used as a starting point for investigating the effects of curvature. Separation between the cladding and the foil at the top, side and centers, which are the same on both sides in the flat plate model, can be seen in Figure 95, Figure 96, and Figure 97.

116
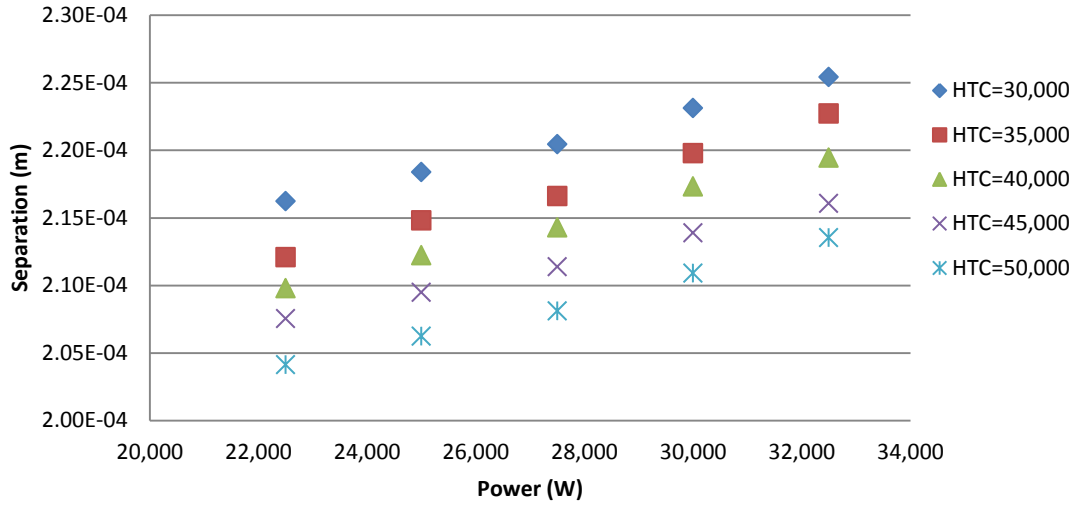
Figure 95. Top flat plate separation
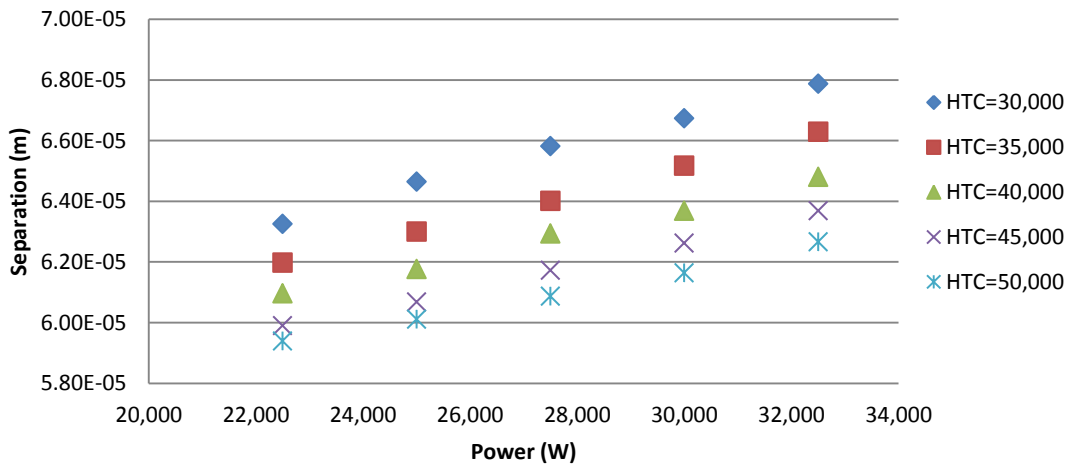
Figure 96. Side flat plate separation
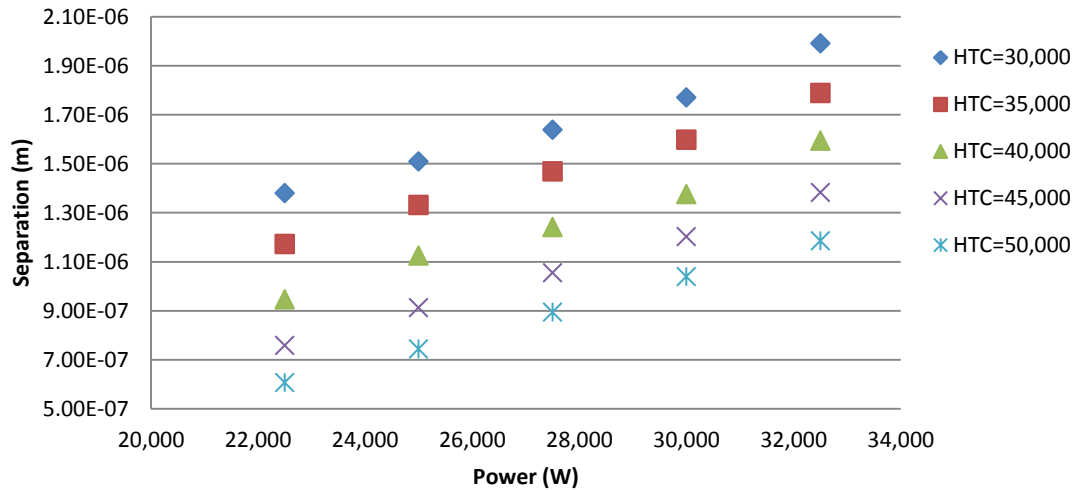
Figure 97. Center flat plate separation

The plots indicate increasing the thermal load and decreasing the heat transfer coefficient will increase separation between the foil and cladding at all monitoring point. Separation occurs because of the unbounded nature of the foil and cladding in the center of the target. Further separation also occurs because of the differences in the thermal expansion coefficients in the aluminum cladding and uranium foil. The material properties in Table 20 show the thermal expansion coefficient of Al 6061 is nearly double the thermal expansion coefficient of uranium. During heating uranium's volumetric expansion will be much less than aluminum leading to separation between the various layers in the target. Comparing the flat model separation results to the allowable separations shows all of the calculated separations will not surpass the allowable separations.

The separation between the cladding and foil at the top, side, and center monitoring points for the 20° curvature model can been seen in Figure 98, Figure 99, Figure 100, and Figure 101 .
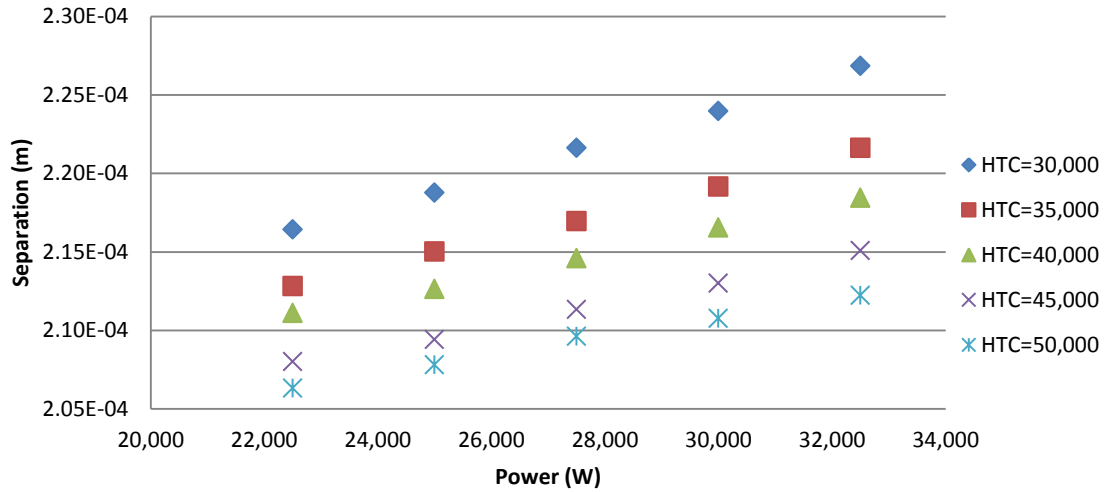
Figure 98. Top separation for the 20° curvature model
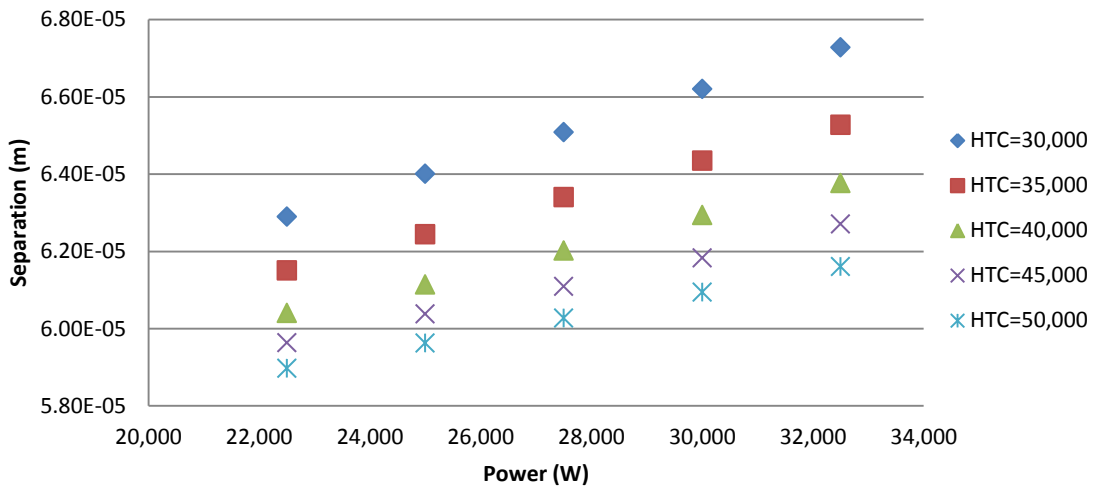
Figure 99. Side separation for the 20° curvature model
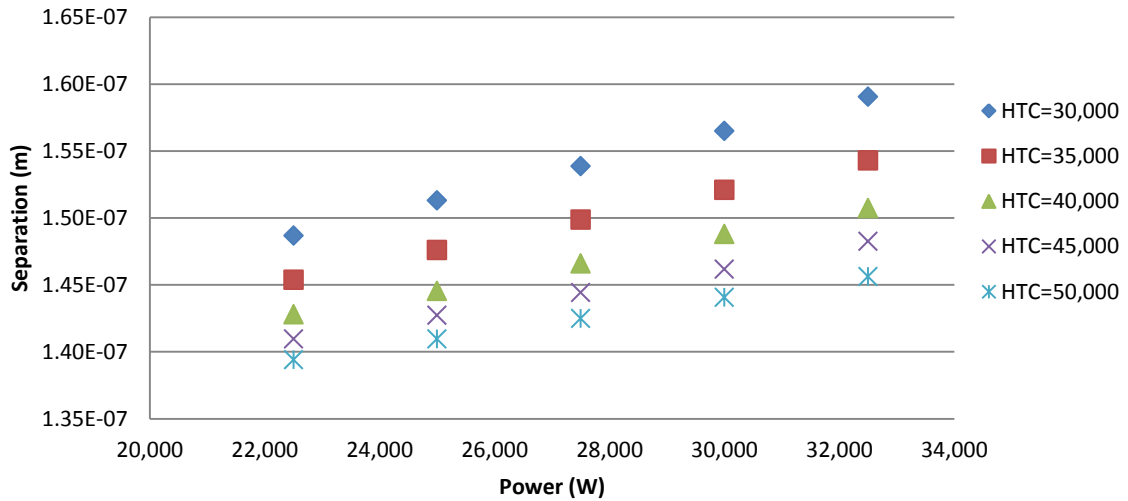
Figure 100. Center 1 separation for the 20° curvature model
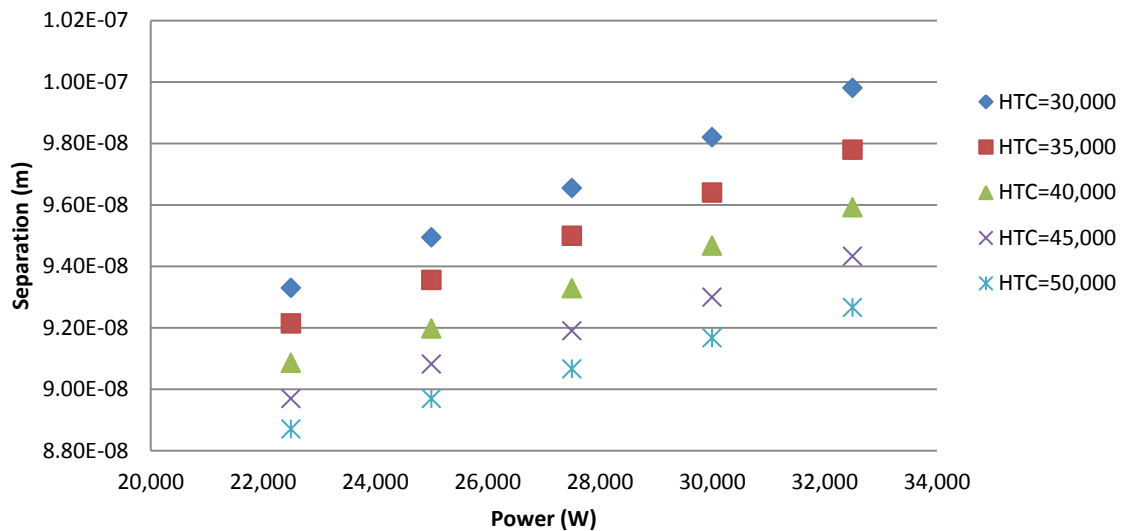
Figure 101. Center 2 separation for the 20° curvature model

The plots indicate increasing the thermal load and decreasing the heat transfer coefficient will increase separation between the foil and cladding at all monitoring points and is again consistent with previous modeling results and the flat plate foil results. The plots indicate separation between the foil and the cladding at the top and side monitoring points will exceed the allowable gap separation. This indicates temperatures in these areas could reach unacceptable levels and should be monitored. Finally, comparing the

120

20° model separation results to the allowable separations shows all of the calculated

separations will not surpass the allowable separations.

Separation between the cladding and foil at the top, side, and center monitoring

points for the 40° curvature model can been seen in Figure 102, Figure 103, Figure 104,

and Figure 105.
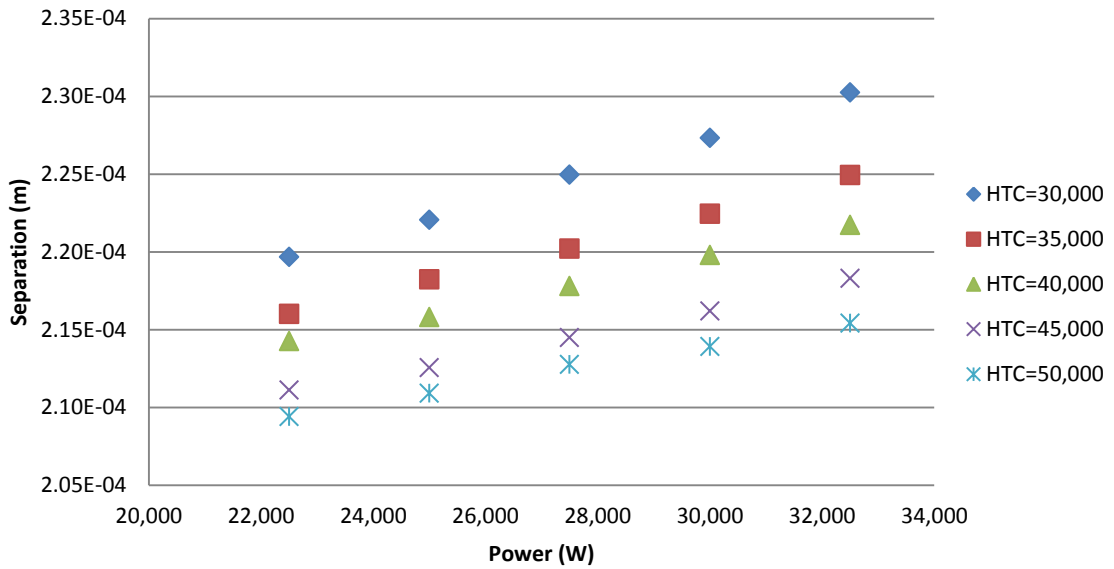
Figure 102. Top separation for the 40° curvature model
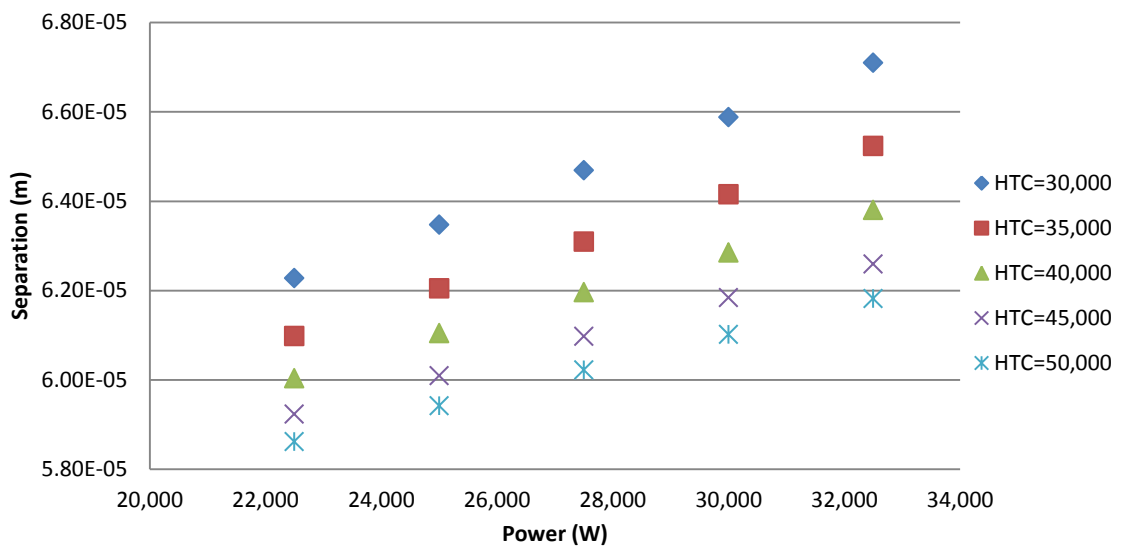
Figure 103. Side separation for the 40° curvature model

121
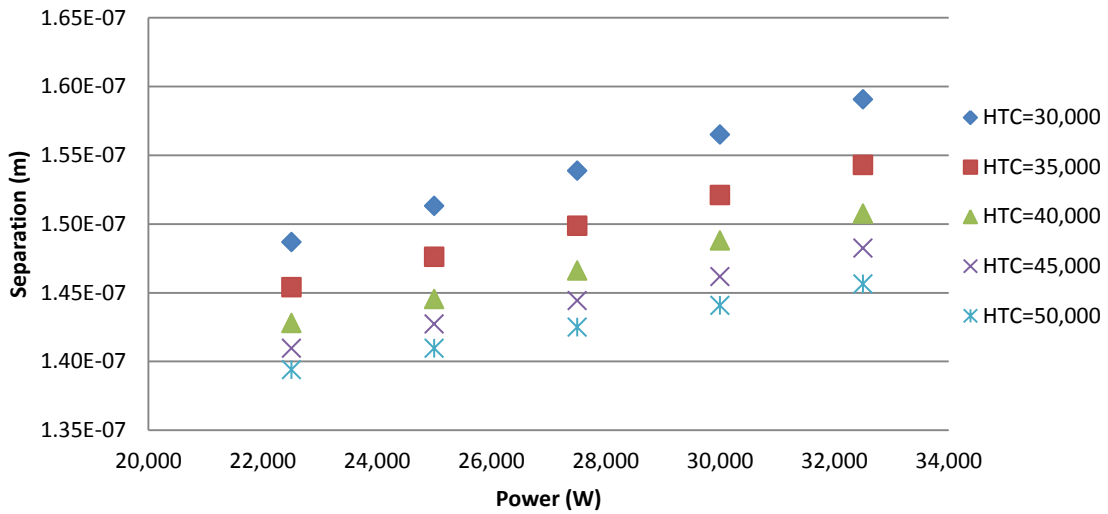
Figure 104. Center 1 separation for the 40° curvature model
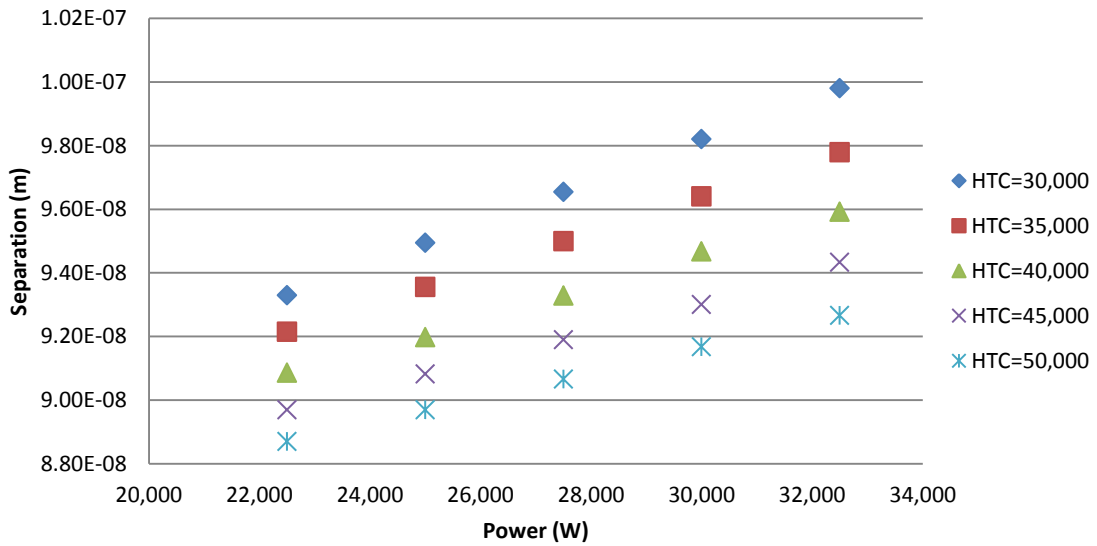
Figure 105. Center 2 separation for the 40° curvature model

The plots indicate increasing the thermal load and decreasing the heat transfer coefficient will increase separation between the foil and cladding at all monitoring points which is consistent with previous modeling results, the flat plate foil, and 20° foil results. The plots indicate separation between the foil and the cladding at the top and side monitoring points will exceed the allowable gap separation. This indicates temperatures

in these areas could reach unacceptable levels and should be monitored. The center

location for both monitoring points was well below the allowable separation gap. Finally,

comparing the 40° model separation results to the allowable separations shows all of the

calculated separations will not surpass the allowable separations.

Von Mises Stress Results

Von Mises stress was used to examine stress formation in the target during

irradiation both for its magnitude and distribution. Values for each of the various levels

of curvature were plotted and compared to the yield strength of several aluminum alloys.

The alloys chosen were Al 1100, Al 3003, and Al 6061. The yield strength for each of

these alloys can be seen in Table 25.

Table 25. Aluminum alloy yield strengths

Al 1100 Yield Strength (Pa)	Al 3003 Yield Strength (Pa)	Al 6061 Yield Strength (Pa)
1.05e8	1.25e8	2.75e8

The von Mises stress values for the flat model at the corner, side, and center

monitoring points can be seen in Figure 106, Figure 107, and Figure 108 respectively.

Figure 106. Corner von Mises stress in the flat model
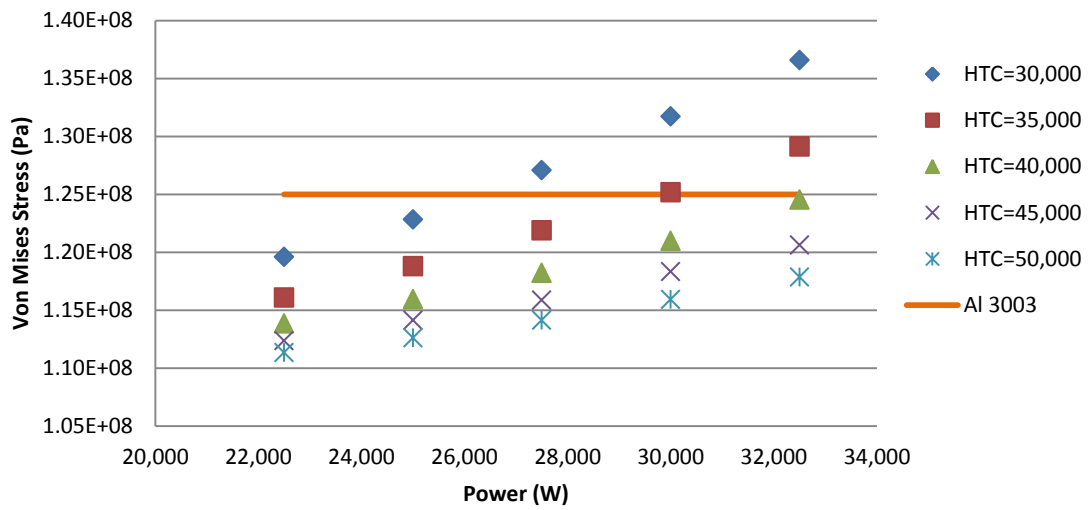
Figure 107. Side von Mises stress in the flat model
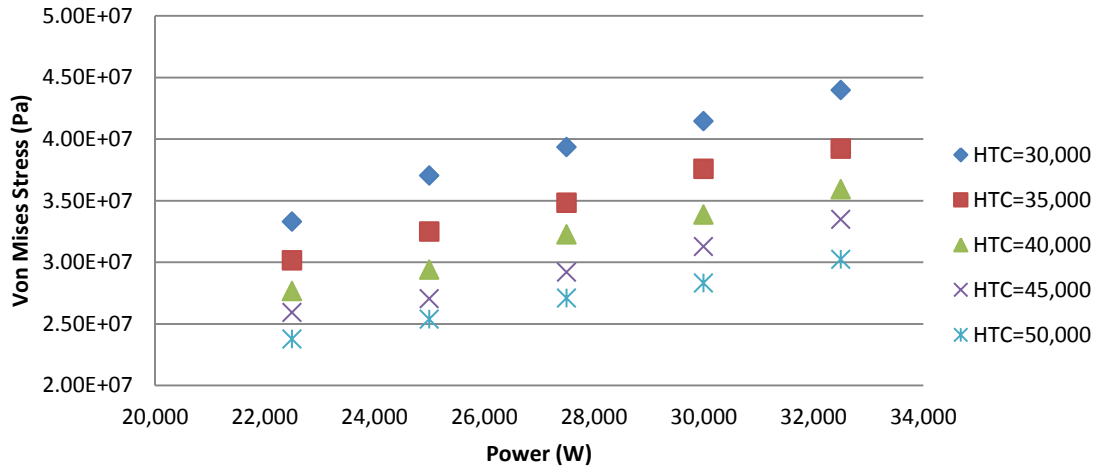
Figure 108. Center von Mises stress in the flat model

The figures indicate an increase in thermal load and a decrease in the heat transfer coefficient will increase the von Mises stress, which is an expected behavior. The greatest stresses will be found on the corner of target followed by the side and then center, meaning the greatest stresses will be seen on the target welds. The stresses on the corner will cause yielding when Al 1100 and Al 3003 are used as the cladding material, only Al 6061 would not yield. The von Mises stresses on the side monitoring point displayed similar behavior: the Al 1100 would yield while the Al 6061 would not. Al 3003 displayed a different behavior and would yield only at the higher thermal loads and lower heat transfer coefficient conditions. The von Mises results at the center location would not yield with any of the alloys. It should be noted the weld monitoring points assume the weld strength is equal to the alloy's yield strength, which is unlikely in the real target.

The von Mises stress values for the 20° curvature model at the corner, side, and center monitoring points can be seen in Figure 109, Figure 110, and Figure 111 respectively.

125
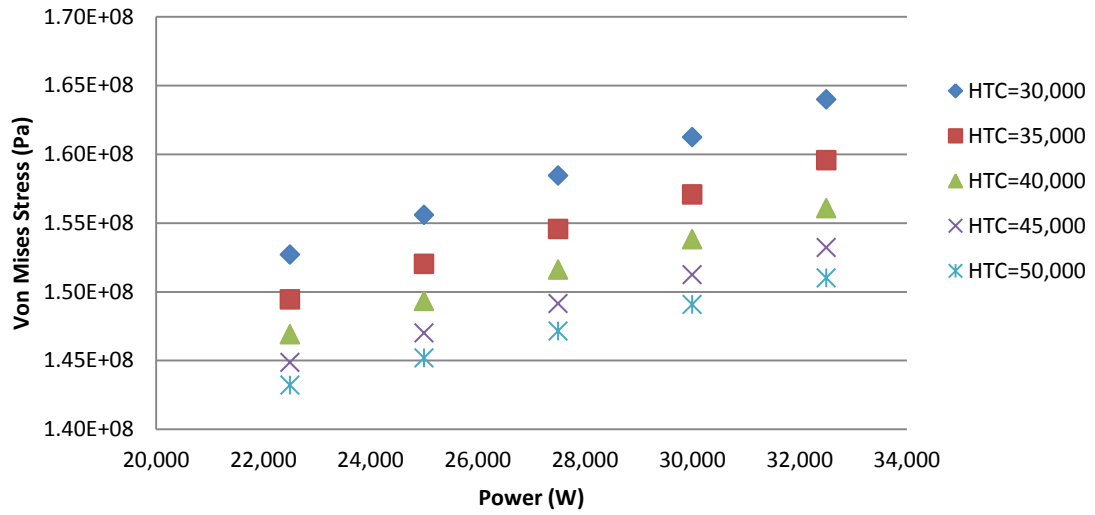
Figure 109. Corner von Mises stress in the 20° curved model
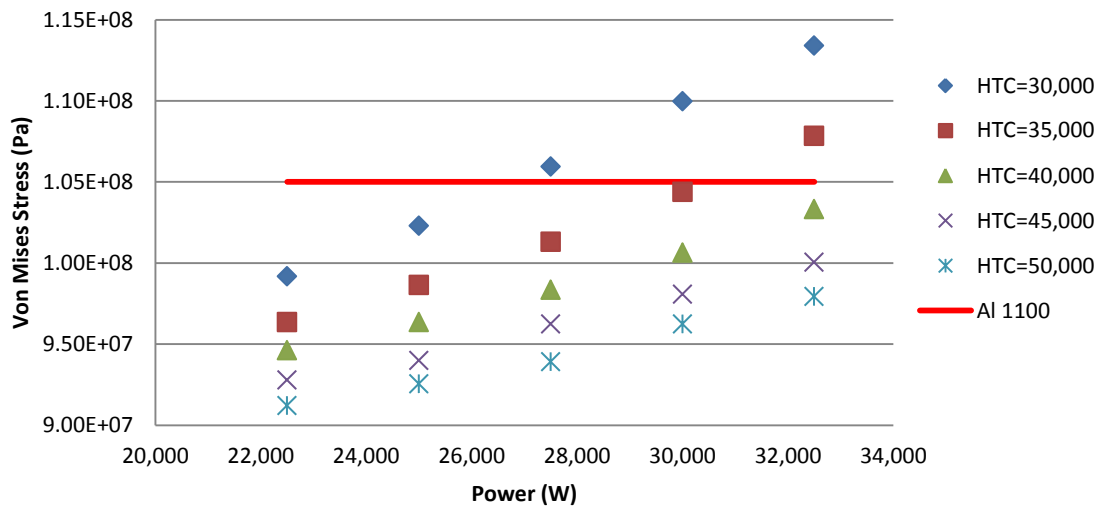
Figure 110. Side von Mises stress in the 20° curved model
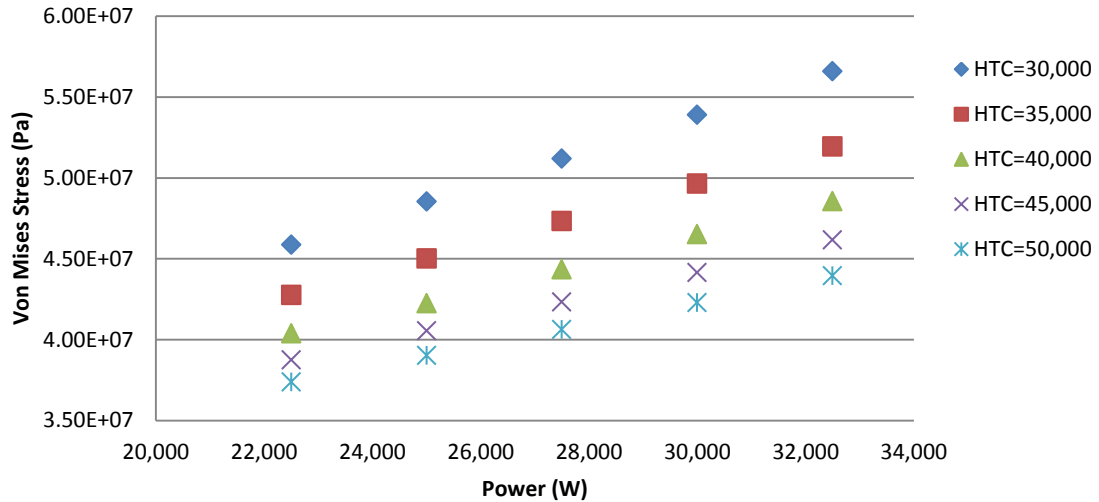
Figure 111. Center von Mises stress in the 20° curved model

The figures indicate an increase in thermal load and a decrease in the heat transfer coefficient will increase the von Mises stress, which is an expected behavior and the same as the flat foil model. The greatest stresses will be found on the target corner followed by the side and then center, meaning the greatest stresses will be seen on the target weld. A comparison of the von Mises stress to the yield strengths indicates the corner will experience the same behavior as the flat plate model. The corner stresses will still yield with the Al 1100 and the Al 3003 and not yield with the Al 6061, but there is a noticeable decrease in the stress magnitude bringing it much closer to the yield strength of Al 3003. The side von Mises stresses also decrease in magnitude and will not yield at the Al 6061 and the Al 3003 yield strengths. The Al 1100 will still have conditions where the cladding will yield. The center continued the trend of the other monitors; also decreasing and will still not yield under the heating and cooling conditions. This again assumes the welds will have the same strength as the un-welded alloy.

The von Mises stress values for the 40° curvature model at the corner, side, and center monitoring points can be seen in Figure 112, Figure 113, and Figure 114, respectively.

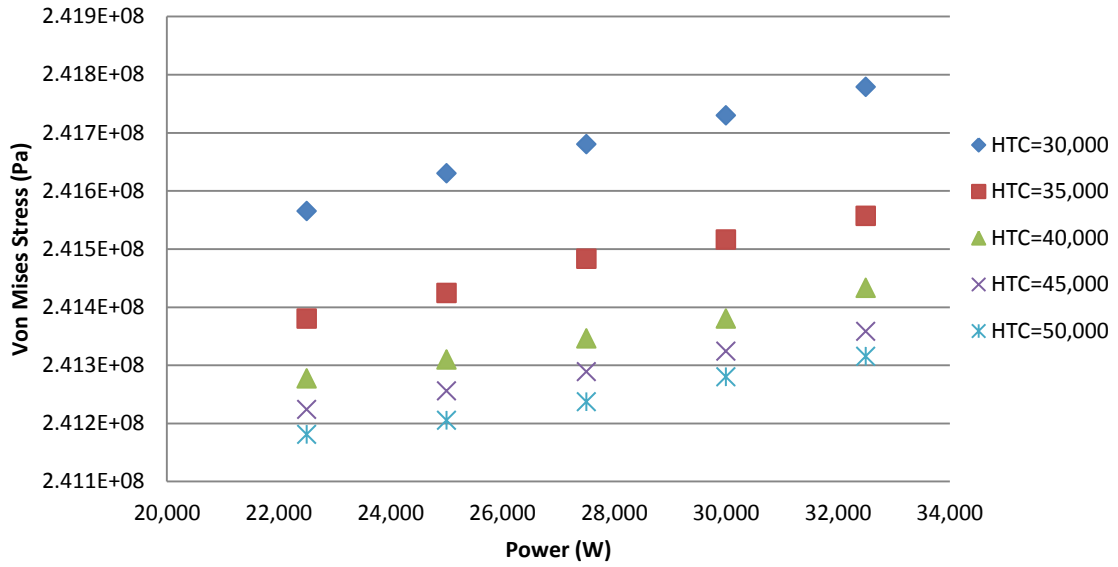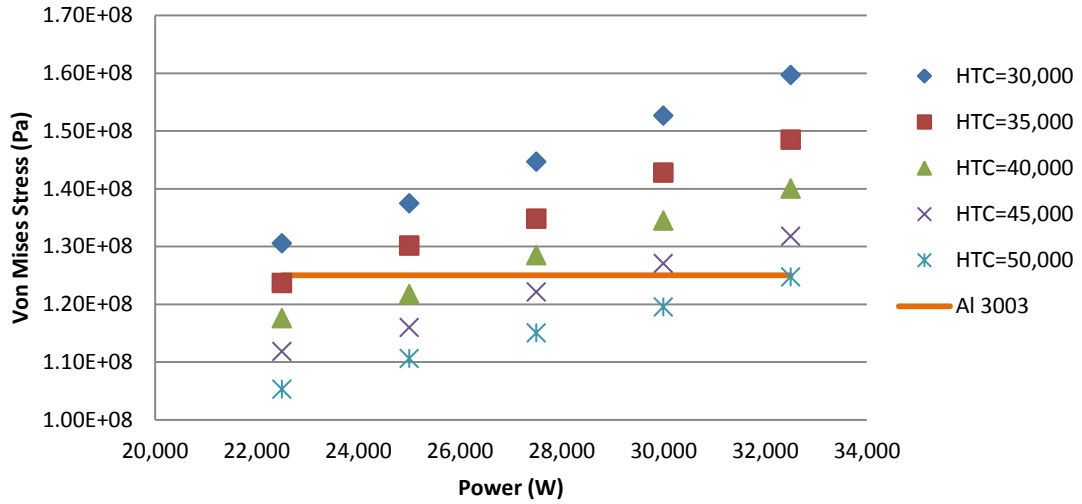**Figure 112. Corner von Mises stress in the 40° curved model**
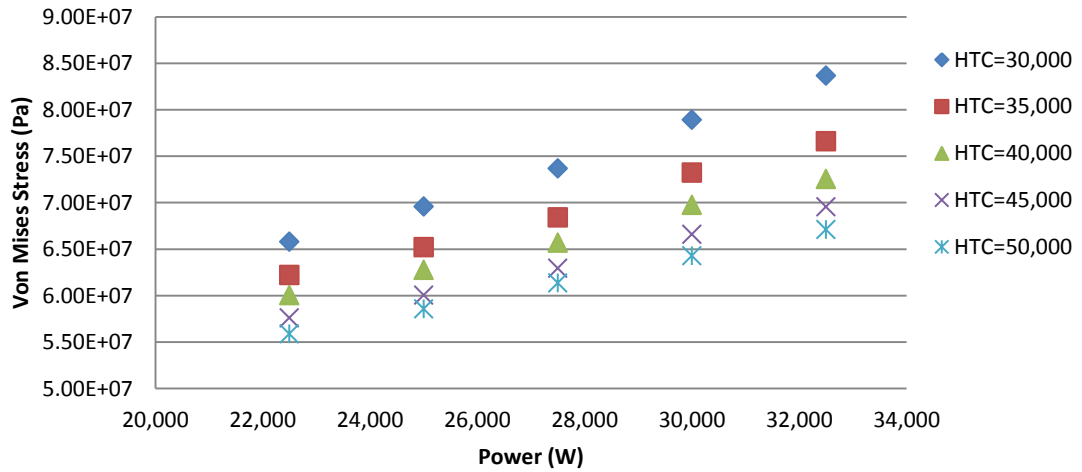
Figure 113. Side von Mises stress in the 40° curved model
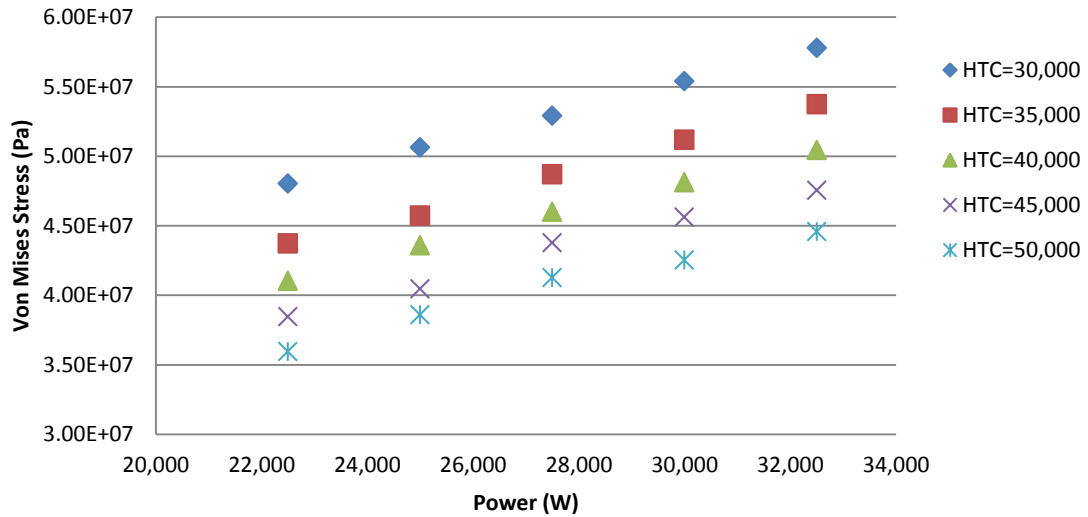
Figure 114. Center von Mises stress in the 40° curved model

The figures indicate an increase in thermal load and a decrease in the heat transfer coefficient will increase the von Mises stress, which is an expected behavior and the same as the flat foil and 20° curved foil model. The greatest stresses will be found on the target corner followed by the side and then center, meaning the greatest stresses will again be seen on the target welds. The decreasing trend in the stresses with an increase in curvature continues for the 40° model. Under the applied heating and cooling conditions the side and center will not yield when any of the aluminum alloys are used. The corner stresses will now not yield with the Al 6061 and under certain conditions with the Al 3003, it will however still yield under all conditions for the Al 1100. This again assumes the welds will have the same strength as the un-welded alloy.

Separation and Von Mises Comparison and the Effects of Curvature

Separations and von Mises stresses at various levels of curvature were directly compared to determine the effect of curvature. The worst, ideal, and middle case heating

129

and cooling conditions were chosen for the basis of this comparison and can be seen in

Table 26.

Table 26. Heating and cooling conditions used for the comparison

Thermal Load (W)	Heat Generation Applied to the Foil (W/m^3)	Heat Transfer Coefficients (W/m^{2}K)
22,500 =	3.040e10	50,000
27,500 =	3.716e10	40,000
32,500 =	4.392e10	30,000

The top, side and center separations can be seen in figures Figure 115, Figure

116, Figure 117, and Figure 118.
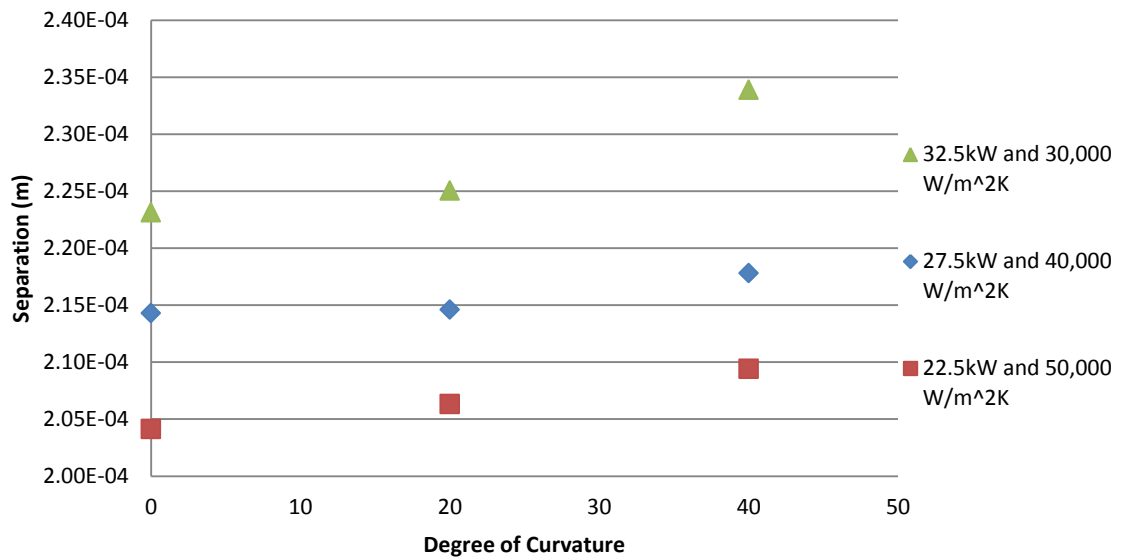
Figure 115. Top separation comparison
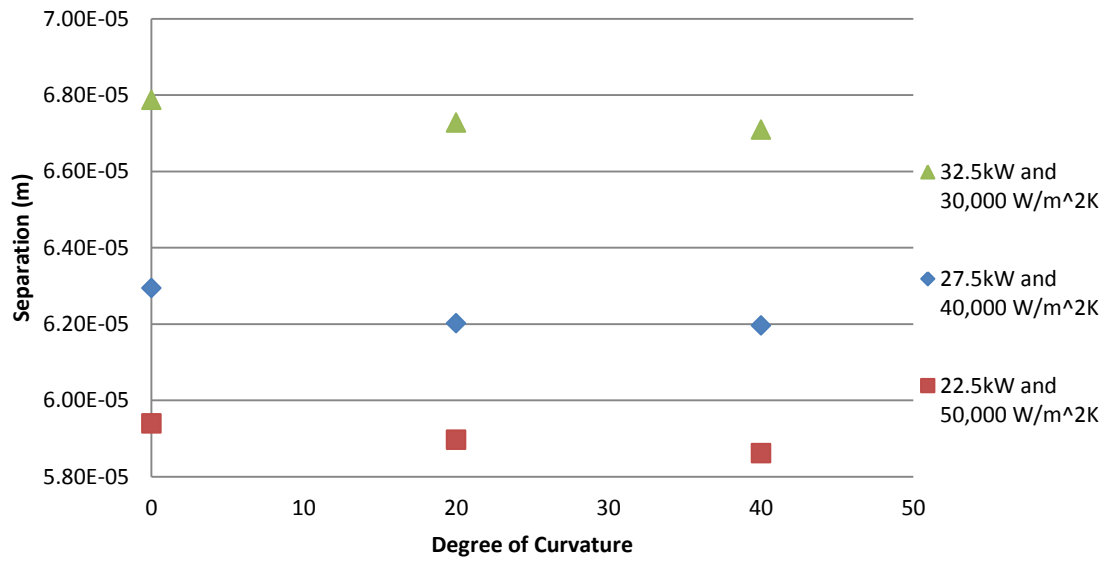
Figure 116. Side separation comparison
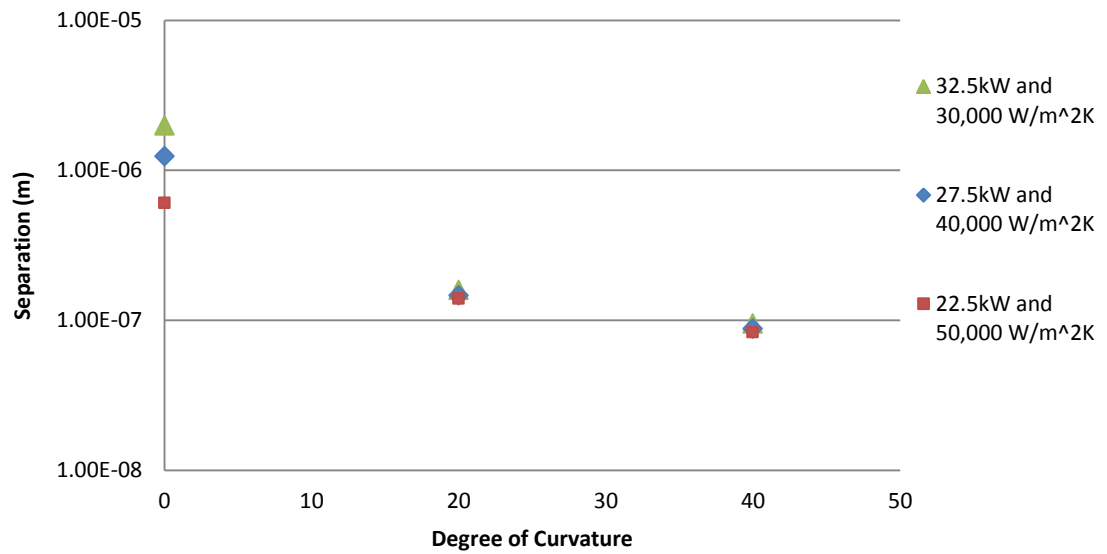
Figure 117. Center 1 separation comparison
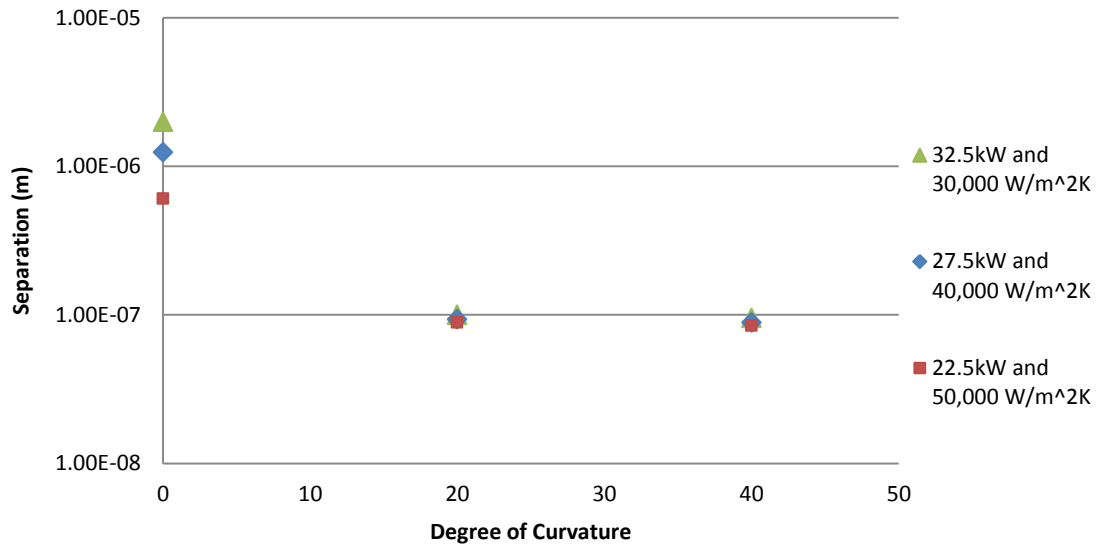
Figure 118. Center 2 separation comparison

The figures give interesting insight into the effect of curvature on the target. The top separation indicates there is a non-linear increase in the amount of separation from the aluminum cladding and the uranium foil, indicating curvature will not aid in decreasing the thermal contact resistance. The increase in separation does not hold in the other monitoring locations. The side separation decreases with the amount of curvature, indicating curvature can decrease the amount of separation on the side location and is non-linear in nature. The center location like the side monitoring point will decrease as curvature is increased. It should be noted manufacturing techniques could be used to introduce residual stresses to decrease or reverse the trend of the separations in the top monitoring locations.

The von Mises stress was also compared but only at the worst case heating and cooling condition. The stresses from these models can be seen in Figure 119.

132
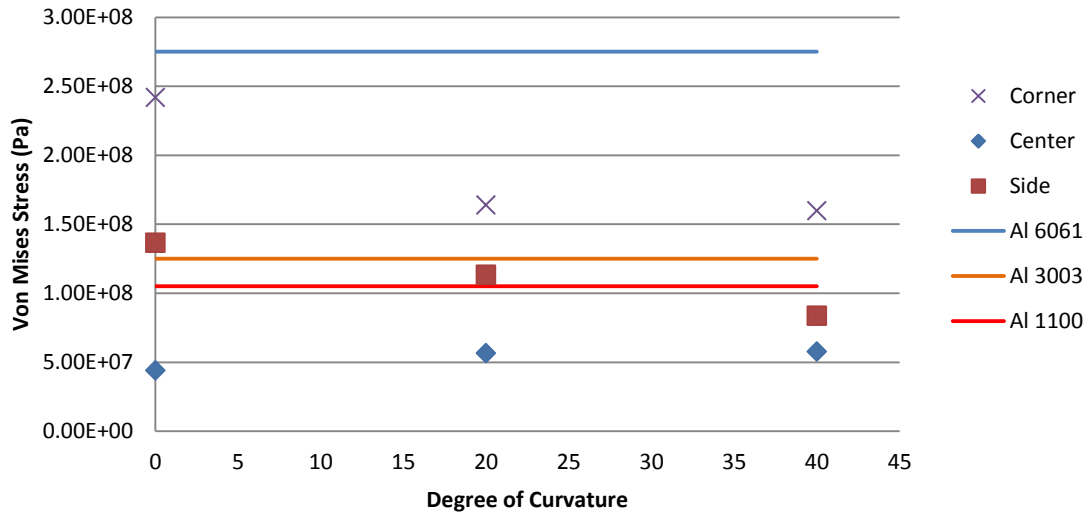
Figure 119. Von Mises stress comparison at 32.5 kW and 30,000 W/m^{2}K

The figure indicates von Mises stress on the corner and side will decrease as curvature is increased and the center will increase slightly then level off between 20° and 40° of curvature. These trends indicate curvature lowers or levels out the von Mises stress in the target and can be used to influence these stresses. The figure also shows the alloy used will greatly affect the chances of yielding and when Al 6061 is used there will be no yielding.

Deflection and Von Mises Stress Contour Plots

Contour plots of the deflection and von Mises stress at various levels of curvature can provide useful insight into the general location of the greatest deflection and stress. Contour plots of deflection for the unconstrained half of the flat, 20°, and 40° models at 32.5 kW and 30,000 W/m^{2}K can be seen in Figure 120, where the darker areas represent lower amounts of deflection and light areas represent larger amounts of deflection.

133
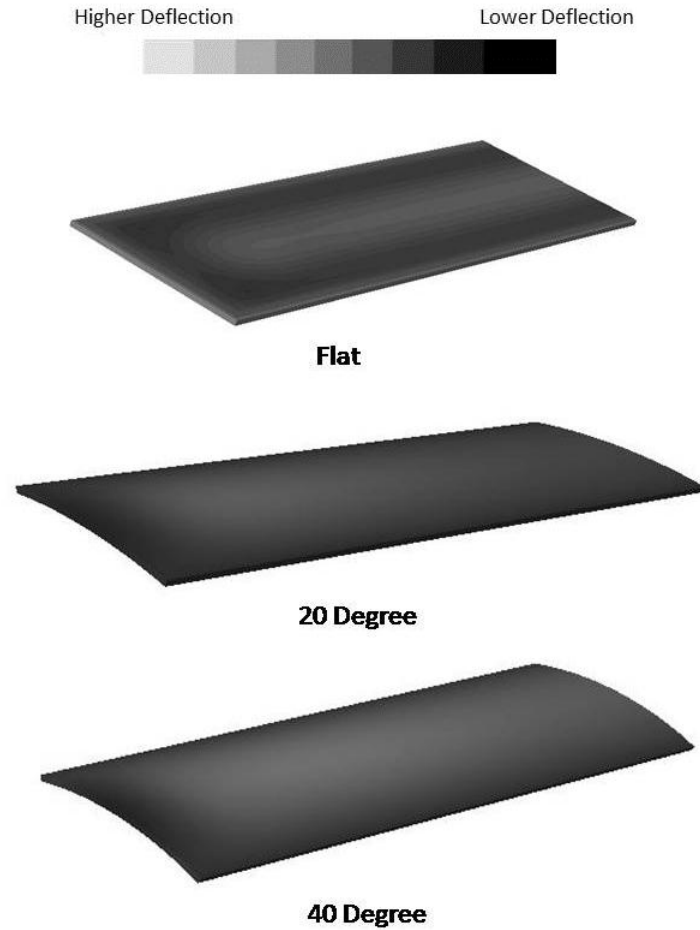
Figure 120. Contour plots of deflection

The plots show that the greatest amount of deflection in the out of plane direction occurs in the central regions of the targets. The figure also shows curvature will change the location of the greatest deflection areas. In the flat model the greatest deflection occurs in the middle then decreases quickly as the edges of the target are approached. In the curved models the greatest deflection occurs in the middle but decreases much more slowly as the edge of the target is approached.

An image of separation between the foil and the cladding can be seen in Figure 121.

134
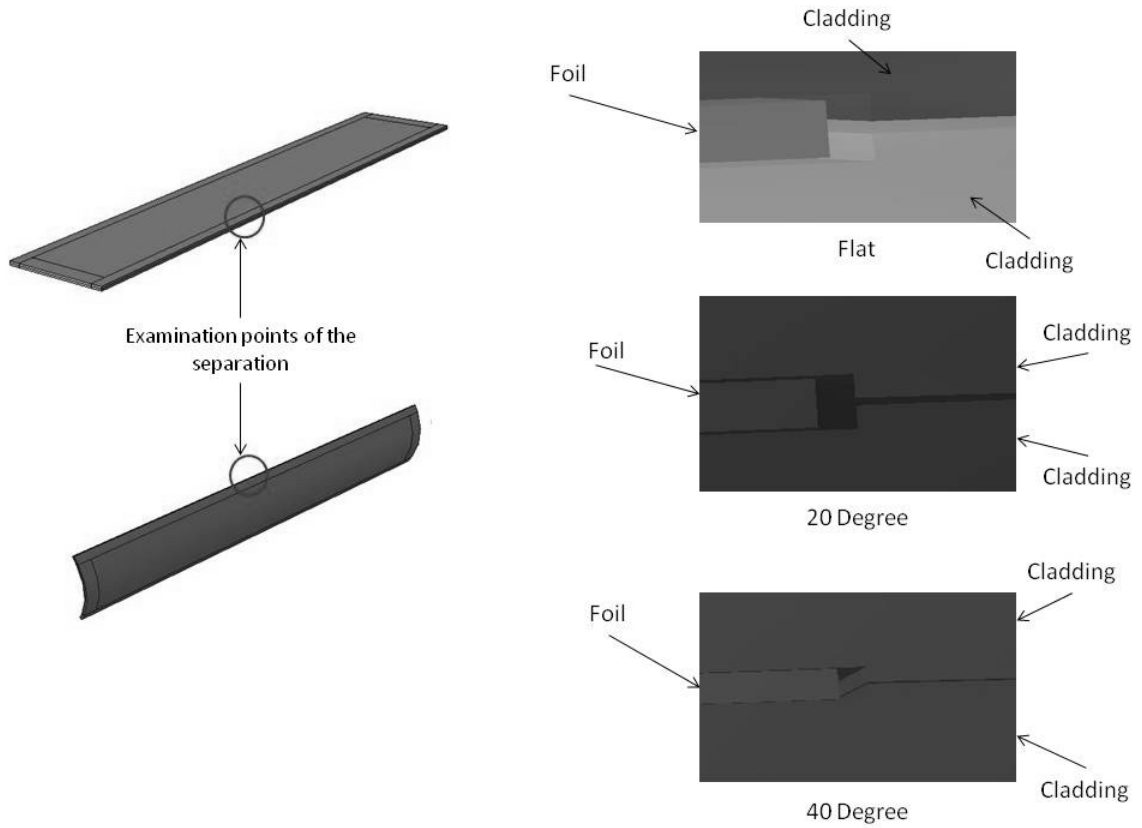
Figure 121. Separation between the foil and cladding

The figure shows there is no discernible difference in the separation behavior as curvature is increased. The figure also clearly shows the locations of separation occurring between the foil/cladding and between the cladding pieces are located on the foil edges.

An image of the von Mises Stress in the target at 32.5 kW and 30,000 W/m^{2}K can be seen for the flat, 20°, and 40° models in Figure 122.
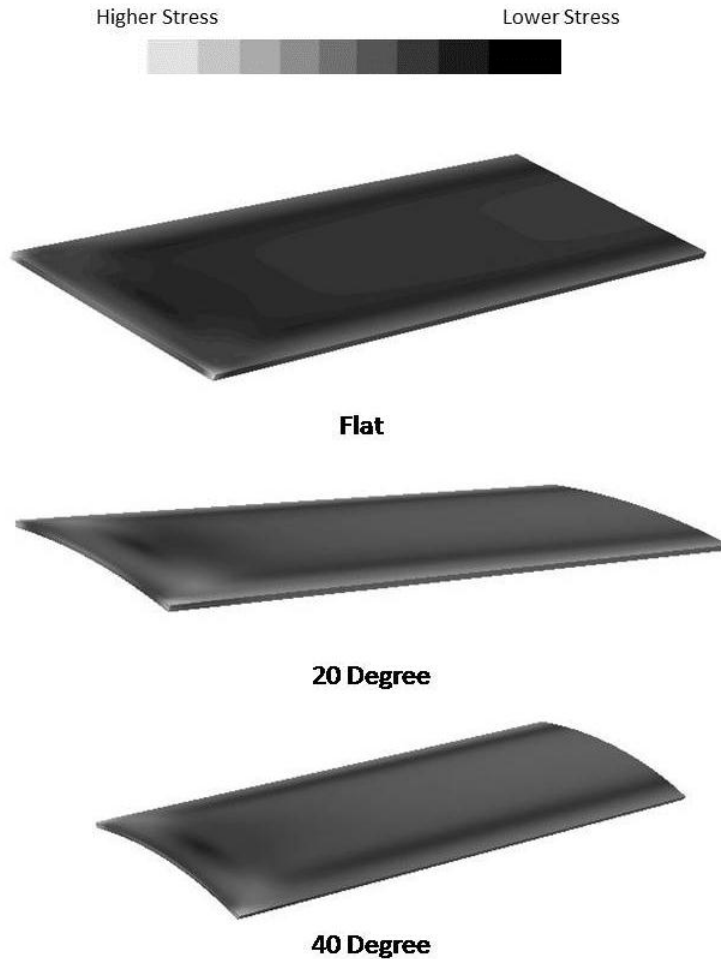
Figure 122. Von Mises contour plots of targets

The figure indicates von Mises stress will be the greatest on the edges of the target where the bond is located. This is consistent with the findings from the previous free edge cladding only models. The stress will then decrease near the approximate edge of the foil then increase again near the center of the target. The figure also indicates the greatest amount of stress will be located at the corners of the target at all levels of curvature. The stress concentrations will also change as a function of the curvature. The plots show as curvature is increased the greatest stress locations, in comparison to the rest of the target, will become increasingly concentrated in the corners of the target. This does

not indicate the magnitude will be greater but that the greatest relative stress locations will be located closer to the target corners.

The results in this chapter give insights into several foil target and curvature trends. First, the separation and von Mises stress behavior at the monitoring points is predominantly linear as the thermal load increased which is consistent with the results from the cladding only models. Second, curvature will tend to decrease the magnitude of both the separation and von Mises stress. The top separation monitoring point is an exception to this trend and actually increases as more curvature is introduced, indicating a possible location for target failure. Third, the majority of the separation and von Mises stress monitoring points will be less than the allowable separations and yield strengths under certain conditions. Depending on the location and aluminum alloy used there are certain combinations of conditions that could lead to target failure. Fourth, the separations will not surpass the allowable air gaps calculated based on the MURR operating conditions. Finally, the greatest separations between the cladding and foil will be seen at the top monitoring location followed by the side and center. The stress will also be greatest at the corner monitoring location followed by the center and then side location.

CHAPTER 11: FISSION GAS RELEASE AND URANIUM SWELLING

During irradiation the LEU foil will fission and produce heat, along with this energy fission products will also be created including gases. Due to the short irradiation time the majority of the gases will remain trapped in the foil. Only a small percent, on the order of 1 to 2 percent, will escape through the foil into the gap between the recoil barrier and cladding. The small percent that does escape the foil is mainly driven from the foil through the kinetic energy of the fission reaction and not diffusion [56, 57]. The gas that does escape will remain trapped in the gap and increase over the irradiation period. As the gas accumulates the gas pressure in the gap will increase exerting a physical force on the cladding. The fission gas pressure will combine with the thermal-mechanical force increasing the overall pressure on the cladding. For the purposes of this study it is assumed all gases produced as fission products will diffuse from the foil and will completely fill the gap between the foil and cladding. Filling the separation gap completely with gas will place the target in a worst case scenario and should provide a bounding case.

Fission Gas Release Setup

The primary gases released during irradiation will be Xe and Kr with fission yields of 6.333% and 0.2712% respectively [58]. It is clear Xe will be the dominate gas in the separation and contribute most to the fission gas pressure. The fission gas pressure was calculated using the Redlich-Kwong equation of state, which is [59]

$$P = \left(R_g T - \frac{a(v-b)}{\sqrt{T}V(v+b)} \right)$$

(11.2.1)

where P is pressure, R_g is the gas constant, T is temperature, and V is volume. The constants a and b are a function of the combined gases in the gap and are given by

$$a = \frac{R_g^2 T_c^{2.5}}{9\xi P_c}$$

(11.2.2)

$$b = \frac{\xi R_g T_c}{3P_c}$$

(11.2.3)

where T_c is the critical temperature, P_c critical pressure, and ξ is a constant equal to 0.259921. The values used for each gas can be seen in Table 27.

Table 27. Gas properties

Gas	T_c (K)	P_c (MPa)	a $(Nm^4 K^{0.5}/mol^2)$	b (m^3/mol)
Xe	289.75	5.9	7.158	3.538e-5
Kr	209.45	5.5	3.411	2.743e-5

The volume and temperature were determined for each level of curvature at the worst case heating and cooling conditions. These conditions were a 32.5 kW thermal load and a heat transfer coefficient of 30,000 W/m^{2}K at all levels of curvature. The volume was determined by subtracting the irradiated expanded volume from the irradiated foil volume. The temperature was determined by averaging the temperatures at the interface

of the foil and the cladding. The calculated volumes and temperatures can be seen in

Table 28.

Table 28. Separation gap volume and gap temperature

Model	Foil + Gap v (m^3)	Foil v (m^3)	Gap v (m^3)	T (K)
Flat	7.69E-07	7.40E-07	2.90E-08	423
20	7.47E-07	7.40E-07	6.57E-09	423
40	7.46E-07	7.40E-07	6.08E-09	423

Using the volumes and temperatures and equation (11.2.1), the pressures for each model

were determined and can be seen in Table 29.

Table 29. Fission gas release pressures

Model	Pressure (Pa)	Pressure (MPa)
Flat	11,709,278 =	11.71
20	51,834,270 =	51.83
40	56,024,607 =	56.02

The pressures are in the MPa range with the smallest pressure occurring in the flat

plate model and increasing to the 40° model. The near constant temperature and

decreasing separation gap volume lead to the increase in the fission gas release (FGR)

pressure in the curved models. The calculated pressures were applied to the models in the

form of a uniform pressure on the model surfaces at the interface of the cladding and foil.

An exaggerated diagram of the FGR pressure application location can be seen in Figure

123.

Cross Section View
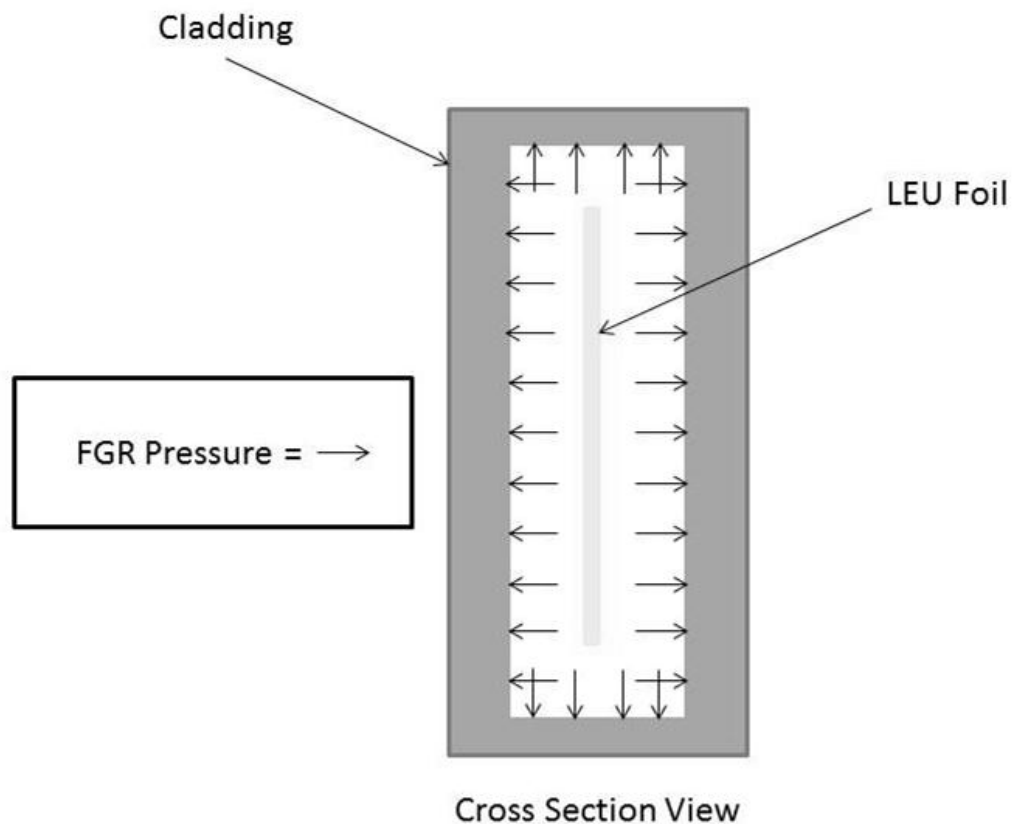
Figure 123. Diagram of FGR pressure application locations

Uranium Swelling Setup

During irradiation the LEU foil will undergo a process known as uranium

swelling. Uranium swelling is caused by the buildup of fission gases in between the

grains of the foil, the solid fission product buildup, and grain realignment in the foil [60,

61]. The majority of the research done on uranium swelling has focused on oxide based

fuels in a dispersion matrix [62]. Information on the behavior of pure uranium metal is

limited and was produced during the 1950's and 1960's [61]. During this research it was

determined pure uranium fuel in a reactor was unpractical and the majority of research

was halted. The information available is limited to very low burn-ups in the 0.1% to 1%

range. It is excepted the target will experience burn-ups in the 10% range. In attempt to

gain insight into the swelling behavior at this burn-up, correlations from U-Mo monolithic fuel were used to determine percent swelling [60].

A correlation for overall fuel swelling is given by

$$\left(\frac{\Delta V}{V_o}\right)_f = 5.0 f_d$$

(11.3.1)

where V_0 is the initial volume, ΔV is the change in volume, and f_d is the fission density in 10^{27} fission/m^3. Fission density is a representation of the burn-up in the uranium and was determined by converting the thermal power of the target into the number of fissions occurring during irradiation. The thermal power was 32.5 kW, which was converted into Joules per week. It was assumed the target would be irradiated for one to two weeks. A week and a half was chosen as the irradiation time and the total amount of Joules per irradiation time was determined and can be seen in Table 30. Assuming a single fission will release 3.2 x 10^{-11} J the number of fissions can be determined for the total irradiation period and can be seen in Table 30 as well [63]. Finally using equation (11.3.1) the amount of volumetric swelling can be determined and is seen in Table 30.

Table 30. Fission density and swelling percent

Total Joules Produced During Irradiation (J)	Total Fissions (f/m^3)	Volumetric Swelling in Percent
2.948e10	1.245e27	6.225%

Abaqus can replicate a temperature independent volumetric expansion using a strain rate in its material specification. The volumetric swelling can be converted into a strain rate by first using [64]

$$DS = (1 + \%Swelling)^{1/3} - 1 \qquad (11.3.2)$$

where DS is the directional strain and %Swelling is the volumetric swelling. The directional strain can be converted in volumetric strain using

$$VS = 3(DS) \qquad (11.3.3)$$

where VS is the volumetric strain. Finally this value can be converted into a strain rate by dividing it by the irradiation time in seconds. The final value based on the values in Table 30 assumes an irradiation time, at a linear burn-up rate, of one and a half weeks and produces a strain rate of 6.724e-8 s^{-1}. The strain rate was applied in the material properties of the uranium foil under the swelling material property and can be seen Figure 124. The same thermal-mechanical coupled element was used in the entire model.
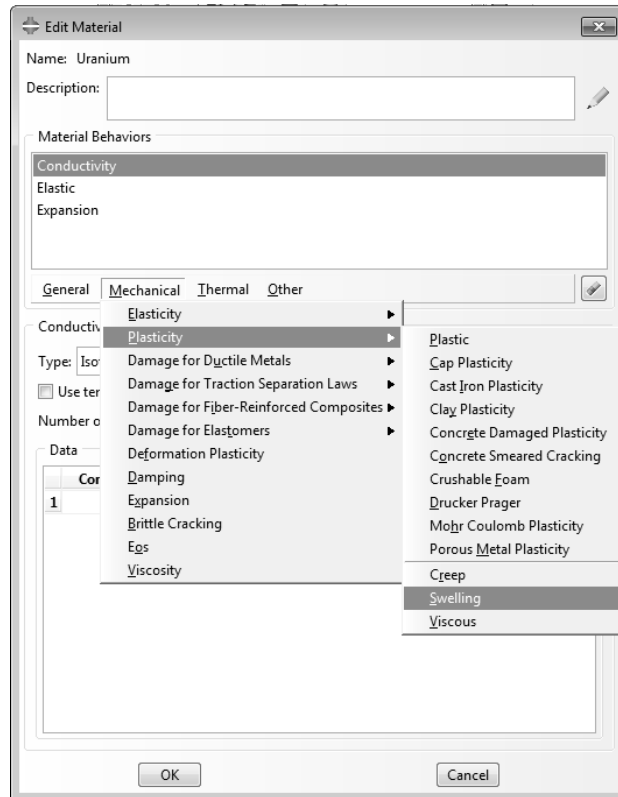
Figure 124. Swelling input location in Abaqus

Fission Gas Release and Uranium Swelling Combined Results

The pressure from the FGR and the effects of uranium swelling were combined

into the flat, 20°, and 40° target models assessing their combined effects. The worst case

scenario heating and cooling conditions were once again applied with a thermal load of

32.5 kW and h=30,000 W/m²K. Separation for the flat, 20°, and 40° models at the

centers, top, and side monitoring locations can be seen in Figure 125, Figure 126, Figure

127, and Figure 128.
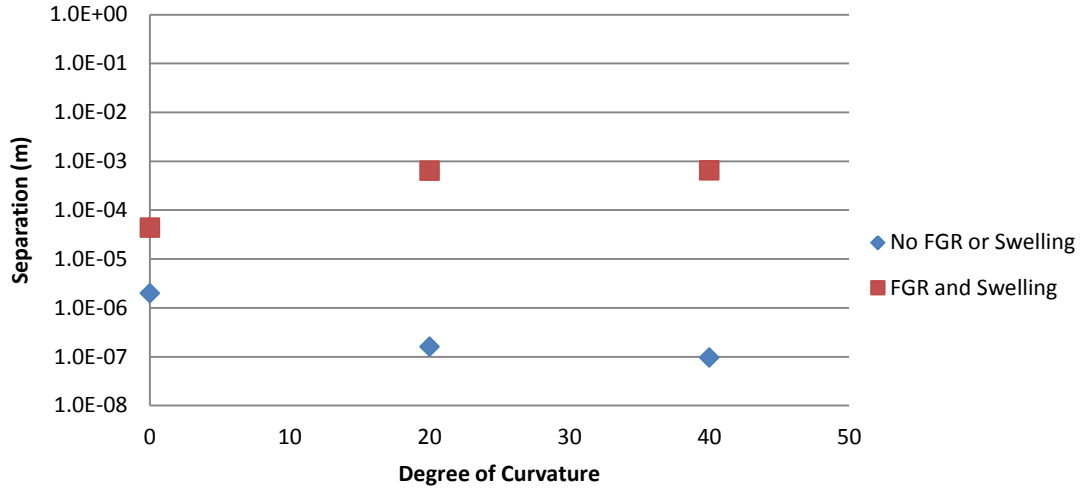
Figure 125. Center 1 monitoring point with and without FGR and Swelling
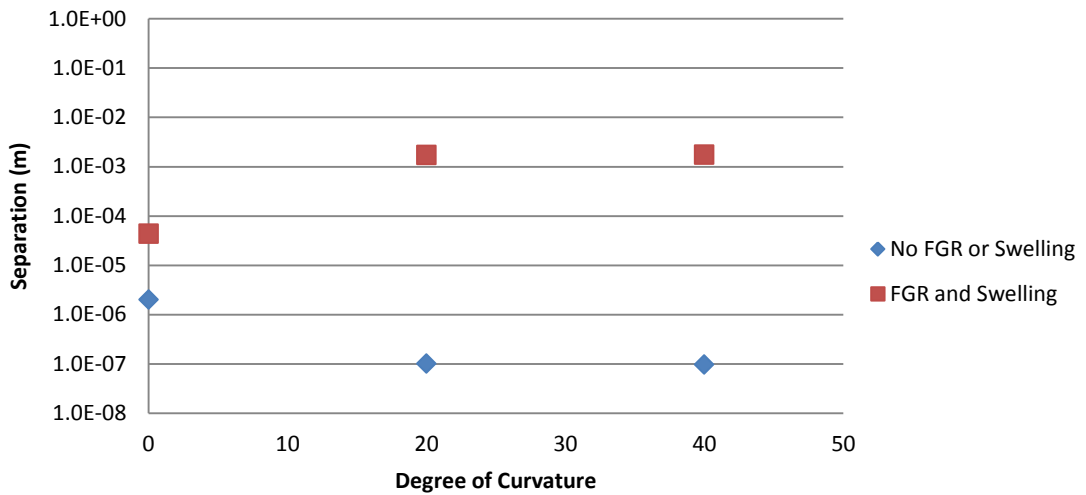
Figure 126. Center 2 monitoring point with and without FGR and Swelling
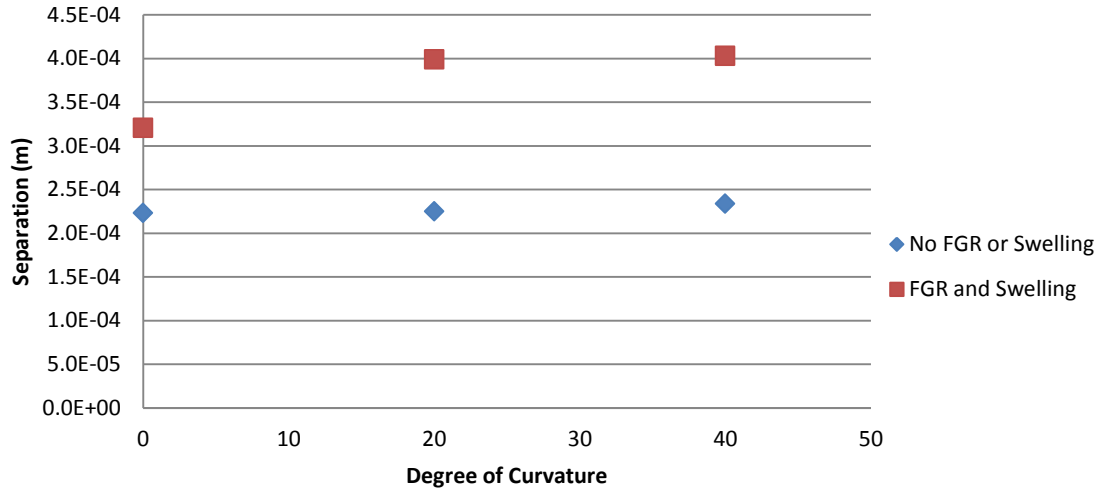
Figure 127. Top monitoring point with and without FGR and Swelling
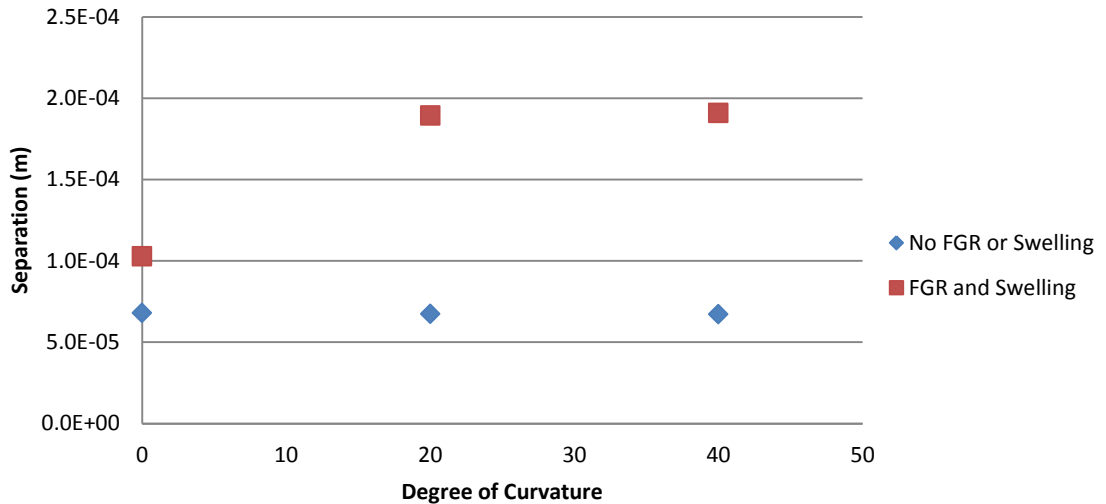
Figure 128. Side monitoring point with and without FGR and Swelling

All FGR and swelling monitoring point separations increased as curvature was increased. Results from the combined FGR and swelling were compared to the results from the curved foil target study. The FGR and swelling increase at the center monitor points was several orders of magnitude larger than the non-FGR and non-swelling. Further, the allowable gas gap separations are violated in all situations. This worst case

146

scenario does not necessarily indicate failure will occur but these are areas of interest to monitor.

Von Mises stress with FGR and swelling was examined along with the separations and compared to various aluminum alloy yield strengths. The same stress monitoring points from the previous chapter were used for the comparison. Von Mises stress for the corner, side, and center monitoring points can be seen in Figure 129, Figure 130, and Figure 131.
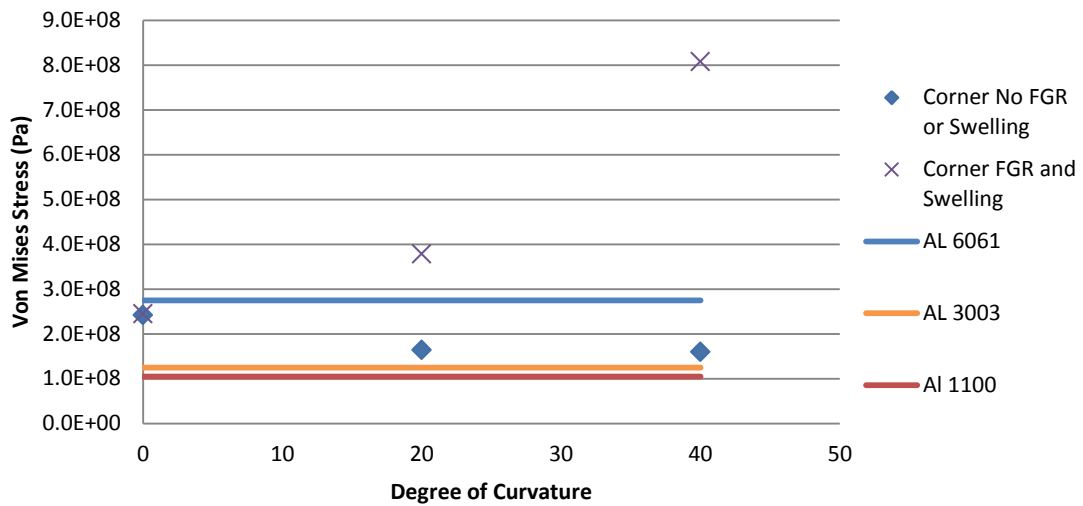
Figure 129. Corner von Mises stress with FGR and Swelling
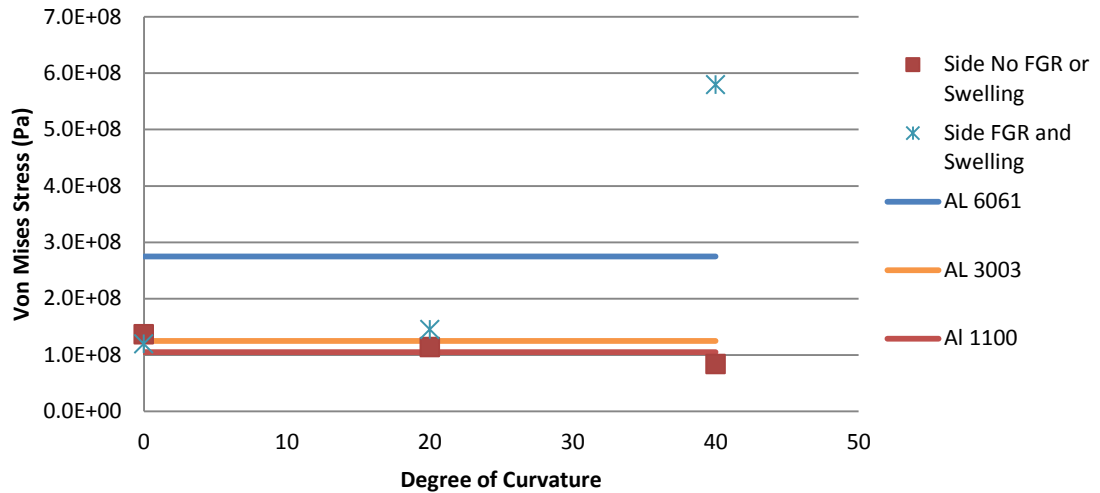
Figure 130. Side von Mises stress with FGR and Swelling
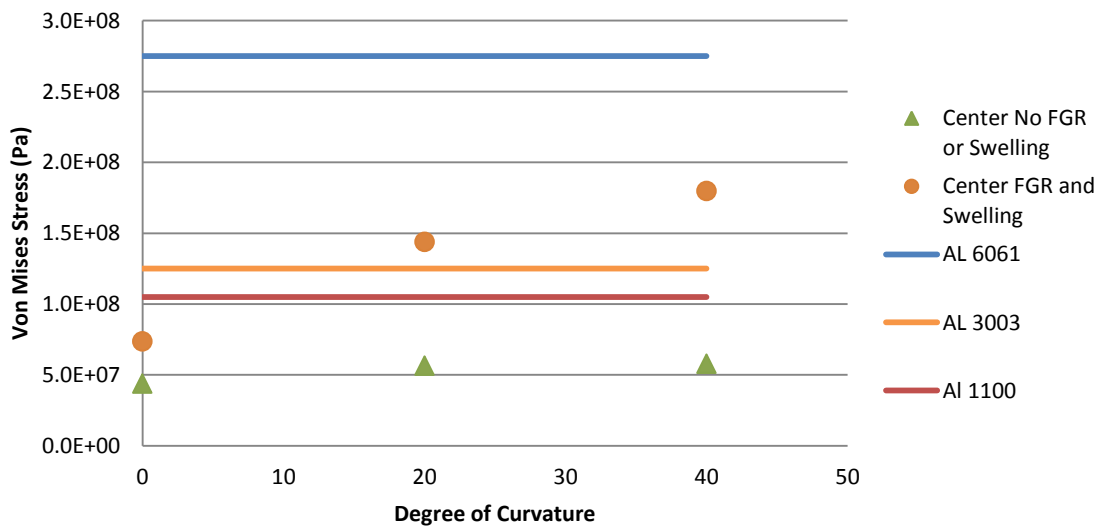
Figure 131. Center von Mises stress with FGR and Swelling

The von Mises stress monitoring points increased at all levels of curvature with FGR and swelling. Unlike previous non-FGR and non-swelling results the von Mises stress on the corner will increase beyond the Al 6061 yield strength somewhere between 0° and 20° of curvature. Finally, unlike the non-FGR and non-swelling models the von Mises stress will increase with an increase in curvature caused by the much higher internal fission gas pressures.

148

The side and corner monitoring points indicate possible failure between the 20°

and 40° of curvature exceeding all yield strengths. The stress trending was opposite the

non-FGR and non-swelling and increased with added curvature due to increased internal

pressure. The center monitoring point indicates possible failure situations exceeding the

yield strengths of Al 1100 and Al 3003 somewhere between 0° and 20° of curvature. The

stress also increased with increased curvature, consistent with the non-FGR and non-

swelling results. It should be noted all comparisons in this section assume a weld will

have the same yield strength as the un-welded alloy.

Deflection and Von Mises Stress Contour Plots with FGR and Swelling

Contour plots of deflection and von Mises stress can provide useful insight into

the overall deflection and stress trending. Further, they allow for a direct comparison of

the non-FGR/non-swelling models and the FGR/swelling models throughout the entire

target. Contour plots of deflection for the unconstrained half of the flat, 20°, and 40°

models at 32.5kW and 30,000 W/m^2K can be seen in Figure 132, where the darker areas

represent lower amounts of deflection and light areas represent larger amounts of
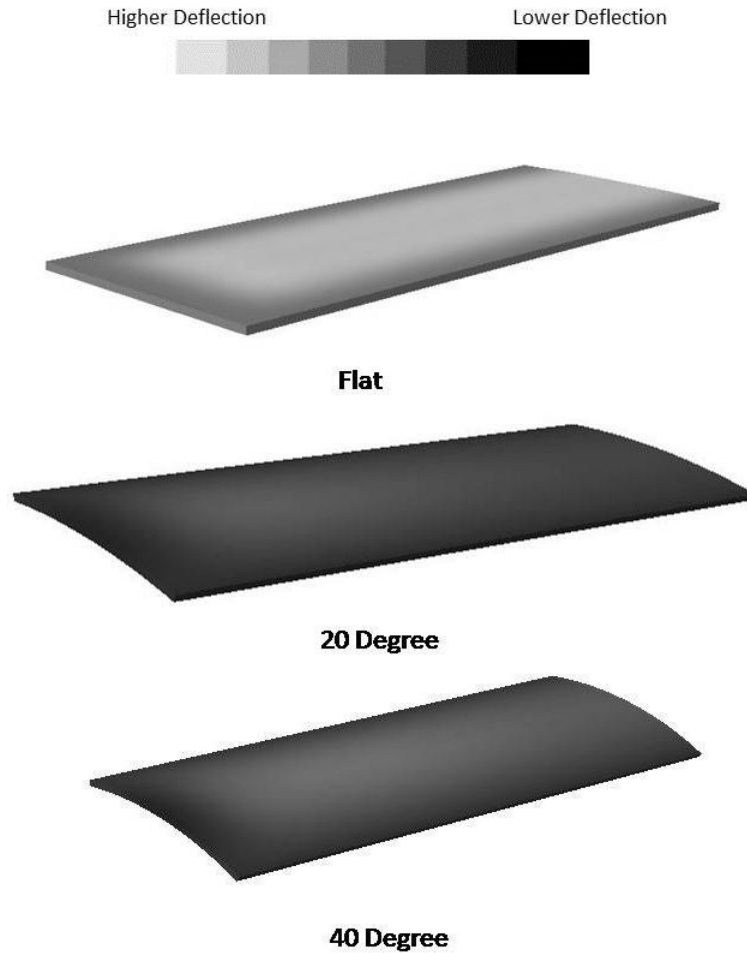
deflection.

Figure 132. Deflection contour plots with FGR and uranium swelling

The plots show the greatest amount of deflection occurs in the central regions of the targets. Further, curvature will change the location of the greatest deflection areas. In the flat model the greatest deflection occurs in the middle then decreases slowly as the edges of the target are approached. In the curved models the greatest deflection occurs in the middle but decreases much more quickly as the edge of the target is approached.

Figure 133 shows contour plots of the separation between the foil and cladding in the flat, 20°, and 40° models.
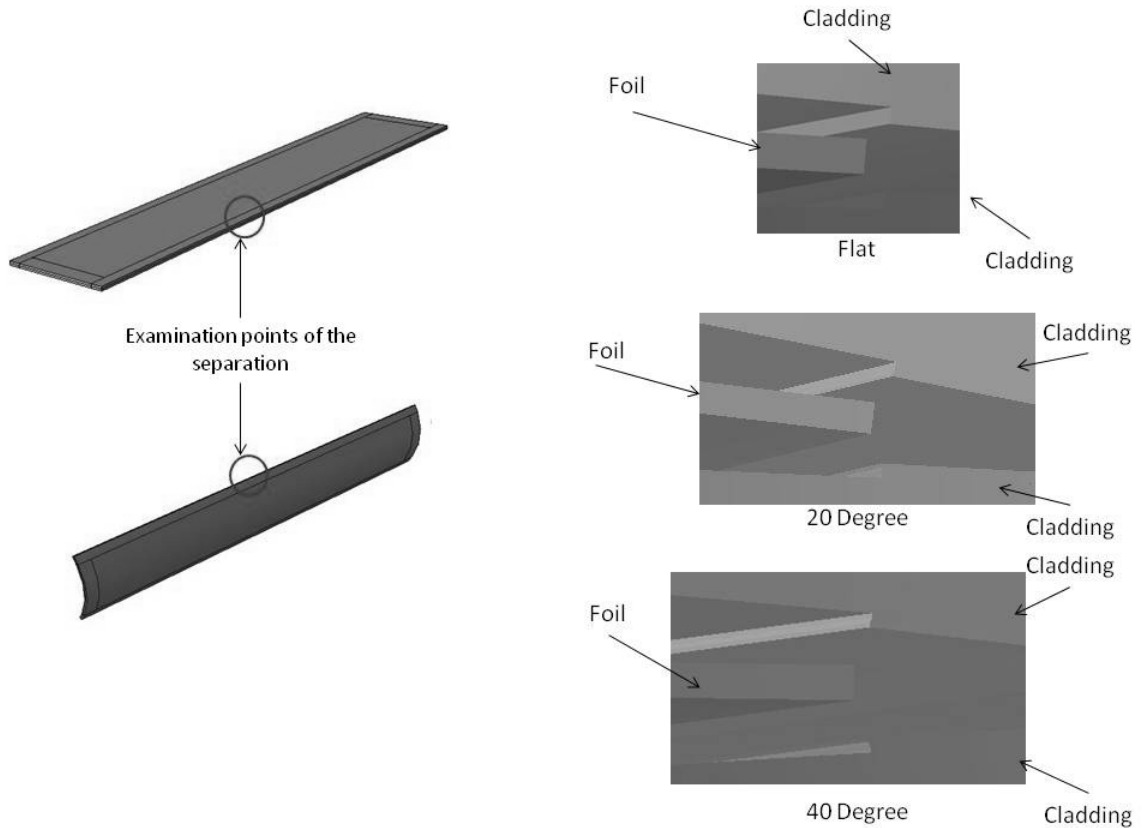
Figure 133. Foil and cladding separation with FGR and Swelling

It appears there is no discernible difference in separation behavior as curvature is increased. The figure also clearly shows separation occurring between the foil/cladding and between the cladding pieces. Finally a comparison to the separation in Figure 121 clearly shows a significant increase in the amount of visible separation.

An image of the von Mises stress in the target at 32.5 kW and 30,000 W/m^{2}K with FGR and swelling can be seen for the flat, 20°, and 40° models in Figure 134.
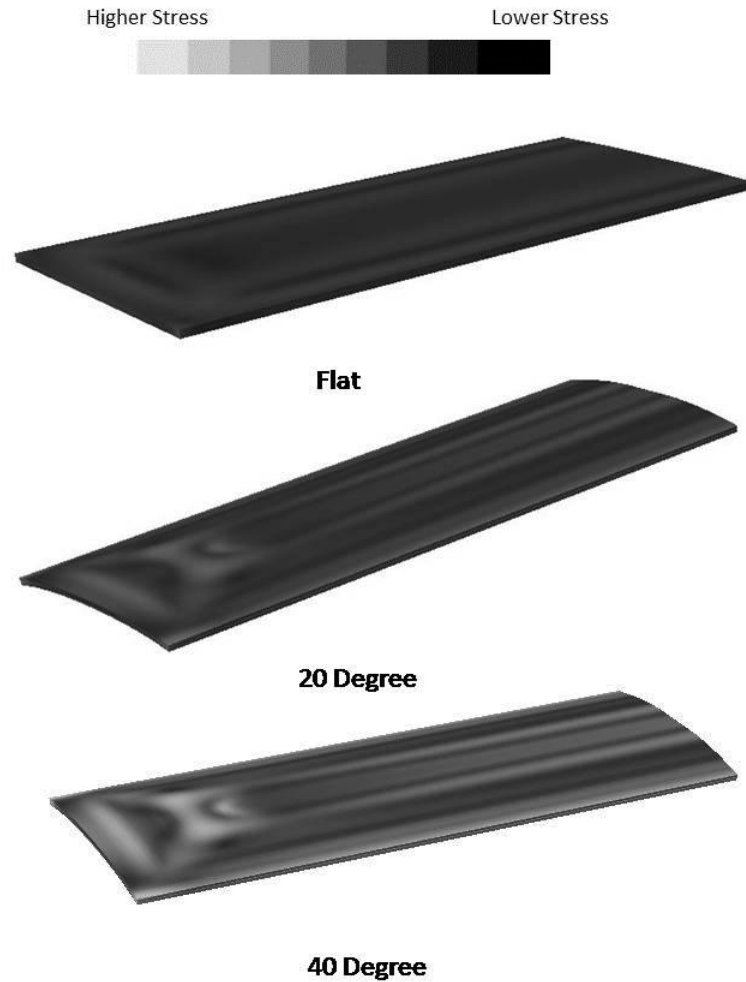
Figure 134. Von Mises stress with FGR and swelling

It is clear Von Mises stress will be the greatest on the edges of the target where the weld is located and is consistent with findings from the previous free edge cladding only and the non-FGR and non-swelling models. Further, the greatest amount of stress will be located at the corners of the target at all levels of curvature and stress concentrations will also change as a function of curvature. The plots show increased curvature produced a noticeable change in the locations of the stress concentrations. The flat model is similar to the non-FGR and non-swelling models but the 20° and 40° models

behave differentially. The stress concentrations in these models increase and decrease as the edges of the target are approached, unlike the previous results.

FGR and Uranium Swelling Decoupling

FGR and U swelling effects were decoupled and investigated separately. Decoupling the effects provides an estimation of the amount each contributes to the separation and von Mises stress in the target. The worst case heating and cooling conditions used in previous studies was again used in this investigation. Separations for both the FGR and U swelling can be seen in Figure 135, Figure 136, Figure 137, and Figure 138.
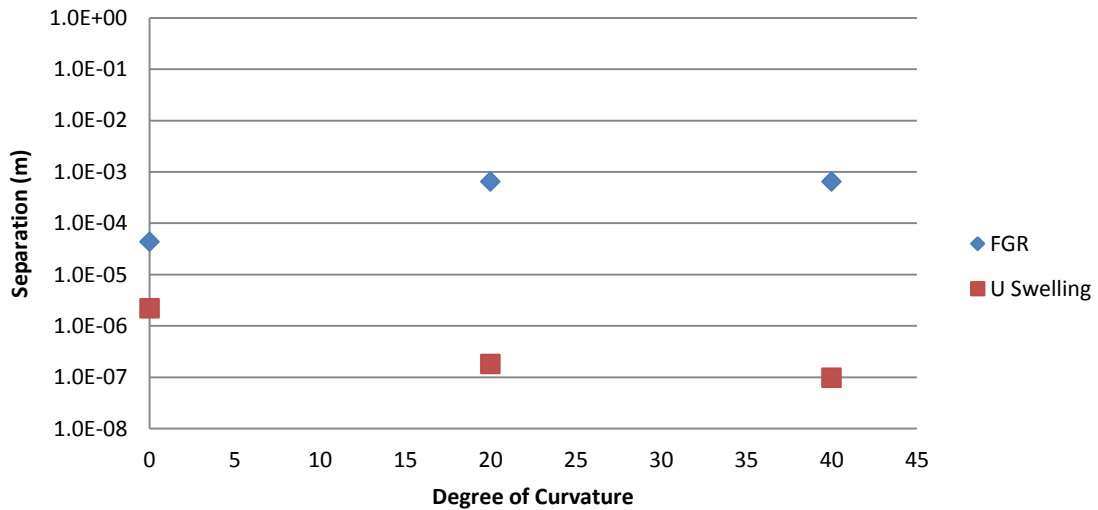
Figure 135. Center 1 separation with decoupled FGR and U swelling
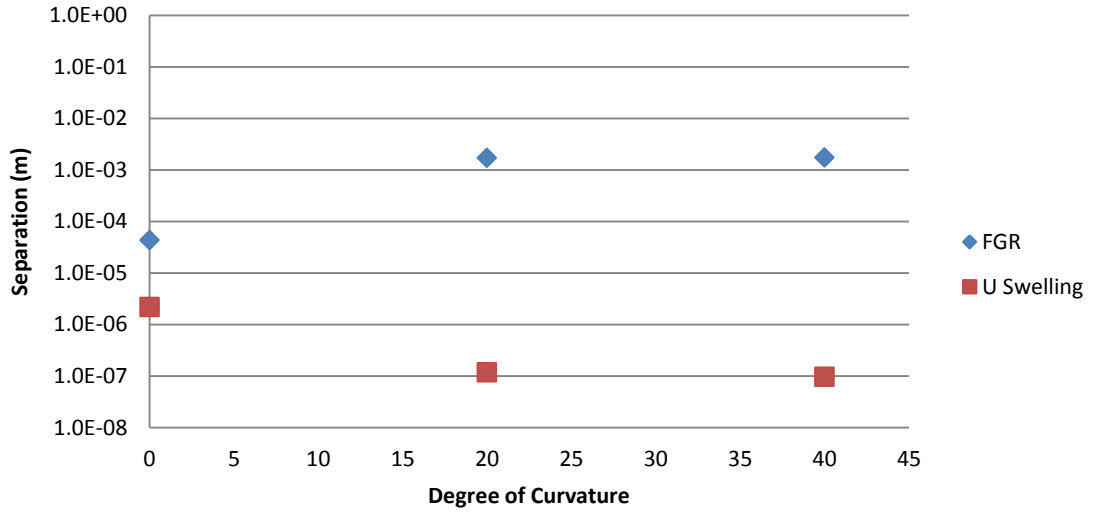
Figure 136. Center 2 separation with decoupled FGR and U swelling
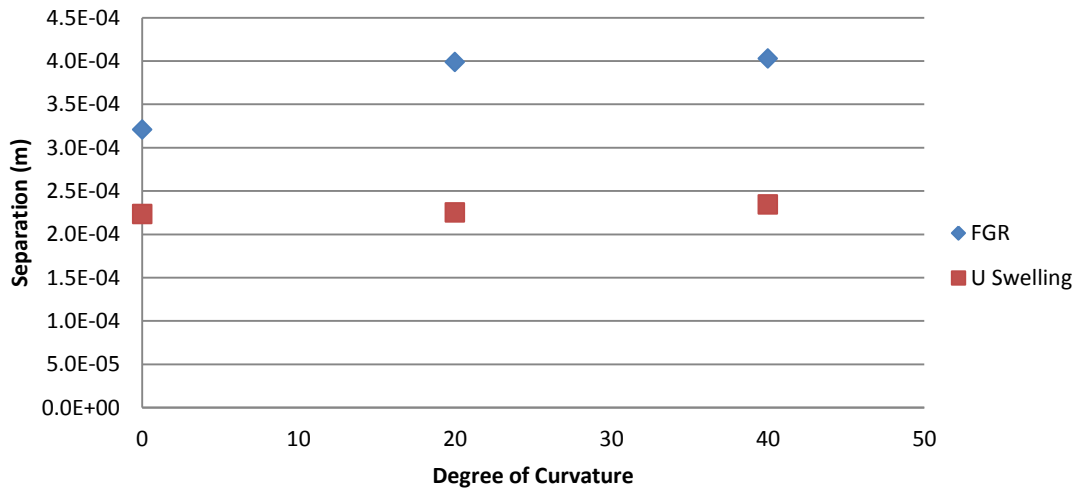
Figure 137. Top separation with decoupled FGR and U swelling
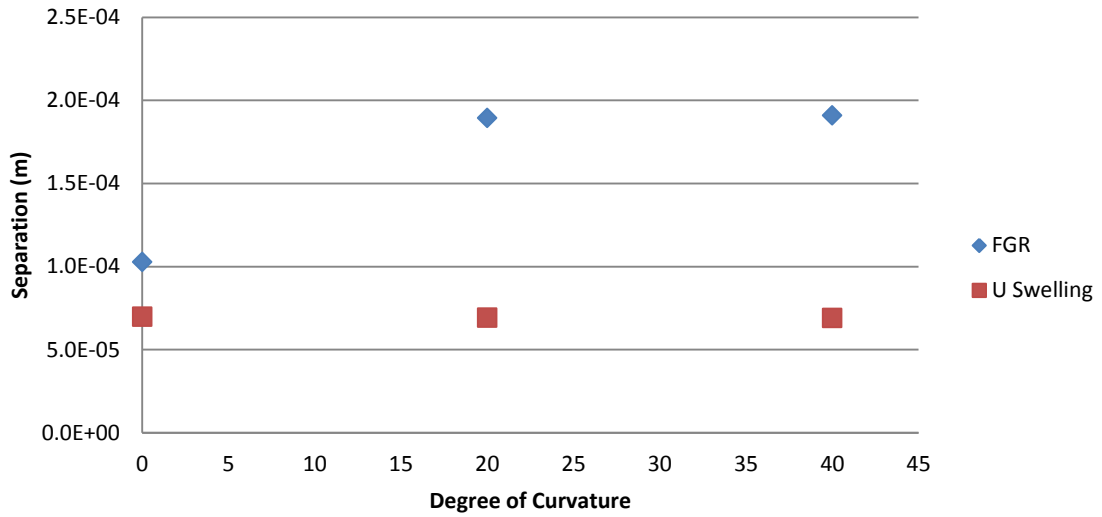
Figure 138. Side separation with decoupled FGR and U swelling

The comparison clear indicates FGR will be the dominate contributor to the separation in the target. Von Mises stresses were also examined and can be seen in Figure 139, Figure 140, and Figure 141.
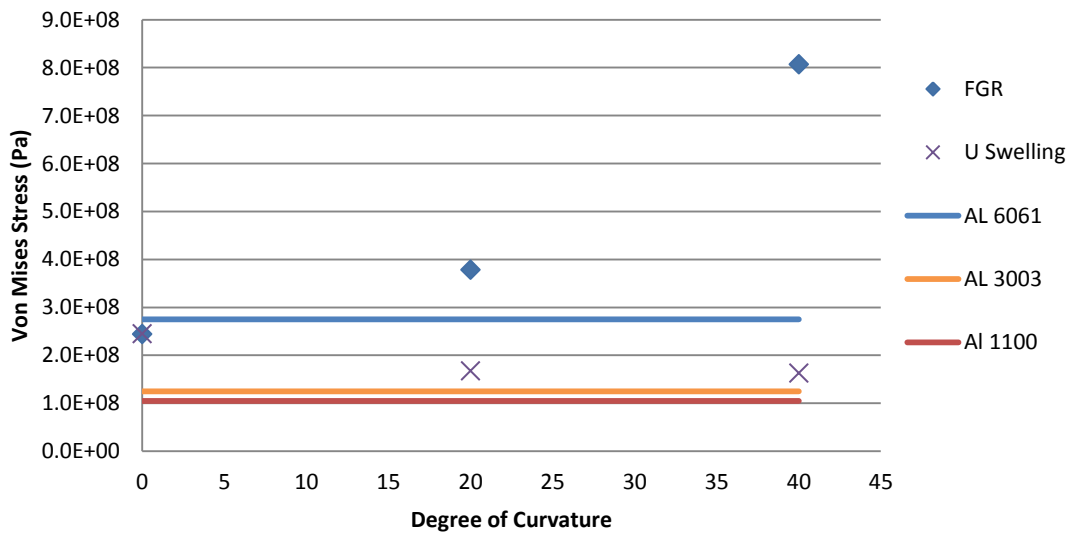
Figure 139. Corner decoupled von Mises stress

155
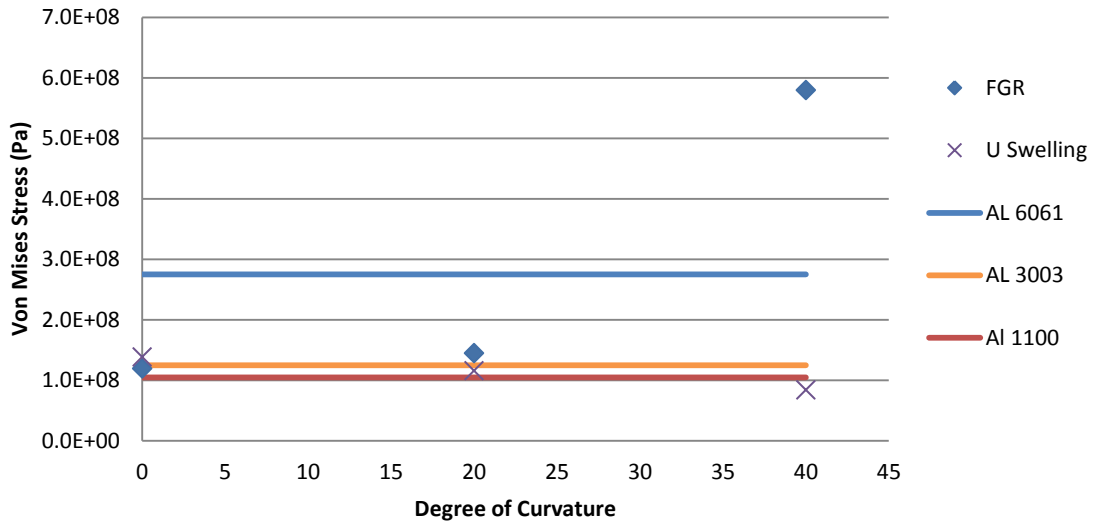
Figure 140. Side decoupled von Mises Stress
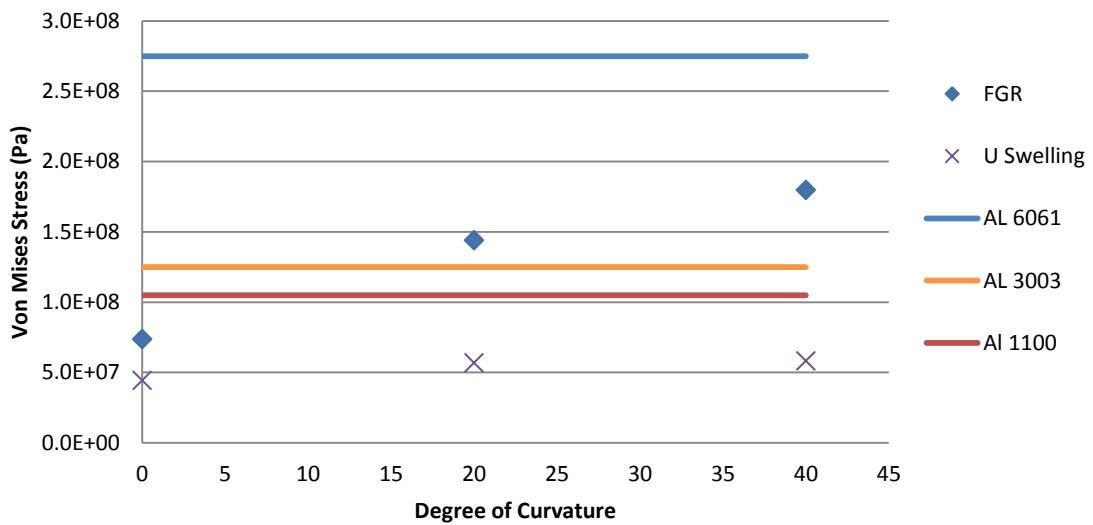
Figure 141. Center decoupled von Mises Stress

The plots indicate FGR will again have the greatest effect on the target and the von Mises stress.

The results in this chapter give insights into several FGR and swelling trends. First, fission gas pressure and uranium swelling will, in all cases, create separation and von Mises stress values greater the non-FGR and non-swelling results. Second, FGR and swelling will increase both the separation and von Mises stress as curvature is increased,

opposite the previous trends in the top separation, corner von Mises, and side von Mises results. Third, von Mises stress will be greater than all alloy yield strengths at high FGR pressures. Fourth, contour plots indicate separation behaviors will be very different then the non-FGR and non-swelling results. Finally, contour plots indicate von Mises stress behaviors will be similar to the non-FGR and non-swelling results slight differences at high curvature values.

CHAPTER 12: PLATE EXPERIMENTAL ANALYSIS

The goal of the experimental setup is to validate the numeric models and gain insights into prototypical target behaviors. During irradiation target power levels could be in the 30 kW range. Reaching 30kW with the available laboratory voltage and current capacities is impossible. Based on available voltage and current capacities a goal of 5 kW was established.

Heater and Surrogate Target

A resistance heater placed between two aluminum plates simulated the LEU foil heat source. The aluminum plates were welded on three edges and a portion of the fourth edge creating partially enclosed environment. Providing interfacial heating without adversely affecting target behavior during testing was one of the greatest challenges. A search began for a commercial heater equivalent to the LEU foil dimensions that could deliver 5kW. After an extensive search a practical commercial heater could not be located and a custom heater would need to be manufactured.

The first custom heater design used tungsten wire but quickly moved to a material more suited for heater applications. Nichrome 80 is commonly used for resistive heater applications. Initial designs using Nichrome 80 utilized a single flatted wire creating a larger heater surface area. A diagram of an earlier design can be seen in Figure 142. Thermocouples were placed near the heater wire in the Kapton film and used to detect possible separation. The thermocouples were bare wire type K thermocouples with a wire diameter of 0.003". A spike in temperature indicates an increase in thermal resistance

meaning separation could be occurring. Powers with this design reached approximately

2.4 kW but did not reach the goal 5 kW due to premature failure.
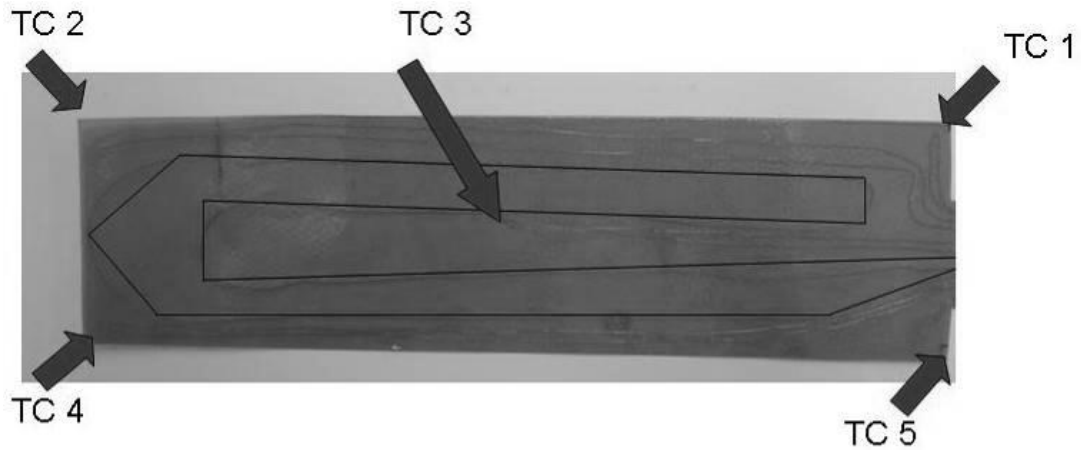
Figure 142. Earlier heater design with thermocouple locations [23]

A post heating examination determined failure occurred because of the high

concentration of energy on the relativity small surface area of the flatted wire. The

damaged heater from the 2.4 kW run can be seen in Figure 143 showing failure was

located on the wire.
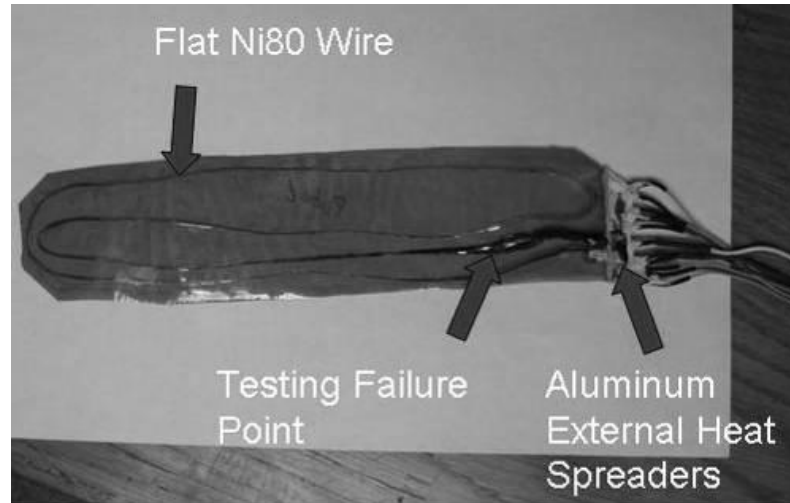
Figure 143. Damaged heater from the previous 2.4 kW experiment [23]

Increasing the surface area of the heater was the goal of the next design iteration.

Nichrome 80 was again used as the heating element but a new manufacturing method was

used to create the heater. The heater was milled from a sheet of Nichrome 80, 0.25 mm

thick. The new design was wrapped in Kapton to prevent shorting between the heater and

the cladding. An image of the new channel heater in Kapton can be seen in Figure 144.

Thermocouples were placed at five points within the heater footprint to detect separation

between the plates. Wiring for the thermocouples and the power to the heater were

delivered to the surrogate target through the un-welded end.
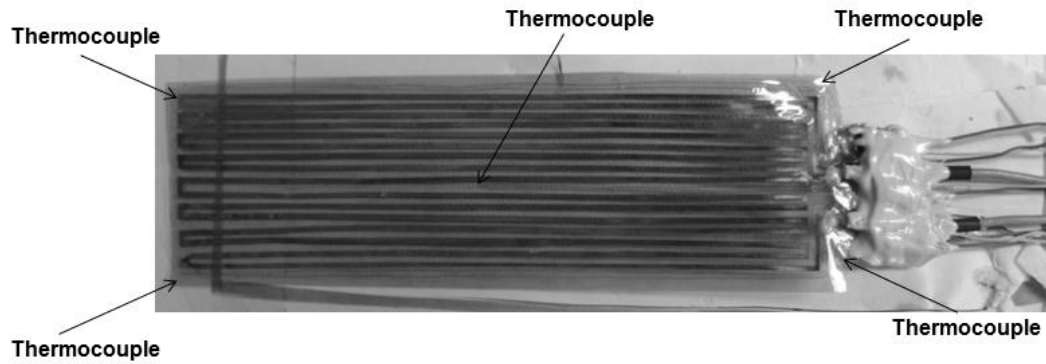
Figure 144. New channel heater design

The heater was placed between two Al 6061 plates with a nominal thickness of

0.001 m and welded using a TIG welder. The excess heat from the welding process was

removed from the target by placing blocks of aluminum on each side of the target. The

whole structure was clamped together with C-clamps putting the target in compression.

The dimensions of the heater, the cladding, and the thermocouple locations can be seen in
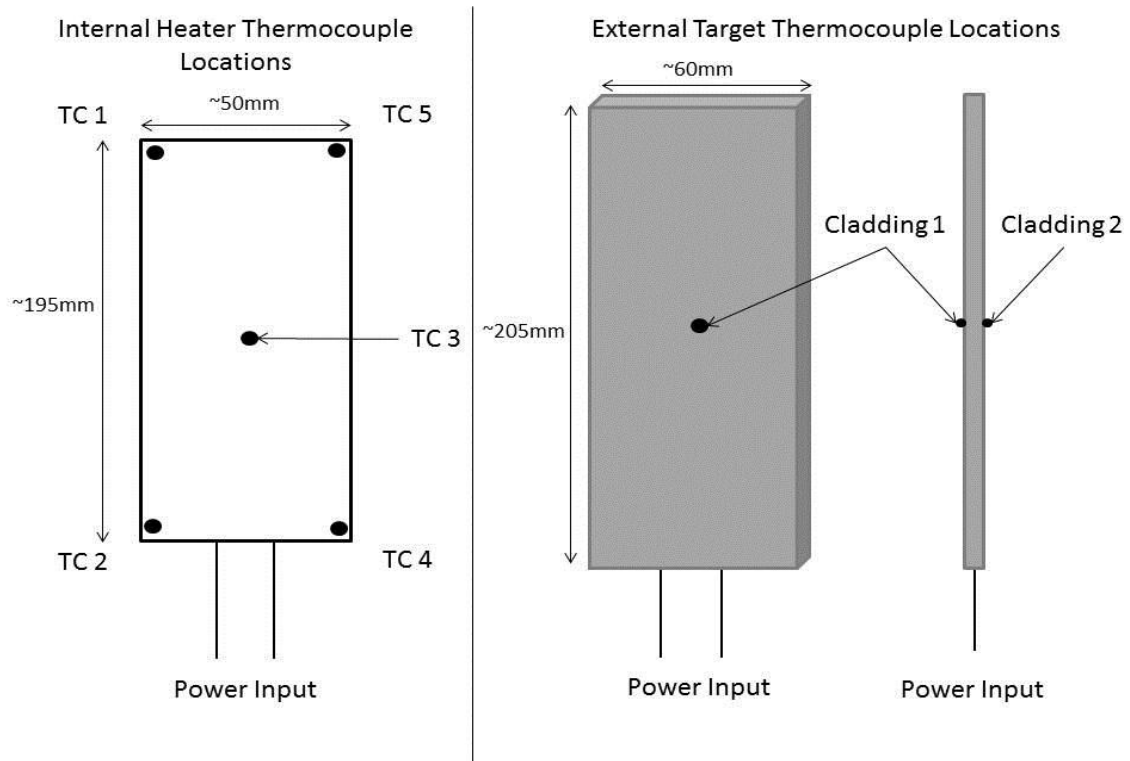
Figure 145.

Figure 145. Internal heater and external cladding thermocouple locations

Flow Loop

      The purpose of the flow loop was to provide cooling to the surrogate target and collect data. The surrogate target containing the thermocouples and power wiring is mounted in a test section. The test section was designed to hold the target for cooling and to pass the thermocouple and power wiring to the outside environment. An image of the welded surrogate target mounted in the test section can be seen in Figure 146.
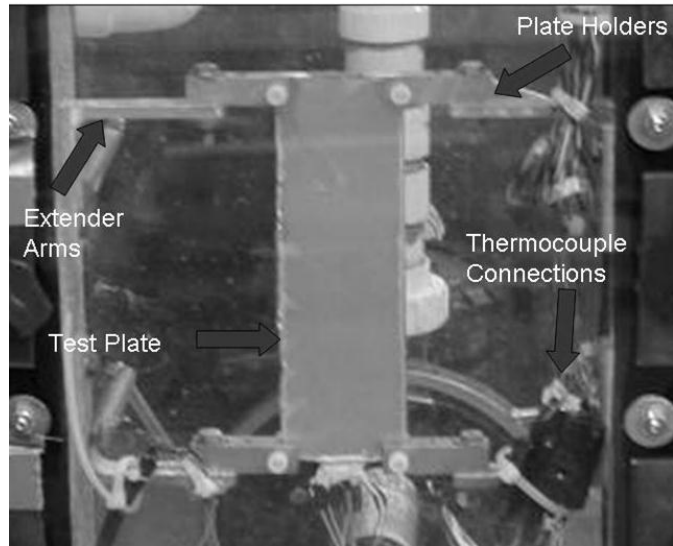
Figure 146. Test section with surrogate plate

Cooling water was provided to the test section through the water inlet and outlets from a pump situated next to the test section which can be seen in Figure 147.
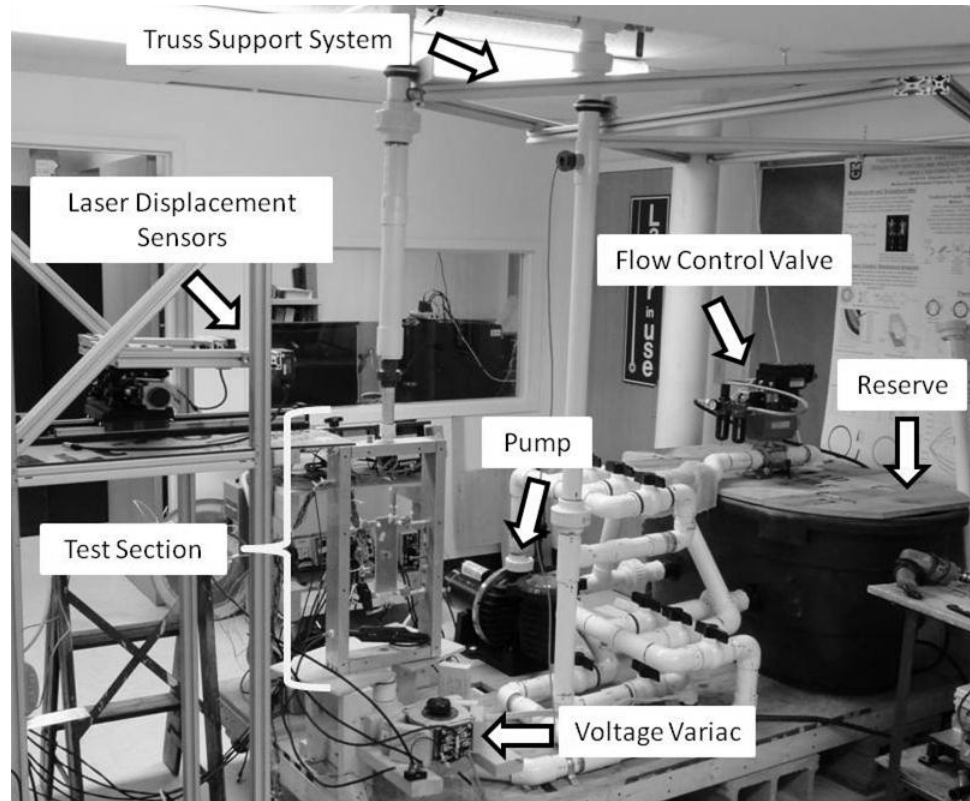
Figure 147. Missouri flow loop with labeled components

The flow loop has a 1 1/2 horsepower constant frequency driven pump which draws and circulates water from a 100 gallon reserve. The pump is capable of reaching flow rates ~3 kg/s and through piping has the ability to place the test section in both a positive and negative pressure environment. A paddle sensor monitors coolant flow and temperature. A variac was used to manually control the voltage supply to the target and a Kiethley data acquisition system was used to acquire temperature and water flow data during testing.

Shakedown Testing

During initial testing, voltage readings across the shunt resistor were questionable. Investigations revealed voltage was leaking from several locations on the loop. The milling process used to create the heater left many burrs on the heater edges. The heat and pressure used during welding allowed the burrs to penetrate through the Kapton causing a short with the heater and the cladding. A diagram showing this can be seen in Figure 148. Efforts were made to remove the burrs and the target was reassembled.
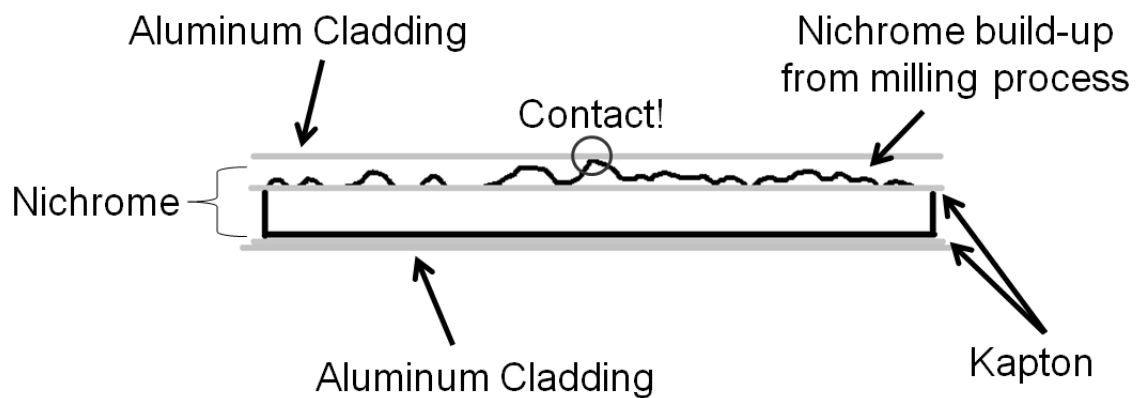
Figure 148. Heater and cladding short

Experimental Results

Low power was first performed to insure issues found during shakedown testing had been resolved. Approximately 200 W at 40 V was applied to the target. The temperatures recorded at steady state along with the power can be seen in Table 31.

Table 31. Steady state power and temperature measurements at low power

Power (W)	TC1 (°C)	TC2 (°C)	TC3 (°C)	TC4 (°C)	TC5 (°C)
205.1	22.0	22.4	26.7	22.6	21.8

The low power test indicated shorting issues had been resolved during shakedown testing. The results appeared reasonable and added confidence in moving forward with a high power test.

Temperatures were recorded at several locations during the high power test. Temperatures monitored during the test were located inside the target, outside the target, and in the cooling water flow. The results from the internal thermocouples, along with the location of each, can be seen in Figure 145 and Figure 149. Plots of each thermocouple temperature reading can be seen in Appendix 3.
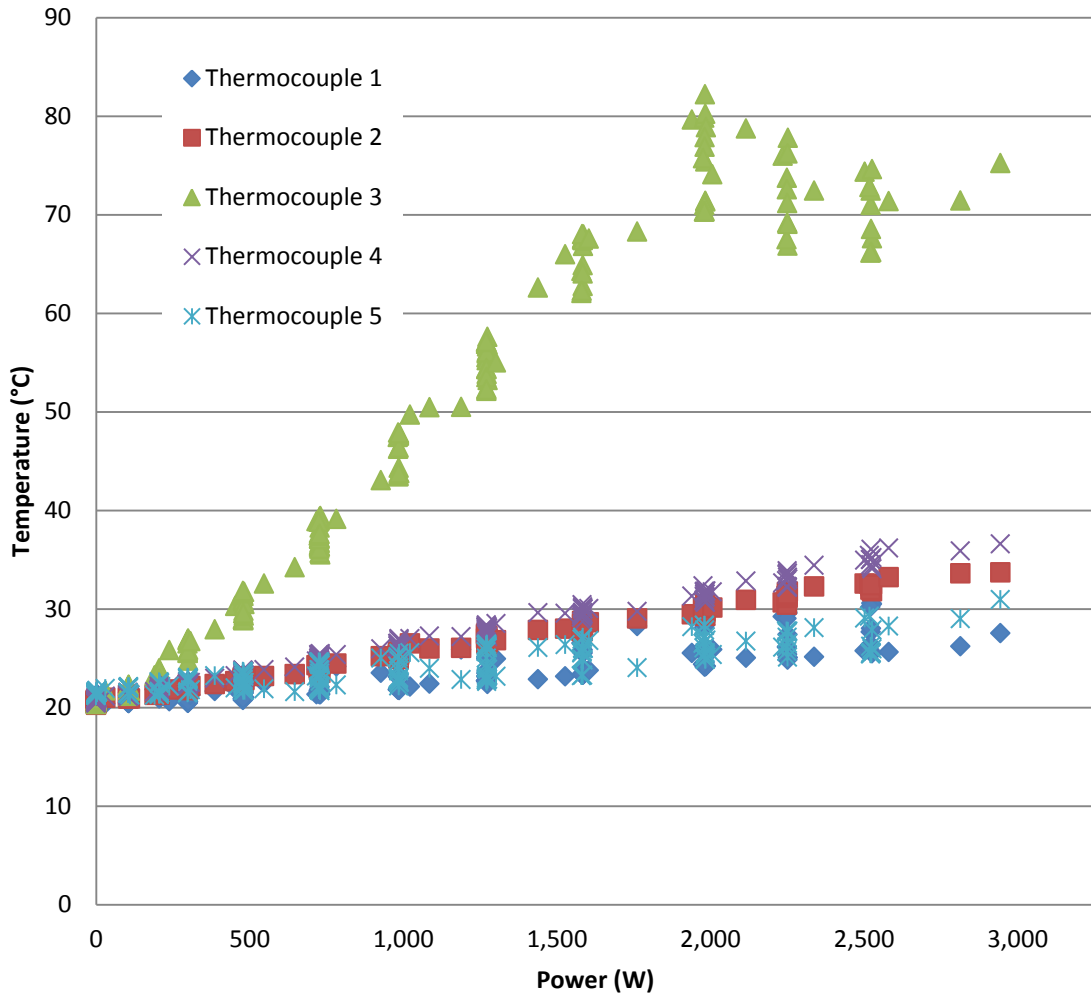
Figure 149. Internal Thermocouple temperatures compared to power

The results indicate all temperatures increased with an increase in power. The thermocouple located at the center experienced the greatest temperature reaching a maximum of approximately 80 °C. All other thermocouples were in the 25 °C to 35 °C range at their maximum. The maximum power reached during the test was approximately 3 kW. A summary of the temperatures recorded at 3kW can be seen in Table 32.

Table 32. Power and the temperatures recorded at that point

Power (W)	TC1 (°C)	TC2 (°C)	TC3 (°C)	TC4 (°C)	TC5 (°C)
2944.0	27.5	33.7	75.2	36.6	30.9

Temperatures were also collected from the center of the cladding and the test section exit water temperature along with flow rate. A plot of the cladding temperatures can be in Figure 150 and the exit flow temperature can be seen in Figure 151.
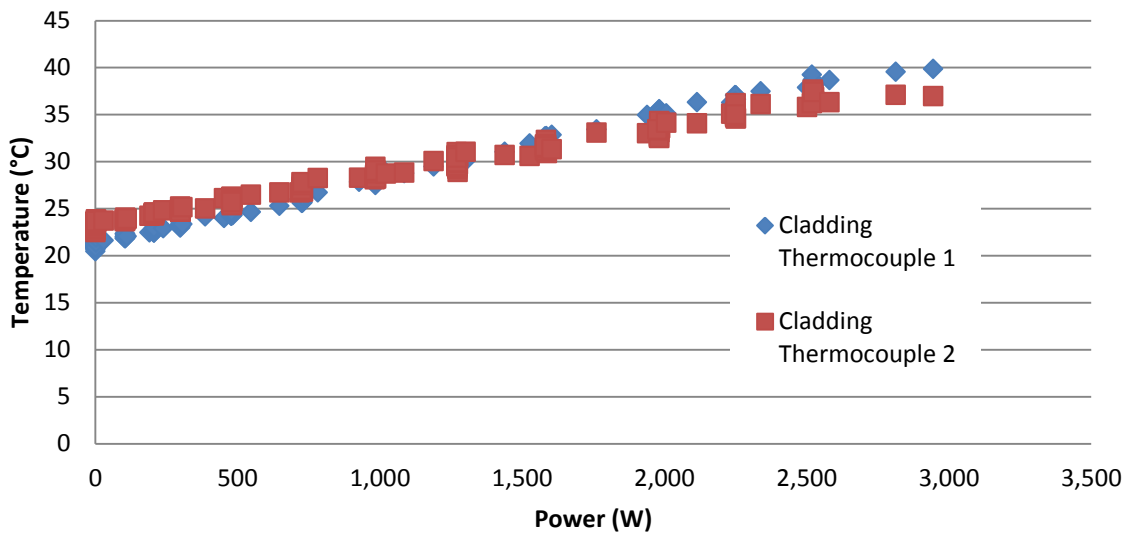
Figure 150. Cladding thermocouple temperatures
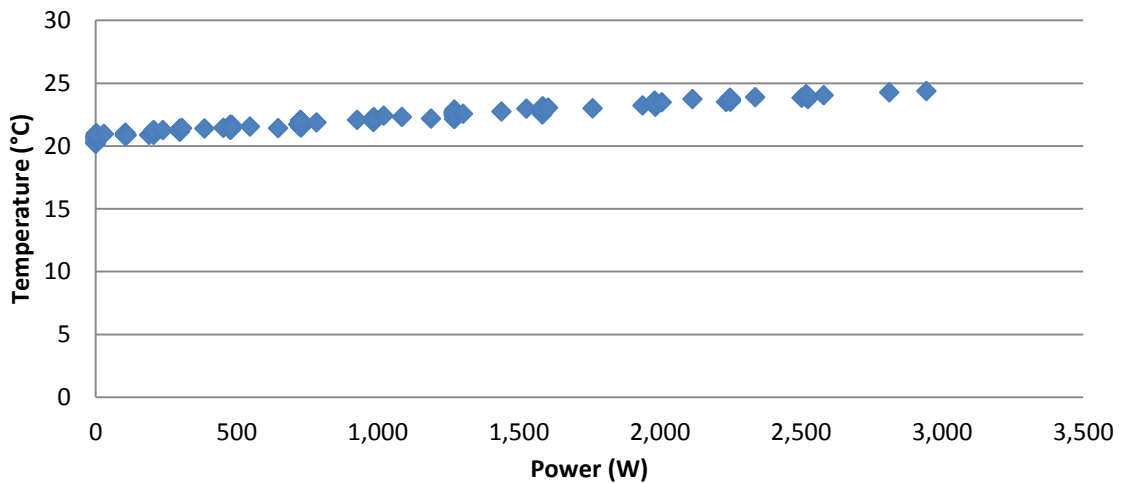
Figure 151. Test section exit water temperature

The cladding temperatures will increase but not they do not approach the temperature of the internal center thermocouple. The water experiences a slight increase in temperature through heating from the pump and the target. A summary of the temperatures at the maximum power can be seen in Table 33.

Table 33. Cladding temperatures, exit water temperature, and flow rate.

Power (W)	Cladding 1 (°C)	Cladding 2 (°C)	Exit (°C)	Flow Rate (kg/s)
2944.0	39.9	37.0	24.4	1.5

Post-Test Target Examination

The target failed shortly after reaching the 3 kW power reading and all temperature measurements began to fluctuate. The target was removed from the test section after the experiment was complete. An initial examination of the target indicated some outward expansion in the target in the form of pillowing. The welded edges of the target were removed and the internal heater examined. Images of the heater after use can be seen in Figure 152, Figure 153, and Figure 154.
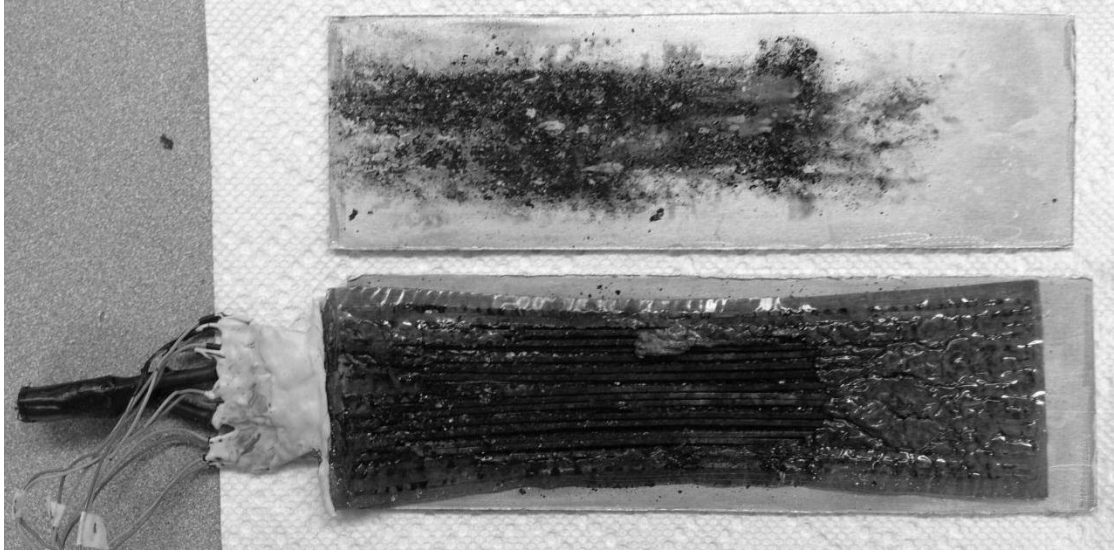
Figure 152. Post-test heater examination
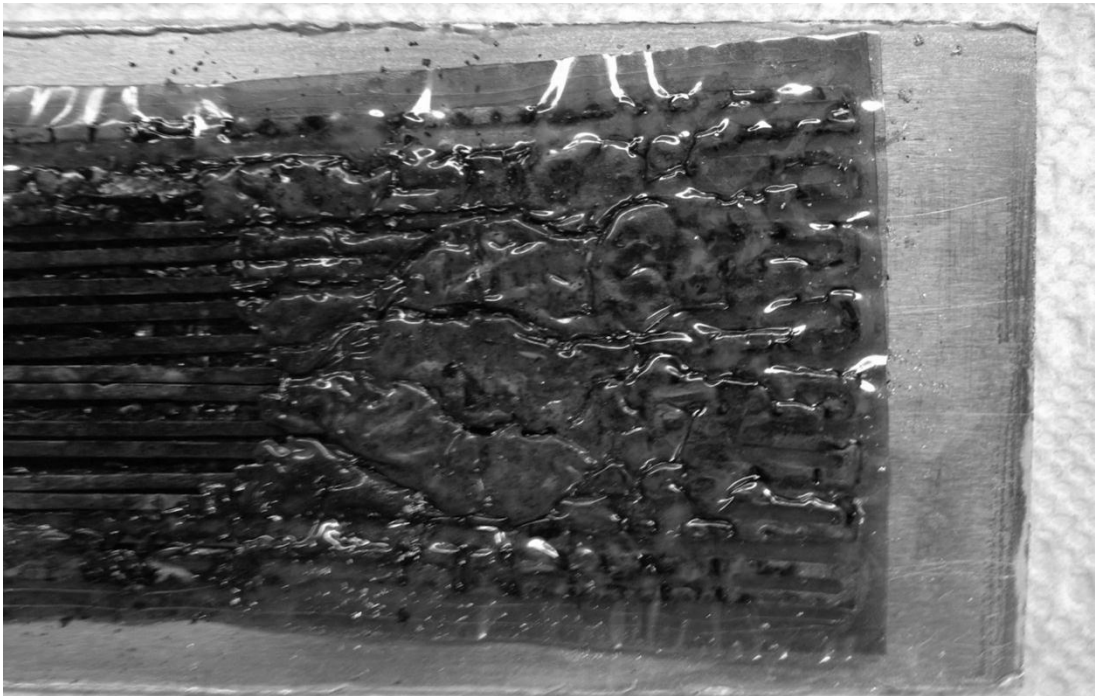
Figure 153. Post-test close-up of bubbled Kapton
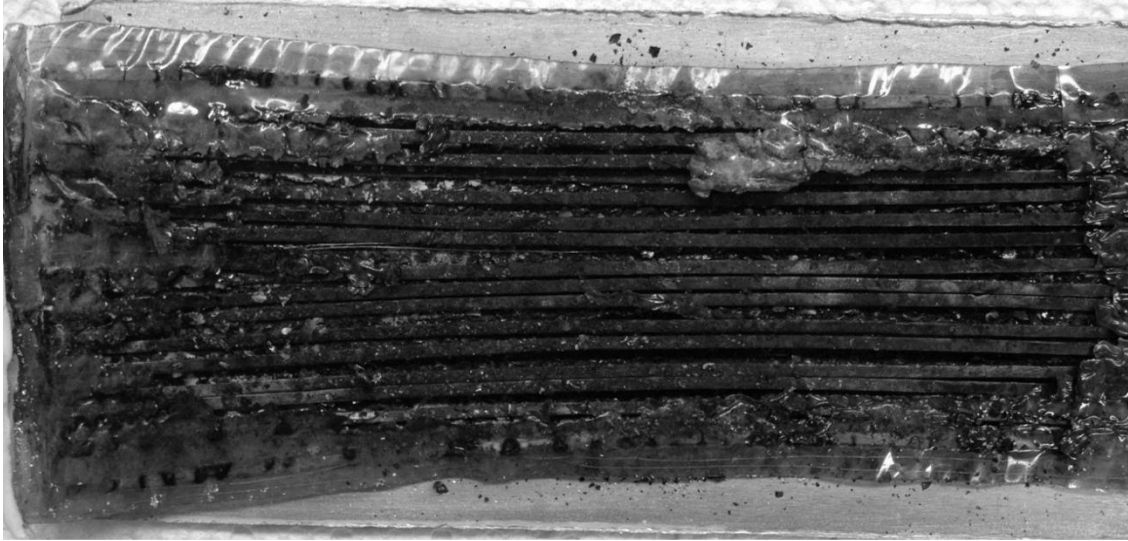
Figure 154. Post-test close-up of completely damaged Kapton

It is clear the heater was significantly damaged during testing. Kapton in the central part of the heater was completely destroyed, exposing the heating element to the aluminum cladding. It is believed the Kapton failed soon after 3 kW was reached, when the temperature measurements began to fluctuate. Figure 152 shows the heater has changed in shape from a rectangular profile to an hourglass profile. During testing the heater along with the Kapton expanded, when the power decreased the temperature decreased and the heater retracted. The damaged Kapton allowed the heater to shrink into its current form. During manufacturing air was trapped in the heater and during testing the air expanded creating bubbles in the Kapton, an example of which can be seen in Figure 153. The air trapped in these bubbles increases the thermal resistance thus increasing the temperature of the heating element. The increased temperature experienced during bubbling can be seen in Table 32, where thermocouple three, which was located in the center, experienced the greatest temperature. Thermocouples located on edges did not experience significant bubble development and had lower temperatures.

171

The exposed heater can be seen in Figure 154 where the Kapton has been completely destroyed. The heating element shows little damage from the test, indicating the Kapton, not the element, was the main failure mode. Finally, all the figures show scorching and melting occurring over a large area of the target. Previous heater designs experience this behavior in a much more concentrated area such as the heater in Figure 143. This design distributes the energy much more effectively over a larger area of the target.

Thermal Resistance through the Target

Thermal resistance through the center of the target was determined using temperature data from thermocouple 3, the cladding temperature thermocouple, and the recorded power data. The thermal resistance as a function of power can be seen in Figure 155.
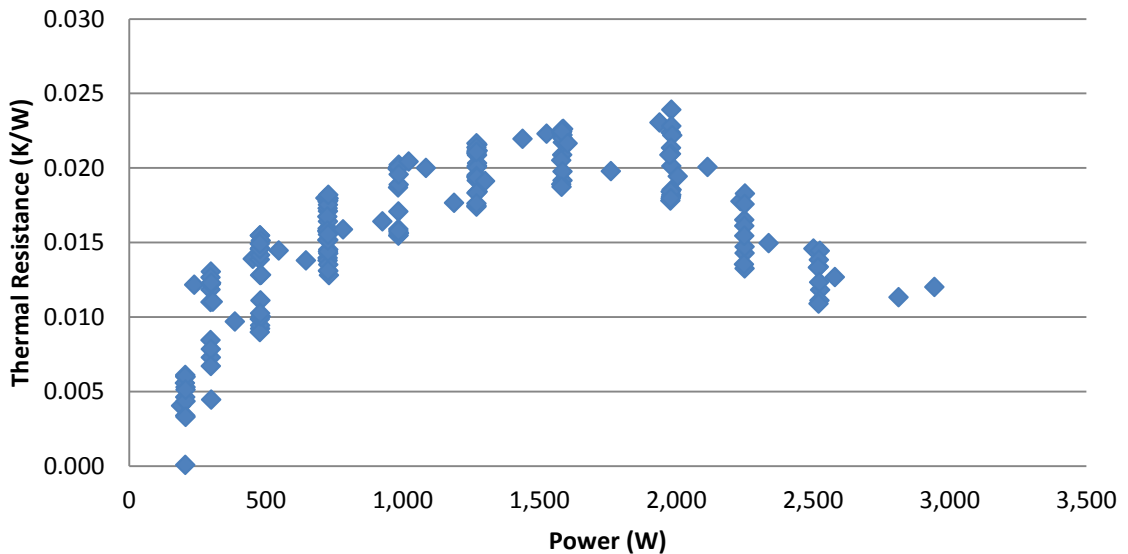
Figure 155. Thermal resistance through the center of the target

The thermal resistance increases but then decreases at approximately 2,000W. The steady increase in the thermal resistance indicates separation is occurring in the target. The sharp decrease in thermal resistance indicates a failure, of the Kapton, in the central section of the heater before the much more substantial heater failure at approximately 3,000W. The thermal resistance was also examined on a corner of the target where no Kapton failure occurred and can be seen in Figure 156.
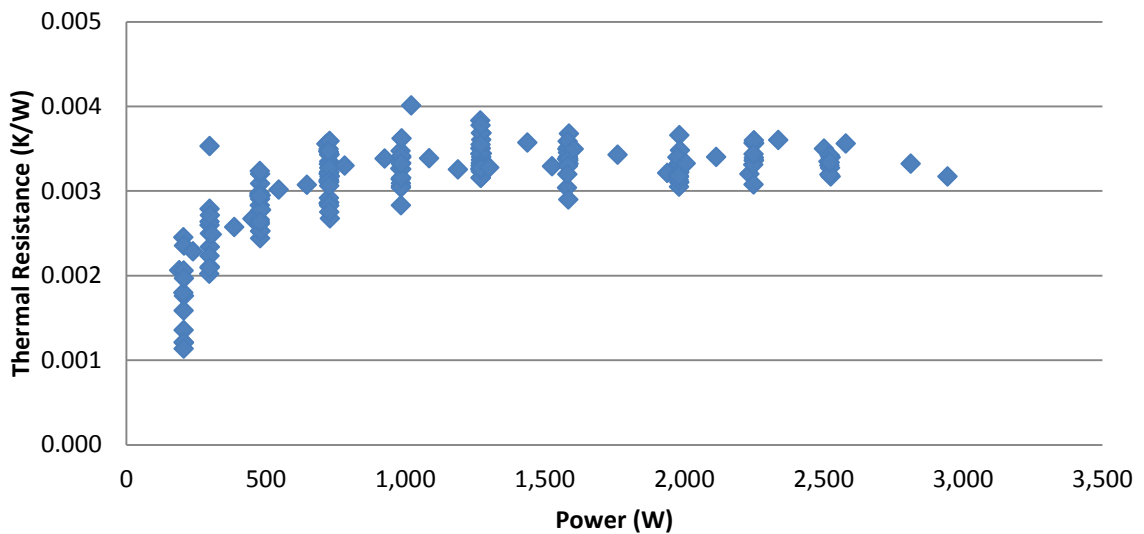
Figure 156. Thermal resistance through a corner on the target

The corner thermal resistance increases throughout the majority of the experiment and levels off toward the end, without experiencing the decrease seen at the center. The post-test examination indicated heater failure at the center and not at the corners. The steady increase and leveling of the thermal resistance at corner without Kapton failure adds further confidence the decrease at the center was the beginning of heater failure. The magnitude of the corner resistance is lower than the center as well. This is consistent with the bubbling and pillowing seen in the target center after heating.

The experimental thermal resistances were compared to the theoretical target operating thermal resistance. The assumed operational values can be seen in Table 34.

Table 34. Thermal resistance assumed operational values

Maximum Internal Target Operating Temperature (K)	Maximum External Target Surface Temperature (K)	Comparison Power (W)
430	373	2944

The calculated operational thermal resistance is 0.0194 K/W. A comparison of the maximum experimental thermal resistances and the operational thermal resistance can be seen in Table 35.

Table 35. Thermal resistance comparison

Maximum Experimental Center Thermal Resistance (K/W)	Maximum Experimental Corner Thermal Resistance (K/W)	Operational Thermal Resistance (K/W)
~0.024	~0.0038	0.0194

The corner thermal resistance is much lower than the operational thermal resistance but the center is slightly larger, indicating the location of possible failure will be located in the center of the target.

Experimental and Numerical Model Comparison

Temperatures from the high power experiment were compared to the numerical modeling temperatures. A heat transfer coefficient was estimated from the recorded mass

flow rate and the dimensions of the test section. An external parallel flow model was used to determine the heat transfer coefficient at approximately 783 W/m^{2}K. Temperatures from the free non-uniform heating without foil models at 1,000W and 5,000W with a heat transfer coefficient of 1,000W/m^{2}K were used for the comparison. The temperatures in the center of the target can be seen in Table 36.

Table 36. Experimental and numerical comparison

Experimental (°C)	Q = 1000W h = 1000W/m^{2}K (°C)	Q = 5000W h = 1000W/m^{2}K (°C)
75.2	96.8	127.3

The numerical temperatures are higher than the experimental at both lower power and higher power. The estimation of the heat transfer coefficient is based on a several assumptions. The velocity was determined using the cross section of the test section. The velocity of the water exiting the inlet on the test section is much higher than the calculated value, further the velocity moving over the plate is noticeably faster than the rest of the water in the test section. The higher velocity flow over the target will produce a heat transfer coefficient which is greater than 783W/m^{2}K. The increased heat transfer coefficient will in turn decrease the temperature in the target and lead to the lower temperature seen in the experimental results.

The results in this chapter show improvement in the experimental design with a thermal load of 3kW; but the goal of 5kW was not reached. Temperatures seen during testing were highest at the target center and lowest on the target edge which is consistent with the heater failure location. The new design successfully spread the heater energy over a larger surface area but an unexpected drawback of this design was the introduction

175

of air in the heater. During testing the air expanded causing bubbles to form in the heater, increasing the thermal resistance and thus increasing the temperature. Areas without bubbling experienced an increase in thermal resistance, leveled off, and did not fail. Finally, a comparison of the experimental and the numerical results show agreement but the experimental results are lower than the numerical results. The assumptions used to calculate the heat transfer coefficient produce a lower velocity then is experienced by the target during testing. The higher heat transfer coefficient would explain the lower temperatures seen in the experimental results. Future designs should focus on reducing the amount of air trapped in the heater during assembly; this could be achieved by building the heater in a vacuum environment.

CHAPTER 13: CONCLUSIONS AND RECOMMENDATIONS

Molybdenum-99 diagnostic imaging is the most commonly practiced procedure in nuclear medicine today with the majority molybdenum-99 produced with proliferation sensitive HEU. International and domestic efforts to develop non-HEU production techniques have taking the first steps toward establishing a new non-HEU molybdenum-99 based supply chain. The focus of the research presented in this work is on the analysis of a new high U-235 density LEU based molybdenum-99 production target. Converting directly to LEU using current manufacturing techniques greatly reduces the molybdenum-99 yield per target making high volume production uneconomical. The LEU based foil target analyzed in this research increases the yield per target making economic high volume production with LEU possible.

The research analyzed the thermal-mechanical response of an LEU foil target during irradiation. Thermal-mechanical studies focused on deflections and stresses to assess the probability of target failure. Simpler analytical models were first used to determine the proper shape of the target, benchmark the numerical modeling software, and determine the relationship between plate thickness and deflection. A non-dimensionalized simply supported model, determined a thin square target would produce the greatest amount of deflection and a thick rectangle would produce the lease. Further, the relationship between non-dimensionalized deflection, thickness, and aspect ratio is nonlinear. During numerical model benchmarking the optimal settings were, a global spacing of 0.001, seven elements through the thickness of each plate, and an 8-node thermal coupled brick with reduced integration. In practice it is assumed a denser mesh will produce better matching between analytical and numerical model results. The

benchmarking study indicated this behavior was untrue and differences between the two models increased when mesh density was increased beyond the optimal settings. Finally, it was determined an increase in thickness does not guarantee a reduction in deflection. Using the simply supported model it was found thickness will have the same effect on both the thermal moment, causing the deflection, and the stiffness of the plate, essentially canceling out the effects of thickness.

Numerical studies using Abaqus focused on analyzing various heating and cooling conditions, the effects of various holding conditions, and assessing the effects of curvature on a foil type target. The uniform heating study concluded an increase in thermal load would increase the deflection and stress, linearly. Further, the holding conditions applied will greatly affect the target's thermal-mechanical response with the free edge holding condition producing the lease amount of both deflection and stress. The results from the uniform heating study were expanded upon in a more prototypical non-uniform heating situation. The non-uniform heating study further confirmed the linear behavior between thermal load, deflection, and stress. It again indicated the free edge holding condition will produce the lease amount of deflection and stress. Finally, the greatest deflections were seen in the center of the target and the greatest stresses were seen on the target edges where the plates were bonded.

Results from previous studies were built upon by introducing a uranium foil, curvature, the effects of fission gas pressure, and uranium swelling creating a more prototypical model. The foil target study concluded that introducing curvature would decrease the center separations to the nanometer scale. Large separations were observed on the top and side locations but the small amount of energy passing through these foil

faces reduces the chance these separations will cause target failure. Fission gas release and uranium swelling were applied to the foil targets as well. When combined and added to the models in the worst case fission gas release scenario, there is a substantial increase in both deflection and stress. A decoupling of the two indicated fission gas release will dominate the effects between these two, during simulated irradiation.

Experiments were performed to simulate low power heating and further benchmark the models. The new channel heater effectively increased the heater surface area but the new heater manufacturing method trapped a large amount of air in the heater. During heating the air expanded, increasing thermal resistance and thus increasing the temperature leading to target failure. Benchmarking of the numerical models showed decent matching. Finally, a comparison of the operational thermal resistance and experimental target thermal resistance indicated the experimental target thermal resistance was near the optional resistance.

In conclusion the results from all of these analyses indicate a LEU foil target could survive irradiation, but there are several analysis areas that could be improved upon in future studies. First, the addition of manufacturing stresses in the Abaqus model. All the results in this research assume the target is placed in the reactor in an unrealistic stress free state. Models should begin to incorporate these stresses and assess their effects on the thermal-mechanical separation and stress. Second, the models could benefit from the addition of plastic and temperature dependent material properties. These properties will further push the models toward simulating more prototypical behavior. Third, the models should incorporate the nickel fission recoil barrier. Additional separations could occur between this additional layer and will increase the thermal resistance through the target.

This will in turn increase the temperature of the foil and could lead to target failure. Fourth, the effects of fission gas pressure and uranium swelling should be examined in more detail. This research established the proper techniques for analyzing these and has shown they will affect the separation and stress in the target. The data collected from the Pitesti experiments should be integrated into the Abaqus models using the new techniques and large parametric studies performed. Fifth, fission gas release and uranium swelling techniques should be applied to the annular target design and a set of parametric studies performed to compare the flat, curved, and annular target designs. Finally, experimental tests should attempt to increase the power beyond 3kW and move closer to original goal of 5kW. Also, strain gauges or the laser displacement system should be used to extract direct deflection data from the experimental target during heating.

VITA

Kyler Turner is originally from Lee's Summit, MO and graduated in 2003 from Lee's Summit North High School. He began studying Mechanical Engineering at the University of Missouri the following fall and graduated with a BS in Mechanical Engineering in 2007. Soon after he began perusing an MS in Mechanical Engineering under the supervision of Dr. Gary Solbrekken working on the development of a novel approach to produce the radioisotope molybdenum-99 using low enriched uranium. Upon graduating in 2009 with an MS in Mechanical Engineering he continued to support the molybdenum-99 project by pursuing a PhD in Mechanical Engineering and completing a MS in Nuclear Engineering in 2009. Kyler has held fellowship and intern positions with the Department of Energy's National Nuclear Security Administration in Washington, DC, the Department of Defense's Defense Threat Reduction Agency in Washington, DC, and the Y-12 National Security Complex in Oak Ridge, TN in support of nuclear nonproliferation. Kyler's immediate family resides in Kansas City, MO and his brother is in Columbia, MO pursuing a MS in Civil Engineering at the University of Missouri.

REFERENCES

[1]   R. W. Williams, "Technetium-99m Production from Uranium-235 Fission," Master of Science, University of Missouri, Columbia, 1976.

[2]   G. B. Saha, *Fundamentals of Nuclear Pharmacy*, 5th ed. New York, New York: Springer, 2004.

[3]   A. Sonzogni. (2011). *Chart of Nuclides*. Available: http://www.nndc.bnl.gov/chart/

[4]   Stefan, "Technetium-99," in *Back Reaction* vol. 2011, ed, 2008.

[5]   I. Zolle, *Technetium-99m Pharmaceuticals: Preparation and Quality Control in Nuclear Medicine*. New York: Springer, 2007.

[6]   W. Miller, "Title," unpublished|.

[7]   "Medical Isotope Production Without Highly Enriched Uranium," N. R. C. o. T. N. Academies, Ed., ed. Washington, DC: The National Academies Press, 2009.

[8]   D.-H. M. Center. *45 year old female with a history of chronic renal failure* Available: http://www.dhmc.org/webpage.cfm?site_id=2&org_id=72&morg_id=0&sec_id=0&gsec_id=1508&item_id=36594

[9]   S. Stiles. (2007, 3/10/11). *Fusion Power: Integrated CT angiography, perfusion imaging makes progress*. Available: http://www.google.com/imgres?imgurl=http://www.theheart.org/displayItem.do%3FprimaryKey%3D795303%26type%3Dimg&imgrefurl=http://www.theheart.org/article/795453.do&usg=__IGUhknpmgnkwmZL-Wc6xy1Q0gds=&h=263&w=350&sz=22&hl=en&start=0&sig2=FAgD9lg0HT0xcWiFvHKN2g&zoom=1&tbnid=GwBwSnWsZ7F4VM:&tbnh=142&tbnw=189&ei=g0V5Tb7sNMa2qwHWyZmVBg&prev=/images%3Fq%3DMyocardial%2Bperfusion%2Bimaging%26um%3D1%26hl%3Den%26sa%3DN%26rls%3Dcom.microsoft:en-us:IE-SearchBox%26rlz%3D1I7WZPC_en%26biw%3D1899%26bih%3D884%26tbs%3Disch:1&um=1&itbs=1&iact=rc&dur=294&oei=g0V5Tb7sNMa2qwHWyZmVBg&page=1&ndsp=49&ved=1t:429,r:0,s:0&tx=61&ty=72

[10]   G. S. T. a. J. Maddahi, "The Technetium Shortage," *Journal of Nuclear Cardiology,* vol. 17, pp. 993-998, 2010.

[11]   C. N. FAQ. *Image of MAPLE Reactors and NRU*. Available: http://www.nuclearfaq.ca/cnf_sectionH.htm

[12]   G. F. V. a. L. Jollay, "Developing a US Supply of Mo-99 Using Low Enriched Uranium," presented at the ANS WInter Meeting 2010, Las Vegas, NV, 2010.

[13]   P. Staples, "Director of the Office of European and African Threat Reduction," ed.

[14]   R. Hamiltion, "Mo-99 Program Manager," ed, 2011.

[15]   J.-M. Vanderhofstadt, "The LEU conversion project of IRE," in *Mo-99 Topical Meeting* Santa Fe, NM, 2011.

[16]   N. N. S. Administration, "United States, Belgium, France, and The Netherlands Announce Joint Statement On HEU Minimization And The Reliable Supply Of Medical Isotopes," ed. http://nnsa.energy.gov/mediaroom/pressreleases/usbfnmediso32612, 2012.

[17]   J. L. Snelgrove. (April 20, 2011, Qualification Status of 6-gU/cm3 U3Si2 Dispersion Targets for 99Mo Production. Available: http://www.iaea.org/OurWork/ST/NE/NEFW/RRS/documents/mo99/SNELGROVEusilicide2011.pdf

[18]   I. C. L. C.K. KIM, K.H. KIM, H.J. RYU, J.M. PARK, S.J. CHOI, "RECENT ACTIVITIES OF KAERI RELATED TO FISSION MO-99," presented at the Mo-99 Topical Meeting, Santa Fe, NM, 2011.

[19]   M. S. S. C.K. KIM, S.J. CHOI, I.C. Lim, J.M. PARK, , "Recent Activities of KAERI Related to Fission Mo-99," in *Mo-99 Topical Meeting*, Santa Fe, NM.

[20]   Y. K. George F Vandegrift, Hector Cols, Cliff Conner, Scott Aase, Magdalin Peter, David Walker, Ralph A Leonard, James L Snelgrove, "PRODUCTION OF MO-99 FROM LEU TARGETS BASE-SIDE PROCESSING," presented at the Reduced Enrichment for Research and Test Reactors, Las Vegas, Nevada, October 1-6, 2000.

[21]   G. L. S. Kyler K Turner, Charlie W Allen, "Thermal-Mechanical Analysis of Varying Boundary Conditions on a LEU Foil based Molybdenum-99 Plate

Processing Target," presented at the ASME International Mechanical Engineering Congress and Exposition, Vancouver, British Columbia, 2010.

[22]   P. B. J. M. Benneker, "Production of Molybdenum by Irradiation of Fissile Targets for Mallinckrodt Medical: Design and Safety Report," Petten, Netherlands May 15, 2002.

[23]   K. Turner, "THERMAL-MECHANICAL ANALYSIS OF TARGETS FOR HIGH VOLUME PRODUCTION OF MOLYBDENUM-99 USING LOW-ENRICHED URANIUM," M.S., Mechanical and Aerospace Engineering Department, University of Missouri, Columbia, MO, 2009.

[24]   J. Salacz, "Prodcution of FIssion Mo-99, I-131, and Xe-133," in *Fission Molybdenum Medical Use*, Karlsruhe, Germany, October 13-16 1987, pp. 129-132.

[25]   K. A. B. a. R. J. Harrison, "Deveolpment of the Mo-99 Process at CRNL," in *Fission Molybdenum For Medical Use*, Karlsruhe, Germany, October 13-16 1987, pp. 35-46.

[26]   P. Staples, "GTRI's Mo-99 Program," in *Mo-99 Topical Meeting*, Santa Fe, NM, 2011.

[27]   D. O. Energy. *Global Threat Reduction Initiative Highlights*. Available: http://www.energy.gov/media/ViennaGTRFactSheetFINAL1052604.pdf

[28]   NNSA. (2011, 3/14/11). *Office of Global Threat Reduction*. Available: http://nnsa.energy.gov/gtri

[29]   SNM. (July 8, 2010). *SNM Cautions that Canada's Chalk River Coming Back Online Will Not Solve Long-Term Isotope Shortage*. Available: http://www.snm.org/index.cfm?PageID=9853

[30]   O. f. E. C.-O. a. D. s. N. E. Agency, *The Supply of Medical Radioisotopes: The Path to Reliability*: Organisation for Economic Co-Operation and Development, 2011.

[31]   C. W. A. a. G. L. Solbrekken, "Feasibility Study - Part 2: Production of Fission Product Mo-99 Using the LEU-Modified Cintichem Process," University of Missouri, Columbia,MOMarch 2007.

[32] A. J. Y. S. Chemerisov, A. Hebden, N. Smith, P. Tkac, C. D. Jonah, J. Bailey, V. Makarashvili, B. Micklich, M. Kalensky, G.F. Vandegrift "Development of the mini-SHINE/MIPS experiments," presented at the Mo-99 Topical Meeting, Santa Fe, NM, 2011.

[33] D. E. G. T. A. Policke, S. B. Aase, D. Amaya and V. Wilkinson, "INVAP/B&W Mini-Loop Production of Mo-99," presented at the Mo-99 Topical Meeting, Santa Fe, NM, 2011.

[34] D. E. G. T. A. Policke, and S. B. Aase, "INVAP/B&W Mini-Loop Production of Mo-99," in *Mo-99 Topical Meeting*, Santa Fe, NM, 2011.

[35] P. W. Evans Reynolds, "BABCOCK & WILCOX MEDICAL ISOTOPE PRODUCTION SYSTEM STATUS," presented at the REDUCED ENRICHMENT FOR RESEARCH AND TEST REACTORS, Washington, DC, 2008.

[36] J. Berger, "GE Hitachi Nuclear Energy," in *Mo-99 Topical Meeting*, Santa Fe, NM, 2011.

[37] A. T. Jennifer Varnedoe , John Berger , Lin-wen Hu "Molybdenum-99 Generation Utilizing Existing Reactor Infrastructure," presented at the ANS Winter Meeting 2010, Las Vegas, NV, 2010.

[38] (2012). *NorthStar Medical Isotopes About Us*. Available: http://www.northstarnm.com/index.php?module=cms&page=8

[39] G. H. I. James T. Harvey, George P. Messina, and Scott D. Moffatt, "Domestic Production of Mo99," in *Mo-99 Topical Meeting* Santa Fe, NM, 2011.

[40] G. H. I. J. T. Harvey, G. P. Messina, and S. D. Moffatt, "Domestic Production of Mo99," presented at the Mo-99 Topical Meeting Santa Fe, NM.

[41] K. M. P. G.R. Piefer, E.N. Van Abel, T.R.Mackie, T.A. Heltemes, R.V. Bynum, T.T. Gribb, R.F. Radel, "Mo-99 Production with a Subcritical Assmebly," in *Mo-99 Topical Meeting*, Santa Fe, NM, 2011.

[42] K. M. P. G.R. Piefer, E.N. Van Abel, T.R.Mackie, T.A. Heltemes, R.V. Bynum, T.T. Gribb, R.F. Radel, "Mo-99 Production Using a Subcritical Assembly," presented at the Mo-99 Topical Meeting Santa Fe, NM, 2011.

[43] T. Ruth, "Direct production of Tc-99m including a Mo-100 supply," in *Mo-99 Topical Meeting*, Santa Fe, NM, 2011.

[44] G. Ball, "Conversion Experience Regarding Transition of 99Mo Production from HEU to LEU in South Africa," in *Mo-99 Topical Meeting*, Santa Fe, NM, 2011.

[45] C. P.-S. F Malouch, X Wohleber, P Durande-Ayme, "Enhancement of Irradiation Capabilities of Moly Targets in the Osiris Reactor," presented at the European Research Reactor Conference (RRFM), Rome, Italy, March 20-24, 2011.

[46] M. I. A. Mushtaq, Ishtiaq Hussain Bokhari, Tariq Mahmood,Tayyab Mahmood, Zahoor Ahmad, Qamar Zaman "Neutronic and thermal hydraulic analysis for production of fission molybdenum-99 at Pakistan Research Reactor-1," *Annals of Nuclear Energy,* vol. 35, pp. 345-352, 2008.

[47] J. Dix, "Mo-99 Project Manager," Mo-99 Discussions ed, 2011.

[48] B. H. Srinivasan, J.C. Johnson, G.K. Vandegrift, G.F. , "Development of dissolution process for metal foil target containing low enriched uranium," presented at the Reduced Enrichment for Research and Test Reactors, Williamsburg, VA, 1994.

[49] C. A. Gary Solbrekken, Lloyd Jollay, John Creasy, "Equivalent Fission Mo-99 Target without Highly Enriched Uranium," in *Mo-99 Topical Meeting*, Santa Fe, NM, 2011.

[50] G. L. S. Kyler K Turner, Charlie W Allen, "THERMAL-MECHANICAL ANALYSIS OF ANNULAR TARGET DESIGN FOR HIGH VOLUME PRODUCTION OF MOLYBDENUM-99 USING LOW-ENRICHED URANIUM," presented at the ASME 2009 International Mechanical Engineering Congress & Exposition, Lake Buena Vista, Florida, November 13-19, 2009.

[51] A. C. a. F. Ugural, S.K., *Advanced Strength and Applied Elasticity*. New York, NY: Elsevier, 1981.

[52] R. B. H. Naotake Noda, and Yoshinobu Tanigawa, *Thermal Stresses*, 2nd ed. New York, NY: Taylor & Francis, 2003.

[53] N. H. Asmer, *Partial Differential Equations with Fourier Series and Boundary Value Problems*. New York, NY: Prentice Hall, 2005.

[54]   D. P. D. Frank P. Incropera, Theodore L. Bergman, Adrienne S. Lavine, *Introduction to Heat Transfer*, 5th ed. Hoboken, NJ: John Wiley & Sons, 2007.

[55]   "LEU-Foil Target Development/Qualification Stakeholder Survey (IRE, Belgium)," International Atomic Energy AgencyAugust 24 - 27 2009 2005.

[56]   G. F. V. Jane D. Kwok, James E. Matos, "Processing of Low-Burnup LEU Silicide Targets," presented at the Reduce Enrichment for Research and Test Reactors, San Diego, CA, 1988.

[57]   G. Vandegrift, "Discussions on fission gas release from U-metal," ed, 2012.

[58]   I. A. E. Agency. (2012). *Chain Fission Yields*. Available: http://www-nds.iaea.org/sgnucdat/c1.htm

[59]   T. F. C. d. E. A. C. The Idaho National Engineering and Environmental Laboratory (INEEL), and The Massachusetts Institute of Technology (MIT), "Development Of Improved Models And Designs For Coated-Particle Gas Reactor Fuels: Final Report Under The International Nuclear Energy Research Initiative (INERI)," 12/2004 2004.

[60]   G. L. H. Yeon Soo Kim, "Fission Product Induced Swelling of U-Mo Alloy Fuel," *Journal of Nuclear Materials,* pp. 291-301, 2011.

[61]   A. R. Kaufmann, *Nuclear Reactor Fuel Elements: Metallurgy and Fabrication*. New York - London: Interscience Publishers, 1962.

[62]   X. J. Shurong Din, Yongzhong Huo, Lin an Li, "Reliability Analysis of Dispersion Nuclear Fuel Elements," *Journal of Nucler Materials* pp. 453-460, 2008.

[63]   S. G. a. A. Sesonske, *Nuclear Reactor Engineering: Reactor Design Basics*, Four ed. vol. One. New York: Chapman & Hall Inc. , 1994.

[64]   H. Ozaltun, "Disscussions on uranium swelling and simulation in Abaqus," K. K. Turner, Ed., ed, 2012.

APPENDIX 1: CHAPTER 4 MATLAB CODE

Matlab code to determine radial stress with internal heating on the cylinder

```matlab
clear
clc
format long g

%Material Properties and conditions
E=6.8947e10; %Youngs modulas Pa
pr=0.3; %posions ratio
alp=2.34e-5; %coeffiecent of thermal exspansion
k=180.073; %W/mK Thermal conductvity
h=21740;   %heat transfer coeffient
tinf=323; %temperature of the room K

%Cylinder Deminsions
a=0.01321; %inner radius
b=0.015075; %outer radius
r=0.01411;

%Heat flux
qflux=1000000; %Per unit area

%Mathmatica solution
tr1=((-a*b*log(qflux*a))/k)-((a*qflux*a^2)/(2*b*h))-
((tinf*a^2)/2)+((a*b*log(qflux*r))/k)+((a*qflux*r^2)/(2*b*h))+((tinf*r^
2)/2);
tr2=((-a*b*log(qflux*a))/k)-((a*qflux*a^2)/(2*b*h))-
((tinf*a^2)/2)+((a*b*log(qflux*b))/k)+((a*qflux*b^2)/(2*b*h))+((tinf*b^
2)/2);

stress_r_math=(E/(1-pr))*((-alp/r^2)*tr1+(((r^2-a^2)*alp)/(r^2*(b^2-
a^2)))*tr2);

%Solbrekken solution

qbar=(qflux*a)/k;
inv_bi=k/(h*b);
tr11=(tinf+qbar*log(b)+qbar*inv_bi+(qbar/2))*((r^2-a^2)/2)-
(qbar/2)*log((r^(r^2))/(a^(a^2))); %Temperature from the innner radius
to the desired position
tr22=(tinf+qbar*log(b)+qbar*inv_bi+(qbar/2))*((b^2-a^2)/2)-
(qbar/2)*log((b^(b^2))/(a^(a^2))); %Temperature from the inner radius
to the outer radius

stress_r=(E/(1-pr))*((-alp/r^2)*tr11+(((r^2-a^2)*alp)/(r^2*(b^2-
a^2)))*tr22)

strain_r=(1+pr)*alp*(tinf+qbar*log(b/r)+inv_bi)-
(((tinf+qbar*log(b)+qbar*inv_bi+(qbar/2))*((r^2-a^2)/2)-
((qbar/2)*log((r^r^2)/(a^a^2))))/r^2)

Temp_yo=tinf+(qbar*(log(b/r)+inv_bi))
```

Matlab code to determine radial stress with external heating on the cylinder

```
clear
clc
%Material Properties and conditions
E=6.8947e10; %Youngs modulas Pa
pr=0.3; %posions ratio
alp=2.34e-5; %coeffiecent of thermal exspansion
k=180.073; %W/mK Thermal conductvity
h=29306;   %heat transfer coeffient
tinf=323; %temperature of the room K

%Cylinder Deminsions
a=0.01321; %inner radius
b=0.015075; %outer radius
r=0.01411;

%Heat flux
qflux=1000000; %Per unit area

%Stress and Strain

qbar=(qflux*b)/k;
inv_bi=k/(h*a);

tr11=(tinf+qbar*log(a)+qbar*inv_bi+(qbar/2))*((r^2-
a^2)/2)+(qbar/2)*log((r^(r^2))/(a^(a^2)));
tr22=(tinf+qbar*log(a)+qbar*inv_bi+(qbar/2))*((b^2-
a^2)/2)+(qbar/2)*log((b^(b^2))/(a^(a^2)));

stress_r=(E/(1-pr))*((-alp/r^2)*tr11+(((r^2-a^2)*alp)/(r^2*(b^2-
a^2)))*tr22)

strain_r=((1+pr)*alp*(tinf+qbar*log(r/a)+inv_bi)-
(((tinf+qbar*log(b)+qbar*inv_bi+(qbar/2))*((r^2-a^2)/2)-
((qbar/2)*log((r^r^2)/(a^a^2))))/r^2))

Temp_yo=tinf+(qbar*(log(r/a)+inv_bi))
```

APPENDIX 2: CHAPTER 5 MATLAB CODE

Matlab code to create the 3-D profile

```
clear
clc

a = 1;%[0.01:0.01:.05];      % X Length, m
b = 1;        % Y Length, m
t = 0.001;    % Thickness, m
z = 0;        % Location in Thickness, m
E = 69e9;     % Young's Modulus, Pa
```

```matlab
v = 0.33;        % Poisson's Ratio, Dimensionless
alpha = 23e-6;   % Coef. of thermal expansion, 1/K
dT = 230;     % Temperature differential across plate, K
wo = 0;          %Intial Deflection

div=39; %Number of divsions along the x and y axis (1 minus of what is
desired)


%Model Profile

hstar=t/a;

% First Plotting Loop moveing along the Y-axis
x = 0:a/div:a;   % m
y = 0:b/div:b; % m


for j=1:size(y,2);

ystar=y(j)/a;

for i=1:size(x,2);

xstar=x(i)/a;

for m=1:2:10;

    am = (m*pi)/1;

    for n=1:2:10;

    bn = (n*pi)/(b/a);

    Fmn = ((-4)/((b/a)))*((alpha*dT*(1-v)/(hstar)))*(((-
1/(m*pi))*cos(m*pi))+(1/(m*pi)))*(((-
(b/a)/(n*pi))*cos(n*pi))+((b/a)/(n*pi)));

    w1(n) = -(Fmn/(am^2+bn^2))*sin(am*xstar)*sin(bn*ystar);

    end

    %Sums
    sumn(m) = sum(single(w1));

end


summx = sum(single(sumn));
w(i)=summx/b;
y_plot(i)=y(j);
```

```matlab
end

figure (1)
plot3(x,y_plot,w)
xlabel('X Axis')
ylabel('Y Axis')
zlabel('Out of Plane Deflection')
grid on
hold on


end
```

Matlab code to examine the center deflection

```matlab
clear
clc
format compact
tic
% Parameters and inputs AL6061 (NEED TO CHECK)

a = 1;%[0.01:0.01:.05];        % X Length, m
b = 1;%[0.01:0.01:.05];         % Y Length, m
t = 0.001;        % Thickness, m
z = 0;            % Location in Thickness, m
E = 69e9;         % Young's Modulus, Pa
v = 0.33;         % Poisson's Ratio, Dimensionless
alpha = 23e-6;   % Coef. of thermal expansion, 1/K
dT = 230;     % Temperature differential across plate, K
wo = 0;           %Intial Deflection

div=29; %Number of divsions along the x and y axis (1 minus of what is
desired)

% Thickness Aspect Ratio loop

ARy=b/a;



hstar=t/a;

% Center Plate Deflection or Max deflection
for k = 1:size(b,2)
x=a/2;
xstar=x/a;
y=(b(k))/2;
ystar(k)=y/a;

for m=1:2:10;

    am = (m*pi)/1;

    for n=1:2:10;
```

191

```matlab
    bn = (n*pi)/(b/a);

    Fmn = ((-4)/((b/a)))*((alpha*dT*(1-v)/(hstar)))*(((-
1/(m*pi))*cos(m*pi))+(1/(m*pi)))*(((-
(b/a)/(n*pi))*cos(n*pi))+((b/a)/(n*pi)));

    w1(n) = -(Fmn/(am^2+bn^2))*sin(am*xstar)*sin(bn*ystar);

    end

    %Sums
    sumn(m) = sum(single(w1));

end


summx = sum(single(sumn));
w(k)=summx/b(k);

end

Center_Deflection = w
```

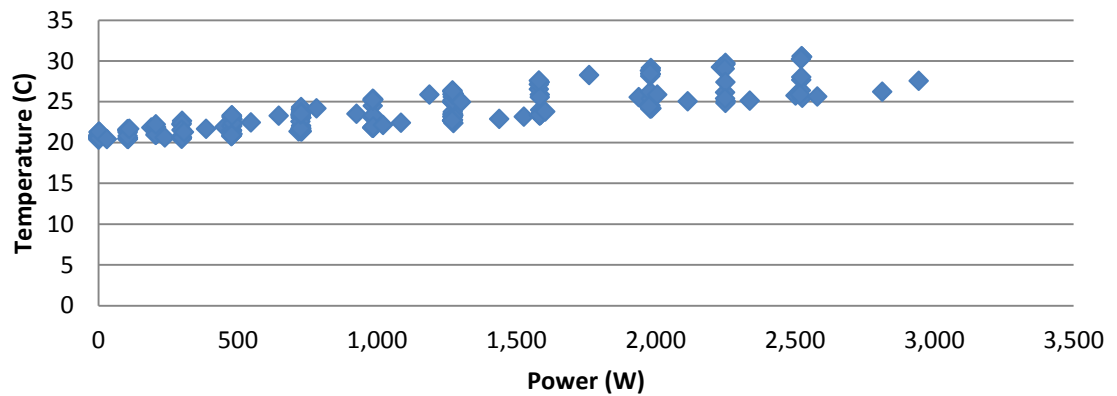## APPENDIX 3: CHAPTER 12 THERMOCOUPLE MEASUREMENTS
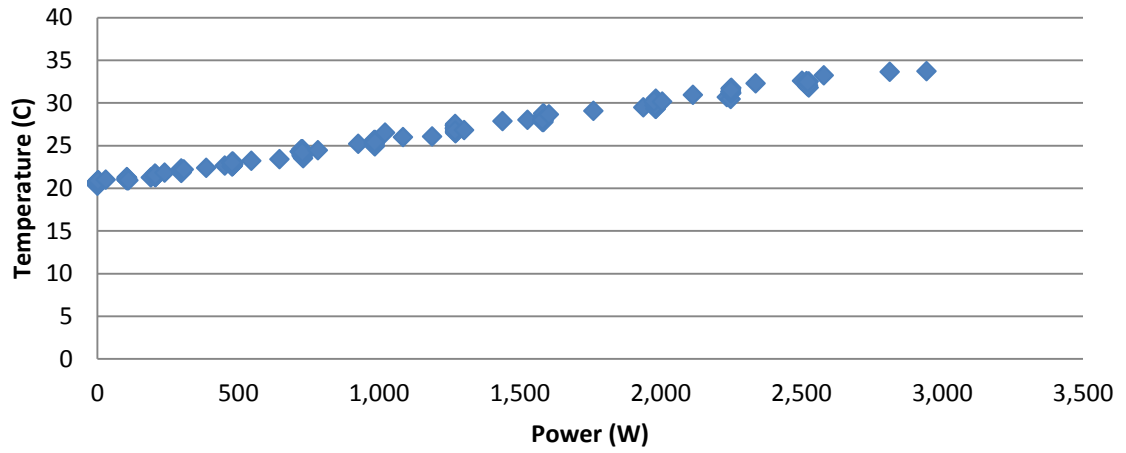

Figure 157. Thermocouple 1 temperatures compared to power

192

Figure 158. Thermocouple 2 temperatures compared to power
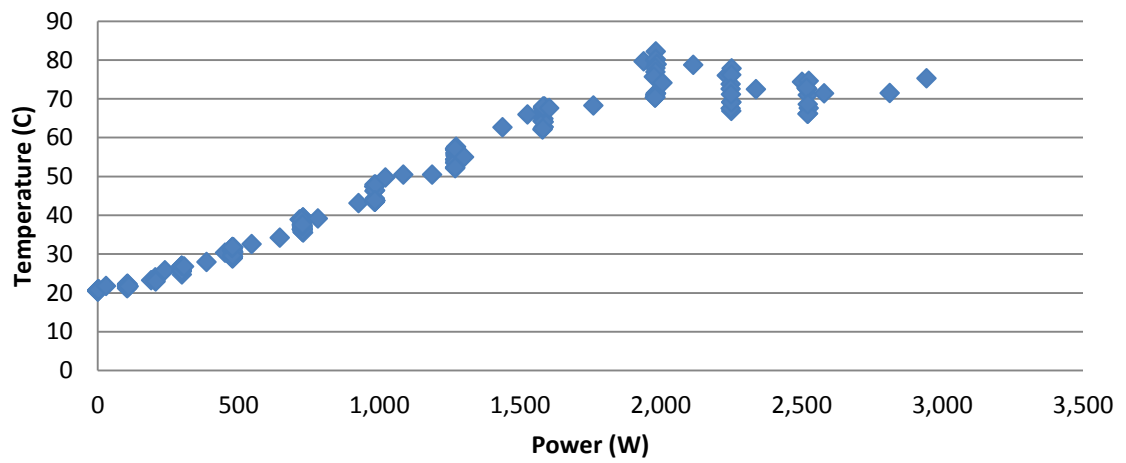
Figure 159. Thermocouple 3 temperatures compared to power
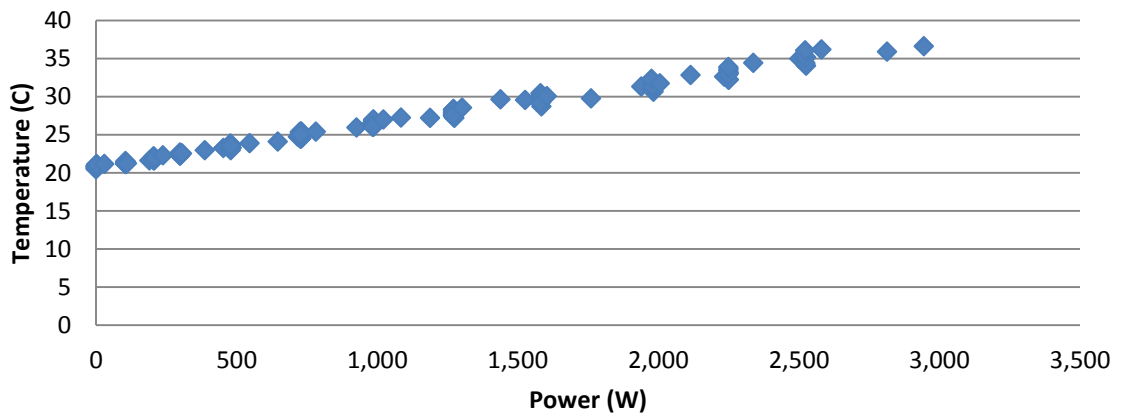
Figure 160. Thermocouple 4 temperatures compared to power
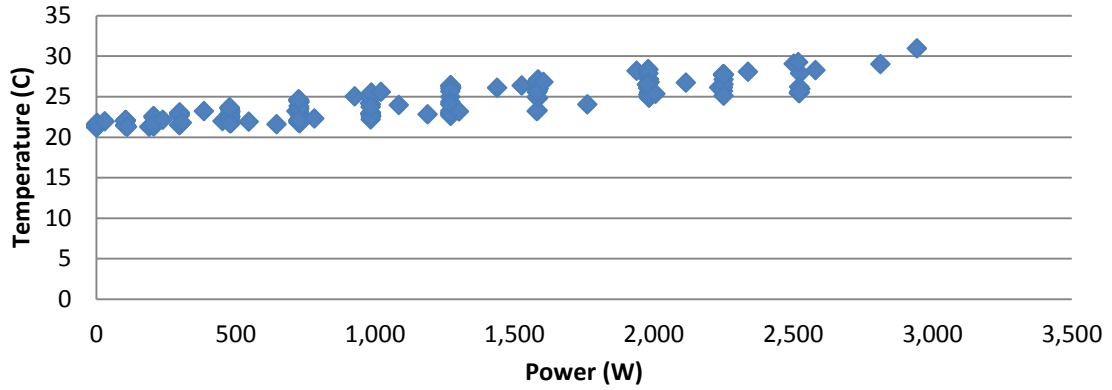
193

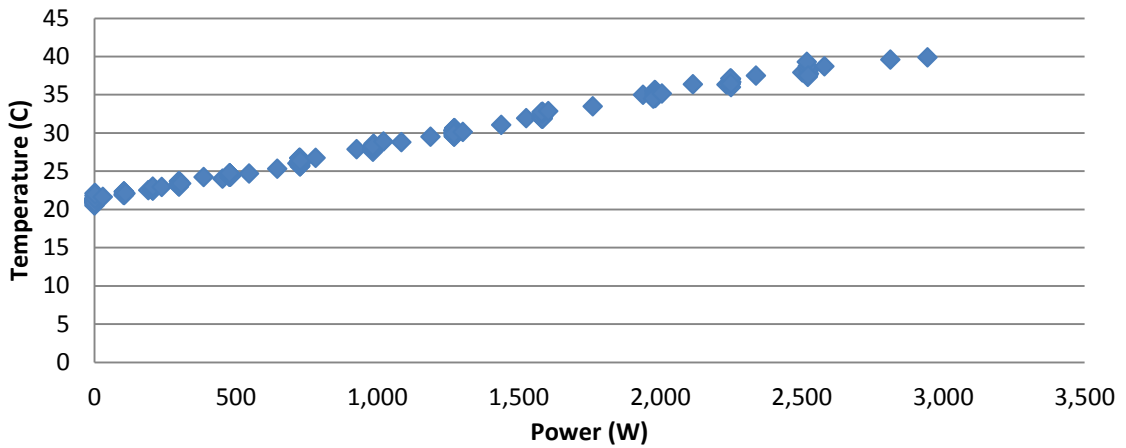**Figure 161. Thermocouple 5 temperatures compared to power**

Figure 162. Cladding 1 thermocouple temperatures
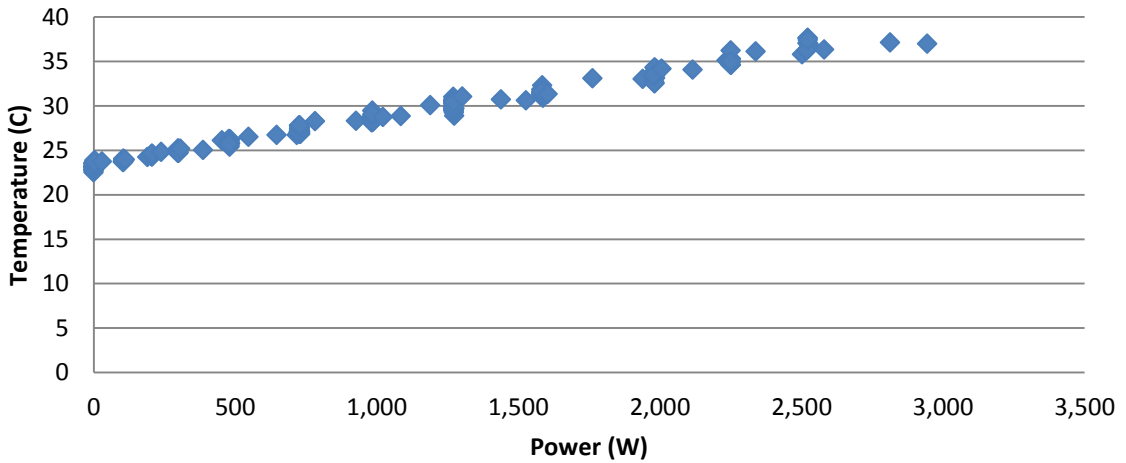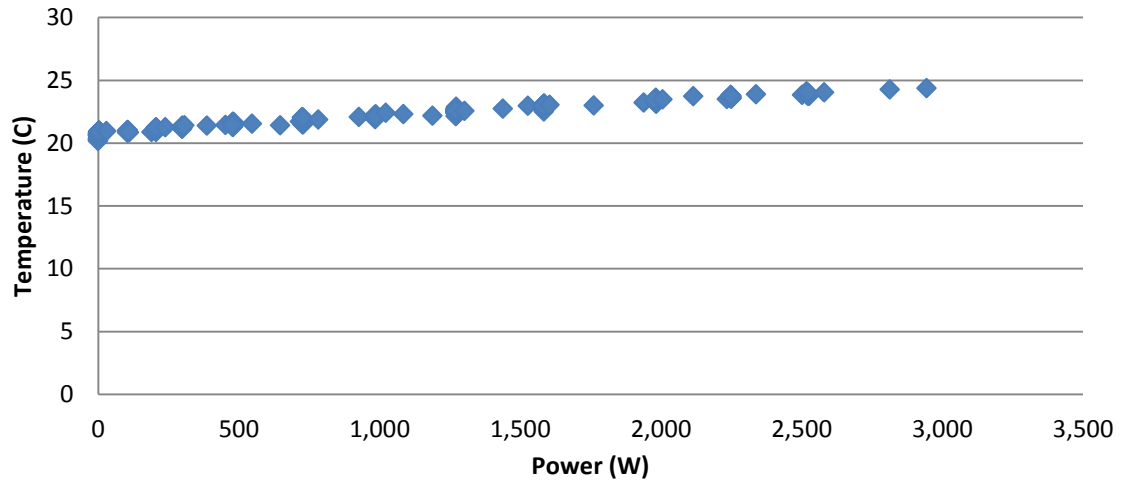

Figure 163. Cladding 2 thermocouple temperatures

Figure 164. Test section exit water temperature